Martin Landfahrer, Dipl.-Ing.

Efficient numerical modelling of real-size reheating furnaces in steel industry highlighting their heating characteristics

Doctoral Thesis

In fulfilment of the requirements
for the degree
Doctor of Technical Sciences

submitted to
Graz University of Technology

Faculty of Mechanical Engineering and Economical Sciences

Supervisor
Univ.-Prof. Dipl.-Ing. Dr. techn. Christoph Hochenauer

Second Supervisor
Univ.-Prof. Dipl.-Ing. Dr. techn. Harald Raupenstrauch

Graz, November 2019

Affidavit

I hereby declare that I am the sole author or this thesis, that I have not used any sources other those cited, and that I have made explicit reference to the sources of all material that was quoted, whether directly or indirectly. The document uploaded to the TUGraz online platform is identical to this text.

Graz,

Date	Signature

Abstract

In steel industry reheating furnaces represent one of the most energy consuming processing steps during steel forming. The common use of fossil fuels also leads to large amounts of CO_2 emissions. Further emissions of NO_x and CO also have negative impacts on the eco-environment. Thus, improving their efficiency is of great importance reducing their ecological footprint and comply with legal requirements. In this, increasing computer power leads to an intensified usage of Computational Fluid Dynamics (CFD). For this various models have been developed to cover all details of industrial applications. In this, the present thesis is intended to establish suitable numerical models to characterize two real-size industrial reheating furnaces within a reasonable time-frame with greatest accuracy possible. The furnaces are a rotary hearth and a walking beam type reheating furnace. Both furnaces differ greatly in their construction and product shape to be heated. This has a significant impact on thermal input and dwelling time affecting the heating characteristics of the steel. The numerical model developed is based on separation into two simulations related by an iterative strategy using the commercially available CFD ANSYS Fluent software. While the complex combustion calculation is treated in a steady-state simulation, the associated steel heating is considered in a transient simulation. This allows to reduce computational effort to a minimum, compared to fully transient models. Special attention has been paid to the correct replication of the way steel is transferred through the furnace. For this, a numerically efficient model has been developed, which can easily be linked to the iterative scheme. With this it is possible to integrate even complex movements of the steel, such as the rotary and translational movement within these furnaces. Within this, also different sub-models have been implemented and compared to each other. Also with the primary aim to find models as exact as possible with low computational complexity. For validation of the numerical models different measuring techniques have been used. Conditions within the combustion chamber have been determined by thermocouples and a gas analyser. However, focus was on the temperature profile of the exiting steel. For this, spatial profiles were measured using an Infrared Camera (IC) and a pyrometer, measuring the steel surfaces. Furthermore some steel goods have been equipped with several thermocouples to capture the temporal behaviour in specific points. After validating the results, the developed model presents a very economic solution allowing for extension without drastic increase in computational effort needed.

Kurzfassung

In der stahlverarbeitenden Industrie sind Wiedererwärmungsöfen die größten Energieverbraucher. Die zusätzliche Nutzung von fossilen Brennstoffen führt zudem zu hohen CO_2-Emissionen. Dieses Treibhausgas hat neben weiteren Emissionen von NO_x und CO, eine starke negative Auswirkung auf die Umwelt. Daher ist die Verbesserung der Effizienz solcher Öfen von großer Bedeutung, um ihren ökologischen Fußabdruck zu verringern und die immer strenger werdenden gesetzlichen Anforderungen zu erfüllen. In jüngste Zeit führt die Erhöhung der Computerleistung zu einer verstärkten Verwendung von CFD Simulationen. Diese werden auch in dieser Arbeit verwendet um zwei reale industrielle Wiedererwärmungsöfen zu untersuchen. Dabei handelt es sich um einen Drehherdofen und einen Hubbalkenofen. Beide Öfen unterscheiden sich stark in ihrer Konstruktion und der zu beheizenden Produktform. Dies hat einen erheblichen Einfluss auf den Wärmeeintrag und die Verweilzeit und beeinflusst zudem die Erwärmungseigenschaften des Stahls. Das entwickelte numerische Modell soll beide Öfen mit größtmöglicher Genauigkeit innerhalb eines angemessenen Zeitrahmens abbilden können. Es basiert auf der Aufteilung in zwei separate Simulationen, die durch eine iterative Strategie verknüpft sind. Die numerischen Untersuchungen werden mit der kommerziell erhätlichen Software CFD ANSYS Fluent durchgeführt. Während die komplexe Verbrennungsrechnung in einer stationären Simulation behandelt wird, wird die damit verbundene Stahlerwärmung in einer transienten Simulation berechnet. Dies ermöglicht es, den Rechenaufwand im Vergleich zu vollständig transienten Modellen auf ein Minimum zu reduzieren. Besonderes Augenmerk wurde auf die korrekte Nachbildung der Art der Stahlbewegung durch den Ofen gelegt. Zu diesem Zweck wurde ein effizientes Modell entwickelt, das leicht mit dem iterativen Schema verknüpft werden kann. Damit ist es möglich, auch komplexe Bewegungen des Stahls, wie die auftretende Dreh- und Schubbewegung, die in diesen Öfen vorkommen, zu integrieren. Weiters wurden auch verschiedene Submodelle implementiert und miteinander verglichen. Dies geschah auch mit dem Hintergedanken, möglichst genaue Modelle mit geringem Rechenaufwand zu finden. Zur Validierung der Auswahl der numerischen Modelle wurden verschiedene Messsysteme verwendet. Die Bedingungen in der Brennkammer wurden mit Thermoelementen und einem Gasanalysator bestimmt. Der Fokus lag jedoch auf dem Temperaturprofil des austretenden Stahls. Dazu wurde die örtliche Stahloberflächentemperatur mit einer Thermokamera und einem Pyrometer gemessen. Darüber hinaus wurden einige Stahlproben mit mehreren Thermoelementen ausgestattet, um das zeitliche Verhalten des Aufheizprozesses in bestimmten Punkten zu erfassen. Nach der Validierung der Ergebnisse stellt das entwickelte Modell eine sehr effiziente Lösung dar, die eine Erweiterung ohne drastischen Rechenaufwand ermöglicht.

Acknowledgements

Contents

List of Figures

List of Tables

Acronyms

BFG Blast Furnace Gas

CFD Computational Fluid Dynamics
COG Coke Oven Gas

DI   Direct Integration
DNS Direct Numerical Simulation
DO   Discrete Ordinates Model
DTRM Discrete Transfer Radiative Method

EAF Electric Arc Furnace
EBM Eddy Break up Model
EDC Eddy-Dissipation Concept Model
EDM Eddy Dissipation Model
EES Engineering Equation Solver

FVM Finite Volume Method

Hex Hexahedron

IC   Infrared Camera
ISAT In-Situ Adaptive Tabulation

LES Large-Eddy Simulation
lhs   Left Hand Side

MDoT Moving Direction of the Tube

NCV Net Calorific Value
NOx Nitrogen Oxides

ODE Ordinary Differential Equation
OEC Oxygen Enriched Combustion

PDF   Probability Density Function
Poly   Polyhedron

RANS   Reynolds-Averaged Navier-Stokes
RHF   Rotary Hearth Furnace
rhs   Right Hand Side
RSM   Reynolds Stress Model
RTE   Radiative Transfer Equation

S2S   Surface to Surface Model
SFM   Steady Flamelet Model

TC   Thermocouple
Tet   Tetrahedron

UDF   User-Defined Function
URF   Under-Relaxation Factors

WSGGM   Weighted Sum of Gray Gases Model

Symbols

Symbol	Description	Unit
Δm	Mass difference	kg
Ω'	Solid angle	Degree, Rad
Φ	Current transport value, Scattering phase function	-, -
Φ'	Fluctuation of the current transport value	-
$\overline{\Phi}$	Average of the current transport value	-
α	Absorptivity	-
α_c	Convective heat transfer coefficient	W/m^2K
ε	Emissivity	-
ε	Turbulent kinetic energy	m^2/s^2
η	Efficiency	-
κ	Extinction coefficient	$1/m$
κ_λ	Spectral extinction coefficient	$1/m$
λ	Thermal conductivity	W/mK
λ_{mod}	Modified thermal conductivity	W/mK
μ	Dynamic viscosity	kg/ms
μ_t	Turbulent viscosity	kg/ms
ν	Kinematic viscosity	m^2/s
ω_i	Weighting factor in the weighted sum of gray gases model	-
$\overline{\omega}_F$	Reaction rate defined by the fuel mass fraction	kg/m^3s
$\dot{\omega}_k$	Reaction rate of species k	kg/m^3s
$\overline{\omega}_{O_2}$	Reaction rate defined by the oxidizer mass fraction	kg/m^3s
$\overline{\omega}_P$	Reaction rate defined by the product mass fraction	kg/m^3s
$\dot{\omega}_T$	Heat release due to combustion	W/m^3
ρ	Density	kg/m^3
$\overline{\rho}$	Mean density	kg/m^3
$\sigma_{s,\lambda}$	Scattering coefficient	$1/m$
σ	Stefan-Boltzmann constant 5.670373×10^{-8}	W/m^2K^4
τ_λ	Spectral optical thickness	-
τ	Stress tensor	N/m^2
ξ	Stochiometric oxygen to fuel mass ratio	-

Symbol	Description	Unit
A	Area; Model constant	m^2, -
B	Model constant	-
$b_{i,j}$	Polynomial coefficients in the WSGGM model	$1/\text{K}^{\text{j}-1}$
$C_1, C_2, C_{1,\varepsilon}, C_{3,\varepsilon}$	Model parameters in the $k-\varepsilon$ model	-
C_g, C_d	Model constant in the SFM model	-
cp_i	Heat capacity of the media	J/kgK
C_μ	Model constant or variable in the $k-\varepsilon$ model	-
cp_s	Heat capacity of the steel	J/kgK
$\overline{D_k}$	Mean species molecular diffusion coefficient	m^2/s
E	Activation energy for the Arrhenius approach	J/mol
e	Mass-specific inner energy	J/kg
$\hat{e}$	Mass-specific total energy	J/kg
f	Mixture fraction	-
$\overline{f_m}$	Mean mixture fraction	-
$\overline{f^2}$	Mixture fraction variance	-
$\vec{F}$	External body forces	$\text{kg}/\text{m}^2\text{s}^2$
G_b	Source term for turbulent kinetic energy due to buoyancy	m^2/s^2
G_k	Source term for turbulent kinetic energy due to velocity gradients	m^2/s^2
$\vec{g}$	Gravity vector	m/s^2
h_k	Mass-specific enthalpy of species k	J/kg
$I_{black,\lambda}$	Radiation Intensity of a black body per unit wavelength	$\text{W}/\text{m}^2\text{sr}$
I_λ	Radiation Intensity per unit wavelength	$\text{W}/\text{m}^2\text{sr}$
$I_{\overline{\lambda}}$	Fraction of Radiation Intensity	$\text{W}/\text{m}^2\text{sr}$
k	Absorption coefficient	1/m
k	Turbulent dissipation rate	m^2/s^3
k_i	Absorption coefficient of each gray gas	1/m
$k_{a,\lambda}$	Spectral absorption coefficient	1/m
k_l	Linear oxidation rate constant	$\text{kg}/\text{m}^2\text{s}$
k_p	Parabolic oxidation rate constant	$\text{kg}^2/\text{m}^4\text{s}$

Symbol	Description	Unit
k_{p0}	Preexponential factor for the parabolic oxidation rate	kg^2/m^4s
L	Beam length	m
Le	Lewis number	-
$\dot{m}_f$	Mass flow rate of the fuel	kg/s
$\dot{m}_i$	Mass flow rate of the media	kg/s
$\dot{m}_s$	Mass flow rate of the steel	kg/s, t/h
n	Refractive index of a medium	-
N_c	Number of polynomial coefficients	-
N_g	Number of gray gases	-
Nu	Nusselt number	-
PL	Product of the sum of all partial pressures and path length	kg/s^2
Pr_ε	Prandtl number for ε	-
Pr_k	Prandtl number for k	-
Pr_t	Turbulent Prandtl number	-
p	pressure	Pa
$\dot{Q}$	External heat source	W/m^3
$\dot{Q}_{Air}$	Heat flux of the combustion air	W
$\dot{Q}_{Cond}$	Conductive heat flux	W
$\dot{Q}_{Conv}$	Convective heat flux	W
$\dot{Q}_{Flue\ gas}$	Heat flux of the exiting flue gas	W
$\dot{Q}_{Fuel}$	Heat flux of the fuel	W
$\dot{Q}_i$	Heat flux	W
$\dot{Q}_{NCV}$	Heat flux due to the net calorific value	W
$\dot{Q}_{Rad}$	Radiative heat flux	W
$\dot{Q}_{Rad_{1 \to 2}}$	Net radiative heat flux between two solid walls	W
$\dot{Q}_{Rest}$	Rest of the heat losses in industrial furnaces	W
$\dot{Q}_{Steel}$	Heat flux transferred to the steel	W
$\dot{Q}_{Wall}$	Heat flux through walls	W
$\vec{q}_i$	Energy flux vector	W/m^2
q_{in}	Incident heat flux	W/m^3
q_r	Radiation flux	W/m^3
R	Universal Gas constant	J/molK
$\vec{r}$	Position vector	-

Symbol	Description	Unit
S	Gas layer thickness	m
S_{Ref}	Constant wall thickness of the scale layer as used in the numerical domain	m
S_{Scale}	Locally calculated scale layer thickness	m
$Sc_{t,k}$	Turbulent Schmidt number for species k	-
$\vec{s}$	Direction vector	-
$\vec{s}'$	Scattering direction vector	-
T	Temperature	K
T^0	Reference Temperature	K
T_g	Gas temperature	K
T_i	Temperature of the media	K
T_{in}	Inlet temperature of the steel	K
$T_k{}^0$	Temperature of species k in infinity	K
T_{out}	Outlet temperature of the steel	K
T_s	Steel Temperature or Surface Temperature	K
t	time	s
$\vec{V}_k$	Diffusion velocity vector of species k	m/s
$\vec{v}$	velocity vector	m/s
x, y, z	Coordinates for cartesian coordinate system	m
Y_k	Mass fraction of species k	-
$Y_k{}^0$	Mass fraction of species k in infinity	-
$\overline{Y_k}$	Favre averaged Mass fraction of species k	-
Z_i	Atomic mass fraction for atom i	-
$Z_{i,f}$	Atomic mass fraction for atom i in the fuel inlet stream	-
$Z_{i,ox}$	Atomic mass fraction for atom i in the oxidizer inlet stream	-

1

Introduction[1]

This chapter presents an overview about industrial reheating furnaces. Special attention is paid to general furnace descriptions and discuss the research that has been done in the numerical description such applications. These cover model development, and evaluation of various characteristics. This PhD thesis is based on five publications that were written by the author under the supervision of Prof. Christoph Hochenauer. They were published in peer-reviewed journals and prove to be a valuable contribution to the scientific community.

[1] M. Landfahrer, R. Prieler, B. Mayr, et al. Development of a numerically efficient CFD model to predict transient temperature distribution of mother tubes moving translative and rotative through a gas fired furnace. *Applied Thermal Engineering*, **123** (2017): 290–300.

[2] M. Landfahrer, R. Prieler, B. Mayr, et al. Characterization of the temperature distribution on steel tubes for different operating conditions in a reheating furnace using CFD and three different measuring methods. *Applied Thermal Engineering*, **133** (2018): 39–48.

[3] M. Landfahrer, C. Schluckner, R. Prieler, et al. Numerical and experimental investigation of scale formation on steel tubes in a real-size reheating furnace. *International Journal of Heat and Mass Transfer*, **129** (2019): 460–467.

[4] M. Landfahrer, C. Schluckner, R. Prieler, et al. Development and application of a numerically efficient model describing a rotary hearth furnace using CFD. *Energy*, **180** (2019): 79–89.

[5] M. Landfahrer, C. Schluckner, H. Gerhardter, et al. Numerical model incorporating different oxidizer in a reheating furnace fired with natural gas. *Fuel*, **268** (2020): 117185.

The first publication [1] presents a numerical model able to represent a walking beam type reheating furnace in detail. It is used to heat seamless tubes. The aim was to develop a model able to incorporate the translational and rotatory motion of the steel, as passing through the furnace. Measurements were performed on the real size furnace at the voestalpine Tubulars

---

[1]Segments of this chapter have already been published in [1–5]

GmbH & Co KG, revealing that there was great resemblance between the numerical results and the real behaviour.

The second paper focuses on extensive model evaluation [2], comparing the numerical results results to the results that were obtained by typical measuring techniques used in high temperature processes. These techniques include an infrared camera, a pyrometer and a test steel blank equipped with thermocouples and dragged through the furnace. In the article, the results are compared to the numerical outcome, demonstrating the benefits of each measuring technique. This was further shown on the basis of a modified heating characteristic.

The third paper [3] provides an extension of the numerical model. It is now able to characterize important scale formation during the heating process dependent on local species, steel composition and temperature. It is able to incorporate the insulating effect of the scale layer formed. To validate the model, results are compared to a simplified analytical approach and measurements taken at the real furnace.

The numerical model was then adapted to do research on a rotary hearth furnace, as presented in the fourth publication [4]. Beside the correct representation of the heating characteristic, focus was on identifying causes for local damages due to thermal stresses. In addition, suggestions for improvements to eliminate weak points are presented in this paper.

The last paper [5], provides a numerical approach to include the usage of several oxidizer and fuels in a single furnace. This is important for many older furnaces which are still in operation today. It was found that their performance can be increased by adding e.g. additional burners, or by using Oxygen Enriched Combustion (OEC). The model, which is introduced in this paper, is kept as simple as possible, allowing an easy applicability for all types of furnaces.

1.1. Industrial Reheating Furnaces

In the fast paced industrial world of today endeavours to achieve ever higher product quality with decreasing production costs are becoming ever more important. In steel industry the effort is even higher, due to of vast energy requirement in its processes. The sector has thus long been the goal of different and intensive investigations. Especially reheating furnaces are a particular focus due to their high energy consumption. Their main function is the reheating of steel: the heat imparts the required plasticity to the steel and enables a subsequent processing of it with shaping tools. The processing include, for example, rolling-, forging- and stamping processes. Another reason for heat treatment is the modification of the mechanical, physical and chemical properties of the steel.

The first furnaces date back to the mid-19th century. Since then, furnaces have evolved, leading to changes in furnace sizes and also introducing the separation into heating zones. This changes made it possible to increase steel dimensions, which required constant adjustments of the burners and their orientation. Industry currently uses different types of reheating furnaces, which can be classified by different characteristics. The following sections will discuss the two main classifications of industrial steel reheating furnaces. The aim is to provide a general overview of such furnaces. For further details on this wide-ranging subject, the reader is referred to relevant literature [6, 7].

Method of Heating

In modern furnaces, two main processes are available for heat generation. One is the use of electrical energy, the other is chemical bound energy. In reheating processes, former is mostly based on inductive or resistance heating, protecting the steels surface from mechanical stresses. Nevertheless, it is not commonly used, due to restrictions concerning the maximum temperature which can be achieved. The maximum temperature depends on the material's Curie-temperature. For low carbon steels, it is about $770\,°C$. This is when it loses its magnetic properties. Thus, it can be used for preheating the material or holding the temperature level. Electric heating, however, is very often used for melting metal scrap in Electric Arc Furnaces (EAFs). Besides this, the utilisation of electric energy is limited due to the relatively high costs of the electricity needed.

The most widely used method in steel industry is heating combustion processes. In this various fuels or oxidizer are available. Classification can be done regarding the fuel type used. While modern furnaces and burners are able to handle solid, liquid or gaseous fuels, the fuel of choice is usually Natural Gas, Blast Furnace Gas (BFG), Coke Oven Gas (COG) and oil. Different burner types have been developed: some handle several fuels, others only work with a single fuel. These differ in the generated flame shapes, lengths and induced turbulences that occur in the flow field. Furnaces can be further classified according to the location of the burners. Thus, furnaces can be "top-fired", "side-fired", "bottom-fired", or a combination of all. Oxidizers, on

the other hand, can either consists of, mostly preheated, air to pure oxygen. This effects the emissions of Nitrogen Oxides (NOx) drastically.

Method of Steel Charging and Movement

In general furnaces in steel industry are based on batchwise operation are distinguished from those based on continuous operation. Most steel reheating furnaces are based on the latter principle. In furnaces based on continuous operation, steel is heated while is transported through the furnace. For steel transport, different mechanisms for steel transportation are available, denominating the furnaces.

The most widely used types of furnaces in the steel industry are the walking beam, walking hearth and pusher type reheating furnace. In all of these, steel transportation takes place in a horizontal and straight manner. The walking beam reheating furnace transports and supports steel using a complex skid system. This system consists of fixed beams, which keep the steel in place, while walking beams, are used for moving it along. In most cases, the skid system is water cooled to withstand the hot atmosphere within the combustion chamber. Figure 1.1 shows the sketch of such an furnace, highlighting the skid system, including the lifting mechanism, the burners and the steel good. In such furnaces, a common problem that arises is the shielding of heat fluxes near the skid system, leading to cooler spots, the so-called skid marks. This construction type allows heating from the bottom, improving heating characteristics, while impacting skid mark severity in a negative way. Side-firing is also possible, including combinations with top and bottom firing. The charge and discharge mechanisms vary between different manufacturers and are made to meet each customer's individual needs. This means that the furnace can be either be charged or discharged from a central location or from the side. There is no general construction form and each individual furnace is built according to the customer's demands.
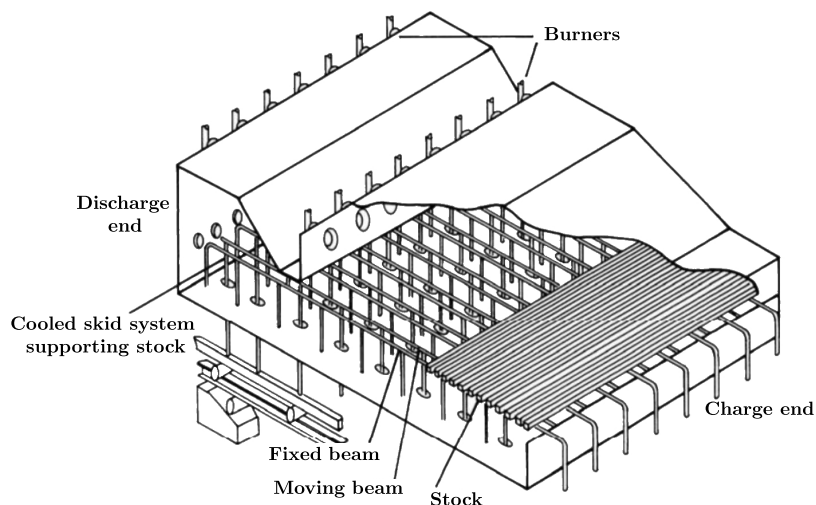
Figure 1.1.: Sketch of a walking beam type furnace adapted from [8].

In the walking hearth furnace, the steel rests on the furnace floor. Transportation is similar to the walking beam type furnace: it is done by means of the walking movement of beams. This prevents any skid mark formations. In both furnaces described, the transportation process is smooth since steel is carefully lifted and moved along. This is essential when dealing with steel with quality requirements. However, the heating characteristics differ greatly since this type of furnace can solely be top-heated.

Another widely used furnace type is the pusher type. In pusher type furnaces, steel is moved by inserting another steel good. With each good inserted, the whole set is pushed further through the furnace. The steel rests on a hearth, a skid system or a combination of the two. Thus, this kind of furnace can also be bottom-heated. However, the length of a single pushing action is limited to the dimension of the steel. Also, it is quite likely for damages to occur on the surface of the steel due to it scratching on the furnace bottom.
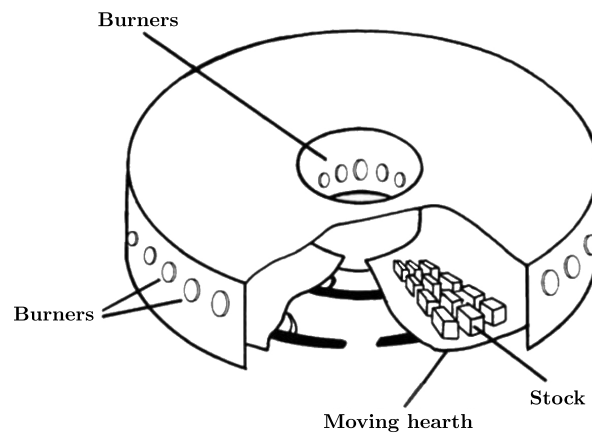
Figure 1.2.: Sketch of a rotary hearth furnace adapted from [8].

A special form of walking hearth furnaces are Rotary Hearth Furnaces (RHFs). These have a wide range of applications: they are used for anything from iron bloom reheating and iron processing to waste reclamation processes. In literature, a large number of works investigate the direct reduction of metallurgical dusts [9–11] and pellets [12]. In terms of bloom heating, these furnaces are quite multifunctional and can be used for hardening processes, reheating, tempering, annealing and much more. Figure 1.2 shows a sketch of a RHF for heating steel blooms. The furnace can be divided into a stationary part and a moving part. The burners are located on the outer and inner stationary furnace walls. In new furnace designs, sometimes even ceiling burners are used. The product to be heated is put on the moving furnace floor and is transported in a circular manner. The entry and exit openings are thereby set close together. Compared to other furnaces, the entire hearth is moving: it is rolling on rails. The main advantage of such furnace types is their outstanding hearth length compared to other types. Still, compared to other furnace designs,the hearth area efficiency is relatively low, due to the complex design. This leads to higher acquisition costs as well as to a high amount of maintenance needed for the seals and refractories [6].

Apart from the furnace types that have already be mentioned, there are countless other types. They will not be discussed in detail here since this chapter is only intended to give a short overview of reheating furnaces used in the industry. Some of the main problems of the furnaces have already been mentioned. They are the skid marks, firing technique and emissions. Once we know more about those furnaces, furnace operation can be optimized. For this, numerical investigations using CFD are a very important tool. Numerical investigations make it possible to modify parameters and to demonstrate their impact on the heating process different without having to perform any measurements. Furthermore, areas exposed to e.g. high thermal stresses can easily be detected and thus, adequate precautions can be taken. In addition, energy efficiency can be examined and even extreme cases can be investigated.

1.2. State of the Art

The demand of industry with regard to increasing production and efficiency with the least possible effort, has led to an increasing number of investigations in recent years. Especially in the steel industry, efforts have been made to improve the understanding of reheating furnaces and show some of the most important influences during the heating process. Expanding our knowledge of such furnaces allows us, among other things, to improve the heating quality of the steel, fuel efficiency and emissions abatement technologies.

Computational models are used to demonstrate weak points and possible improvements. Mayr et al. [13] developed a simple approach, to calculate all heat fluxes, as well as gas and wall temperatures based on thermodynamic correlations. Their approach can be applied to any furnace, from lab scale up to industrial scale. Chen et al. [14] used an algorithm to discover areas of the furnace with the greatest potential to improve slab thermal efficiency. Other algorithms, such as those of Hu et al. [15], are able to improve heating accuracy and average deviations using fuzzy rules. With increasing computer performance, more and more simulations are used. In the course of this many models of different complexity have been developed. The simplest models consider the whole furnace as a set of single zones with constant wall and gas temperature. Kim et al. [16] has been one of the first using this so called "zone model" in a walking beam type furnace. The results have been compared to measurements revealing slight differences due to neglected convection. Han et al. [17] has extended the model comparing slab heating for different wall- and gas temperatures depending on fuel input. Variation in fuel feed distributions revealed an increase in temperature gradients within the exiting steel, with increasing soaking zone temperatures. These simple approaches allow the investigations of varying parameters, such as the emissivity of the steel and the furnace walls, within a reasonable time period. Thus, they have become a precious tool for scientists, developers as well as operators that allow them to investigate the impact of various factors on the heating process. Nevertheless, the neglected gas flow inside the furnace leads to an ideal uniform temperature profile of the steel. In real-size industrial furnaces this represents an ideal, non-realistic condition.

Improvements of the developed computational models allow us to incorporate convective heating. Although the heating of the raw steel product is mainly caused by radiation, the hot gas flow inside the combustion chamber also has a significant impact on the steel heating process. Emadi et al. [18] considered a walking hearth furnace based on the zone model. Local differences in convective heat flux has been taken into account by a varying convective heat transfer coefficient. The model is based on the findings of Lebedev and Sokolov [19] taking into account local gas mass flow rates. Additionally, gas properties, area and equivalent diameter are included. This results in a maximum difference in transferred heat flux, using this modified coefficient and an assumed constant value, of approximately a factor of 2. This shows that gas flow has significant influence on the heating characteristics of the steel. Its importance in furnaces, causing possible temperature inhomogeneities, should not be underestimated. This has been proven by Singh and Talukdar [20], comparing two models based on the zone model, calculating the heating of the slabs by using MATLAB, with a model solely using FLUENT. In FLUENT the periodic movement of the slabs is realized by a User-Defined Function (UDF). In most of the publications referred to the influence of the convective heat transfer is completely neglected and steel is heated by radiation only.Another publication by Singh and Talukdar [21] compared different models based on the zone-model with constant wall and gas temperatures and a model which additionally implies the convective part. This was realized by injecting hot flue gas though burners into the combustion chamber. This resulted in a significant heat flux imbalance, which translates across the furnace width to the steel. The calculated temperatures also revealed an improved accordance with measured data. This confirmed the statement about the importance of convective heating in real furnaces.

Increases in computer performance allowed the development of more complex models, including fuel combustion. Among the first researchers who payed attention to the turbulent reactive flow were Kim et al. [22]. Their model is based on a steady-state simulation of the furnace providing detailed spatial heat fluxes on the slabs. The heat flux profiles were further used in a two-dimensional simulation considering slab heating. A clear tilt in the heat flux distribution over the steel width becomes notable. This is evoked by the lateral burners, causing a non-uniform temperature distribution within the combustion chamber. A more detailed description of the steel heating is provided by Han et al. [23] considering the heating of a slab in a bench scale furnace. Therefore, transient simulations have been performed revealing a resemblance with measured temperatures for gas- and steel. This model has been further developed to incorporate the heating process in a walking beam type reheating furnace [24]. The periodic transport of the slabs is described by a UDF. A clear impact of the flames and the skid system can be seen. The big drawback of this model is the high computational demand for the transient simulation. However, a comparison with measurement data and information about computing time needed is pending. Further investigation of a walking-beam type reheating furnace was performed by [25]. The software STAR-CD was used to calculate the furnace. The results reveal a good accordance with measurements, although several assumptions were made, such as an adiabatic treatment of the walls. Casal et al. [26] presented a new method to depict the movement of the steel. Introducing a new source term to the energy balance

equation of the solid, the energy contained in a billet is moved forward periodically. Due to this adaptation the whole furnace can be treated as stationary, which allows a significant reduction in computational time. A big advantage to include the combustion process, is the possibility to investigate emission reduction, such as CO_2 and NO_x [15, 27–29]. Mayr et al. [30] investigated the effects of different oxygen enrichments on heat flows and temperatures inside a lab-scale furnace. The simulations show only slight deviations from measurement, revealing a fuel saving and an increase in efficiency for oxygen enriched combustions. Also extensive validation and comparison of different combustion models has already been performed for example found in [31–33] for example. These kind of models are also a very precious tool for burner investigations, developments and improvements. This is addressed by several publications [34–38].

The great diversity of models, differing in the computational effort needed, allow us to select the most suitable for the given problem. Simple approaches allow fast statements about the impact of billets emissivity [39, 40] and the emissivity of the furnace walls [40] on the heating characteristics of billets to be made.

Improvements to furnace efficiency have also been investigated [41], varying the distance between the billets influencing the steel throughput. More complex models allow one to investigate the impact of the skid system on the temperature distribution in the billet [21, 39, 40]. The individual beams of the skid system cause local reduced heat fluxes to the billet and skid mark severities, which clearly needs to be decreased. The temperature difference can be affected by the shape and height of the skid buttons as shown in [22]. Han et al. [42] has investigated the impact of different steel residence times on the skid mark severity. An optimum residence time has been found, keeping the temperature gradient caused by the skids below the desired 50 °C. Complex models are also able to investigate the influence of scale on billet temperature. Several theoretical models are present in the literature, dealing with the correct description for scale formation, physical properties etc. Whereas, Jang et al. [43] is one of the few who studied numerically the insulating effect during steel heating. Even though several simplifications needed to be made, reasonable values were received. A similar investigation was done by Jaklič et al. [44], investigating the impact of the insulating scale layer during billet transport. The negative effect of the insulating effect on the heat transfer of superheater tubes has been demonstrated by Qi et al. [45]. The temperatures of the superheater tubes reach critical values and, thus, different materials have to be used to avoid overheating effects. Also the impact of different air humidities have been investigated by Cheng et al. [46]. However, the impact of scale on the steel surface structure is negligibly small [47, 48]. It can be concluded, that temperature and time affects the composition of the scale, but has negligible influence on the steel roughness. However, large amounts of detached scale can also reach dimensions that influence flow patterns inside the combustion chamber of furnaces as evaluated by Tang et al. [49].

Independent of the model complexity, experimental data are necessary to validate the numerical results. Most investigations, therefore, use the steel- and gas temperature. Dependent on the

measuring problem, sometimes one is restricted to use a specific measurement technology. Beside this, applicability in other areas, such as cutting processes, is given to detect and prevent temperature peaks which prolong the life of tools [50]. The heat flux can also be measured using an Infrared camera, as shown by Švantner et al. [51]. In general, temperature measurements inside the combustion chamber are not an easy undertaking; thus, several measuring methods have been developed for that purpose. Thermocouples represent the most common measuring type in steel industry. Temporal heating characteristics of the steel can be measured by trials. Han et al. [52] equipped steel to measure the temporal behaviour during heating in a bench-scale reheating furnace. In industrial-size furnaces steel is equipped with several thermocouples and is traced through the furnace. The big disadvantage is the limitation to a few thermocouples to be used. Thus, no statement about an actual temperature variation on the steel surface can be made. Instead, distinctive points inside the steel good can be measured. Therefore, for example, the essential core temperature, important for voluminous steel blocks, can be measured.

In some cases, however, it is not possible to use thermocouples, and a contactless method is widely used in their place. Contactless methods include the use of infrared cameras, radiation pyrometers, thermocolours, and materials with known melting points or the ability to change their microstructure. Such techniques are mostly fast, accurate, and economical. The disadvantage of these techniques is the limited application to measurements inside the combustion chamber. Here, the extreme atmosphere impedes their usage. Beside the usage in the steel industry, most techniques are also applicable in other working areas. Astarita [53] showed that it is possible to use infrared thermography to measure wall convective heat fluxes and surface flow fields. In the steel industry however, the temperature of the steel as it enters and exits the furnace is mostly recorded by means of radiation pyrometers. The temperature of the exiting steel is of especially great importance for its subsequent processing. Here, problems can occur and reduce product quality if the temperature of the steel is too low or if the product exhibits an excessively wide temperature range. In literature only a few works use contact-less methods to validate the numerical results [26, 54, 55]. All of these capture a clear temperature inhomogeneity along the steel axis.

1.3. Motivation and Aim of this Thesis

The high demand of the industry for numerical investigations of real size furnaces provokes constant developments of the numerical models. Researchers strive for faster solutions with an even higher information content. This thesis intends to develop numerical models able to characterize two real-size industrial furnaces for the production of seamless tubes, within a reasonable time and with the greatest accuracy possible. The models are based on the commercially available CFD ANSYS Fluent software, using implemented models and customized codes.

The steel processed at the voestalpine Tubulars GmbH & Co KG is delivered from the company's own steel plant. It comes in the shape of round steel blocks. The individual production steps of the tube-forming process are visualized in Figure 1.3. The main steps are characterized by heating and subsequent forming of the steel block for it to become a finished shape tube. In the following, a short description of each step is provided:

1. Heating of the blooms in the rotary hearth furnace to approx. 1,280 °C.
2. Forming into shells in the cross-roll piercing mill.
3. Rolling of the hollows on the push bench.
4. Removal of the mandrel bars, which are inside the hollows, using a reeler.
5. Reheating the hollows in a reheating furnace to approx. 1,000 °C.
6. Rolling of the tubes into defined diameters in the stretch-reducing mill, obtaining a certain wall thickness.
7. Cooling.
8. Cutting into the desired lengths, using layer saws.
9. Further processing into the specific end product in additional production steps, or shipping.
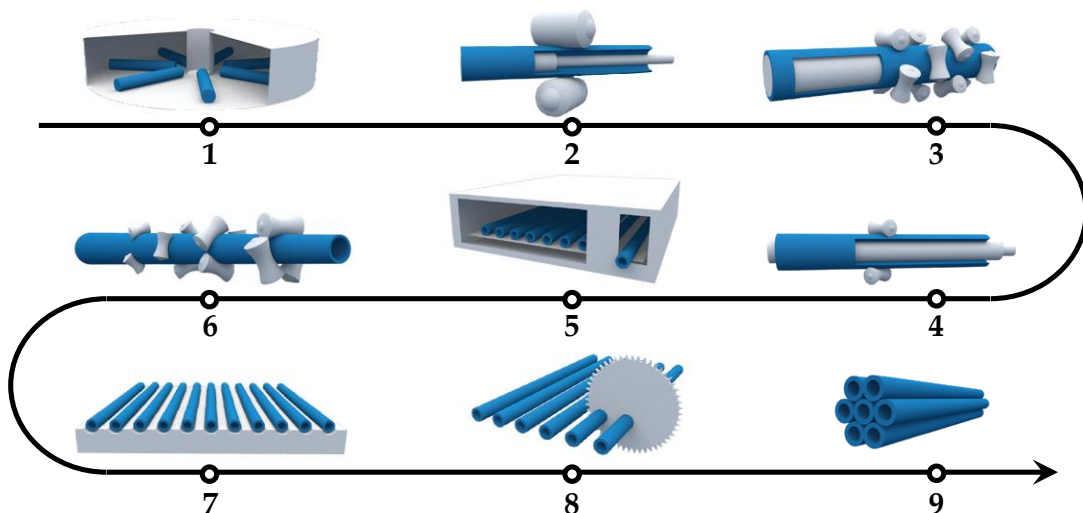
Figure 1.3.: Schematic visualization of the steps in the tube-forming process adapted from [56]

One furnace investigated within this thesis is the rotary hearth furnace, which is used to complete the first step in the tube forming process as shown in Figure 1.3. After some steel forming steps, the hollows are reheated in a walking beam type reheating furnace which is used in step five. This furnace is the other furnace which has been investigated within this thesis. The two furnaces differ greatly in their construction, and in the product shape to be heated. The different steel shapes to be heated significantly affects thermal input as well as the heating characteristics and heating time of the steel.

Nevertheless, a numerical model should be introduced to cover both furnace types. The development steps correspond to the structure of this work and can be roughly summarized as follows:

- Recording of process data and measurements.
- Numerical investigation of a common operating case.
- Characterizing the influence of different factors on steel heating.
- Numerical investigation of a modified case.

In regards to industrial furnaces, data collection usually plays a subordinate role. In many cases, data is recorded, but not stored. Sometimes several readings are combined to save storage memory. Both cases should be prevented since valid data is much needed for future investigations. In fact, it is quite simple: the more data we have, the more detailed the validation process will be. As a result, this will lead to more detailed models. Moreover, the different measuring methods used for data recording have to be validated. In furnaces, the temperature of the hot exiting steel is of utmost importance. In this thesis, an infrared camera, a two-colour pyrometer, and the results of a test tube equipped with four thermocouples are compared. These methods differ in their measuring principles, as well as in terms of their spatial and temporal resolution. While the infrared camera and the pyrometer are utilized to record the temperature distribution of the entering and exiting steel, the test tube provides information on the temporal heating characteristics. The atmospheric condition inside the combustion chamber is also of great importance as it influences the heating characteristics and scale formation. Therefore, the following values are usually measured inside the combustion chamber: pressure, temperature and oxygen content. Those values are used to control the furnace. A detailed exhaust gas analysis system is installed before discharge of the flue gases into the external atmosphere. This is necessary to comply with environmental regulations, but it also represents a further possibility for validation. In industrial furnaces, these measuring techniques and points are always present. Additional installations for measurements require modifications and openings, which are to be avoided. Therefore, the main question is:

- What is the optimal measuring technique in industrial furnaces and what is the optimum number of measuring locations to allow reasonable validation?

After the preparation of process data, the numerical simulations can be performed. This requires an accurate transformation of the real furnace geometry into a numerical model. Due

to the great age of many furnaces in operation, not many digital drawings exist, resulting in a great constructive effort. At this stage, simplifications have to be made, to minimize the computational effort needed. These should be considered separately to analyse their influence on different aspects. Besides the geometrical aspect, the numerical models used have to be examined. On the one hand the models must be compared to each other finding the most suitable one, for example regarding computing demand. At the same time, comparison with measured data is crucial to prove their accuracy.

- Is there an optimum degree of simplification to ensure a maximum degree of detail while minimizing computational effort?
- What is the most suitable model to reflect the real behaviour as best as possible?

Based on the optimized model, suggestions for improving the real furnaces can be made. In this context, different heating characteristics and their effect on efficiency and steel exiting temperature and possible imbalances have been investigated. Also, the cause for damages due to excessive thermal load has been revealed and proposals for improvements are made. Another very important factor in steel production is the formation of scale on the steel surface. This undesirable oxidation of the metal, on the one hand, leads to mass losses. On the other hand, the insulating effect provokes an increase in heat flux to the steel at a constant target temperature. An existing numerical model to include the scale formation, depending on the local steel temperature and surrounding atmosphere, has been modified to integrate the insulating effect.

2

Modelling

The following sections provide deeper insight into main characteristics of reheating furnaces. A theoretical background is provided to describe occurring heat transfers. These constitute the basis of the numerical models and their selection criteria. State-of-the-art numerical approaches are presented to incorporate all characteristics of such furnaces mentioned.

2.1. Energy Balances in Reheating Furnaces

This section provides an overview of heat transfers in reheating furnaces. An overall energy balance of such furnaces, as well as a more detailed view on the main heat transfer mechanism will be presented. This should deepen the understanding for the whole heating process and provide a basis for the description of the numerical models used.
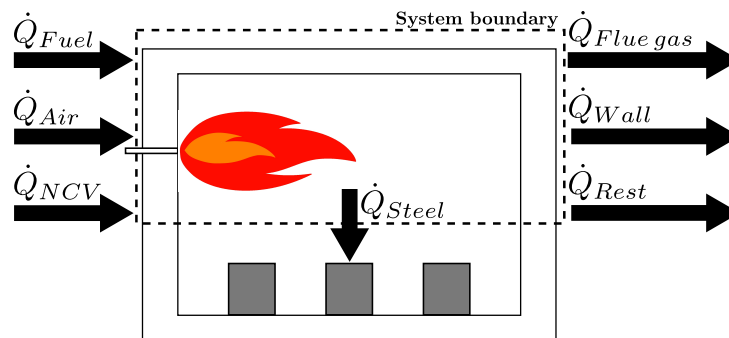
Figure 2.1.: Energy balance of a simplified furnace.

A simplified system is considered in Figure 2.1, visualizing the main heat fluxes entering and exiting. The individual heat fluxes, their analytical description and relevance when dealing with industrial furnaces are discussed in the following paragraphs.

Heat fluxes entering the system are due to the volume flows of the fuel and combustion air. These are indicated by the Heat fluxes $\dot{Q}_{Fuel}$ and $\dot{Q}_{Air}$, respectively. Both can easily be described by Eq. 2.1, using the mass flow rate, specific heat and temperature of the media when entering the system. These values are mostly measured, allowing to control industrial furnaces. Only

T^0, a reference temperature, is assumed and most of the time set to 0 °C. With fixed values for mass flow rate and specific heat, an increase of the heat flux can be achieved by raising the temperature T_i. In most furnaces, a preheating of the fuel is not common, hence, the value for $\dot{Q}_{Fuel}$ is comparatively low. On the other hand, it is common to preheat the combustion air to a few hundred degrees to increase efficiency [57]. The biggest values in the entering heat fluxes are due to the combustion process itself, calculated by Eq. 2.2, depending on the fuel mass flow rate $\dot{m}_f$ and the fuel type used. Each fuel type has a different Net Calorific Value (NCV), thus the produced energy differs. In the furnaces analysed, only natural gas is used as fuel, with a NCV of 50.03 MJ/kg. Other common fuels used are BFG and COG. These are the major off-gases during steel production. It has been shown that composition varies strongly, influencing the NCV of the gases [58–61].

$$\dot{Q}_i = \dot{m}_i \, cp_i|_{T0}^{T_i} \left(T_i - T^0 \right) \tag{2.1}$$

$$\dot{Q}_{NCV} = \dot{m}_f NCV \tag{2.2}$$

$$\dot{Q}_{Steel} = \dot{m}_s \, cp_s|_{T_{in}}^{T_{out}} \left(T_{out} - T_{in} \right) \tag{2.3}$$

In Figure 2.1, $\dot{Q}_{Steel}$ indicates the heat flux transported to the steel, described by Eq. 2.3. It states that the heat flux needed to lift the steel temperature from the inlet temperature (T_{in}) to the required outlet temperature T_{out}. Both temperatures are usually determined by the process and cp_s is a fixed steel property, heat flux can only be influenced by the mass flow rate $\dot{m}_s$. As shortened cycle times, which affect the overall heating time of the steel, are desirable, the mass flow rate of the steel must be raised. This behaviour triggers an increase in heat flux transferred to the steel to ensure the same steel outlet temperature, influencing the furnace efficiency, characterized by:

$$\eta = \frac{\dot{Q}_{Steel}}{\dot{Q}_{NCV}} \tag{2.4}$$

On the rhs of Figure 2.1, exiting heat fluxes, characterising heat losses, are visualized. $\dot{Q}_{Flue\ gas}$ marks heat losses due to the hot flue gas exiting the furnace. Similar to the fuel and air streams entering the furnace the hot flue gas losses can be described by Eq. 2.1. The value for specific heat has to be calculated for the mixture of the flue gas, based on a species balance calculation or measurements. The flue gas temperature is mostly measured at the flue gas outlet to control the furnace. It cannot be classified as pure heat loss since a portion of it is used to preheat the combustion air as was mentioned previously. This is mostly done in a central downstream recuperative heat exchanger, which is beyond the system boundary as shown in Figure 2.1. Thus, it attributes to the heat losses as well as to the usable heat at the same time, affecting $\dot{Q}_{Air}$. Wall losses resulting from the insulation of the furnace walls are indicated by $\dot{Q}_{Wall}$. Real industrial furnaces have a more complex energy balance due to different heat losses than visualized in Figure 2.1. In this illustration, this is accounted for by $\dot{Q}_{Rest}$, including heat losses due to the cooling of the skid system, doors or entry- and exiting mechanisms. Enough measuring points permit an assessment of them, by measuring the temperature of the cooling

media and using Eq. 2.1. However, $\dot{Q}_{Rest}$ also comprises other elusive heat losses, like losses due to leaks and sealing. These leaks contain mass losses of exiting hot flue gases and radiative losses. Also mass- and heat gains by cold air infiltration are covered by the leaks. To improve the efficiency of industrial furnaces, heat losses have to be minimized. The aim is to reduce energy losses caused by the exhaust gas, wall conduction, conveying and cooling system should be striven for. The easiest approach is to increase the insulation thickness or to use more appropriate materials. Both methods reduces heat losses due to conduction. Efficiency can also be increased by either lowering the temperature or by decreasing the mass flow rate of exiting flue gases. The former is generally attained by implementing recuperative systems in industrial furnaces or by extending the convection zones. A reduction in exhaust gas volumes also minimizes losses. This can be achieved by using OEC, decreasing the nitrogen content in the flue gas, offering the possibility of saving fuel. However, the economic benefit has to be evaluated by comparing fuel saving potential to the costs of oxygen. Another possibility is the usage of waste heat boilers for steam generation. In general, the aim should be to strive for improvements in furnace sealing, while also reducing the number and size of openings.

In order to discuss improvements to be made in industrial furnaces, the main heat transfer mechanisms are explained in slightly more detail in the next sections. These include convective, conductive and radiative heat transfers, as schematically visualized in Figure 2.2.
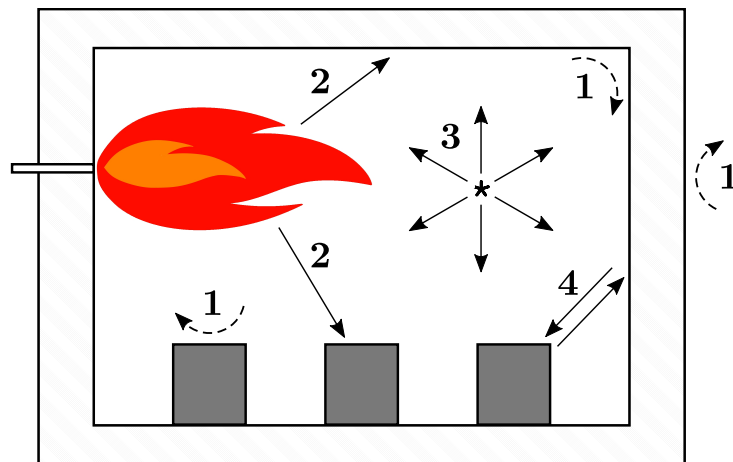
Figure 2.2.: Convective (dashed lines) and radiative (solid lines) heat fluxes including the convective transfer between fluid and solid (1), flame radiation (2), gas radiation (3) and radiative interaction of steel and furnace walls (2).

Convection

Convection is the heat transfer between a solid (e.g. steel) and the surrounding moving gases (e.g. hot flue gas): it is visualized in Figure 2.2 by the dashed arrows marked with 1. As indicated, convection occurs within the combustion chamber as well as on the outer furnace walls. Inside reheating furnaces, the amount of convective heat flux can vary. It is mainly influenced by the burner type, which is responsible for generating different flame shapes. Most common types are outlined in [6]. Some burners create long and high speed flames. Depending

on the burner position, these are in direct contact with the furnace load or walls, increasing local convective heat transfer significantly. Other burner types create flames focused on radiative heat transfer and avoid excessive flame impingement on the load. Outside the combustion chamber, convective heat transfer occurs between the furnace walls and the surrounding atmosphere. Here, natural convection occurs because of a temperature difference generating buoyancy. The heat transport can generally be calculated by:

$$\dot{Q}_{Conv} = \alpha_c A (T_g - T_s) \tag{2.5}$$

Characterizing α_c is challenging due to the dependency of the Nu number. In general, it can be stated that convective heat transfer is increased in areas with high velocities. This is the case near the burner or in areas where the cross-section is narrowed, as shown by Prieler et al. [62]. In most industrial furnaces, a maximum of 10 % of total heat flux is transferred to the steel by convection [63, 64]. Nevertheless,the importance of the convective heat flux in reheating furnaces has been demonstrated [18–20]. A clear impact on the gas temperature distribution within the combustion chamber and, thus, on the exiting steel temperature can be seen.

Conduction

Conduction plays an important role in reheating furnaces. It appears within all solid regions of the furnace. To be more precise, conduction occurs in the insulating furnace walls, skid system as well as inside the steel. In addition, it appears in contact areas of two solids, namely the contact surfaces between the steel and the skid system.

In pusher type furnaces, conduction also appears between the steel and furnace floor, as well as between two touching steel goods. Both effects have absolutely be taken into account. The equation that characterizes conduction within an object is:

$$\dot{Q}_{Cond} = -\lambda A \, grad \, T \tag{2.6}$$

λ is the temperature-dependent thermal conductivity of the specific material. Insulating refractory material, as used in industrial furnaces, has very low values of about 0.04-0.4 W/mK. The walls of most furnaces are made from a combination of different materials with varying properties. Knowledge about the real overall thermal conductivity is necessary to calculate appropriate heat losses [65]. This has also been investigated for degraded industrial refractory materials, which shows increased values for energy losses [66]. The values for steel vary widely, depending on the alloys used. Typical values range from 20 to 50 W/mK and are thus well above the values of the insulation. Conductivity is temperature-dependent, revealing the biggest differences between unalloyed and high-alloy steel at room temperature. The differences decreases with increasing temperature, and has almost vanished at 900 °C [67].

Radiation

The most important role in terms of heat transfer inside industrial furnaces is attributed to radiation [68]. A schematic representation of radiative fluxes is provided in Figure 2.2 - represented by the solid arrows with the numbers from 2 to 4. The arrows depict flame radiation, gas body radiation (2, 3) and solid body radiation (4). Their differences are described in the subsequent paragraphs.

Radiative heat transfer can be generally described with the help of Stefan Boltzmann law (Eq. 2.7). It describes any radiative heat flux in dependency of the emissivity ε, the Stefan-Boltzmann constant σ, the area and temperature. The fourth-power of the source temperature clearly shows the big impact of heat transfer in high temperature processes. The emissivity describes the amount of radiation intensity emitted by a real surface compared to an ideal black body, characterized by $\varepsilon=1$. It should be noted that this value is not constant and its correct determination is complex. It depends on temperature, wavelength, the angle of contact and the surface condition of the emitting source. However, most of the time, a constant value is assumed in technical applications.

$$\dot{Q}_{Rad} = \varepsilon \sigma A T^4 \tag{2.7}$$

Solid body radiation occurs between all walls, inside a reheating furnace, as indicated by the arrows marked by 4 in Figure 2.2. In the interest of simplicity and clarity, only the mutual influence of the load and furnace walls is visualized, although solid body radiation occurs between all solids, including wall-wall and load-load interactions. While Eq. 2.7 describes the emitted radiative heat flux, the same statement can be used for the absorbed incident radiative heat flux. A real surface does not absorb total incident radiative heat flux. The amount is described by the absorption coefficient. Considering a system in radiative thermal equilibrium, which can be assumed for reheating furnaces in stationary operation, it is possible to equate emissivity and absorptivity of walls according to Kirchhoff's law of thermal radiation [7, 69]. Thus, the net radiative heat flux of a radiator (1) to a source (2) - both have the identical size A, but different emissivities and wall temperatures - is:

$$\dot{Q}_{Rad_{1 \to 2}} = \frac{\sigma A (T_1^4 - T_2^4)}{1/\varepsilon_1 + 1/\varepsilon_2 - 1} \tag{2.8}$$

Mayr et al. [64] showed that in industrial furnaces the main part of heat transferred to the steel is due to solid body radiation. This means that homogeneous wall temperature distribution is decisive for optimal, uniform heating of the load. Ahmed et al. [63] introduced a graphical demonstration of radiative heat transfer in a walking beam type furnace. In this demonstration, the high dependency of the wall temperature on the heat flux to the steel becomes obvious. The wall temperature is influenced by the burner arrangement, the flame shape and the convective heating of the furnace walls. Considering Eq. 2.8, it becomes apparent that with decreasing temperature, differences between the solids, solid body radiation decreases. In the case of

diminishing wall temperature differences gas body radiation intensifies, which is the case in the rear end of furnaces (soaking zone), where the steel reaches almost its final temperature.

Gas body radiation describes radiative thermal transport from hot gases to solid regions as shown in Figure 2.2 by the arrows marked with 2 and 3, including radiative heat transfer from hot gases to other gases. Gas body radiation also contains the decrease of radiation intensity due to absorption by surrounding gases. In general, a distinction must be made between flame or hot gas radiation and radiation from soot particles [6]. In the present thesis, soot radiation will not be discussed since only natural gas, usually operating at increased air-fuel ratios, is regarded and soot formation is negligible [70]. Determination of the absorptivity and emissivity of clear gases proves to be more complicated compared to solid body characterization. This is due to the dependency of the gas properties on temperature, partial pressure, composition or species fractions and gas layer thickness. An increase in heat flux can be achieved by higher gas temperatures and by increasing the gas blanket volume (optical thickness) [6]. The influence of individual species on optical behaviour is of significant importance to characterize absorptivixy and emissivity in a proper manner. The presence of three atomic gases in particular, such as CO_2, H_2O in the flue gas is important. It can be stated that the radiation of diatomic gases, such as O_2 and N_2 is negligibly small, with the exception of carbon monoxide (CO). Each of the radiating gases has a distinctive wavelength band at which emission and absorption is decisive. According to Zhang et al. [71], the total absorptivity α and emissivity ε of a gas inside a volume can be expressed by an exponential expression:

$$\alpha = \varepsilon = 1 - exp\{-\kappa L\} \tag{2.9}$$

This equation is based on the Bouguer law, representing the correlation of gas properties with the extinction coefficient of the gas κ and beam length L. The former is depending on the pressure of the gas mixture and its temperature, while the latter characterizes the layer thickness in which the radiation intensity changes. Section 2.2.5 will look at these quantities in greater detail deepening the understanding. Some correlations for simple problems are presented by Hottel and Sarofim [72]. Mayr et al. [64] show the dependency of the absorption coefficient on furnace height, temperature and species composition. The absorption coefficient increases with increasing oxygen content in the oxidizer. This dependency is attributed to the lowered concentration of N_2, increasing CO_2 and H_2O content.

2.2. Numerical Modelling

The correct presentation of the physical effects within industrial furnaces is of great importance in numerical simulations. In the following sections, the key models for the characterization of turbulent reactive flows are presented. The underlying equations are shown as 3D-representations.

2.2.1. Flow Modelling/Conservation Equations

Most modern CFD codes are based on the Finite Volume Method (FVM). The basic idea underlying this method is to spatially divide the numerical domain into smaller domains. In the numerical model, this is constituted by the numerical grid, also referred to as mesh. In each of the cells in this mesh, the whole set of conservation equations is solved in an iterative manner. Thus, the mesh size and local resolution can influence the results and computing time significantly. It is advisable to use a mesh as coarse as possible, reducing the number of cells and saving computing time. In the course of this, it is recommended to investigate different meshes to eliminate a possible influence of the cell number on the calculated result. Chapter 4 shows how such investigations are conducted. For a more detailed discussion of this topic, interested readers are referred to appropriate literature [73–75]. In the next few sections the set of conservation equations for reactive flows is explained in more detail.

Continuity Equation

The conservation of mass within a numerical domain can be stated by a general equation as shown below. This equation states that for each phase the change of mass within a defined volume has to be equal the net mass flow. Sink or source terms can arise due to chemical reactions, leading to a mass exchange between the different phases. They introduce an additional term on the rhs of the presented equation.

$$\frac{\partial \rho}{\partial t} + \nabla \cdot (\rho \vec{v}) = 0 \tag{2.10}$$

Conservation of Momentum

Newton's second law describes the relationship between the change of momentum and the sum of forces acting on a volume, shown by Eq. (2.11). On the lhs, temporal and convective changes of momentum are described. The remaining terms on the rhs characterize surface and body forces acting on the volume. To be more precise, these terms characterize pressure forces, viscous forces (described by the stress tensor τ), body forces due to gravitation and external forces.

$$\frac{\partial(\rho \vec{v})}{\partial t} + \nabla \cdot (\rho \vec{v}\vec{v}) = -\nabla p + \nabla \cdot \tau + \rho \vec{g} + \vec{F} \tag{2.11}$$

Energy Equation

The energy conservation equation can be expressed in many different ways. A general form is visualized in Eq. (2.12), describing the change of total specific energy $\hat{e}$. This quantity can be further described by Eq. (2.13) as the sum of specific internal and kinetic energy. For mixtures, the internal energy can be formulated as shown in Eq. (2.14). It is dependent on the enthalpies

of each individual species h_k, the corresponding mass fractions Y_k, for the total number of species (N) that are considered, as well as the system pressure and density. Similar to the momentum equation, the two terms on the lhs of the energy equation (Eq. (2.12)) account for temporal and convective changes. The terms on the rhs describe energy changes due to pressure and shear stresses. Energy flux ($\vec{q}_i$) is defined in (2.15). The equation includes a heat diffusion term based on Fourier's law and a species diffusion term, taking into account the corresponding enthalpy and mass fraction of each species. $\vec{V}_k$ is the diffusion velocity vector for the species k. The last two terms in the energy equation indicate heat sources due to external sources ($\dot{Q}$) and combustion processes ($\dot{\omega}_T$).

$$\frac{\partial(\rho\hat{e})}{\partial t} + \nabla \cdot (\rho\vec{v}\hat{e}) = -\nabla \cdot (p\vec{v}) + \nabla \cdot (\tau \cdot \vec{v}) - \nabla \cdot \vec{q}_i + \dot{Q} + \dot{\omega}_T \qquad (2.12)$$

with:

$$\hat{e} = e + \frac{u_i u_i}{2} \qquad (2.13)$$

$$e = \sum_{k=1}^{N} h_k Y_k - \frac{p}{\rho} \qquad (2.14)$$

$$\vec{q}_i = -(\lambda \nabla T) + \rho \sum_{k=1}^{N} h_k Y_k \vec{V}_k \qquad (2.15)$$

Species Transport

In combustion modelling, the species transport is of essential importance. Eq. (2.16) shows the general form of species conservation of species k. The left-hand side describes the transient and convective parts, while the right-hand side shows the diffusion term and the reaction rate of a species k.

$$\frac{\partial(\rho Y_k)}{\partial t} + \nabla \cdot (\rho\vec{v}Y_k) = -\nabla \cdot (\rho Y_k \vec{V}_k) + \dot{\omega}_k \qquad (2.16)$$

2.2.2. Describing Turbulent Flows

In general, turbulent flows are determined by an unsteady, three-dimensional and highly fluctuating velocity field. Those fluctuations are characterized by different length scales with varying frequencies. This complex phenomenon is also of significant importance in most combustion systems. It influences the combustion process, the flame shape and in extreme cases, it leads to flame quenching [76, 77]. This is why the correct presentation of turbulence is of significant importance in all numerical problems. There are three main numerical approaches are available in CFD, each of which is based on a different level of complexity [78].

The most precise approach to be used in CFD is the Direct Numerical Simulation (DNS). The whole set of Navier-Stokes equations is solved directly without any restrictions. It demands a

very fine grid to capture even the smallest eddies on the Kolmogorov scale. Furthermore, it is essential to treat the simulations as transient while the usage of a small time step size is crucial. Therefore, this approach is not suitable for most technical investigations. Rather, it is applied in academic studies of simplified domains or it is used to evaluate different turbulence models [79].

In the Large-Eddy Simulation (LES), large turbulent scales are calculated directly, while smaller ones are modelled using closure rules. This technique is based on the assumption that larger eddies have a stronger impact on the information transport in turbulent flows than smaller ones. The size of the turbulent structures to be simulated must be preset by the user. To achieve this, the grid size has to be adjusted to the size of the eddies to be simulated. Vortices smaller than the grid width have to be modelled. This procedure allows the use of a coarser grid, resulting in a lesser computational effort compared to DNS. As with the DNS, the LES requires the transient Navier-Stokes equations to be solved. Thus, the computational effort needed is still quite high.

The Reynolds-Averaged Navier-Stokes (RANS) equations represent the third and most widely used approach for turbulence characterization. A drastic reduction in computational effort is achieved by modelling all vortices, covering the whole energy cascade. This approach is based on a statistical method, describing the flow by a mean and turbulent part, as described in (2.17). This operation is called Favre averaging, expressing all quantities by mass-weighted averages, called Favre averages.

$$\Phi = \overline{\Phi} + \Phi' \tag{2.17}$$

Applying this approach to the Navier-Stokes equations, the RANS equations for continuity and momentum can be derived:

$$\frac{\partial \rho}{\partial t} + \nabla \cdot (\rho \vec{v}) = 0 \tag{2.18}$$

$$\frac{\partial (\rho \vec{v})}{\partial t} + \nabla \cdot (\rho \vec{v} \vec{v}) = -\nabla \overline{p} + \nabla \cdot \tau - \nabla \cdot (\rho \overline{\vec{v}' \vec{v}'}) + \rho \vec{g} \tag{2.19}$$

In Eq. (2.19), an additional term occurs due to the averaging approach. This is the so-called Reynolds stress tensor ($\rho \overline{\vec{v}' \vec{v}'}$). It constitutes a connection between the averaged and fluctuating part, characterizing turbulent momentum transfer. In CFD, numerical models have to be used to close the set of equations ("Closure-Problem").

Simpler models are based on the Boussinesq-approximation, describing the transport of turbulent momentum as a diffusive process. In this concept the turbulent viscosity (μ_t) is introduced, which is a proportionality factor between the Reynolds stresses and the mean velocity gradients. In general, different models are available, classified by the number of

equations needed. These range from one- to two-equation models. The best known one-equation model is the Spalart-Allmaras model developed for aerodynamic applications. While the applicability has been proven by Zhen et al. [80], clear limitations of the model could be observed regarding general turbulence descriptions due to restriction on a single variable [81]. Several two-equation models are available in commercial CFD codes. The most popular are the $k - \varepsilon$ and $k - \omega$ models, describing turbulences using two properties each. Descriptions for both models can be found in literatures, for example in *Turbulence Modeling for CFD* by Wilcox [82]. Both models are based on one equation describing the turbulent kinetic energy (k). The second equation, however, differs in the description of dissipation. One uses the dissipation rate to describe the turbulent kinetic energy (ε), while the other one characterizes a specific dissipation rate (ω) [83]. Both models have advantages and disadvantages and several improvements have been developed to enhance their applicability. Their suitability has been tested extensively in different fields [84–89]. Within this thesis, a version of the $k - \varepsilon$ model , the realizable $k - \varepsilon$ model, has been used. Thus, it will be explained in more detail in the next section.

At this point, more complex models, represented by the Reynolds Stress Model (RSM), need to be mentioned. This model is based on direct calculation of the Reynold stresses. Taking the anisotropic behaviour of the flow into account, seven additional equations are necessary for a 3D case. These represent the stresses in six directions and one equation for dissipation rate. Although this procedure increases the accuracy of the calculated results, it also raises the computational effort needed compared to simpler models. However, in some investigations, the results reveal larger discrepancies than the ones achieved from simpler models [90–92].

$K - \varepsilon$ model

The most commonly used turbulence models, which are based on the approach of Boussinesq are the two-equation models based on the kinetic energy (ε) and the dissipation rate (k) of the turbulent motion. These two variables are sufficient to describe the turbulent viscosity, as presented in Eq. (2.20). This quantity is a flow property and stipulates and in combination with the dynamic viscosity of the fluid μ, it stipulates the effective viscosity of a turbulent flow. Within this work, the realizable $k - \varepsilon$ model has been used. To deepen the understanding of all $k - \varepsilon$ models are briefly described in the following paragraph.

$$\mu_t = \rho C_\mu \frac{k^2}{\varepsilon} \tag{2.20}$$

The model was initially developed by Jones and Launder [93]. It is referred to as the Standard $k - \varepsilon$ model. Its advantages regarding applicability, as well as CPU requirements and well known limitations make it a popular model for industrial investigations. While it is able to describe global simple flow fields with adequate accuracy, it fails to calculate near wall effects, flow separations, low-Reynolds flows, swirls and flows with strong streamline curvature [94]. To overcome these restrictions and to achieve better results several improvements of the model

were developed. The most popular ones are the RNG $k - \varepsilon$ and the realizable $k - \varepsilon$ model. The former is based on the renormalization group theory and was proposed by Yakhot and Orszag [95]. It uses a different formulation for k and ε, with an additional source term in the dissipation equation. These changes improve the calculations of rapid strained flows including high streamline curvatures and high shear rates [96]. The latter, the realizable-$k - \varepsilon$ model, uses the same formulation for kinetic energy as the Standard $k - \varepsilon$ model while another equation is used for the dissipation rate [97]. Both transport equations are visualized in the Eqs. (2.21) and (2.22). Similar to the conservation equations a temporal and convective term appear on the (lhs), whereas a formation term, a diffusion term and a destruction term appear on the rhs of the equation. The extended formulation of ε increases reliability using physics by preventing normal stresses becoming negative. The main equations are displayed in Eq (2.23) to (2.25); Pr_k, Pr_ε, C_2 and $C_{1\varepsilon}$ are model constants. Another improvement affects the formulation of the turbulent viscosity by changing C_μ from a constant (C_μ=0.09) to a variable. It is a function of the local mean flow deformation with dependency on shear, rotation and turbulence. A positive effect on calculating stagnation points and open jets, which include rotation, boundary layers, strong pressure gradients, separation and recirculation, can be achieved. Van Maele et al. [98] compared these three $k - \varepsilon$ models to each other when calculating a swirl burner. It appears that the realizable $k - \varepsilon$ model revealed the best results.

$$\frac{\partial}{\partial t}(\rho k) + \frac{\partial}{\partial x_i}(\rho k u_i) = \frac{\partial}{\partial x_j}\left[\left(\mu + \frac{\mu_t}{Pr_k}\right)\frac{\partial k}{\partial x_j}\right] + G_k + G_b - \rho\varepsilon \tag{2.21}$$

$$\frac{\partial}{\partial t}(\rho\varepsilon)\frac{\partial}{\partial x_i}(\rho\varepsilon u_i) = \frac{\partial}{\partial x_j}\left[\left(\mu + \frac{\mu_t}{Pr_\varepsilon}\right)\frac{\partial\varepsilon}{\partial x_j}\right] + \rho C_1 S\varepsilon - \rho C_2 \frac{\varepsilon^2}{k + \sqrt{\nu\varepsilon}} + C_{1\varepsilon}\frac{\varepsilon}{k}C_{3\varepsilon}G_b \tag{2.22}$$

$$C_1 = max\left[0.43, \frac{\eta}{\eta + 5}\right] \tag{2.23}$$

$$\eta = S\frac{k}{\varepsilon},\ S = \sqrt{2S_{ij}S_{ij}} \tag{2.24}$$

$$S_{ij} = 1/2\left(\frac{\partial u_j}{\partial x_i} + \frac{\partial u_i}{\partial x_j}\right) \tag{2.25}$$

2.2.3. Chemical Reaction Theory

In physical chemistry and thermochemistry, a lot of research has been done on gas phase combustion in the last decades. The aim was to increase the understanding of combustion processes and the involved reaction chains. These can range from approximately ten to several thousand reaction steps depending on the chemical process and condition. Table 2.1 shows the number of species and reactions involved in some common combustion-reaction mechanisms.

Hydrogen oxidation is the smallest mechanism whereby effort increases with molecule size due to the increasing number of species and reactions involved. A wide range of fuels have been studied: a significant number of measurements have been carried out and a lot of theoretical studies have been conducted. They focused on fuels, ranging from hydrocarbon to even aromatic hydrocarbons and their reaction rates were determined. The results can be found in literature - they include a broad range of reactions, including secondary reactions. A collection of literature data is, for example, presented by Baulch et al. [99], Lide [100] and Tsang and Hampson [101]. These publications present data for reaction rates ($\dot{\omega}_k$) for many species and reactions which are needed to calculate the chemical source term ($\dot{\omega}_T$) from Eq. (2.12) & (2.16) Based on this data, numerical models can be generated for computational investigations of chemical kinetics and dynamics. Highly detailed reaction mechanisms require thermodynamic data for each species, including heat of formation, enthalpy, heat capacity and also transport coefficients. These sort of mechanisms take into account a large number of reactions and species, describing reactions on a molecular level. They are also referred to as complete mechanisms and form the basis for any developer of simplified numerical kinetic mechanisms. However, while several thousands of species and reactions need to be considered, their applicability is mostly limited to 1D flame simulations [102]. For simpler mechanisms, such as the H_2-O_2 mechanism, as shown in Table 2.1, complete mechanisms can be used. In the case of natural gas combustion, reduction is not absolutely necessary, but mostly done. Therefore, simplifications lead to the relatively detailed mechanisms such as the popular Gri-Mech 3.0 mechanism [103], which comprises 53 species and 325 reactions that can be used in simpler simulations. This mechanism includes NOx formations and is applicable in a broad range of temperature, pressure and equivalence ratios. Several other reaction mechanisms are available for numerical simulations and have been described and compared to each other [104]. Although numerous different models are available, some connections between the individual approaches can be observed. These connections were outlined by Rolland and Simmie [105], showing the number of species and reaction that the models have in common.

Table 2.1.: Number of species and reactions for some common fuels and oxidizer [106].

Mechanism	Reacting species	Reactions
$H_2 - O_2$	≈ 9	≈ 50
$H_2 - O_2 - N_2$	≈ 15	≈ 100
$CH_4 - O_2$ (lean)	≈ 30	≈ 200
$C_2H_6 - O_2$ (lean)	≈ 30	≈ 200
$CH_4 - O_2 - N_2$	≈ 50	≈ 350
$Octane - air$ (no NOx)	≈ 800	≈ 3000

For the simulation of complex problems, such as industrial-size applications, the complexity of these detailed mechanisms is too high. One way to achieve reduction in computational effort is through reduction of those detailed mechanisms since a direct correlation between the number of species and the number of reactions can be found [106]. The objective is to receive an efficient model, while preserving the accuracy needed. Several methods of mechanism reduction are available, such as sensitivity analysis, singular perturbation and eigenvector analysis. These

methods are used to filter reactions or species which are either classified as unimportant or which can be combined with other reactions or species already implemented in the model. Further reduction can be achieved by stiffness analysis. A stiff system is characterized by a wide range of physical and chemical time-scales occurring in the model [107]. While the physical time-scale is mostly fixed by the problem, chemical stiffness can be reduced by neglecting fast depleting species or fast reactions. Detailed information on these methods can be found in [102, 108].

When applying the approaches mentioned above to complete mechanisms, it can be observed that reduction in complexity leads either to semi-detailed or so-called skeletal mechanisms [109]. While the former are based on the fundamental reactions and are mostly valid in a broad range of conditions, skeletal mechanisms focus on applicability in a given regime [110]. They can be fixed by a set of concentrations, pressures and temperatures, limiting their field of use. Both exclude reactions which are non-relevant, being able to predict the central objective of the combustion with sufficient accuracy [111]. However, the sizes of the mechanism can vary greatly, whereby the applicability to very complex simulations is still not given. In industrial combustion processes, mostly natural gas is used for heat generation. Thus, several simplified reaction mechanisms and comparisons for CH_4 can be found in literature, for example demonstrated by Magel et al. [112]. The DRM mechanisms [113], are reduced reaction kinetics mechanisms based on an older version of the GRI mechanism (GRI-Mech 1.2). To be more precise, the DRM22 includes 22 species with 104 reactions. The DRM19 comprises 19 species with 84 reactions. For both models reduction was achieved by flux analysis combined with a subsequent sensitivity analysis of the DRM19. Numerical investigations and comparisons of different mechanisms can be found in literature [114–116]. Within this thesis, the skeletal25 mechanism proposed by Peeters [117] was used. This is a skeletal mechanism including 17 species and 25 reversible reactions. The good applicability of the skeletal25 mechanism is highlighted in several studies. The studies were conducted with natural gas using air and pure oxygen as an oxidizer [30, 118]. The whole set of reactions for this mechanism can be found in the Appendix A.1.

The last category comprises global reaction mechanisms. It is the simplest way to incorporate finite rate chemistry in numerical approaches [119]. The extreme case is represented by a single step mechanism, using a single reaction neglecting all intermediate species. Westbrook and Dryer [120] developed a model for single step hydrocarbon (C_xH_y) combustions described by Eq. (2.26). The values for n_i have to be adapted to the fuel used. In case of pure natural gas (CH_4) used as fuel, they will be 2, 1 and 2 respectively. A parameter study of different reaction rate expressions was conducted. A strong dependency on flame speed could be observed. This value is a commonly used flame property for model evaluation, beside peak flame temperature and species distribution [109, 121]. While an optimized setting to fit flame speeds can improve the calculated results, the flame temperature is over-predicted. This can be attributed to the neglection of dissociation effects in the highly reactive area by erasing any intermediate and

additional product species.

$$Fuel + n_1O_2 \rightharpoonup n_2CO_2 + n_3H_2O \tag{2.26}$$
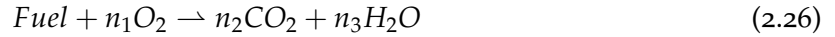
To overcome this issue, slightly extended formulations have been developed, neglecting a majority of intermediate species. Most of them consist of a maximum of 5 reactions, involving 5 to 10 species altogether [110, 122]. In these mechanisms, reaction kinetic rates are mostly simplified by a pseudo order, using adapted parameters matching experimental data. Thus, reaction kinetics do not reflect real molecular kinetic data and have to be determined for each problem. Therefore, the validity is only given in a certain range, similar to skeletal mechanisms [119, 123]. One of the best known and simplest mechanisms is proposed by Westbrook and Dryer [120]. It consists of an oxidation reaction for methane and one for carbon monoxide, neglecting any reversible reactions as shown in Eq. (2.27) and (2.28). The only reaction products are thus assumed to be CO_2 and H_2O.

$$CH_4 + 1.5O_2 \rightharpoonup CO + 2H_2O \tag{2.27}$$

$$CO + 0.5O_2 \rightleftharpoons CO_2 \tag{2.28}$$

Abou-Taouk and Eriksson [124] proposed modifications of the kinetic parameters to improve applicability to the Sandia Flame D. A clear improvement could be achieved in carbon monoxide prediction by comparing the results using the initial values. The effect of inaccurate CO prediction is even stronger under oxy-fuel conditions. To overcome this issue, Andersen et al. [125] suggest a parameter modification for the reversible carbon monoxide oxidation reaction, disclosing an improvement in calculated flame temperature and the distribution of CO species. This modification proves that these simple approaches are applicable in a broad range of conditions, by simply adapting the parameters. Thus, their usage is very common when modelling detailed transport models since computing time expenditure is limited [126]. Even though these mechanisms are mostly sufficient for engineering tasks, neglecting dissociation effects can have a tremendous effect on flame temperature and species distribution. To overcome this issue, several extensions of the two equation models have been developed. Two different three-equation models are presented by Peters and Williams [127] and Rückert et al. [128], which differ significantly. Peters and Williams use the steady-state and partial equilibrium assumptions to reduce a mechanism with 40 reactions. Rückert, however, assumes a water-gas-shift equilibrium. This results in a different reaction equation describing CO oxidation. These models highlight the various possibilities that exist to minimize the complexity of mechanisms; each path leading to different schemes. However, intermediate species, which need to be taken into account within all described schemes, are limited to carbon monoxide. The models have been developed further, leading to increasingly complex models, such as the mechanisms by Peters and Rogg [129], presenting a four and five-equation model. While the five-equation model has been derived from a C1 mechanism, similar to Peters and Williams, the four-equation model shows a further deduction by assuming steady state for CH_3. Both

mechanisms include atomic hydrogen and its reaction to molecular hydrogen. Bilger et al. [130] derived a similar four-step mechanism, from a complex mechanism, neglecting the atomic hydrogen reaction, but including the formation of oxyhydrogen gas. This four -step mechanism was achieved by assuming steady state for the "O" atom. Another very popular four-step mechanism is the one introduced by Jones and Lindstedt [131]. It is based on two methane break down reactions and two oxidation reactions of hydrogen and carbon monoxide (water-gas-shift). The big advantage of this mechanism is the excellent likeness to measurements over a wide spectrum. Due to its popularity, suggestions for improvement have been presented by many authors. Kim et al. [132], for example, investigated the mechanism initially proposed by Jones and Lindstedt and two modifications of it. One is based on the adaptation of the hydrogen and carbon monoxide reactions. Both modifications are treated as irreversible; in both of them different reaction parameters are applied. Besides this, the hydrogen oxidation is identical in the two modifications, while the CO oxidation is fundamentally different. The other one uses the initially proposed reaction scheme, solely adapting the hydrogen oxidation kinetic parameters. The second modification revealed a more realistic species prediction when compared to measurements. This has also been demonstrated by Yin et al [133]. They make a clear recommendation when dealing with oxy-fuel combustion. Further investigations of this scheme can be found in [134, 135]. The reaction kinetic, including the corresponding reaction rate equations and constants for the Arrhenius equation, are visualized in Table 2.2.

Table 2.2.: Theraction mechanism proposed by Yin et al [133].

No.	Reactions	Reaction rate equation $[kmol/m^3 Ts]$	A	b	E
1.	$CH_4 + 0.5O_2 \rightharpoonup CO + 2H_2$	$\frac{d[CH_4]}{dt} = AT^b e^{-E/RT} \cdot [CH_4]^{0.5}[O_2]^{1.25}$	4.4×10^{11}	0	1.26×10^8
2.	$CH_4 + H_2O \rightharpoonup CO + 3H_2$	$\frac{d[CH_4]}{dt} = AT^b e^{-E/RT} \cdot [CH_4][O_2]$	3.0×10^8	0	1.26×10^8
3.	$H_2 + 0.5O_2 \rightleftharpoons H_2O$	$\frac{d[H_2]}{dt} = AT^b e^{-E/RT} \cdot [H_2][O_2]^{0.5}\ (forward)$	5.69×10^{11}	0	1.465×10^8
4.	$CO + H_2O \rightleftharpoons CO_2 + H_2$	$\frac{d[CO]}{dt} = AT^b e^{-E/RT} \cdot [CO]^{0.5}[H_2O]\ (forward)$	2.75×10^9	0	8.36×10^7

In the previous paragraphs, theoretical reaction pathways have been discussed with focus on models that are able to predict hydrocarbon oxidation with sufficient accuracy. A significant factor in technical combustion processes is the presence of turbulence, which intensifies microscopic mixing influencing the combustion process. The combustion in turn causes an expansion of the fluid, thus further turbulences are generated. Turbulence is present in most technical processes and it is absolutely necessary to take it into account. This illustrates the importance of the correct representation of turbulence and combustion and its mutual influences in CFD [106]. As a result, several numerical models have been developed to illustrate the stiff set of Ordinary Differential Equations (ODEs), describing the evolution of species interactions. Since these numerical models represent a very computationally expensive part in CFD, the aim was to develop a stable, computationally inexpensive, but accurate model [136]. The last two points are of significant importance in reactive flow problems. The subsequent section will provide an overview of different approaches to incorporate the reaction kinetics

in the CFD simulation that are available in the software. Information on other models can be found in [137].

2.2.4. Combustion/ Turbulence-chemistry interaction modelling

When Favre averaging (Eq. (2.17)) is applied to the species conservation equation, the RANS equation for species can be derived. This includes the average values and, similar to the momentum equation, an additional term, which is mostly characterized by a classical gradient assumption occurrence. The diffusion term from Eq. (2.16) consequently transforms into:

$$\rho Y_k \vec{V}_k \rightarrow - \left[\overline{\rho D_k} + \frac{\mu_t}{Sc_{t,k}} \right] \nabla \overline{Y_k} \tag{2.29}$$

The individual terms in Eq. (2.29) characterize laminar diffusion fluxes by a mean diffusion coefficient $\overline{D_k}$ and by turbulent diffusion. The latter is described by the turbulent viscosity (μ_t) and Schmidt number ($Sc_{t,k}$). The two last named parameters are described by the turbulence model. Furthermore the reaction rate $\dot{\omega}_k$, mostly described by the Arrhenius law, induces critical problems during Favre averaging. Additional terms have to be closed in order to be able to describe the reaction rate. Therefore, several approaches have been developed to describe a correlation between turbulence and chemistry in numerical modelling. A distinction needs to be made between premixed and non-premixed combustion systems, characterizing the fuel and oxidizer fed into the system. The three models for non-premixed combustion proved to be of great importance for this thesis. Therefore, they will briefly be summarized below. For further information, please go to [138–140].

Eddy Dissipation Model (EDM)

The original Eddy Dissipation Model (EDM), which was proposed by Magnussen and Hjertager [141], is based on the Eddy Break up Model (EBM), which was developed by Spalding [142]. Both are turbulent mixing approaches, assuming the fast burning of the fuel. In this assumption, the reaction time scale is orders of magnitude smaller than the mixing time scale. Accordingly, it can be assumed that the combustion process can exclusively be described by turbulent mixing, neglecting any influence by the chemical reaction rates. In many cases this is an inadequate assumption, as for example shown by Buchmayr et al. [31, 143], using the EDM on numerical investigations on a biomass furnace.

In the EDM model the reaction rates are calculated based on the turbulent mixing time (ε/k), the model constants (A, B) and, unlike with EBM, based on the mean mass fraction of the minor species ($\overline{Y_i}$). Thus, the model choose one equation, as visualized in the Eq. (2.30) to (2.32), resulting in the lowest reaction rate ($\overline{\omega}_i$). Moreover, these equations depend on the stoichiometric oxygen to fuel mass ratio (ξ).

$$\overline{\omega}_F = -\overline{\rho} A \overline{Y_F} \frac{\varepsilon}{k} \tag{2.30}$$

$$\overline{\omega}_{O_2} = -\overline{\rho} \frac{A \overline{Y_{O_2}}}{\xi} \frac{\varepsilon}{k} \tag{2.31}$$

$$\overline{\omega}_P = \overline{\rho} \frac{A\,B\overline{Y_P}}{(1+\xi)} \frac{\varepsilon}{k} \tag{2.32}$$

The model constants A and B are fixed by the user and have default values of 4.0 and 0.5, respectively. The model constant A depends on the structure of the flame and the reaction rate. Thus, it is important for the simulation of diffusion flames, while B is needed for premixed flames. Magnussen and Hjertager propose an adaptation of the model constants to gain reasonable values for a particular problem. There is no valid general proposal for the model constants, making measurements unavoidable. In literature, several investigations can be found regarding the effect of model constants on the combustion process. Scharler et al. [144] showed the effect of a different A on the calculated temperature distribution in a wood log stove. Shiehnejadhesar et al. [145] performed a similar investigation for biomass grate furnaces. Based on model improvements proposed by Magnussen et al. [146], Wang et al. [147] introduced a variable formulation for A, depending on a constant and the turbulent Reynolds number. This means that the variable can differ according to location as visually presented by Scharler et al. [148]. This allows us to overcome the manual adaptation of the constant. However, another constant is introduced which significantly affects the calculated results, shown by Li et al. [149]. They tested the model by Wang in a gas turbine, using different values for the constants. The results revealed a strong dependency of the parameters, which implies that the users are still forced to adapt them according to the individual task. Another drawback is the limitation to a maximum of two reactions to be considered. This represents very simple global reaction kinetics, as described in the previous section, neglecting nearly all intermediate species. This is due to the simplification to a single reaction rate that ought to account for the whole combustion process, while actual reaction rates differ strongly in multi-component mechanisms. Consequently, the calculated temperature is significantly overestimated without any model adaptation using a global reaction mechanism. Nevertheless, this model is frequently used for investigations of reheating furnaces. This is due to the fact that the computing effort needed is relatively low. In addition, multiple fuels or oxidizers can be used with this model. It allows the user to gain insights into different effects, in a time efficient manner. It is, thus, also used within this thesis to investigate the impact of simultaneous fuel-air and fuel-oxy combustions on the heating characteristics of the steel in both furnaces.

Eddy-Dissipation Concept Model (EDC)[1]

To overcome the restrictions associated with the EDM model, Magnussen [150] introduced an improved model. This model is independent of the reaction mechanism size, allowing us to incorporate reaction kinetics ranging from simple global assumptions to very detailed ones, such as the GRI mechanism. The model assumes reaction to occur in fine scales, the so-called Kolmogorov length. Within these fine structures, species are mixed on a molecular level and reactions take place. The model treats each of these fine structures as a perfectly stirred reactor. Outside of these fine structures, the fluid is treated as non-reactive, splitting the fluid domain into two zones (reactive and non-reactive) [151]. Some investigations and modifications have been presented over the years by Magnussen et al. [152–154]. They affect the calculation of the reaction rate. Magnussen et al. also present a different formulation for the fine structure definition. For a detailed insight into the modelling approach, one is referred to the presented literature.

Similarly to the previously described EDM model, the Eddy-Dissipation Concept Model (EDC) is used in many investigations of reheating furnaces, allowing one to incorporate several types of fuels or oxidizers in the numerical simulation. This model increases the accuracy of the calculated results. Within this thesis, the EDC was mainly used to evaluate other models. Overestimations of flame temperature can be prevented by using the extended global scheme proposed by Yin et al. [133]. However, due to the elaborate chemistry integration in each time step, the computational effort is very high compared to the EDM. The degree of complexity and computing time strongly depends on the number of species and reactions that are taken into account in the reaction kinetic scheme. This means that using detailed kinetics, such as the GRI mechanism, is mostly unfeasible. Therefore, the user is restricted to global or reduced (skeletal) schemes. During the investigations performed within this thesis, it was discovered that the computing time of the EDC was about five times longer, than when using the EDM. This shows the limitation of using the EDC in combination with detailed reaction mechanisms in complex real size applications. To diminish restrictions caused by the size of the reaction mechanism, different methods have been developed. Their aim is to reduce computational effort needed using comprehensive reaction kinetics. Using the EDC model, two methods to perform chemistry integration are available, the Direct Integration (DI) and the In-Situ Adaptive Tabulation (ISAT) method [155], differing in the computational effort needed. The DI method is a very CPU intensive method due to the iterative calculation of the stiff species differential equations. Whereby the ISAT method is very intensive in computer memory needed. This is due to the continuous storing and reading of the generated look-up tables. These tables have to be cleared in certain times to purge entries from the initial condition demanding a periodical manual operation. Laubscher [156] investigated the impact of the mesh size on computing time and RAM needed, using the EDC with DI, ISAT and an approach based on artificial neural networks. It is getting obvious, that the difference in calculation time, between the DI and ISAT method, increased linearly, leading to a longer calculation time using DI. On

---

[1]Segments of this section have already been published in [5]

the other hand, the difference in RAM needed revealed an exponentially behaviour for the benefit of the DI method. Thus, with increasing mesh sizes, the RAM requirements become decisive and the limiting step. Further reduction in computational effort can be achieved by chemistry agglomeration and dimension reduction. They either condense regions with similar composition or reduce the number of species to be calculated, assuming the suppressed species to be near equilibrium. Both methods are appropriate when detailed reaction kinetics have to be used.

Steady Flamelet Model (SFM)

In non-premixed turbulent reactive flows, the most successful approaches are mixture fraction models. This approach was originally proposed by Bilger [157] and adapted for turbulent flames [139]. The important quantity is the mixture fraction, describing the thermochemical state of the fluid, such as temperature, species etc. The big advantage of this approach is the unnecessary complex calculation of the mean reaction rates, limiting combustion calculations to a simple mixing problem. This means that only the transport equation for the mixture fraction need to be solved. The mixture fraction is based on the elements rather than the species [158]. This leads to the major advantage by allowing to eliminate the source and sink terms in its transport equations. In the case of natural gas as the fuel and air as the oxidizer, the occurring elements are C, H, O and N. Many definition of this scalar can be found in literature, but most commonly a normalized form is used, as implemented in the used software presented in Eq. (2.33). Z_i characterizes the atomic mass fraction in the fuel and oxidizer streams, indicated by f and ox, respectively. In simple terms: it describes the total mass fraction originating from the fuel stream in any position in the fluid[159].

$$f = \frac{Z_i - Z_{i,ox}}{Z_{i,f} - Z_{i,ox}} \tag{2.33}$$

The Steady Flamelet Model (SFM) is based on the assumption that the shape of turbulent flames can be described by an ensemble of small laminar flamelets. The approach is visualized in Figure 2.3. On the lhs of this illustration, there is a burner with separate inlets for the fuel and the oxidizer. Here, Y_k^0 stands for the mass fraction and T_k^0 for the temperature of the oxidizer ($k = O$) and the fuel ($k = F$) at infinity, respectively. Each position of the stoichiometric isocontour can be described by a flamelet forming a stable planar flame form. Each of them is based on counterflow diffusion flames, characterized by an opposite fuel and oxidizer stream, as shown on the rhs of Figure 2.3 [161]. These laminar flamelets have been well studied in experiments and can be described as an one-dimensional problem assuming that chemistry is fast (high Damköhler number), but not infinitely fast [162]. This also limits the field of application of the SFM. As it is limited to fast chemistry it provides wrong results for slow chemical processes such as pollutants [158]. In the case of natural gas combustion the chemical time step is very small. Therefore, it is allowed to assume the reaction to take place in a
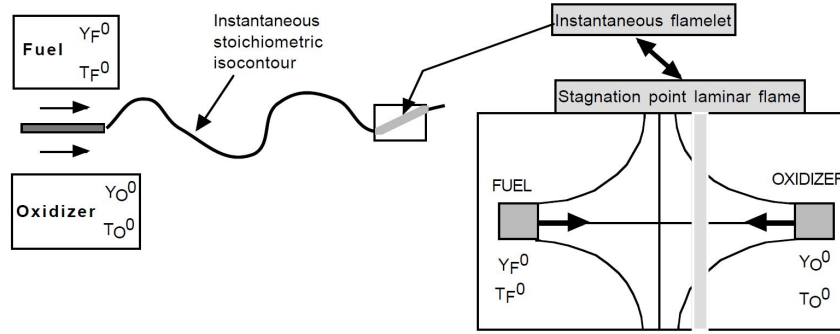
Figure 2.3.: Flamelet approach [160].

thin layer that is smaller than the Kolmogorov eddy. This means that the flamelets can be described in dependency of the mixture fraction and the scalar dissipation rate (strain rate) only, allowing us to characterize flame structures [158]. In the numerical approach, several flamelets are calculated for different strain rates, until flame extinction. In case of turbulent flows, temporal and spatial fluctuations of temperature and species mass fraction occur. These values are connected by a joint Probability Density Function (PDF), describing the mean values in dependency of the mixture fraction and its variance. The transport equations for both quantities are given in Eqs. (2.34)-(2.35). The shape of the PDF is presumed to follow a β-shape function [163]. The flamelets and corresponding PDF are calculated independently in a previous step and stored as library. This procedure decouples the flame structure calculation from flow dynamics, reducing the computational effort needed [140, 161]. The numerical investigations within this thesis revealed even lower computing times than needed when using the EDM. This is the case although more complex reaction kinetics (skeletal25) are used. However, this model is restricted to a single fuel and oxidizer each. In many cases, this numerical model is still sufficient to represent most industrial furnaces, such as those regarded within this thesis. Applying this model, furnace operations using additional burner types with a different oxidizer cannot be depicted and a more sophisticated approach has to be used.

$$\frac{\partial}{\partial t}(\rho \overline{f_m}) + \nabla \cdot (\rho \vec{v} \overline{f_m}) = \nabla \cdot \left(\frac{\mu_t}{Pr_k} \nabla \overline{f_m} \right) \tag{2.34}$$

$$\frac{\partial}{\partial t}(\rho \overline{f^2}) + \nabla \cdot (\rho \vec{v} \overline{f^2}) = \nabla \cdot \left(\frac{\mu_t}{Pr_t} \nabla \overline{f^2} \right) + C_g \mu_t (\nabla \overline{f_m})^2 - C_d \rho \frac{\varepsilon}{k} \overline{f^2} \tag{2.35}$$

2.2.5. Modelling Radiation

As was already mentioned in section 2.1, the most important heat transfer in industrial reheating furnaces is due to radiation. Many different aspects have to be taken into account when calculating radiation, such as the local temperature, the absorption capacity, and the scattering ability of the media. Regarding the flame, also optical properties, size, density and radiative wavelength are important. All the listed effects influence the radiation intensity I along its direction path. This is visually displayed in Fig. 2.4, characterizing the change over a finite length ds. A mathematical presentation is described by the Radiative Transfer Equation (RTE), as shown in Eq. (2.36), indicating the change of spectral intensity I_λ [164].

$$\frac{dI_\lambda(\vec{r},\vec{s})}{ds} = -\left(k_{a,\lambda} + \sigma_{s,\lambda}\right) I_\lambda(\vec{r},\vec{s}) + k_{a,\lambda} I_{black,\lambda}(\vec{r}) + \frac{\sigma_{s,\lambda}}{4\pi} \int_{4\pi} \Phi\left(\vec{s}',\vec{s}\right) I_{\overline{\lambda}}\left(\vec{s}'\right) d\Omega' \qquad (2.36)$$

In this formulation, I_λ depends on $\vec{r}$, characterizing the location in the domain and the unit vector $\vec{s}$. Changes of radiative intensity due to absorption and emission can be described using $k_{a,\lambda}$. The absorption is characterized by the entering radiation intensity, while the emission term uses the spectral intensity of a black body characterized by the Stefan-Boltzmann law ($I_{black} = \sigma \frac{T^4}{\pi}$). The first term on the rhs of Eq. (2.36) additionally contains the scattering coefficient $\sigma_{s,\lambda}$, describing intensity attenuation due to scattering. In literature, the combination of these coefficients in the first term is referred to as the extinction coefficient κ_λ [165]. It can be interpreted as the reciprocal of the penetration distance. This means that with an increase in absorption or the scattering properties of the fluid, it gets more opaque and decreasing penetration distance. In some cases, the term optical thickness τ_λ is used, describing the ability to attenuate radiation along a given path length. In Eq. (2.37), the mathematical formulation is shown in a spectral manner for a gas layer thickness S. Augmentation by scattering is influenced by several directions, thus, it has to be described using the solid angle Ω' as shown by the last term on the rhs of Eq. (2.36). In this equation, Φ is referred to as the scattering phase
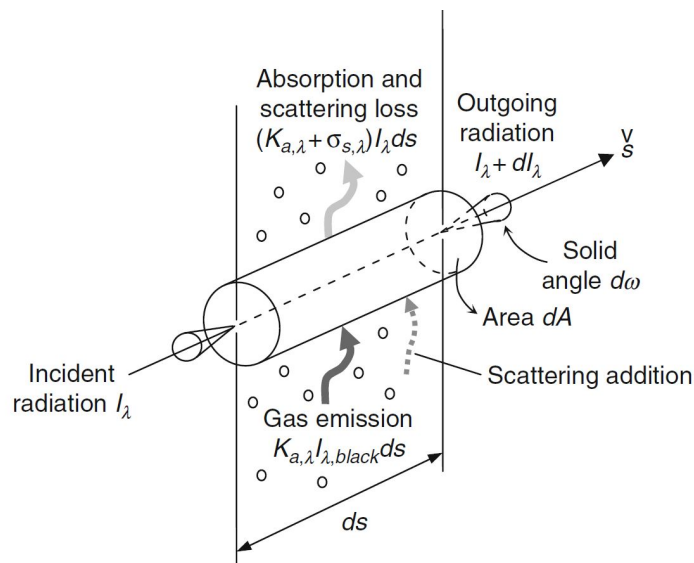
Figure 2.4.: Radiative heat transfer in absorbing medium [136].

function. It predicts the probability of radiating intensity redirected from any direction [70].

$$\tau_\lambda(S) = \int_0^S \kappa_\lambda(S)dS \tag{2.37}$$

In most engineering applications, scattering effects are neglected, characterized by $\sigma_{s,\lambda}$=0. This is permitted when the main combustion products are water vapour and carbon dioxide as it is the case in natural gas combustions. Consequently, Eq. (2.36) is simplified to Eq. (2.38), stipulating that the intensity's rate of change is equal to the net gain in radiant energy. This statement can be further divided into losses of radiative intensity due to absorption and an increase by emitted radiation of the surrounding gases. This formulation is still dependent on the wavelength. To describe the total radiation intensity, the individual terms have to be integrated over the entire wavelength spectrum. In the following two sections, the main issues concerning the modelling of gas properties (absorption, emission) are discussed. Furthermore, solutions to the RTE are presented.

$$\frac{dI_\lambda(\vec{r},\vec{s})}{ds} = -k_{a,\lambda}I_\lambda(\vec{r},\vec{s}) + k_{a,\lambda}I_{black,\lambda}(\vec{r}) \tag{2.38}$$

Radiative Properties of Combustion gases

To model the absorption capacity and emissivity of the combustion gases, several models with varying complexity have been developed. In industrial steel reheating furnaces, most of them are fired by natural gas - the main combustion products are water vapour (H_2O) and carbon dioxide (CO_2). Both species are characterized by very low scattering and very different spectral radiation bands [6]. The distinctive radiation bands are visualized in Fig. 2.5.

In numerical models, the assumption of gray gases, based on Beer-Lambert's law, is a widely used approach. This simple gray gas model determines the absorption and emission coefficients in dependency of the temperature, pressure and path length. The important dependency of the wavelength is neglected. An extension of this model is provided by the Weighted Sum of Gray Gases Model (WSGGM), which was first proposed by Hottel and Sarofim [72]. The WSGGM accounts for spectral influences formed by a set of gray gases. Total absorption and emission can be expressed by emissivity as the sum of all gray gases, displayed in Eq. (2.39). This model connects the individual absorption coefficients k_i, which are regarded as wavelength independent in some regions of the spectrum, with PL which outlines the product of the sum of all partial pressures and the path length. ω_i indicates the weighting factors, which are defined by Eq. (2.40). The equation represents a polynomial dependency of the temperature of order (N_c-1), using the polynomial coefficients $b_{i,j}$. The latter are obtained through experiment results. Within this thesis, the coefficients proposed by Smith et al. [166] have been used. Several authors tested the model, proving its suitability [167–169]. Some, however, recommended to
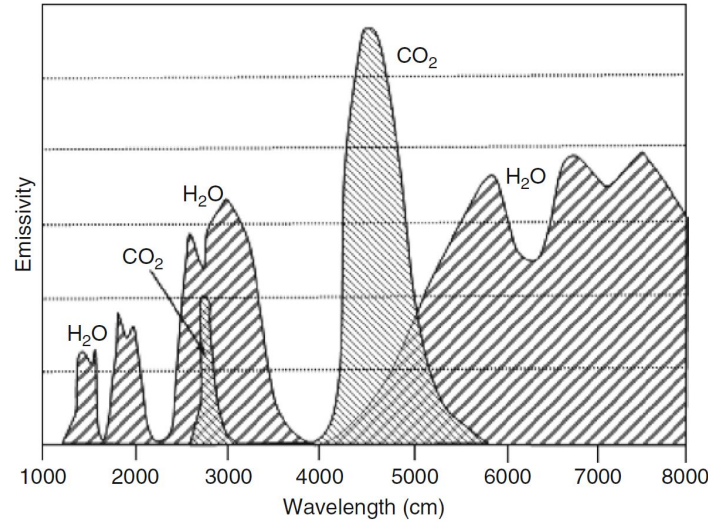
Figure 2.5.: Emissivity of the main combustion products dependent on the wavelength [136].

adapt these parameters according to different conditions [170–172].

$$\varepsilon = \sum_{i=1}^{N} \omega_i \left(1 - e^{-k_i PL} \right) \tag{2.39}$$

$$\omega_i = \sum_{j=1}^{N_c} b_{i,j} T^{j-1} \quad \text{with} \quad i = 1, 2, ..., N_g \tag{2.40}$$

Numerical Models

To integrate the RTE equation into the simulations, different numerical models have been developed. These range from simple to complex models, differing in the way angular dependencies and spatial variations are taken into account. Additionally, certain limitations of applicability arise due to the validity of media with special optical properties. The simplest models, which are available in the software used, are the P1 and Rosseland model, initially developed for a rectangular coordinate system. They are only valid for optically thick media ($\tau_\lambda > 1$). Regarding industrial furnaces, this restriction is only valid to a limited extend. Especially in the furnaces which were investigated within this thesis, as they are fired by natural gas with a very high amount of methane, the assumption of a high optical thickness is not applicable. The P1 model describes radiative intensity by a series of spherical harmonics. The radiation flux can be defined by Eq. (2.41). It depends on the incident radiation q_{in}, the absorption coefficient k, the refractive index n, the Stefan-Boltzmann constant σ and temperature.

$$-\nabla \cdot q_r = k q_{in} - 4k n^2 \sigma T^4 \tag{2.41}$$

In the P1 model, a transport equation is solved for the incident radiation q_{in}. The Rosseland model can be derived from the P1 model, assuming radiative equilibrium. This results in

the usage of the black body intensity at gas temperature for q_{in}. Another simple concept is presented by the S2S, considering only the radiative heat transfer between two gray-diffuse surfaces, neglecting absorption, emission or scattering of radiation. The exchange of energy within a domain thus only depends on the size, distance and orientation of the walls and is taken into account by a view factor. In case of a large number of radiating walls, the computational effort could become quite extensive. It can be reduced by clustering the surfaces, while radiative flux is preserved. This model is not commonly used for numerical simulations of reheating furnaces. The cause for this are the restrictions regarding absorption or scattering effects. Furthermore, there is a computational limitation in the surfaces which can be taken into account. In most cases only a limited number is included to keep computing time in a certain range. The total radiative heat flux can be described by an emitted and reflected portion as shown in Eq. (2.42), using $(1 - \varepsilon)$ for the reflectivity.

$$q_r = \varepsilon \sigma T^4 + (1 - \varepsilon) q_{in} \tag{2.42}$$

A more sophisticated model is presented by the Monte Carlo model. It is a statistical model, that is based on simulation of a bundle of representative photons from their inception to extinction, describing radiative intensity. On their paths, changes of spectral intensity of the photons due to absorption, emission and scattering are taken into account. The number of these bundles that are considered affect accuracy and also the computational effort needed. This results often in high CPU and RAM requirements [173], which also limit the model's applicability to real size reheating furnaces.

The last method to calculate radiative heat transfer, that will be mentioned in this thesis, is the DO model. As the terminology suggests, this model solves the RTE (Eq. (2.36)) in a set of discrete directions N. The number of directions is fixed by angular discretizations, using the divisions and pixelation in polar and azimuthal angle. By increasing the number of directions, the model accuracy can be controlled. This, however, also increases the computational effort needed since the RTE have to be solved in each direction [174]. For highly directional problems, it is advised to increase the number of discretizations significantly to receive reasonable results [175]. Using the software Fluent, each octant of angular space at any spatial location is divided into solid angles. The divisions are preset by the user. A big advantage of this model is its capability to deal with a wide range of optical regimes. This feature distinguishes it from the simpler models, however, it also increases computational effort. Compared to the Monte Carlo model, the DO model needs less computing effort, which has been shown by Cohen et al. [176]. They noted marginal differences in the calculated results. The same findings are presented by Cho and Miller [177], highlighting the efficiency of the DO model. The calculation time when using the Monte Carlo model was found to exceed the DO by a factor of eight. Some authors developed a model based on a combination of the Monte Carlo and the DO model [178]. The aim was to create a radiative model with high accuracy, but little computing time. Nevertheless, the DO model is one of the most commonly used ones when dealing with reheating furnaces. It is able to incorporate specular wall reflections and it also allows to incorporate non-gray

radiation by a band model. Within this thesis, it is thus the main model used to capture the radiative heat transfer inside the combustion chamber.

2.3. The Developed Numerical Scheme [2]

The numerical models that were presented in the previous sections are used to characterize the flow, combustion, species and heat flux distributions in the simulations, combined in a steady-state or transient manner. Above all, the computational effort, which influences calculation time, plays an important role in numerical investigations. This means that many cases are considered as stationary, representing a permissible simplification regarding combustion and flow calculations. The developed numerical scheme is based on the proposal from Prieler et al. [62] and has been adapted to comprise any type of steel movement. Within this section, the overall scheme and the type of modification implementation is discussed in detail. The exact modifications themselves depend on the furnace type and will thus be described in a later chapter, when the construction descriptions will be looked at in detail.

In general, the numerical scheme is based on a steady-state combustion and a transient steel heating simulation, alternating in an iterative manner, visualized in Figure 2.6. The process begins with a steady-state combustion simulation of the whole furnace. This simulation is schematically visualized in Figure 2.6 (a). It includes all of the furnace details, and focuses on the combustion of the fuel and the oxidizer as well as the resulting temperature, species and heat flux distributions. In this illustration three steel goods are indicated, which are subtracted from this simulation domain leaving only their outer surface area. The initial condition for the iterative process is an assumed temperature distribution, based on process data, applied to these surfaces, as indicated by T_s in Figure 2.6 (a). In general, any spatial distribution, or even a constant temperature, can be assumed, affecting the number of iteration loops needed to reach the final resolution. The number of iterative loops will be lower if the assumed distribution is close to the final one. Within this thesis, a temperature profile was assumed for all furnaces, which increases linearly in the direction of the steel movement. The minimum temperature is set near the steel inlet and its maximum near the corresponding outlet.

After reaching a convergent solution, the calculated heat flux distributions to the individual steel goods are extracted. Before these can be used as boundary conditions in the subsequent transient simulation of steel heating, the mentioned modification need to be integrated. To illustrate this, the origin of the integrated modification will be briefly discussed in the following. In most reheating furnaces, steel performs a periodical movement. To be more precise, the steel stays in one position for a defined period of time before it is transferred to the next position. The individual positions within the furnace are schematically indicated in Figure 2.6 (a). This figure shows three steel goods, numbered from 1 to 3. During a transfer, the steel good, which was previously heated in position 1, is transferred to the next position (2), while a new good is

---

[2]Segments of this section have already been published in [4]

placed in the combustion chamber. Simultaneously the other steel goods are also transferred to the next position and the last one is discharged. In pusher type furnaces, the steel goods are pushing each other further, scratching on the furnace floor. Walking beam type furnaces lift up the good an put it in the next position. For this to work, a complex skid system is needed, comprising fixed and walking beams. While the former are used to keep the steel in place in each heating position, the walking beams are used for the transfer to the next position. Within the considered walking beam type furnace, the tubes perform an additional rotational movement. The reason behind this will be described in a later chapter 5. This chapter also looks at how the rotational movement are implemented in the numerical models. To implement any of the moving patterns, the heat flux profiles must be modified before usage in the transient simulation. Therefore, the position of the profiles, fixed by the cartesian coordinates (x, y, z), is changed according to the moving scheme.

In the transient heating simulation of the steel, only the solid region of a single steel good is to be taken into account, as indicated in Figure 2.6 (b). A big advantage of this small domain, regarding only solids, is the possible neglection of the calculations of flow, turbulence, radiation and species. As a result only the energy equation has to be solved for the transient heating simulation. This also affects the stiffness of the equation system positively since only steel has to be considered. Thus, the computational effort needed is reduced. To include the general steel movement, as described above, the individual heat flux profiles, from entry to discharge, are successively defined as boundary conditions, which introduces the temporal aspect. This means, that the heat flux which is calculated at the first position is used as a boundary condition for the resting time in one position. Subsequently, the heat flux profiles of the other steel goods are applied sequentially. Each of those profiles is used for the resting time on each position. During the individual resting phases, the individual heat flux profiles remain constant.
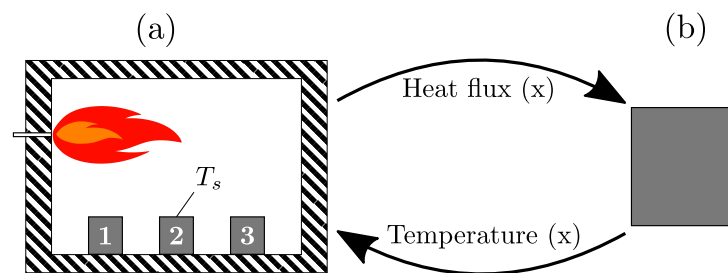
Figure 2.6.: The iterative scheme based on the steady-state combustion (a) and the transient heating simulation (b) adapted from [4].

The big advantage of this small computational domain of a single steel good makes it possible to use a small time step size without significant increase in computing time. This simulation provides a temporally and locally highly-resolved temperature distribution of the steel blocks. The calculated steel surface temperatures are then used in the next iterative loop as a new boundary condition of the blocks in the steady-state simulation. When the relative temperature deviation of the blocks between individual iterations was below 0.5 %, the iteration loop was deemed successfully terminated. The big advantage of this iterative procedure in comparison to fully transient models is the significant lower calculation time needed. All of these simulations

were performed on an Intel i7 with a 6 core CPU and 32 or 64 GB RAM, respectively, which required only two weeks to reach the final solution. The decisive factor is, beside the numerical model used, the size of the generated mesh of the steady-state simulation. This mesh consists of about 12 million cells and is described in detail in a later chapter.

3 |

Measurement[1]

In steel industry a number of common methods for determining the temperature distribution of steel goods are available. In reheating furnaces, knowledge of the inlet and the outlet temperatures is of great importance since these temperatures have a significant effect on both, the gas input to the furnace as well as downstream processes. Excessive temperature fluctuations are mainly caused by the condition inside the combustion chamber. An uneven distribution of gas and wall temperatures influence the heating characteristics of the steel drastically. This means that improving the temperature distribution within the furnace results in less excessive temperature fluctuations of steel goods, close to the target temperature.

Several measuring methods have been developed to measure temperatures over a wide range for industrial purposes. In the steel processing industry, one of the most common contact temperature measurement techniques used are thermocouples. Various situations restrict their range of application, forcing user to apply contactless methods instead. These include different techniques, such as infrared cameras and radiation pyrometers. They represent the most common methods used in the steel industry. The application of thermocolours or materials with known melting points is usually restricted to laboratory experiments. Within this thesis, different measuring techniques have been used and compared. These are evaluated with regard to their ability to determine the temperature profile of hot steel tubes exiting a reheating furnace. For this purpose, a two-colour pyrometer, an infrared camera, and the results of a test tube equipped with several thermocouples is used. These methods differ in their measuring principles, as well as in terms of their spatial and temporal resolution. In the following sections, the devices are briefly described. The results will be presented in a later section.

3.1. The Wwo-Colour Pyrometer

The pyrometer used is a two-colour pyrometer, the Raytec MR1SA [179]. The big advantage of this tool is its ability to determine temperature without knowledge of the object's emissivity. This is done by measuring the radiation intensities at two different wavelengths. The ratio

---

[1]Segments of this chapter have already been published in [1, 2]

of both measured signals is calculated, which allows to determine the target temperature by eliminating dependency of the emissivity, assuming $\varepsilon_1 = \varepsilon_2$. In this, the indices 1 and 2 indicate the emissivities of one body at both wavelengths. As long as this assumption is valid, and properties of both wavelengths are affected in the same way, the pyrometer works properly. To enhance the applicability, wavelengths are set close together, eliminating dominant effects on emissivity. In order to measure correct temperatures for bodies with varying emissivity, the so-called e-slope adjustment is usually incorporated in most devices [180, 181]. As a result, these types of pyrometers are well suited to measure hot steel that is possibly forming scale.

This pyrometer is mounted right after the tube outlet of the walking beam type reheating furnace. There, it measures the steel surface temperature of the passing tubes. Cooling between the steel outlet and the temperature measuring point is marginal due to the high discharge velocity of almost $2\,m/s$. Thus, the temperature of the steel after heating can be determined. Furthermore, the operator obtains information on any temperature fluctuation in the tube axis. However, it is not possible to make any statements about any changes on the circumference of the tube. In the mounted sector, the tubes' surfaces still contain some scale. The necessary descaling, using high pressure water jets, takes place right after the pyrometer.

3.2. The Infrared Camera

Similar to pyrometers, ICs are based on the same measuring principle: both measure the radiation intensity of a surface at a specific wavelength. The big difference to pyrometers, is the limitation to a single wavelength. Thus, influences due to possible scale on the surface cannot be avoided. Another difference is the measurable area. The pyrometer measures only one distinctive point (or area), while the IC is able to measure the surface temperature at specific areas of varying sizes. Creating images of the temperature variation. The main advantage of both approaches is the simple, fast and economical measurements.

Within this thesis, the FLIR T1030sc [182] has been used. This high-speed imaging camera records at 30 fps with 1024×768 HD resolution. Thermal sensitivity is below $20\,mK$ with a maximum in measurable temperature of $2000\,°C$. This makes the device highly suitable for measuring many different areas in the steel industry. During measurement the correct setting of environmental conditions is essential. The set parameters, such as air humidity, distance to the measuring object, ambient temperature, etc., were adjusted to reflect environmental conditions. Another important parameter is the emissivity of the object to be measured. Larciprete et al. [183] determined the temperature dependent emissivity of several woven, knitted, or non-woven steel textiles, showing the influence of the surface texture. In this thesis, the surface of the tubes is relatively uniform allowing the same emissivity, as used in the simulations, to be used. Further information on the emissivity used is provided in later chapters. The measurements were carried out directly after the tube outlet. Every attempt was made to set the measuring points of the IC and the pyrometer as closely together as possible to ensure a

very good comparison. It shall be noted that possible influences of hot exiting gases on the measured steel temperature have been evaluated. Therefore, several tubes have been measured from different angles. During stationary operation, each of the exiting tubes indicates a very similar temperature profile. This facilitates a comparison of the different angles measured.

3.3. Transient Temperature Measurements by Tracing Thermocouples

The third measuring technique, regarded within this thesis, is often used in the steel industry: an unfinished steel product is equipped with several thermocouples and then dragged through the furnace. This makes it possible to measure the temperature at specific points during heating. Due to the limitation of a low number of thermocouples being used, no statement about a detailed temperature profile is possible. Instead, important temperatures, such as the core temperature, can be measured. Nevertheless, this kind of measurement is both costly and time-consuming since the steel has to be prepared in advance.

(a) Sketch of the test tube   **(b)** Thermocouples at tube end
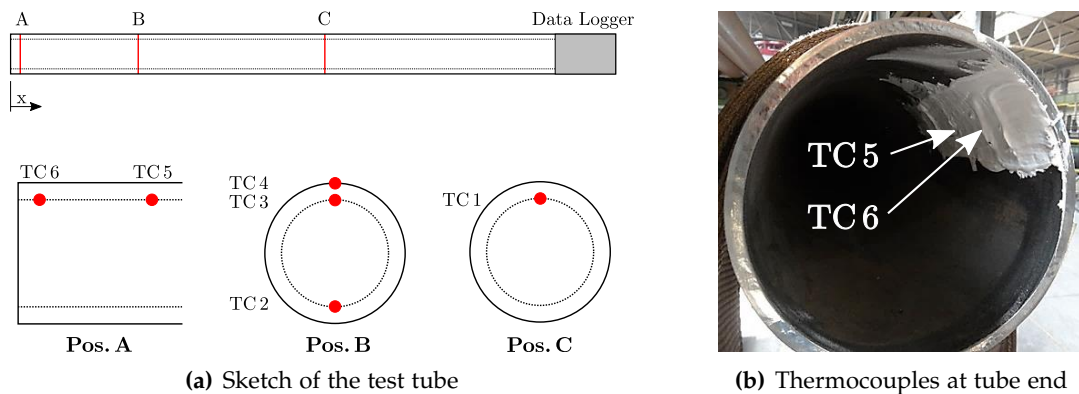
Figure 3.1.: Location of the thermocouples in the test tube adapted from [1].

Table 3.1.: The positions of the thermocouples used in the measurement [1].

No.	Distance x from tube end [m]
$TC\,1$	9.5
$TC\,2$	4
$TC\,3$	4
$TC\,4$	4
$TC\,5$	0.15
$TC\,6$	0.03

Within this project, two experiments have been performed. In both cases only half a tube has been examined due to the limitation of the length of the thermocouples. The location of the thermocouples are sketched in Figure 3.1(a), indicating the data logger at the rhs, which represents the middle of the total tube length. Three areas have been chosen for placing K-TE type thermocouples, marked by A - C. At each of these locations several thermocouples are

mounted, marked by red dots in the lower part of this illustration. It is quite obvious, that all thermocouples are arranged in a vertical plane mounted at the inner and outer part of the tube's surface. The thermocouples mounted on the inner surface were glued to the surface as visualized in Figure 3.1(b). This illustration indicates that the thermocouples which are mounted close to the end face (TC 5 and TC 6) are exposed to the most intense heating. TC 4 has been placed inside the steel, very close below the outer surface to prevent radiation influence. TC 2 is the only thermocouple mounted on the opposite side to record the rotational influence. The detailed locations of the individual thermocouples can be seen in Table 3.1.

The experiments required a preheating of the test tube in order to ensure that the elevated inlet temperature is the same as in real operation. The preheating has been performed in a separate industrial furnace. The whole experiment can be divided into 4 sections. This is visualized in Figure 3.2, which shows the temperature profile of a single thermocouple (TC 3). The aim of this illustration is to visualize the conduction of the whole experiment. It does not present any results. In this Figure, ① indicates the tube preparation, including the installation of thermocouples. This part of the experiment is the most time consuming one and is shortened to improve clarity. ② represents the preheating process, in which the steel was heated to about 730 °C. In part ③ of the experiment, the subsequent transportation of the steel to the reheating furnace takes place. Scale formation during preparation time can be excluded as the temperature stays below the 750 °C mark, known as the starting condition for this process. After reaching the desired inlet temperature of approx. 420 °C, the tube enters the furnace. This is when the actual experiment starts as indicated by ④.
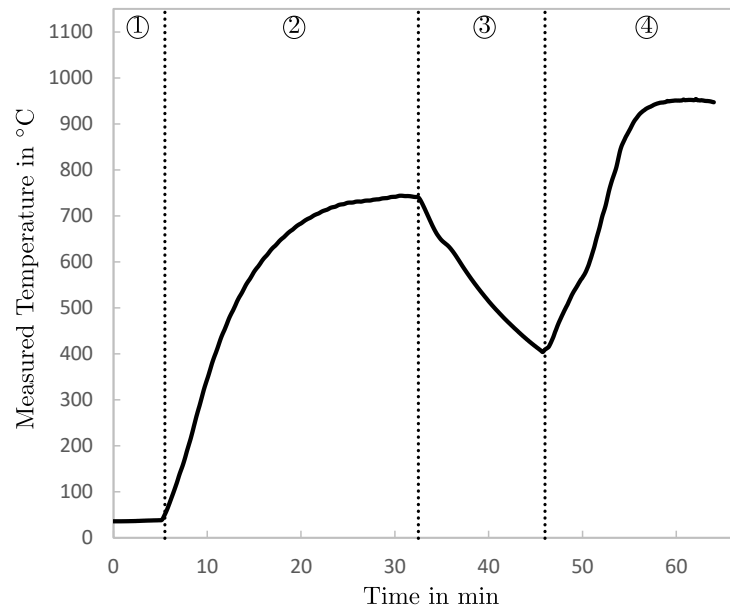
Figure 3.2.: Measured temperature during the whole experiment, indicating the four main sections.

3.4. Measuring Point

In case of the pyrometer and infrared camera, the measuring point is decisive. Fig 3.3 shows the dependency of the measured temperature on the perpendicular angle. When the measuring device is ideally placed, the object's temperature can be measured correctly. Discrepancies increases with increasing inclination, resulting in large deviation close to 90°. This means that the measuring point should be ideally be perpendicular to the tube axis. The orientation is of significant importance when measuring strongly curved surfaces as it is the case in this thesis. Therefore, in the measurements using the pyrometer and IC a measuring point in tube centre was chosen. Furthermore, the emissivity of the measured surface is set to 0.7, as was used for the steel tubes in the simulations. Values up to 0.9 can be found in literature for different steel types depending on the surface condition [100, 184]. This does not affect the test tube experiment, in which the measuring points are fixed on the previously selected position.
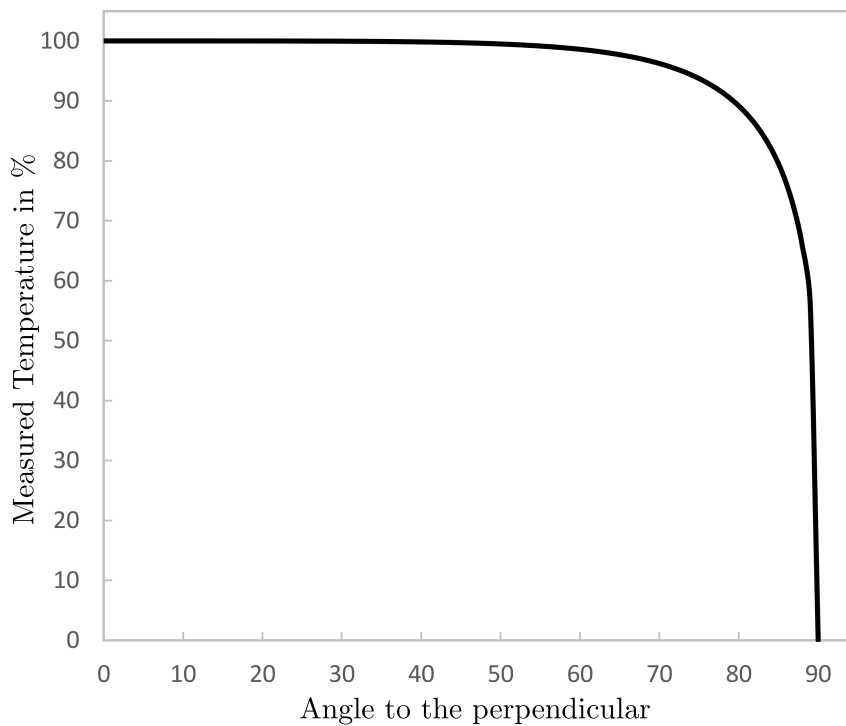
Figure 3.3.: Dependency of the measured temperature on the angle to perpendicular.

4

Preliminary Studies[1]

In numerical studies, it is common practice to investigate models and their effects on the calculated results in smaller domains. Therefore, lab-scale furnaces are often constructed and used for conducting tests. They are important tools for developing burners and numerical models. A well - studied furnace is the one of IFRF, which has been measured extensively [185, 186]. Such furnaces are very expensive, thus investigations in CFD are commonly performed in fictitious smaller domains. This allows the researchers to compare different numerical models and to provide essential information on their impact on flame prediction within a reasonable timeframe. Very complex or thoroughly examined models are used as a benchmark. In numerical combustion simulations, the most important models are those to describe turbulence, its interaction with chemistry and radiation. This chapter focuses on the comparison of a number of radiation and turbulence-chemistry interaction models. Therefore, small sections of the real furnaces, including their main burner types, are investigated. The aim was to find an optimum model setting to be utilized in the real size simulations.

4.1. Flat Flame Burner

The correct simulation of flat flame burners in the walking beam type reheating furnace is of significant importance. The impact of different turbulence models, using a flat flame burner, has already been evaluated by Prieler et al. [62]. In this work, the complex RSM and realizable k-ε have been compared to each other. It was found, that the error in resulting heat flux distribution is below 1 %, indicating a high degree of accordance. In this work, only the DO model has been used.

It has already been mentioned that the use of this special type of burner is of great importance to the radiative heat transfer. This also shows the importance of choosing the right radiation model. In order to evaluate this, three different radiation models have been investigated in a simplified domain within this chapter. This can be seen as the cuboid part of the whole domain, taking into account a single burner. This domain corresponds to approximately a 1/96

---

[1]Segments of this chapter have already been published in [1, 4]

of the real walking beam type reheating furnace. The four adjacent burners would be in the corners of this geometry. The small case is ideal for investigations of grid dependency and for evaluating different numerical models keeping computational effort low.
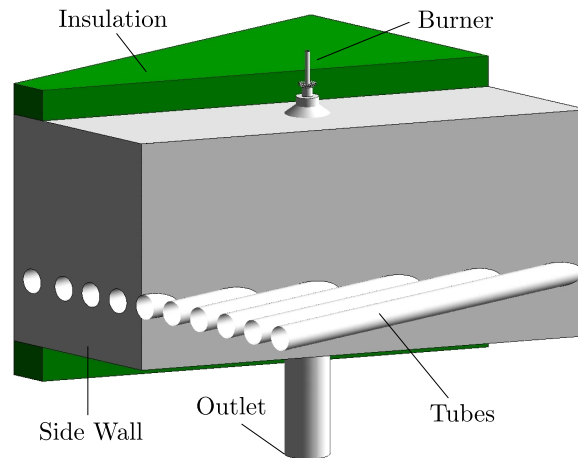
Figure 4.1.: The geometry of the test case, indicating the insulation (green) and fluid region (grey)

It was already mentioned in a previous section (2.2.5) that the DO model is very CPU intensive when taking into account a large number of directions. Therefore, the aim of this chapter is to compare simpler models to the DO model, which is treated as benchmark, to avoid unnecessary computing time. This is of significant importance when applied to real size applications with high complexity. The considered models are the simple P1 and the S2S models. Their theoretical backgrounds and validity ranges were outlined in section 2.2.5. They are decisively influenced by the radiative properties of the surrounding fluid, as described by the optical thickness. This value is dependent of the composition of the combustion gases and the beam length (fluid volume). Thus, it is important to note that the simplified domain has a smaller optical thickness compared to the real size walking beam type furnace. This is of particular significance for the P1 model, which is limited to optically thick media. When the results are meaningful in this small domain and of high accuracy, the model is expected to behave the same on the real-size furnace. In case of the DO this is insignificant due to the coverage of many optical regimes. It is also negligible for the S2S since it neglects any optical influences of the fluid. Besides this, turbulence has been modelled with the realizable k-ε model according to the findings of Prieler et al. [62]. The numerical domain is illustrated in Fig 4.1, indicating the burner, the solid insulation (green) and the fluid region (grey). The domain is clearly simplified, with a single central flue gas outlet. Geometric dimensions are similar to the real furnace, using the same height and insulation thickness. Also, the tube dimensions and positions are equal to the real furnace. Within this simplified case, only the outer steel tube surfaces, with a diameter of 177.8 mm are present. In a first attempt, the beam system has been neglected, so the tubes are floating in a height of 0.46652 m. Further assumptions have to be made regarding the side walls, which are treated as adiabatic.

Within this chapter the combustion process was modelled using the SFM model. This model allows the detailed skeletal25 reaction mechanism to be used, while keeping computing times

relatively low. In the simulations, pure methane with an inlet temperature of 25 °C is used as fuel. Continuous measurements of the natural gas used, show that it mainly consists of methane (98.4 %), while the rest is nitrogen and carbondioxid (~ 1%), and longer chained hydrocarbons (~ 0.6%). Thus it can be assumed, that the assumption of pure methane is valid. The air is heated up to a temperature of 300 °C with the downstream heat exchanger. The air is also simplified to a composite of 79 % nitrogen and 21 % oxygen. All inlets are modelled as mass flow inlets with a turbulent intensity of 10 % using their respective hydraulic diameters. The mass flow rates of fuel and oxidizer are $0.004\,kg/s$ and $0.0865\,kg/s$, respectively. This corresponds to the maximum possible thermal input (200 kW) with excess oxygen of 4 % wet based. In the real size furnace, those burners are operated mostly in partial load. The outlet has been modelled as pressure outlet, with a backflow temperature of 1000 °C and a turbulent intensity of 5 %. The tubes' surfaces have been regarded as walls with a constant temperature of 700 °C, representing tubes in the preheating zone of the real furnace. Their emissivity is, similar to all other inner furnace walls, set to 0.7. Thermal conductivity of the insulation is set to $1\,W/mK$ according to [187]. As described in the model description for the SFM model (see section 2.2.4) the flamelets and PDF are calculated in a previous step. These require the definition of fuel and oxidizer composition used and parameter settings for flamelet and PDF calculation. The settings regarding flamelet calculations are modified from Fluent's default settings. The number of grid points in flamelets and their total number has been increased to a total of 40 each. Although solution time and memory usage increase with increasing number, this seems to be a good compromise between accuracy and effort needed. The number of mean mixture fraction points and its variations are also increased in the PDF parameters. These are set according to Prieler et al. [62] presenting a resolution with sufficient accuracy. A summary of the flamelet and PDF parameters used can be found in the Appendix B.1. The numerical solution is moreover affected by the spatial discretization. In case of the flat flame burners with their strongly curved flame, it is recommended to use the PRESTO! scheme for pressure discretization [188]. Other scalars are discretized using the Second Order Upwind scheme. This is superior when flow is not aligned with the mesh, which cannot be guaranteed in the case of the flat flame burner. All settings are summarized in the Appendix B.3. Other important settings during the simulations are the Under-Relaxation factors. These represent a damping function of the solver and allow for control of stability and convergence rate of the iterative process. For complex problems initial values for Under-Relaxation Factors (URF) are lowered and are manually increased with calculation progress. The final values should be as large as possible facilitating reaching the final solution. The URFs as used in the converged simulation are shown in the Appendix B.2.

4.2. Dependency of the Mesh

The grid is essential in numerical investigations. A balance among computational effort and accuracy needed, has to be found. While a fine mesh is important in order to capture high gradients in velocity, species concentration and temperature, a preferably coarse grid should be striven for. Prieler et al. [32] investigated the impact of different mesh types, using either Hexahedron (Hex),Tetrahedron (Tet) or Polyhedron (Poly) cells. The simple geometry allows one to use a very fine structured hexahedron mesh which is aligned with the flow. This reduces numerical diffusion, leading to more accurate results. More complex geometries, such as the present swirl-burner, require the usage of an unstructured Tet or Poly mesh. Polyhedral cells are transformed from several tetrahedral cells, which is done directly in the simulation software. In order to obtain a fine polyhedral grid after transformation, an even finer tetrahedral grid is required. Three meshes have been compared, consisting of Tetrahedral-Hexahedral, Tetrahedral

Table 4.1.: Number of cells.

Mesh	Number of cells used
Tet-Hex	$1,932,750$
Tet	$1,973,296$
Poly	$410,765$

Table 4.2.: Heat flux distribution in the test case in kW for $200\,\mathrm{kW}$ thermal input.

	Tet-Hex	Tet	Poly
Heat due to combustion	199.34	199.13	198.92
Wall heat losses	31.63	31.55	31.50
Flue gas losses	76.54	75.98	76.38
Heat transferred to the tubes	125.74	123.72	121.52

or Polyhedral cells. The number of cells of the three meshes are shown in Table 4.1. The Tet-Hex and the Tet meshes consist of approx. the same number of cells. The Poly mesh has been transformed from the Tet mesh using edge and face-centroids of neighboring Tetrahedral cells forming a polyhedral cell. This leads to a comparatively coarse grid, with almost a fifth of the tetrahedral number of cells. The DO model has been used as the radiation model, neglecting any influences by solar load. The angular discretization has been set to 4 divisions in both angular coordinates Theta and Phi. Using the WSGGM, the number of bands used in the Non-Gray model is set to zero. The settings are summarized in the Appendix C, Table C.1.

Figure 4.2 shows the temperature distribution in a cross-sectional plane for different meshes. Although the number of cells differs strongly in each cases, there are little differences in temperature distribution, proving the small impact of the mesh type. The same behaviour can be seen in the heat flux distribution of all three meshes, as shown in Table 4.2. It also outlines the heat that is generated due to combustion for each case. A slight deviation between the
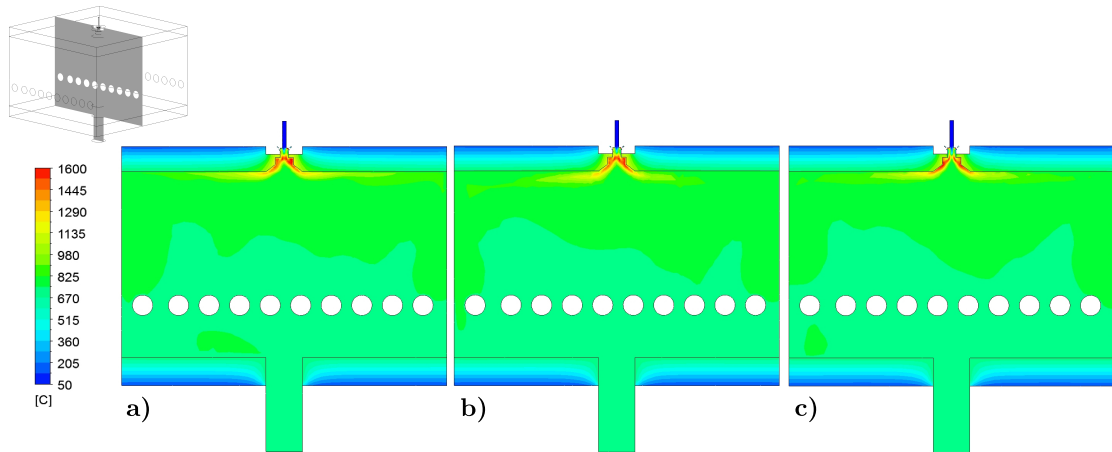
Figure 4.2.: Temperature distribution in a sectional plane for the a) Hex-Tet mesh, b) Tet mesh and c) Poly mesh

individual cases can be seen (0.42 kW), which can be considered as minor. Besides this, the heat fluxes via walls, the exiting flue gas losses and the heat flux which is transferred to the tubes are also quite similar for all cases. The same is true for the flue gas temperature and composition, as shown in Table 4.3. The maximum gas temperature is 736.8 °C as calculated by the Tet-Hex case. There is a maximum in deviation of 4.8 °C when compared to the Tet case. Very similar distributions, indicating total fuel burnout, can also be seen when looking at the molar fractions of the main species.

Table 4.3.: Calculated flue gas temperature and species composition at the outlet.

		Tet-Hex	Tet	Poly
Temperature	°C	736.8	732.0	734.3
Mole fraction in mol/mol E-02				
O_2		3.9722	3.9681	4.0064
CO_2		7.6437	7.6455	7.6293
CO		0.0444	0.0445	0.0434
H_2O		15.2604	15.2640	15.2312
N_2		72.8575	72.8560	72.8708

It can be concluded that the flame shape is hardly dependent on the mesh type at all, although the Poly grid is coarser. The impact of the mesh type on the calculated solution is negligibly small when a fine mesh is ensued in the vicinity of the burner. For further investigations, polyhedral cells will be used. They allow the computational effort to be kept relatively low while hardly any information is lost. Tests on grid size dependencies were not carried out at this stage. Instead, they were conducted in the real-size furnaces as will be shown in chapter 5.1. In the following section, different radiation models are tested using the Polyhedral mesh.

4.3. Effect of Radiation Models

Within this section, the complex DO model will be compared to the P1 and S2S models. The results that were obtained using the DO model, shown in Figure 4.3 a), are the same as in the mesh dependency, which were discussed in the previous section (see Figure 4.2 c). The boundary conditions used are equal to the settings from the previous section. Only, the radiation models have been changed. The settings used are briefly described within the next paragraph. Using the P1 is simpler than the DO model since angular dependencies are neglected. Only solar radiation and the number of bands for the Non-Gray model have to be set. During the simulations, solar radiation was neglected, using the WSGGM approach, similar to the DO model (Appendix Table C.2). The S2S model, on the other hand, needs more input. This model uses view factors to calculate the radiation emitted by all walls and the resulting incident radiation on each surface. The computational effort increases with the increasing number of emitting surfaces. However, clustering is an effective method ti reduce the computing effort. The computational effort can also be influenced by the right choice of surfaces. Within the performed simulation, the default settings are used. They can be found in the Appendix C, Table C.3
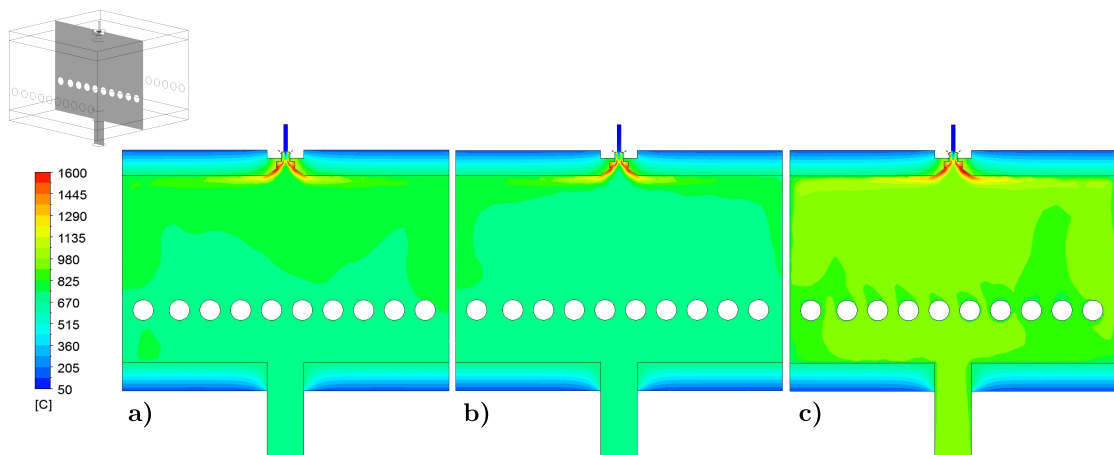
Figure 4.3.: Temperature distribution using the a) DO, b) P1 and c) S2S radiation model.

The calculated temperature distribution inside the combustion chamber is visualized in Figure 4.3. The DO and P1 models reveal approx. the same temperature profile, with the DO model reaching a slightly higher level. On the other hand, the calculated temperature using the S2S model is clearly higher. This is due to the different calculation for radiation and the neglected impact of gas radiation. This neglection has a significant influence on the heat flux distribution in the whole domain. This is outlined in Table 4.4, indicating the calculated heat fluxes. The results of the DO and P1 model reveal a very similar heat flux distribution within the domain. This means that, the impact of the model limitation to optical thick media is incisive within this simulation. The S2S underestimates the total heat flux to the tubes. This results in higher gas temperatures within the furnace, also raising the heat flux of the exiting flue gas. For further comparison, the radiative component of the heat flux transferred to the tubes is visualized in Table 4.4. In the casees of the DO model end the P1 model, the radiative share of

total heat flux is about 94 %, which corresponds to values found in literature for whole furnaces [189–191]. The radiative share using the S2S model is about 66.5 % which underestimates the radiative heat transfer. This can be attributed to the neglected gas radiation. Figure 4.4 shows the total heat flux distribution to the tubes in more detail. It has become obvious that all cases indicate a clearly different behaviour. The DO model reveals the maximum heat flux on the upper surfaces of the tubes, with a value of about $12\,kW/m^2$. The local minimum can be found on the lower surfaces with $2\,kW/m^2$. This behaviour is expected to reflect the real behaviour since the main radiative flux is emitted from the flame and the hot upper surfaces. The P1 model, calculating a similar value of the total heat flux transferred, shows a completely different distribution. According to this model, the maximum can also be located on the upper part ($9\,kW/m^2$), while no local minimum can be spotted. This behaviour seems doubtful since the main heating comes from the ceiling. In addition to the maximum, the tubes receive a specific heat flux of about $7\,kW/m^2$. The strong deviation to the DO model can be attributed to the model's limitation to optical thick media. This affects the locally transferred heat flux distribution to the tubes significantly, leading to a distorted heat flux distribution The S2S, as shown in Figure 4.4 c), also reveals a completely different behaviour. According to this model, the maximum can be found in the tube centre of the domain with $12\,kW/m^2$, which is caused by the hot flame which is positioned above this spot. In lateral areas, the specific heat flux is decreased significantly due to the neglected gas radiation. However, the upper and lower limit of the specific heat flux transferred is similar to the DO model. The calculation showed that the maximum can be found on the upper part of the tubes, whereas a decreased heat flux can be detected in the lower part.

The calculated results imply the suitability of the DO model when dealing with industrial size reheating furnaces. Its ability to deal with a wide range of optical regimes including locally varying absorption coefficients makes it superior. The limits of the simpler models (P1 and S2S) often restrict their applicability to simpler problems. In this context, mostly the optical regime is decisive, which has been proven with the performed simulations. Both simpler models fail to predict the local heat flux distribution to the steel. This is due to the restriction of the P1 model to optical thick media, while the S2S neglects any absorptive power of the gases. Both represent special cases which cannot represent reheating furnaces in which a wide range of optical regimes occur simultaneously. Inaccurate calculation of the heat flux distribution to the steel has a significant impact on the heating characteristics of the steel in reheating furnaces. This is the case since the impact on the resulting temperature distribution within the steel is

Table 4.4.: Heat flux distributions using different radiation models.

	DO	P1	S2S
Heat due to combustion	198.92	198.44	198.30
Wall heat losses	31.50	31.00	30.78
Flue gas losses	76.38	76.03	99.02
Heat transferred to the tubes	121.52	125.40	102.40
Radiative heat transferred to the tubes	114.30	118.32	68.04
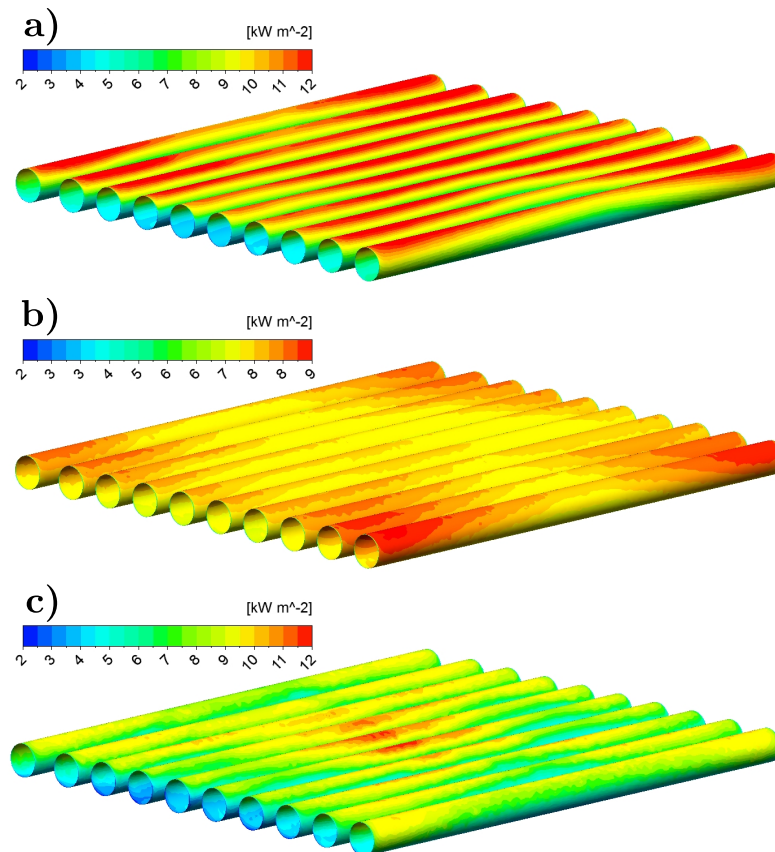
Figure 4.4.: Total heat flux to the tubes calculated with the a) DO, b) P1 and c) S2S radiation model.

major. Thus, it can be concluded that using either of these simpler models in real-size furnaces would lead to a completely different heating characteristic of the steel, resulting in wrong temperatures.

4.4. Regenerative Burner

This section serves to validate four different numerical combustion models regarding their accuracy and economy. Particular attention is paid to the correct prediction of flame shape and temperature, as well as the heat flux to the blocks and flue gas temperature. For this, the regenerative burners of the RHF have been chosen since they are responsible for the majority of thermal input. Errors would have major consequences on the calculated condition within the combustion chamber and the resulting steel temperature. The burners are mounted in pairs, whereby 17 are installed in the three main heating zones in the real furnace. The simplified geometry consists of a wedge of the entire 3D model of the RHF, representing about 1/25 of the real furnace. The numerical domain is visualized in Figure 4.5, in which the pair of regenerative burners, insulation (green), fluid and the block surfaces are indicated. The numerical domain corresponds to the stationary combustion simulation, neglecting the blocks solid region, leaving their outer surface. The transient simulation is, similar to the investigation of the single flat flame burner, not performed to test this model. The small test case shown is only used for
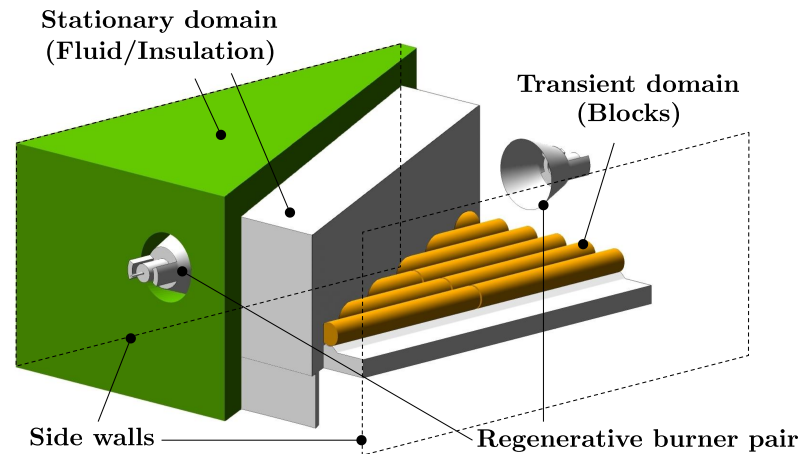
Figure 4.5.: The test case considering a pair of regenerative burner with a cut through the fluid region and insulation (green), additionally visualizing the side walls (dashed) and the transient domain (orange) adapted from [4].

testing numerical models in search of the most suitable one. In order to be able to make a statement about the accuracy of the simulation using the SFM model, the results are compared to the flamelet generated manifold model (FGM), the eddy dissipation model (EDM) and the eddy-dissipation concept model (EDC). To describe the radiative heat transfer, the DO model has been used. Its superiority over simpler modelswas demonstrated in the previous section, when dealing with real-size reheating furnaces fired with natural gas.

The construction of the regenerative burner is not as complex as the flat flame burner, which was discussed in the previous section. The regenerative burner consists of a central fuel inlet and two big lateral air inlets without any swirls. Thus, it is possible to use a pure hexahedral and flow-aligned mesh near the burner. However, the simulations of the flat flame burner revealed high quality results by using a polyhedral mesh. This is why the mesh used for this test case is based on a combination of polyhedral and hexahedral cells. It is visualized in Figure 4.6, indicating the dense mesh near the burners where high gradients occur. A total number of 376,187 cells is used for the test case. The maximum skewness of the cells is below 0.89 and maximum aspect ratio occurring is below 34. As a first step a mesh independence study was performed. For this purpose two additional meshes with about 800,000 and 250,000 cells were investigated. The results of the three cases were almost identical, whereby the coarse mesh revealed small discrepancies. Thus, the mesh with 376,187 cells revealed the best mix of computing time and accuracy.

As mentioned before, the regenerative burners are mounted in the three main heating zones of the furnace. In each of them, the burner load is about 90 % of the maximum possible ($1750 kW$). Based on this, the mass flows for natural gas and air are similar to those of the second heating zone, which is explained in more detail in chapter 7. The values used for natural gas and air are $0.03167\,kg/s$ and $0.67295\,kg/s$, respectively. During steady operation, each regenerative burner pair consists of an active and inactive burner. While the active burner heats the combustion chamber, the inactive aspirates hot flue gases, heating the ceramic packing material. The outlets of each inactive regenerative burner are modelled as mass flow outlet. The amount of flue
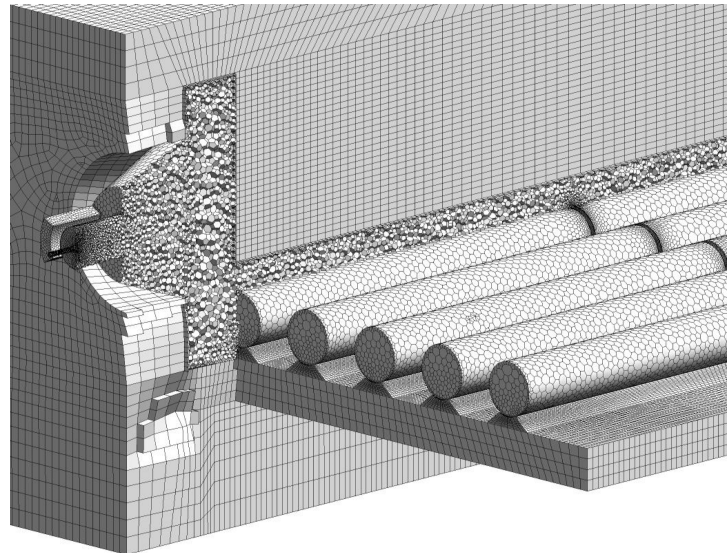
Figure 4.6.: The mesh used in the test case adapted from [4].

gases aspirated by each burner differs in each zone of the real furnace. Thus in zone 1 to 3, respectively 75, 73 and 70 % of the mass induced by the active regenerative burners is aspirated by the inactive burners to heat the packaging. The data also represents time averaged values over several cycles. To avoid the usage of any additional outlet it was assumed that the total amount of gases are aspirated by the opposite inactive burner. The combustion air is thus heated up to 900 °C by the integrated regenerator packing. The inlets are modelled as mass flow inlets with a turbulent intensity of 10 % and using their respective hydraulic diameters. The insulation of the furnace was also included in all simulations. The thermal conductivity was set to 2.2 W/mK, which is relatively high compared to the previous investigation of the walking beam furnace and other studies [62, 192]. This is due to the fact that the furnace has a comparatively large outer surface with a large number of openings that are hard to hermetically seal and has to include all possible leakages. The emissivity of the inner walls was set to a value of 0.7, while 0.8 was used on the steel surface. The outer wall of the furnace was modelled as a convective boundary condition. The free stream temperature was set to 25 °C and a heat transfer coefficient of 10 W/m^{2}K was used. The boundary conditions of the preliminary study are the same as those used in the simulation of the whole furnace, with three exceptions:

- The block wall temperature is constant at 826 °C.
- The inactive burner aspirates 100 % of the mass induced by the single active burner.
- The side walls are considered to be adiabatic.

In Figure 4.7, the temperature distribution in a horizontal plane at the burner's installation height of 0.64 m is visualized for all four models. Due to the construction of the burners with their two lateral air inlets, two flames are generated. In this illustration one seems to be shorter, but both are almost the same length. The shorter one is simply slightly above the plane shown, due to slightly more buoyancy effects. All models show approximately the same flame shape, indicating a slightly different temperature distribution in the upper left area of
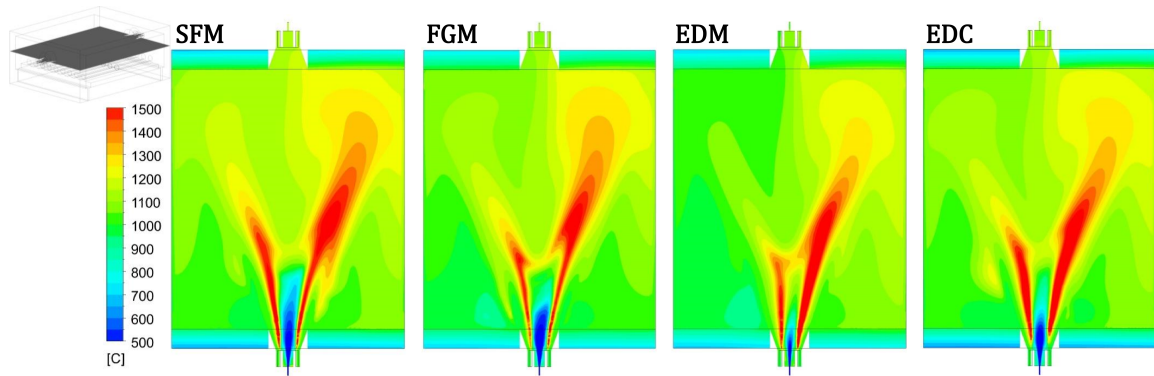
Figure 4.7.: Temperature distribution in a plane at burner height for the SFM, FGM, EDM and EDC model adapted from [4].

Table 4.5.: Comparison of the results from the preliminary study [4].

		SFM	FGM	EDM	EDC
Calculation time	s/IT	9.94	12.51	12.38	96.31
Outlet temperature	°C	1088.0	1108.6	1076.6	1093.0
Block heat flux	kW	1127.3	1116.3	1149.3	1143.9
Mole fractions at the outlet in mol/mol 10^{-2}					
O_2		4.032	4.037	4.027	4.028
H_2O		15.35	15.34	15.37	15.40
CO_2		7.674	7.672	7.678	7.677
CO		3.2e-03	3.12e-03	1.1e-04	1.7e-03
N_2		72.944	72.948	72.925	72.893

Figure 4.7. The long flames fill more than two-thirds of the combustion chamber, which can be seen when looking into the combustion chamber via an opening. The long flames lead to an undesirable high local surface temperature on the opposite inner wall (approx. 1240 °C for the SFM model). Such high temperatures can cause damage to the refractory material leading to more frequent repairs, which should be prevented. Another important value is the aspirated flue gas temperature, which could cause damages to the recuperative part of the burner in case it becomes too high. To evaluate this, the calculated temperatures (outlet temperature) have been compared. A detailed comparison of them can be found in Table 4.5. All models calculate similar temperatures which stay clearly below the maximum temperature of 1200 °C that is allowed to be aspirated. The highest deviation, of 32 °C, occured between the FGM and EDM model, corresponding to less than 3 % based on the results of the SFM. Another difference between the models can be seen near the active burner. Due to the assumption of the fast "*mixed is burnt*-approach", the EDM model shows a significantly shortened cold methane streak, leading to a shortened flame length. This also has a direct impact on the heat flux transferred to the blocks in this area, as shown in Figure 4.8. The EDM model has the highest heat flux in this area compared to the other models. It also reveals the highest heat flux near the burner, due to its fast combustion approach, followed by the EDC model. Furthermore, in Figure 4.8 the EDM model exhibits a reduced heat flux in the left region of the test case, when compared with the other models, showing similar results. This is in agreement with the findings regarding the flame shape. Nevertheless, only small deviations in the total heat flux to
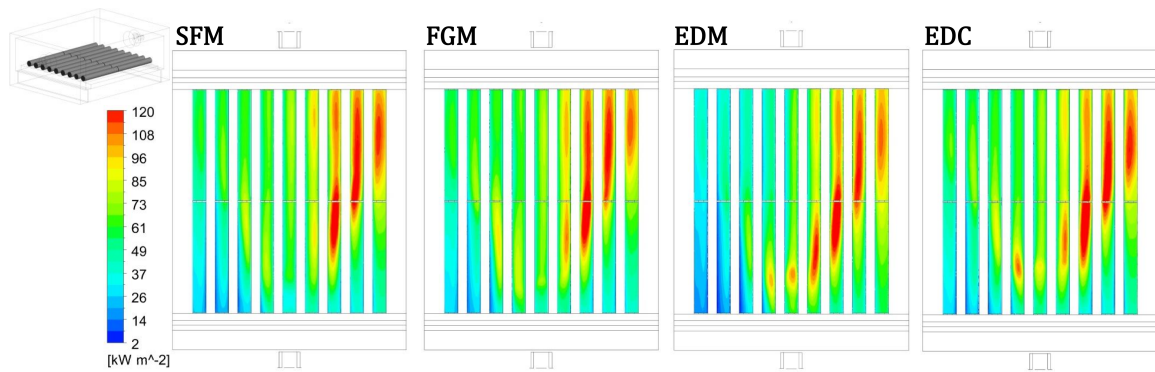
Figure 4.8.: Heat flux distribution on the block surfaces for the SFM, FGM, EDM and EDC model adapted from [4].

the blocks become apparent, as seen in Table 4.5. Once again, the maximum deviation occurs between the FGM and EDM model, at 32.9 kW, which is equal to less than 3 % based on the SFM. Table 4.5 also shows a comparison of the mole fractions of oxygen, water, carbon dioxide, carbon monoxide and nitrogen in the flue gas. All models show very similar values, indicating an almost total burnout. Only the EDM model resulted in less CO at the outlet, due to the high reaction rates near the burner, as discussed by Prieler et al. [32]. The maximum deviation in the species distribution between the individual models, based on the SFM, is below 0.002 % and can thus be seen as negligible. In conclusion, all four models exhibit similar behaviour. The deviations in terms of flame shape and heat flux profile are almost negligible. Nonetheless, there are significant differences in terms of the computing time required, as indicated by the time needed for a single iteration step in Table 4.5. All investigations were performed on an Intel i7 with a 6 core CPU with 64 GB RAM. In addition to the time required for a single iteration step, the total number of iterations that is needed to gain a converged solution is important to determine the total amount of computing time needed. The EDC model required the highest number of iterations to reach a convergent solution, due to the stiffness of the model. Compared to the SFM, it takes about ten times as many iterations to reach a converged solution. Also, the time required for a single iteration step is significantly higher than with the SFM, as visualized in Table 4.5. This leads to the EDC model to stand out by several orders of magnitudes of total calculation time, compared to the other models (using skeletal25). With the methane-air 2-step mechanism, as used by the EDM, the calculation time can be reduced by 25 %. However, the number of iterations needed stays the same, nevertheless leading to high computing times compared to other models. Thus, it can be stated that it is not suitable for a consideration of the entire furnace. When using the EDM, the computing time is significantly lower compared to the EDC. The EDM model required about 1.5 times as many iterations as the SFM, revealing also slightly higher calculation times per iteration. The computational effort is within reasonable range, yet due to the limitations that come with a two-step reaction kinetic , it is not suitable for solving many problems. However, it has benefits in other areas, such as the possibility to include different oxidizer or fuel stream compositions. For ordinary operations of the two furnaces discussed (heated solely by natural gas and air), this model offers no advantages over the SFM. The last model to be mentioned is the FGM, which requires about the same number of iterations as the SFM model, though it takes slightly more time per

iteration.

In conclusion, it can be said that each model is able to properly capture all important details of the combustion process, such as the flame shape and the temperature- and heat flux distributions. However, significant differences can be observed regarding the computational effort needed. In this regard, the SFM in particular stands out, requiring the least amount of iterations to reach the final converged solution. In addition,it requires the shortest calculation time per iteration. Still, this model is able to handle any reaction kinetic mechanism with a number of reactions and species to be taken into account. The computational effort needed is never affected by this, making this model suitable for a wide range of applications. One of the limitations of this model is the restriction to a single composition for fuel and oxidizer, respectively. When dealing with multi-fuel problems, the usage of other models is more reasonable.

5

Industrial Walking Beam Type Reheating Furnace[1]

The walking beam type reheating furnace is used to heat tubes that have different inlet temperatures (approx. 400 °C-600 °C) to a temperature of about 950 °C. The tubes are heated prior to further processing into seamless tubes in a downstream stretch reducing mill. The inner dimensions of the furnace (combustion chamber) are L×W×H: 13 m×24 m×1.66 m. Due to the furnace width, manageable tube dimensions are fixed with a length of 22 m. However, the tubes can have varying outer diameters and wall thicknesses, whereby extreme dimensions force a partial occupancy of the furnace, reducing the specific load of the skid system. This implies that the total number of positions for the tubes on the skids is reduced.
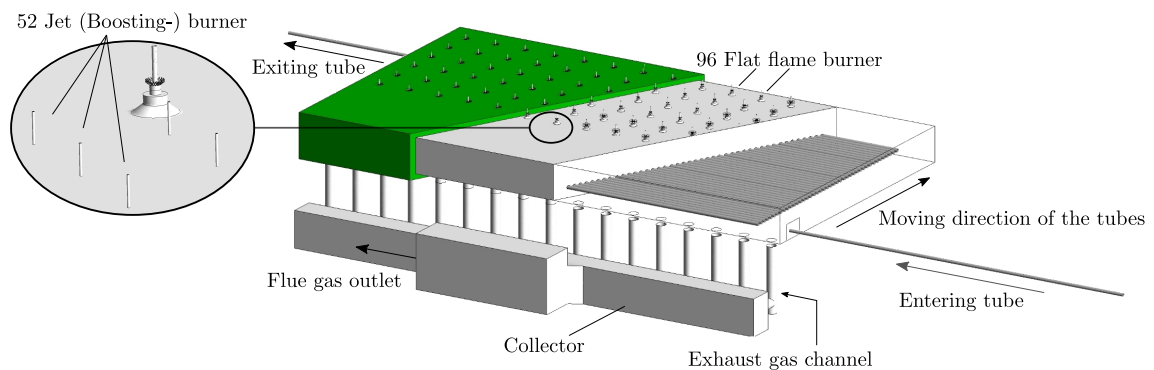
Figure 5.1.: The considered Furnace.

Figure 5.1 shows the furnace, with cuts through the insulation, coloured in green, and the combustion chamber, uncovering the tubes. The combustion chamber has a rectangular cross-section without any constrictions. In the front region (at the tube entry side), 17 exhaust gas channels lead the flue gas into a collector and further to the downstream heat exchanger and chimney. Thus, the main flow direction is from the rear end to the front of the furnace. Additionally, an entering and exiting tube are indicated to improve the understanding of this

---

[1]Segments of this chapter have already been published in [1, 5]

furnace. Those tubes are not present in the numerical model of the furnace. This illustration also indicates the moving direction of the steel tubes. The steel is heated in a counter-current manner, similar to most reheating furnaces. This is shown in the subsequent illustration (Figure 5.2). The fuel input is provided by 96 flat flame burners, which are mounted in a uniform distribution at the ceiling in the rear end of the furnace. Between each of those burners there is a distance of about 1.5 m. The distribution of the flat flame burners can be seen in Figure 5.1. Those burners are fired with natural gas and preheated air. For special operations, an additional 52 jet burners are installed in the front region of the furnace. They are fired with natural gas and pure oxygen. Some are visualized in the lhs of Figure 5.1. Those burners are used to permit heating of special tube dimensions with an increased wall thickness. They also allow you to heat tubes with a reduced inlet temperature. This means that for most tube dimensions produced in steady operation the jet burners are not activated. A detailed description of the burner types is presented in a later paragraph.

Similar to other furnaces, the walking beam type reheating furnace can be divided into individual heating zones. This is schematically illustrated in Figure 5.2, showing the flat flame burner, the jet burner and the moving direction of the tubes within the combustion chamber. This furnace includes 5 walking beams in tube moving direction with a total of 43 loading bays as sketched in Figure 5.2. Across its width there are 16 rows of beams. There is a distance of 1.4 m between each of those rows. In the following, the individual tubes are identified by their number, which corresponds to their position inside the furnace. Tube number 1 is the first tube when entering the furnace, while tube number 43 is the last tube inside the furnace as indicated in Figure 5.2. Additionally, the main gas flow direction and the way to the outlet is schematically visualized in this figure. This illustrates the counter-current heating of the tubes. The individual heating zones are numbered from 1 to 4, whereby 1-1 indicates the additional heating zone that is activated in case the jet burners are switched on. Otherwise, this zone contributes to the previous convective zone (zone 1). The names of the individual zones are:

1.   Convective Zone.
1-1. Boosting Zone/ Convective Zone.
2.   Preheating Zone.
3.   Heating Zone.
4.   Soaking Zone.
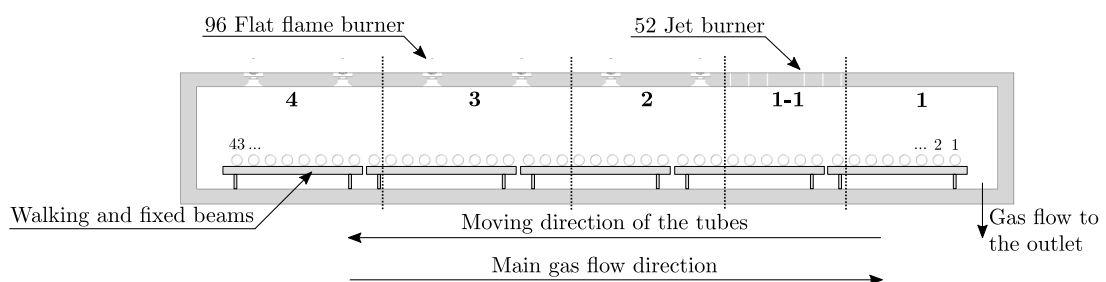
Figure 5.2.: The zones of the furnace and some additional details.

Within this furnace, the zones are divided by the burner arrangement. So each of the lateral zones (zone 2, zone 3, zone 4) consists of two flat flame burner rows with 16 burners each. This results in a total number of 32 burners for each individual zone. Each heating zone is further subdivided into four sub-zones across the furnace width, with 8 flat flame burners each. A thermocouple is mounted in the centre of each sub-zone for online temperature monitoring, mounted about 200 mm above the tubes' upper surface. The thermal input of each sub-zone can be controlled separately. The Boosting zone is also divided into four sub-zones with 13 jet-burners each. Unlike the flat flame burners, which are controlled as a group, with one controller for each sub-zone, each jet-burner can be controlled individually. This is necessary to avoid active burner to burn beside the tubes. This can cause the flames to hit the walking and fixed beams of the skid system as well as the furnace floor beneath, decreasing their lifetime due to the high local thermal load. This is the case when, for example, shorter tubes are processed which do not fill the whole furnace width. In this case, the lateral burners are shut down. In the next paragraphs, the two burner types and the transport mechanism of the tubes are explained in more detail. A single flat flame burner is shown in Figure 5.3(a), indicating the natural gas inlet and air inlets as black faces. While the fuel inlet is a centred straight pipe, the combustion air is introduced via a swirl-vane assembly. This swirl makes the flame to adhere to the ceiling, as indicated by the streamlines in the same illustration. These are coloured according to the gas temperature only in order to improve clarity. Here, blue indicates cold gas, while red areas indicate hot gas. Figure 5.3(b) shows a jet burner. Again, the inlets are indicated

(a) Flat flame burner (Zone 2 to 4)   **(b)** Jet burner (Zone 1-1)
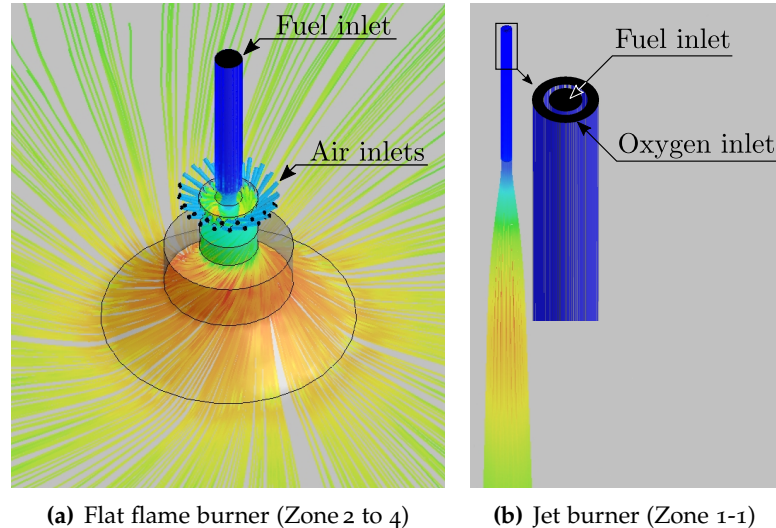
Figure 5.3.: Installed burner in the walking beam reheating furnace.

by black faces and the streamlines which elucidate the dominant flow generated. This type of burner creates flames with a high momentum. During normal operation, the flames hit the tubes surfaces with a high temperature, increasing the local heat flux radically. Attention must be paid to keep this effect within certain limits, otherwise the steel temperature distribution at the outlet would not meet the quality requirements. In this furnace, this effect is reduced by the moving mechanism of the tubes. The moving mechanism is of significant importance for this furnace and is described in detail in the following paragraph.

After the tubes enter the furnace via a roller system, they are immediately moved to the first position inside the furnace. During heating, the tubes rest on fixed beams in individual loading bays. Walking beams are used to move the tubes to the next loading bay. Due to the shape of the beams, an additional rotary motion is imposed on the tubes. This means that the tubes are moved translationally, and in addition, rotatory through the combustion chamber. Figure 5.4 is intended to illustrate the movement of the tubes, showing a single transfer of a tube, highlighting the rotation by small arrows to mark the same position on the tube. The movement can be divided into three steps marked by 1 to 3. In the first step the tubes rests on the fixed beams and the moving beams, which are lower, move upwards. The tubes roll into the loading bay of the moving beams and are transported to the next loading bay. This procedure is schematically visualized by step 2, indicating the tube as placed on the moving beam. The moving beams lower and the tubes roll again into the loading bay of the fixed beams, characterized by 3. The moving beam then moves back to its initial lower position. Due to this motion scheme, the tubes perform several rotations, as passing through the furnace. The
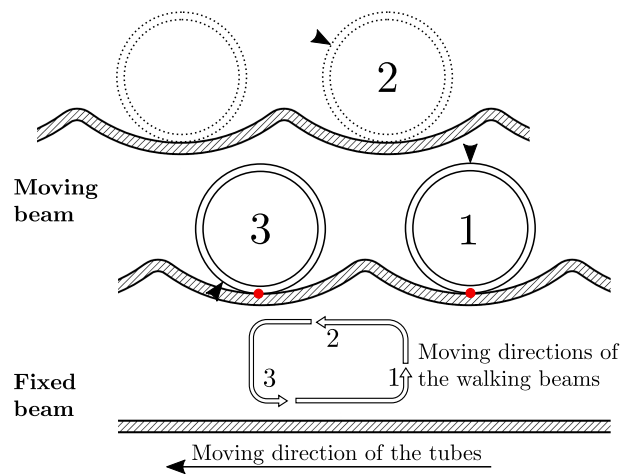
Figure 5.4.: The movement of the tubes and beam system adapted from [1].

arrows in Figure 5.4 also reveals another important effect caused by the rotating movement: The tubes are heated more uniformly over the circumference by inducing a shift of the temperature profile. This means that the previously heated area is rotated to another part during one transfer. This is schematically indicated in Figure 5.4. The black arrows always mark the same point on the tube's surface, the position of which changes during the moving process. In the first position, marked by 1, the point that is indicated by the arrow is in the upper position. After a single transfer, however, the point reached its final position (3) in the lower part of the tube. This effect is not mentioned in literature as only the heating process of solid slabs or billets is discussed. They are commonly transported by a merely translational motion. This rotational movement of the tubes also decrease potential influences of the skid system on potential uneven heating. On the one hand, this caused by the changing contact areas between tube and skid system. The influence is further reduced because the single beams are not cooled as it is the case in most furnaces of this type. This means that after some time of continuous processing, the skids adopt the temperature of surrounding gas. Another big difference of round objects to slabs, is the small contact area between the steel and skids, reducing mutual

influences due to conduction. As it can be seen in Figure 5.4 the contact area between the tubes and the beams, marked by red dots, is very small, which is enhanced by the small width of the beams of about 6 cm. Therefore, mutual conductive influences are restricted to small areas. Another big differences of heating tubes compared to full geometries, such as billets and slabs, is the much larger surface to volume ratio.

It can be concluded that the rolling motion of the tubes has a very important effect on tube heating and must be taken into account in the CFD simulations. As the model should be able to consider any tube dimension, a correlation with the angle of rotation has to be found. It can be expected that the angle of rotation is only a function of the outer diameter of the tubes, when sliding motions between tubes and beams are neglected. This assumption is reasonable since sliding motions occur only with cold tubes. This relation is shown in Fig. 5.5, indicating six typical tube dimensions and their corresponding angles of rotation within an entire transfer. This is illustrated by means of black dots. A second-order polynomial fit (dotted line in Fig. 5.5) indicates their relation. To underline the dependency of the outer diameter on the angle of rotation, a sketch of the first part of the moving scheme, in which the moving beams are moving upward, is additionally provided in Figure 5.5 for three typical tube dimensions. Considering the tubes' rolling path, which is almost identical for all tube dimensions shown, it becomes obvious that the angle of rotation differs. Thus, it can be stated that, with decreasing dimensions, the tubes perform bigger rotations.
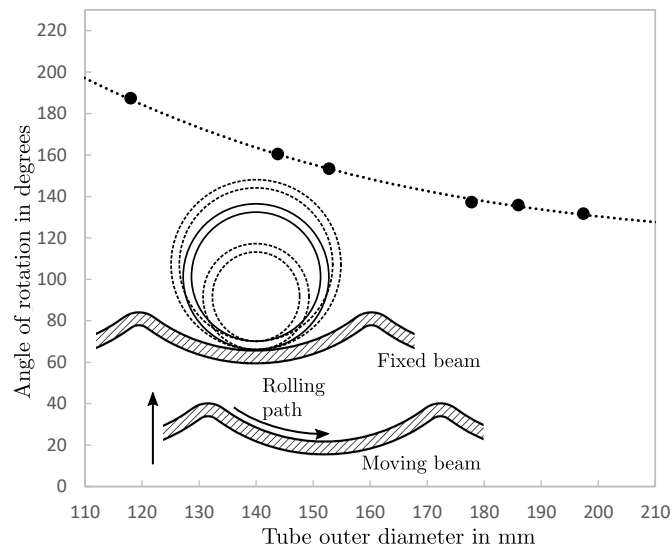
Figure 5.5.: Dependency of the outer diameter and the angle of rotation.

In order to incorporate this rotative motion into the global numerical model, that is to be based on a stationary and transient simulation, two approaches are conceivable. Both are based on the adaptation of the transient model. The first one assumes the numerical domain to be rotated. This includes the whole domain, the mesh, all boundaries etc., to be rotated during the numerical simulation each time the tube executes a transfer. The calculated heat flux profiles

from the steady state simulation, remain unmodified and can be used directly. The other approach, as used within this thesis, is based on the modification of the calculated heat flux profiles. The big advantage of this approach is that the domain of the transient simulation does not have to be changed. Instead, the location of the heat flux profiles is modified. The heat flux profiles, calculated by the steady state simulation, are each rotated before the actual transient simulation begins. This is done to incorporate the rotative motion of the tubes in the furnace. This requires an additional post-treatment of the calculated temperature profiles so they can be usable in the following steady-state simulation. Given the importance of this procedure, the following paragraph is aimed to deepen the understanding of the implementation procedure into the numerical model.

The method is visualized in Figure 5.6 for a single iteration step, showing the heat flux and temperature profiles for the first four tubes after entering the furnace. A whole iteration step can be divided into four steps marked with 1 to 4, which are described in this paragraph. To highlight the rotary movement in Figure 5.6, the starting positions, indicating the maximum in local heat flux, are marked by small arrows under the single tubes. The tubes moving direction is also indicated, to increase clarity. Next, the four steps are explained in more detail: 1) shows
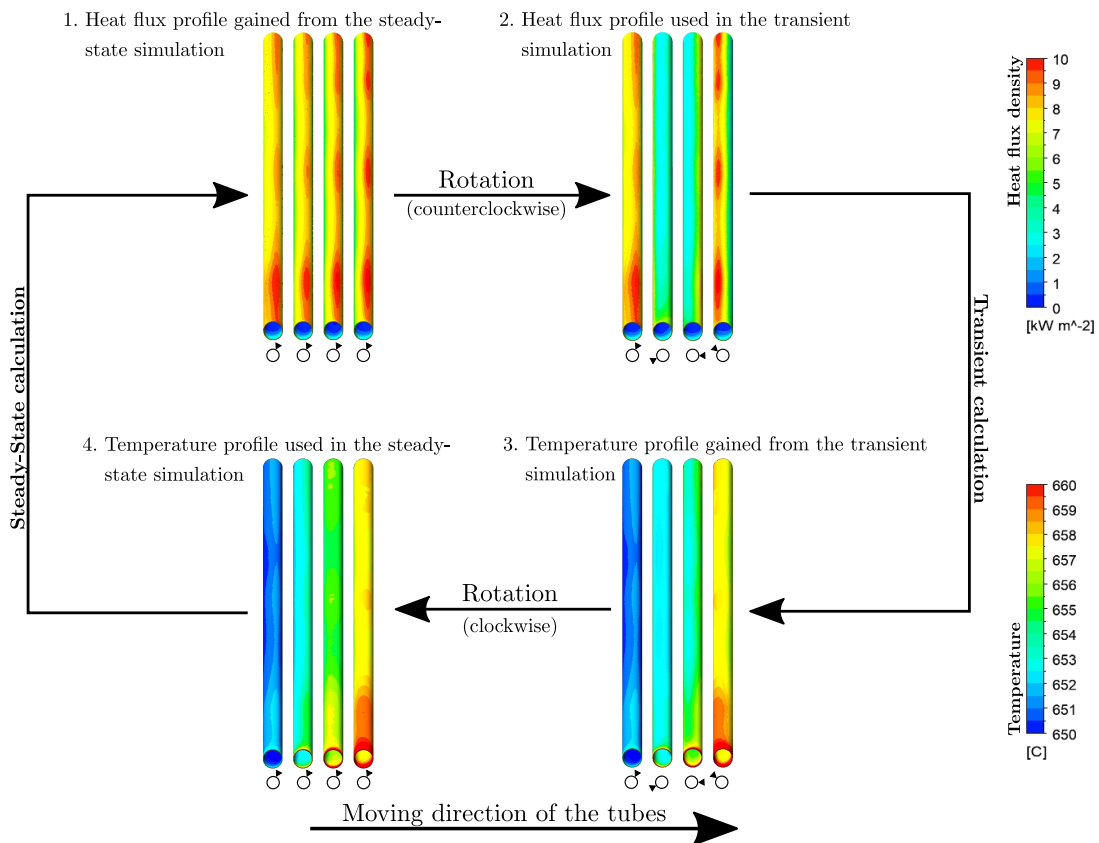
Figure 5.6.: Manipulation of the heat flux and temperature profiles adapted from [1].

the heat flux profiles calculated by the steady state simulation, whereby the position is marked at the same position for all tubes. The heat flux profiles , containing information on the position (x, y, z) and the actual heat flux value, are extracted for all cell surfaces. The values are rotated counter clockwise against the real rotation of the tubes. This is visualized in 2) and can be

visually explained by the rotation of the whole furnace around the individual tube's axes. This merely requires an adaptation of two coordinates since no changes in tube length occurs. This is done with Mathwork's® MATLAB, keeping computational effort low, although each profile contains about 40.000 entries. However, the value of the first tube is applied directly without embossing a rotation. This can be vindicated by the immediate transport of the entering tube to the first loading bay. The following are each rotated further by the angle of rotation(see Figure 5.5), leading to more than one full turn for the last tube shown (4th tube). These modified heat fluxes serve as a boundary condition for the subsequent transient simulation, providing the detailed temperature distribution inside the tubes. Step 3) shows the extracted surface temperatures of the tubes obtained by the transient simulation. The temperature profiles of the individual tubes are still in the rotated position, and have to be rotated clockwise, reversing the effect of furnace rotation. It converts it to a tube rotation and allows the temperature profiles to be used as new boundary conditions in the subsequent steady state simulation, as shown in the last step 4)

The aim of this section was to present the investigated furnace and demonstrate its characteristics. It focused on the design of the furnace and the arrangement of the burners. Furthermore, the position of the tubes and their special type of movement, which influences their heating characteristic, was pointed out. An adaptation of the numerical model was presented to include the rotative tube movement in the numerical model. It is based on the iterative scheme, using a steady state and transient simulation.

5.1. The Used Mesh and Boundary Conditions[2]

Within the following sections, the mesh and boundary conditions used for both, the steady-state and transient simulations, are explained. The former simulation, regards all details from the burners and furnace geometry, including the combustion process and the heat flux distribution. The latter considers only the heating of solid steel based on the results of the combustion simulation. The right choice of boundary conditions is essential for both simulations. The critical factors are the type of boundary condition and their position within the numerical domain. Such factors can seriously affect the numerical results and therefore special attention has to be paid to them.

Steady-State Combustion Simulation

In a first attempt, the furnace was considered as symmetrical, which means a significant simplification of the model. In this attempt, only half of the geometrically full furnace was taken into account, allowing us to reduce the number of cells drastically. This made it easier to investigate simple effects and to customize the presented global scheme to the furnace

---

[2]Segments of this section have already been published in [1, 2]

type. The numerical model used, which calculates the combustion process in the steady state simulation, is the same as used for the investigation of the single flat flame burner (Section 4.1). The SFM (including the detailed skeletal25 reaction mechanism, using the k-ε turbulence model and DO radiation model) is used in the presented simulations. Some boundary conditions are changed to reflect the real-size furnace to scale in detail. These are discussed within this section.

As already shown in the previous section 4.1, Polyhedral cells are superior to Hexahedral and Tetrahedral cells regarding the complex geometry of the installed burners. Thus, meshes solely based on polyhedral cells are used for the steady-state case within this chapter. The generation of mesh is conducted based on the same strategy as used in section 4.1. Some adaptations have to be made in order to keep the number of cells at a certain level. However, special attention has been paid to avert any loss of quality with regard to flame shape or species distribution inside the furnace. In the symmetrical case, a mesh was used consisting of about 6.2 million polyhedral cells with a maximum skewness of the cells below 0.9 and an maximum aspect ratio of 29. These values do not occur in a single cell, instead they characterize the worst cells within the whole mesh. Care was taken to keep the growth rate of the cells near the burner at a lower level ($\sim$ 1.08) during the generation of the mesh. A section of the mesh that was used for this purpose is visualized in Figure 5.7. The fine mesh inside the burners and in the upper part of the combustion chamber, as also around the tubes becomes obvious. This is important in order to capture high gradients of the transport values calculated. Near the burners this is essential to capture the temperature and species distribution within the flame with high accuracy. In
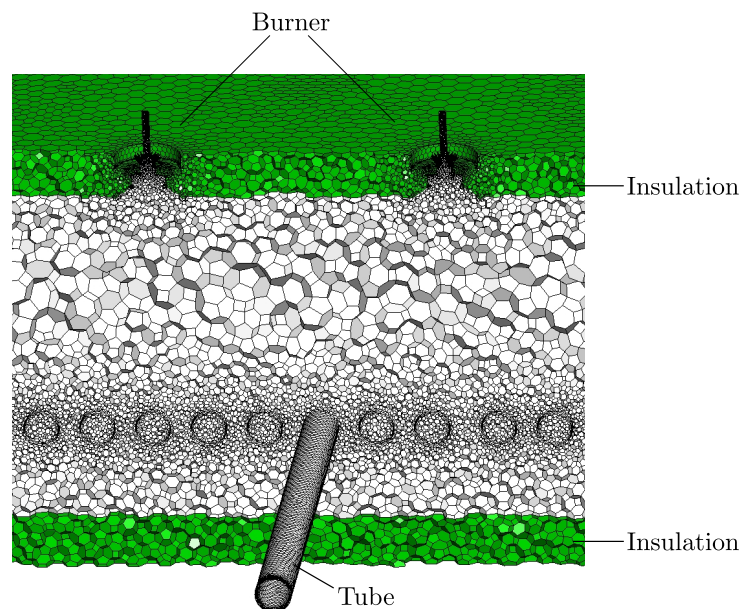
Figure 5.7.: A section of the mesh used in the steady state combustion simulation, indicating the insulation (green), the fluid (white), the burner and a single tubes' surface adapted from [1].

order to keep the computational effort within a certain limit, the mesh, that was used for considerations of the whole furnace, was locally adapted. Attention was paid to maintain a high resolution in areas where needed. Therefore, the growth rate of the cells near the burners

was kept at 1.08, while it was increased to 1.2 at a distance from the burners. The mesh that was created taking into account all of these factors consisted of almost 9.5 million polyhedral cells. The mesh quality was still sufficient, the worst cells had a maximum skew of less than 0.9 and a maximum aspect ratio of 35.

In industrial furnaces, real stationary operation is characterized and influenced by temporal fluctuations. These arise from disturbances in the process itself, or from upstream/downstream parts. These evoke short stops in the process, influencing the temporal variety in gas and air volume flow rates. This is visualized in Figure 5.8, indicating the total gas and air flow rates and the corresponding moving frequency of tube movement within 5 hours of stationary operation. The frequency of tube movement describes the time the tubes rest in one position. For the present operating mode, this is set to 22.5 s by the operator. Due to several disturbances, several fluctuations that range between 50 s and 22.5 s can be seen. These fluctuations clearly affect the thermal heat input needed, represented by the gas and air volume flow rates. With increasing moving frequency, indicating longer heating time, the flow rates drop. To implement
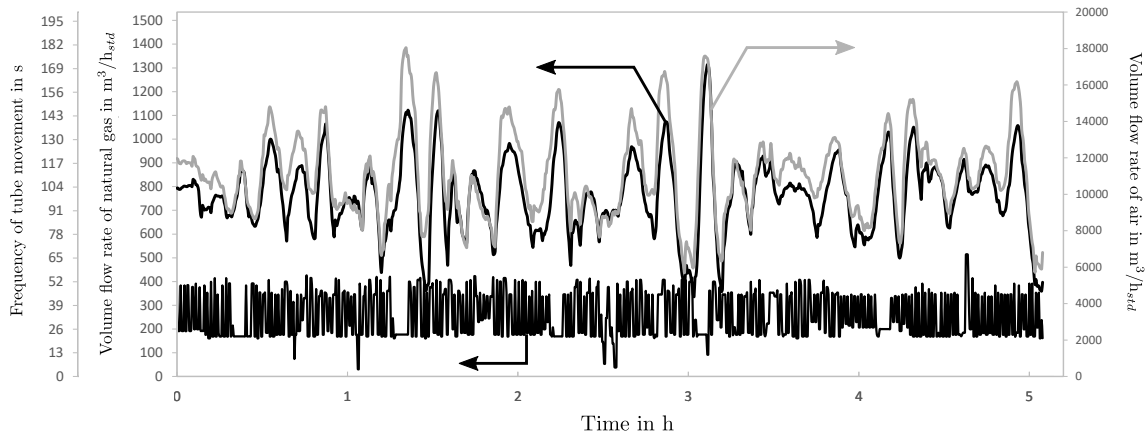
Figure 5.8.: Total volume flow rates for natural gas and air, and frequency of tube movement, during data recording.

this behaviour in a numerical model, transient considerations are needed. Using steady-state simulations, temporal averaged values have to be used. Eight hours of real data have been used for the presented boundary conditions, whereby extreme deviations, that led to a stop longer than 1.5 minutes were excluded. The mean values, as used in the numerical simulations, are shown in Table 5.1. The individual heating zones of the furnace were looked at separately, which is important to describe the heating with sufficient accuracy. As already indicated in Figure 5.2, zone 1 (in tube moving direction) is the convective zone. In this zone, the heat of the hot off-gases is used to preheat the tubes. This is mostly done by convection since there is no energy input in this zone, thus the name. In this consideration, only the flat flame burners are active. Thus, in zone 1-1, containing the inactive jet-burners, the mass flow rates for fuel and air are also zero, extending the convective zone. In the subsequent zones, thermal input increases towards the heating zone (see Table 5.1). At the tubes outlet, in the soaking zone, thermal input is decreased again. This is done to keep furnace temperature steady, enforcing a tube temperature homogenization.

Table 5.1.: The calculated mean values for gas and air flow rates in m^3/h_{std} [1].

	Fuel	Air
Zone 1 (Convective)	0	0
Zone 2 (Preheating)	150	2400
Zone 3 (Heating)	360	5010
Zone 4 (Soaking)	310	4430
Σ	820	11840

Similar to the test case shown in section 4.1, the fuel and oxidizer were simplified to pure methane and a mixture of O_2 and N_2, respectively. Also the emissivities of furnace walls and tubes remained unchanged with 0.7. Only the thermal conductivity of the insulation has to be lowered to $0.7\,W/mK$ in order to capture heat losses through walls and openings in a high degree of accordance with balances. Differences to the small test case from section 4.1 can be attributed to the bigger surface to volume ratio of the whole furnace, and the adiabatic treatment of the side walls. Before the actual CFD simulation, an energy balance for the whole furnace has been drawn. This is shown in Figure 5.9 for the present operation condition of the furnace. The individual heat fluxes are calculated based on their mass flow rates and thermal characteristics according to the formula presented in the previous chapter 2.1 (Eq. 2.1 to 2.3). The required data is on the one hand gained by measurements, but also from literature data. The measured data includes volume flow rates for fuel and preheated air, measured by measuring orifices. Also the temperatures of both streams, as well as the flue gas temperature, before and after the recuperator, have been measured using thermocouples. The density and specific heat for both media (natural gas and air) has been taken from literature data [193]. Special attention has to be paid to thermal characteristics of the flue gas. A total burn-out was
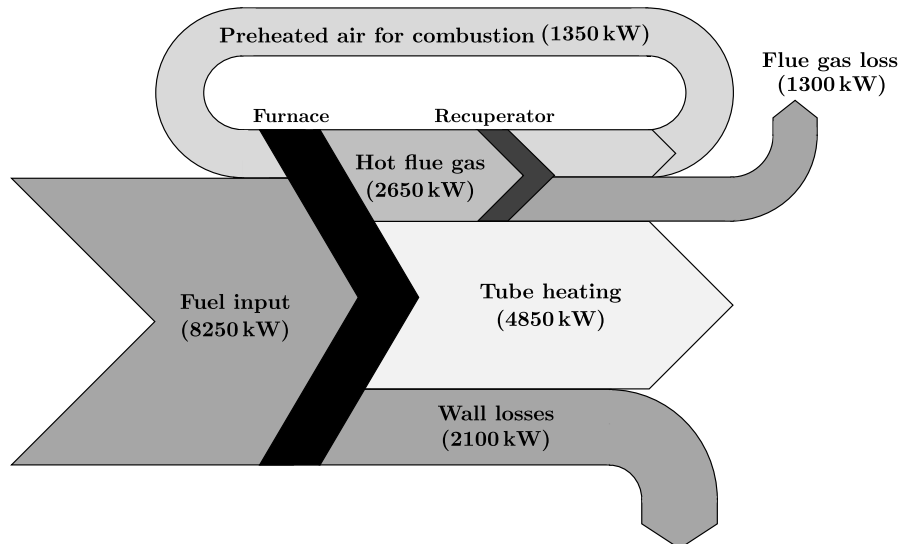
Figure 5.9.: Energy flow diagram of the whole furnace adapted from [1].

assumed, so the mixture, exiting the furnace, consists of CO_2, H_2O, N_2 and O_2. The specific heat was then calculated for the actual mixture resulting from the combustion, using the software

Engineering Equation Solver (EES). This software has a large database for a large number of species, allowing to derive an equation for the temperature dependent characteristics of the given mixture [194]. The calculation of the heat flux to the tubes is also of significant importance in order to derive a correct heat flux balance. Here again, data for the mass flow rate, specific heat and temperatures at the tube inlet and outlet are of significant importance. The mass flow rate of the steel tubes can be calculated using their dimensions (volume), the moving frequency of the steel, which is monitored, and the steel density which has been measured. Also thermal characteristics for the steel, including specific heat capacity (cp) and thermal conductivity (λ), were measured with differential scanning calorimetry [195] and laser flash analysis [196]. The steel which was investigated is an unalloyed tempered steel with a carbon content of 0.32 %.. Finally, the temperature of the tubes at the furnace inlet and outlet has been measured with a pyrometer. With it, the surface temperature is measured and averaged when the tubes are passing by. In the presented case the tubes enter the furnace with a mean temperature of 643 °C and are heated to a mean temperature of 920 °C. The last heat flux in Figure 5.9 to be characterized, the wall heat loss, is very difficult, or merely impossible, to calculate. It includes all irregularities of the furnace walls, such as cracks in the insulation and even leakage through openings. Thus, in the present energy balance, this heat flux is not calculated, instead it is used to close the balance.

Transient Heating Simulation

The heating of the tubes is considered in a transient simulation of a single tube. In the first symmetric consideration of the furnace, the tubes are also affected. Within this simplified simulation, the tubes are bisected. Thus, in the transient simulation only half the tube length has to be taken into account. The symmetric tube is resolved by a mesh with 60,000 hexahedra, with a maximum aspect ratio of 24, as visualized in Figure 5.10. The same meshing strategy is used for the whole tube, leading to a total number of 120,000 cells. Prior to the final decision to use this mesh, a grid independence study has been carried out. The mesh used was compared to a mesh with 8000 hexahedrons and to one with 150,000 hexahedrons, revealing that the small grid is not adequate for capturing all the details. The large grid, using 6 cells over the wall thickness, showed negligible small differences in temperature, demonstrating that use of this mesh is reasonable. To calculate the temperature distribution across the tube wall, three cells were arranged over the thickness of the wall, as shown in Figure 5.10. Also the condensed mesh at the tubes' end faces, to capture the stronger heating at the edges, can be seen.

Only the conduction of heat inside the steel has to be taken into account during the transient simulation. Thus, the flow equations can be neglected, and only the energy equation needs to be solved, which further reduces the computational costs. The low computational effort needed allows a minimum time step size of 0.5 s to be selected. Tube moving was characterized by a periodical adaptation of the heat flux boundary conditions. This was already described in detail at the beginning of this chapter, characterizing the furnace geometry and type of
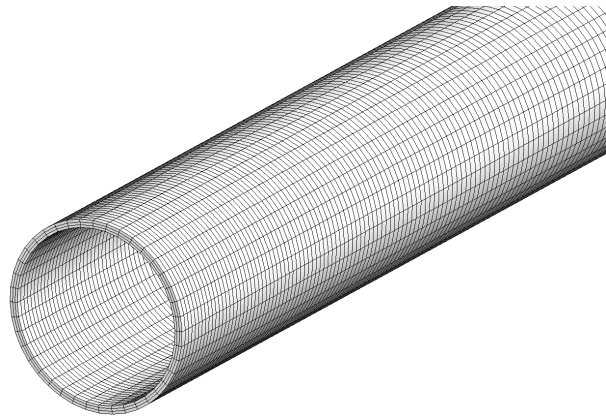
Figure 5.10.: The mesh used in the transient simulation adapted from [1].

tube movement. Within the present operation, the residence time of the tubes per loading bay is 25.5 s. In combination with the chosen time step size, the heat flux profiles have to be adapted every 51st time step, characterizing the movement from one loading bay to the next. Accordingly, the total residence time of a single tube is 1096.5 s to pass all 43 loading bays, from tube inlet to their outlet as shown in Figure 5.2. The tubes considered are made from high alloy steel with an inlet temperature of 643 °C. The density has been adopted as a constant value of $7489\, kg/m^3$. In the simulations these temperature-dependent values were taken into account by user-defined functions.

5.2. Results of the Steady-State Combustion Simulation[3]

Within this section, the results of the steady state simulation of the gas phase combustion are discussed. In particular, focus was on the temperature distribution and the velocity field of the gas phase inside the combustion chamber. This represents only one part of the iterative model. The second part deals with the transient heating of the tubes and is described in the subsequent section. All results shown correspond to the final iterative loop, satisfying the termination criterion, representing the real behaviour of the furnace. Considering the computational effort needed, the initial simulation can be seen as the limiting one. It needed about 1 week, using the presented models and hardware, to gain a finally stable converged solution. Any other iteration loop needed about 8 h to reach a converged solution.
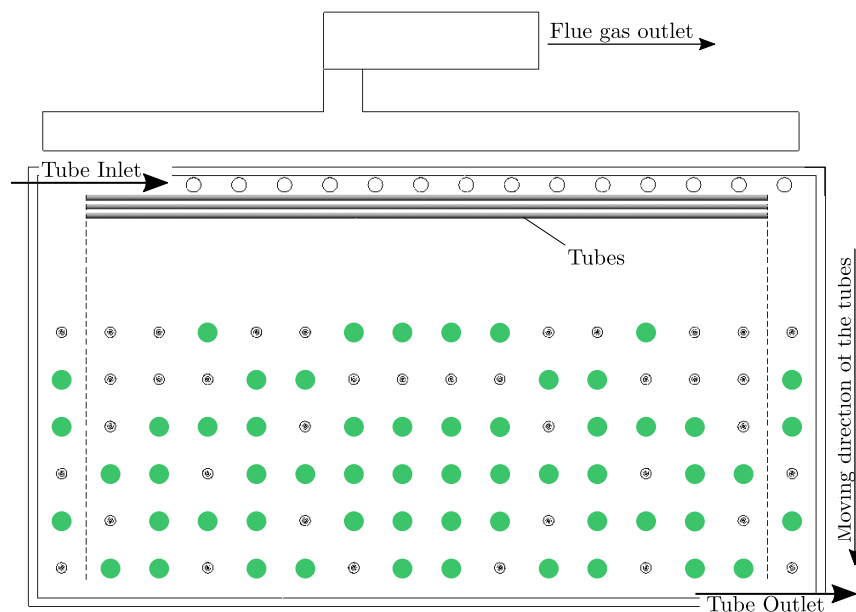
Figure 5.11.: Illustration of the active burners (green dots) as used in the steady-state combustion simulation adapted from [1].

During constant operation not all burners are active. The number of active burners depends on the heat input per heating zone. If the value is low, some burners are inactivated to avoid burner limitations. These are characterized by the minimum and maximum flow rate of natural gas of 4 and $20\,m^3/h_{std}$, respectively. The scheme of active burners is automatically generated by the control system. It is influenced by the tube length; more burners are active in sections with tubes. This means that in the case of shorter tubes that are positioned in the furnace centre, more burners are active in the central area, while in lateral areas only a few burners are active. In the present case, comparatively long tubes are used, leading to a roughly even distribution over the furnace width. A schematic illustration of active burners, as used within the simulation presented in this section, is presented in Figure 5.11, marking active burners with green dots. 58 of the 96 burners are active in the considered reference case. Nevertheless,

---

[3]Segments of this section have already been published in [1]

all burners were spatially resolved in the simulation. This was done to allow a fast investigation of different schemes and their impact on the tube heating process. The presented scheme leads to single burner loads of 13 to 15 m^3/h_{std}, depending on the heating zone.
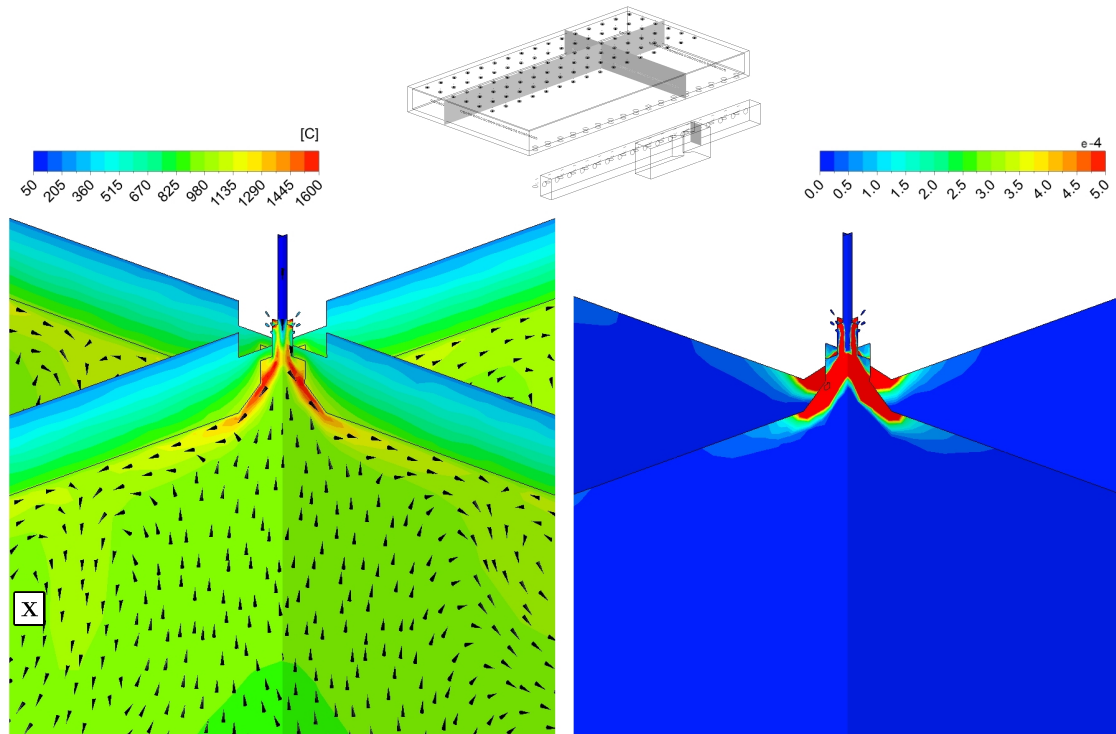
Figure 5.12.: Calculated temperature plot with velocity vectors (lhs) and OH radical mole fraction (rhs) of one burner in the heating zone using the symmetric consideration adapted from [1].

On the lhs of Figure 5.12 the temperature distribution in two orthogonal planes through an active burner in the heating zone is visualized. As already indicated in the previous section 4.1, the burner swirl-vane assembly leads to a flat flame adhering to the furnace ceiling. The resulting flow field mainly affects the flame shape. To underline this behaviour, vectors, indicating local flow directions, are inserted in this illustration. The combustion gases are accelerated radially, attracting gases from below. All burners indicate a very similar behaviour, leading to an encounter of combustion gases of two adjacent active burners. This can be clearly seen in the lower left corner of Figure 5.12, marked by an "X". Here, the clashing combustion gases are deflected downwards. The impact of this local flow on tube heating is explained later. The general superimposed flow direction of the combustion gases is from the rear end of the furnace, where the discharge of the tubes is located, forward to the flue gas outlet. On the rhs of Figure 5.12 the mole fractions of the OH radicals are shown. These radicals are produced solely as an intermediate product and exist within the flame at high temperatures due to dissociation effects. This species permit a statement to be made about the shape of the highly reactive zone. This reveals the advantage of the skeletal scheme used, considering some important radicals. In most global reaction schemes, the OH molecules are neglected, instead H_2 is to be considered. However, with this fast dissociating species it can be clarified that a fine grid in the vicinity of the burners is crucial to capture all the details of flame shape, temperature and species distribution. In the vicinity of the burner, no difference between the symmetric and geometric

full case can be observed. The global flow field, however, is influenced by the swirl direction of the burners, also affecting the temperature distribution within the combustion chamber. This is explained in detail in the following paragraphs.
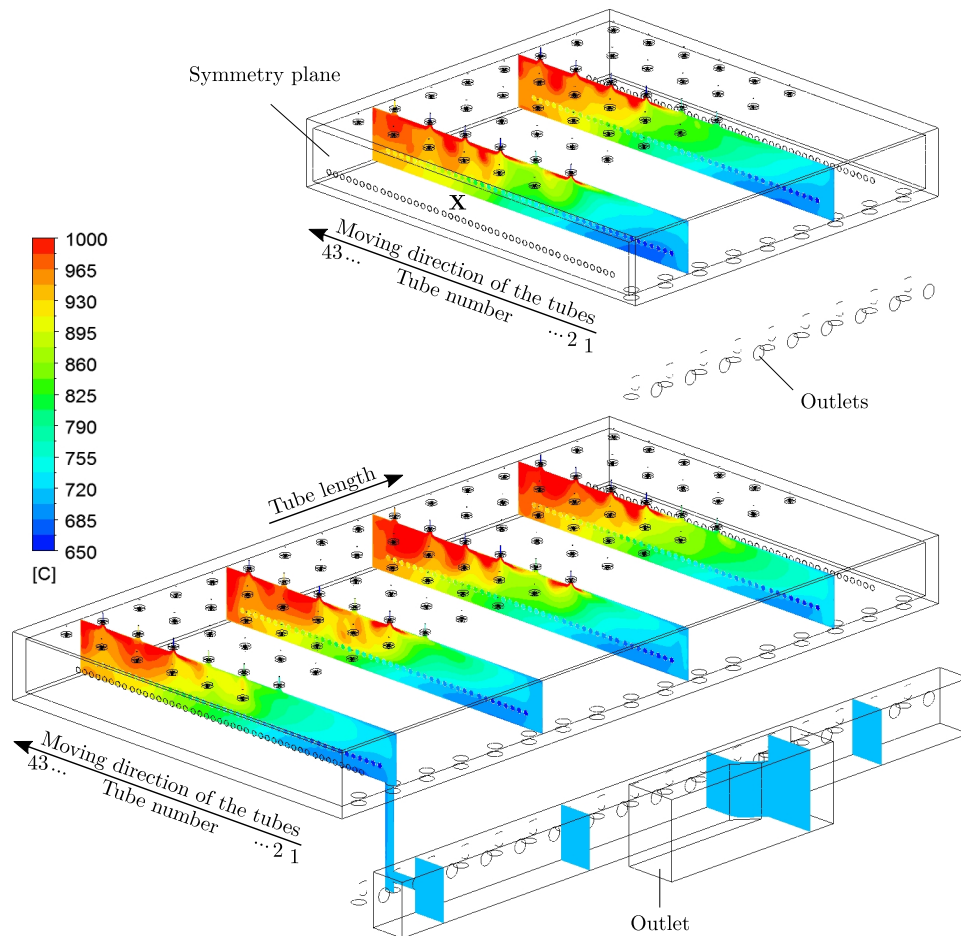
Figure 5.13.: Temperature distribution in the combustion chamber for the symmetric (upper) and geometric full case (lower).

Figure 5.13 visualizes the temperature distribution in some planes for the symmetric and full case. This illustration indicates the moving direction of the tubes and the corresponding tube number, tube length, symmetry plane and outlets for both cases. The latter differs for both since the downstream collector channel has been neglected in the symmetric case due to geometrical reasons. However, both cases show a similar trend of temperature inside the combustion chamber. In the front region, after tube entry, the coolest area can be seen. This is due to the cold tubes in this area of the furnace. The further into the furnace, the higher the gas temperatures. The maximum gas temperature can be detected in the rear area of the furnace. This can be attributed to the high energy input, while the tube temperature is already high. The geometrical full case also reveals the slight impact of the spin direction on the temperature distribution within the furnace width. Since all burners have the same spin direction, the hot gases accumulate in one half. This can be seen in the most upper plane, complying with the rhs in tube moving direction. This behaviour cannot be captured by the symmetric case since spin directions is mirrored by the symmetric boundary condition. The consequences are shown

in the following sections. In Figure 5.13 the impact of adjacent active burners becomes obvious. This forces the hot gases to be directed towards the tubes, as marked by an "X" in the symmetric case. The full case reveals an influence on the gas temperature distribution due to the swirl direction of the tubes. This leads to a slightly imbalanced temperature distribution over the furnace width. This is recognizable in the right rear area, in tube moving direction, indicating slightly higher gas temperatures. This behaviour cannot be recorded using the symmetric case. However, this case is very well suited to show global trends and influences. For example, both cases reveal lower gas temperatures below the tubes over the entire furnace length. This can be explained by the shielded combustion gases not penetrating the lower regions, as further clarified by the velocity distribution shown in Figure 5.14. Furthermore radiation is shielded by the closely spaced tubes in this area leading to lower temperatures. The same effect can be discovered inside the tubes, where the gas remains at a lower temperature level. At this point it should be noted that another case regarding the skid system has been investigated. The results revealed a minor influence on tube heating, due to several factors. The uncooled skids take on the surrounding gas temperatures after some time of steady operation. Excluding big influences due to conduction since the contact surface between the tubes and skids is very small. Also, the main source of heating is from the ceiling due to the burner arrangement. Thus, the skid system does not shield essential radiation. These effects show the valid argument to neglect the skid system.

The velocity distribution in the same planes is shown in Figure 5.14. High velocities, can be determined near the burners, caused by the radial acceleration due to the combustion process. Also high velocities appear in in the exhaust channels due to the cross-sectional constriction. The plane on the right side in tubes moving direction reveals also high velocities on the ceiling in the convective zone. This is caused by the active burners in the preheating and heating zone. These lead to a hot and relatively fast gas stream towards the gas outlet. This is only slightly affected by the symmetrical consideration. Besides turbulent fluctuations, the main flow is in the upper part of the furnace, leading the hot combustion gases from the rear end (soaking zone) to the front end of the furnace. At the vertical front wall, at the tube inlet side, the gases are redirected downwards to the flue gas channels. Some parts exit the furnace, while the rest of the gases are redirected below the tubes into the combustion chamber. This illustration emphasises once more the admissibility of the skid system neglection, since the backflows are mainly parallel to the beams of the skid system. Thus, extraordinary influences on flow can be excluded.

To validate the simulations, the measured temperatures of the fixed mounted thermocouples have been compared to the numerical results and are displayed in Table 5.2. On the one hand, the results show a very high accordance between the symmetric and full case. A maximum deviation of about 20 °C can be found in the heating zone underlining the suitability for both models. This is also underlined by the comparison of both calculated cases with the measured data. The biggest difference can be seen between the symmetric case and the measurement in the soaking zone with almost 24 °C. The full case shows a reduced maximum deviation of
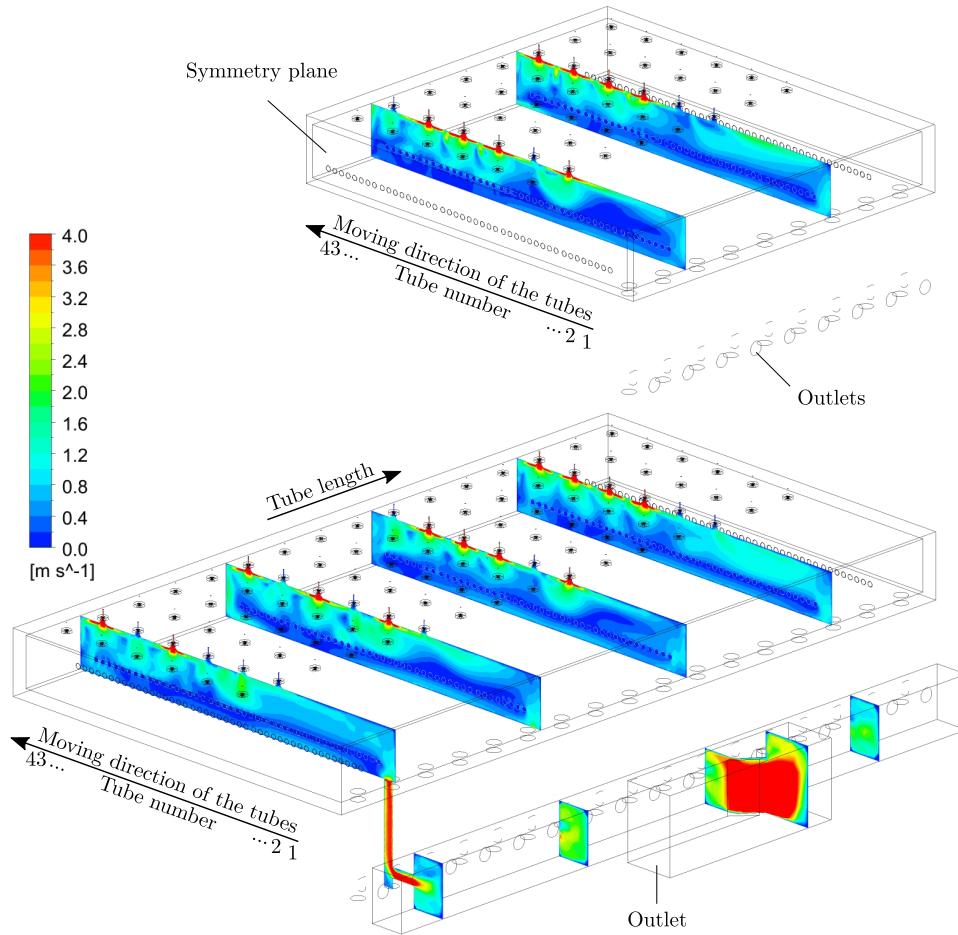
Figure 5.14.: Distribution of the Velocity magnitude in the combustion chamber for the symmetric (upper) and geometric full case (lower).

about 17 °C. Another important effect, as mentioned before, is the temperature imbalance over

Table 5.2.: Calculated and measured mean zone temperatures in °C [1, 2].

	Symmetric case	Full case	Measurement
Convective Zone	726.6	733.8	736.4
Preheating Zone	802.6	812.4	822.4
Heating Zone	887.2	907.4	890.2
Soaking Zone	963.0	950.5	939.0

the furnace width. The measured results reveal a maximum in temperature difference below 34 °C in the convective zone. This decreases towards the tube outlet, reaching its minimum in the soaking zone of almost 9 °C. The full case reveals a similar behaviour with the absolute maximum in the convective zone with a value below 37.5 °C and minimum in the soaking zone with about 22.5 °C. The symmetric case, however, shows also a decreasing trend from the convective zone ($\sim$ 28 °C) to the heating zone. The maximum, however, can be found in the soaking zone with a value of about 55 °C. This is comparatively high, which can be ascribed to the local downward flow of hot gases caused by the clash of the flames, as described before. The high accordance between both models and measured data proves that the selected models are well suited to describe industrial size furnaces in detail. In particular, this is related to the

models for turbulence, combustion, radiation as well as the reaction mechanism which affects combustion drastically.

The next paragraph serves to deepen the understanding of the tube heating process, while the actual transient tube heating calculation is presented in the next chapter. The specific heat flux densities to the tubes are visualized in Figure 5.15 for both cases. In the convective zone, corresponding to the front area of the furnace after tubes inlet, both cases reveal the lowest heat fluxes transferred to the tubes. The maximum transferred heat flux is located in the heating zone, which is located near the centre of the furnace. In the rear end of the furnace the transferred heat flux decreases, due to the already high tube temperature. Here, the gas radiation becomes more influential. This effect was previously described by Mayr et al. [64] in their investigation of a lab-scale and an industrial scale reheating furnace. As shown by the temperature distribution within the furnace, the heat flux distribution is affected by the spin direction of the burner. In the upper area of the total furnace, heat fluxes to the tubes are increased. The impact on a possible temperature imbalance is shown and discussed in the following section. Another impact of the burners on the flow inside the combustion chamber, causing a deflection of the off-gases by the mutual influence of active burners, is shown. The downward deflected heat fluxes hit on the tubes' surfaces increasing local heat fluxes as marked by "X" in Figure 5.15.
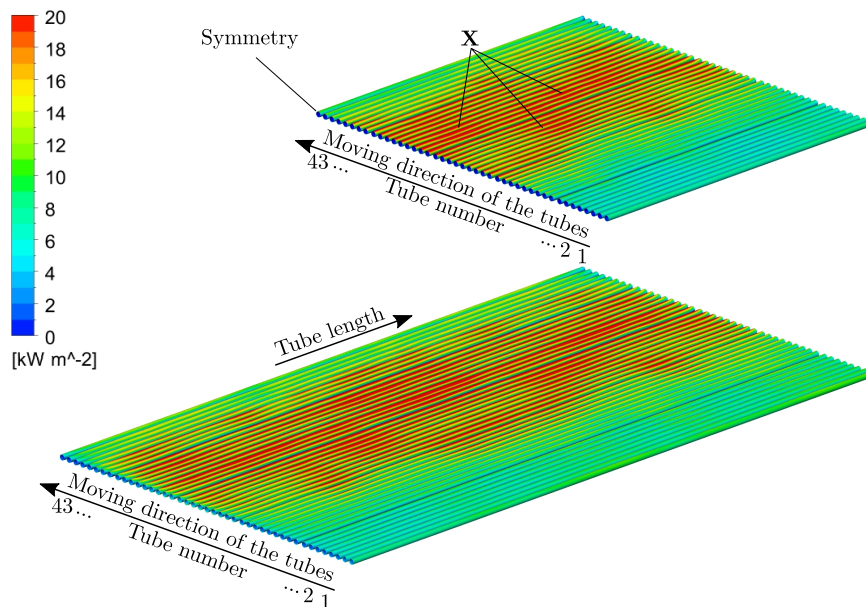
Figure 5.15.: Heat flux distribution for the symmetric (upper) and geometric full case (lower).

The simulation reveals that about 99.35% of total heat flux is received by the outer surface of the tubes. The inner surface and end faces receive 0.59% and 0.06%, respectively. The small share received on the inner surface can be explained by the mostly shielded radiation, and the very low gas velocity within the tubes. This means that the main heating is due to the burners mounted at the ceiling. The results indicate a 20 times higher heat flux transferred to the upper part of the tube than underneath. In general, the heat flux profile exhibits a more

or less symmetrical behaviour along the tube length, indicating a slight shift to the tube inlet side regarding the full case. Nevertheless, the difference between both cases seems negligible. To demonstrate this, the total heat flux transferred to each tube is visualized in Figure 5.16. The black dots mark the total heat flux transferred to each tube in the geometrical full case, while the grey dots indicate the symmetrical case. This illustration clarifies the small deviation between both cases. Identical to the graphical presentation from the previous Figure 5.15, a clear variation in transferred heat flux distribution in tube moving direction can be detected. In the front part, indicated by tube numbers 1 to 28 (convective and preheating zone), the differences are negligible. The first tubes within the heating zone also reveal the most similar values. After the peak in transferred heat flux, located in the heating zone, an approximately constant offset between the results for the symmetric and full case can be detected. This deviation extends into the soaking zone, while decreasing for the last three tubes (tube numbers 41 to 43). Nevertheless, the difference in heat flux transferred is 175.58 kW, corresponding to 3.5 %, stating the suitability of both models.
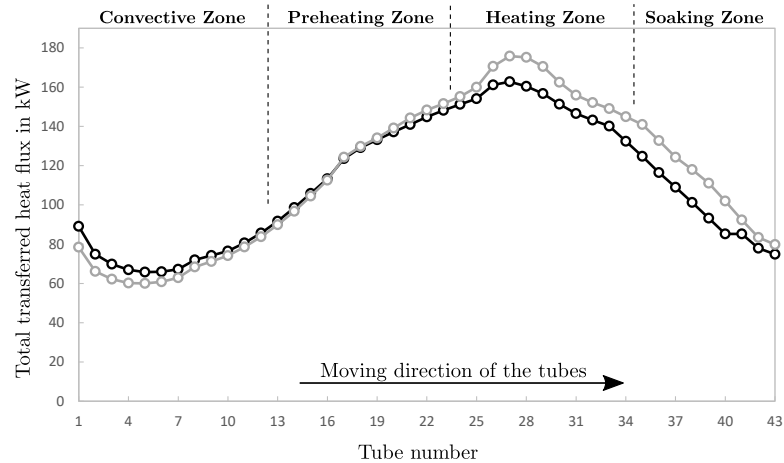
Figure 5.16.: Total heat flux transferred per tube for the symmetric (grey circles) and geometrical full case (black circles) adapted from [1, 2].

5.3. Results of the Transient Heating Simulation[4]

This section provides the results of the transient heating simulation. On the one hand, the impact of the symmetric consideration is to be evaluated, furthermore, the numerical results are compared to the measurement data. In Figure 5.17, the surface temperature profiles of the symmetric and total furnace are visualized. This corresponds to the last tube in the furnace before exiting, which matches the tube on the 43rd position (see Figure 5.2). The symmetric case is mirrored to improve clarity. Both cases show roughly the same temperature distribution on tube surfaces. It can be seen that the rotative motion of the tubes, caused by the shape of the skid system (see Figures 5.4 and 5.5), results in a very homogeneous distribution of heat. A maximum of Δ=5 °C over the circumference can be detected in the case of the geometrical full

---

[4]Segments of this section have already been published in [1, 2]
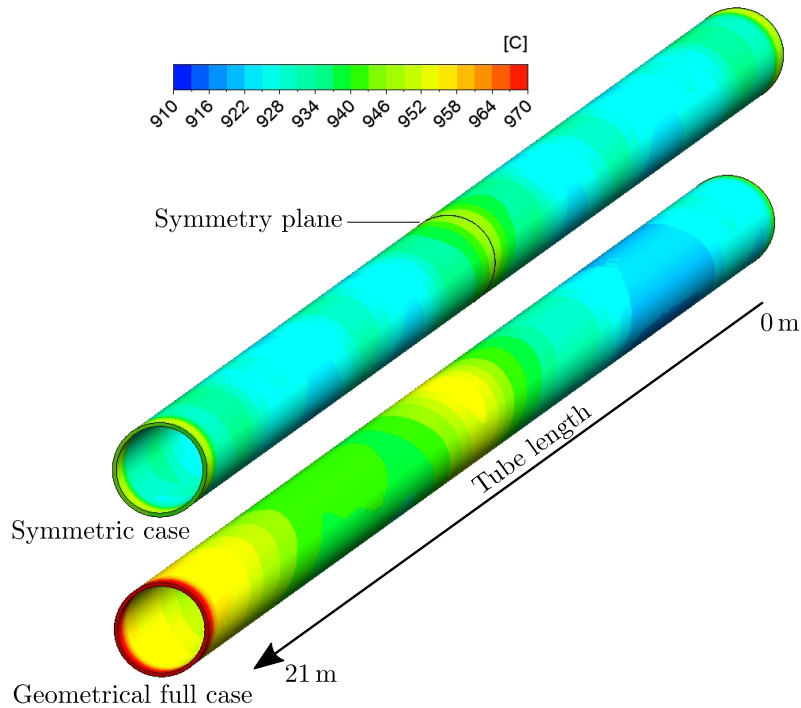
Figure 5.17.: The calculated temperature distribution of the exiting tube (position 43) using the symmetrical and geometrical full case adapted from [1, 2].

case. Besides this, peaks in temperature on either tube end and in the central region, causing a "w-shaped" profile, can be detected. In addition, the full case also indicates a slight imbalance over tube length. To investigate this, several tubes have been measured using an infrared camera. The data of the fix mounted pyrometer at the furnace outlet has also been used for a thorough validation of the CFD model. The cause for this is the similar spin direction for all burners affecting the temperature and heat flux distribution across the width of the furnace. This has been highlighted in the previous section, showing the results for the steady state simulation (see Figures 5.13 and 5.14).

The results from the thermographic camera measurements and the pyrometer measurements for the corresponding tube are compared in Figure 5.18. At this point it should be mentioned that several tubes were measured with the IC and the pyrometer, but no significant difference was found between the individual tubes. For the sake of clarity, the numerical CFD results are not shown in Figure 5.18 and are compared to the measurements afterwards. The IC results are displayed in Figure 5.18 as grey points, revealing a maximum local scattering of about $50\,°C$. These fluctuations can be explained by a possible scale formation on the tube surface, which has been described in chapter 3. A fourth degree polynomial was fitted in order to compare the data with the pyrometer and the simulation results as efficiently as possible. This curve captures the trend of the measurement quite well. It is possible to observe that the whole profile inclines to the left. A temperature difference of about $27\,°C$ between the two global minima at 3 and $17.5\,m$ of tube length occurs. The maximum temperature in the middle range is approximately $957\,°C$ and is slightly shifted to the right. Comparing the data with the pyrometer measurements, visualized by black circles, no large local fluctuations can
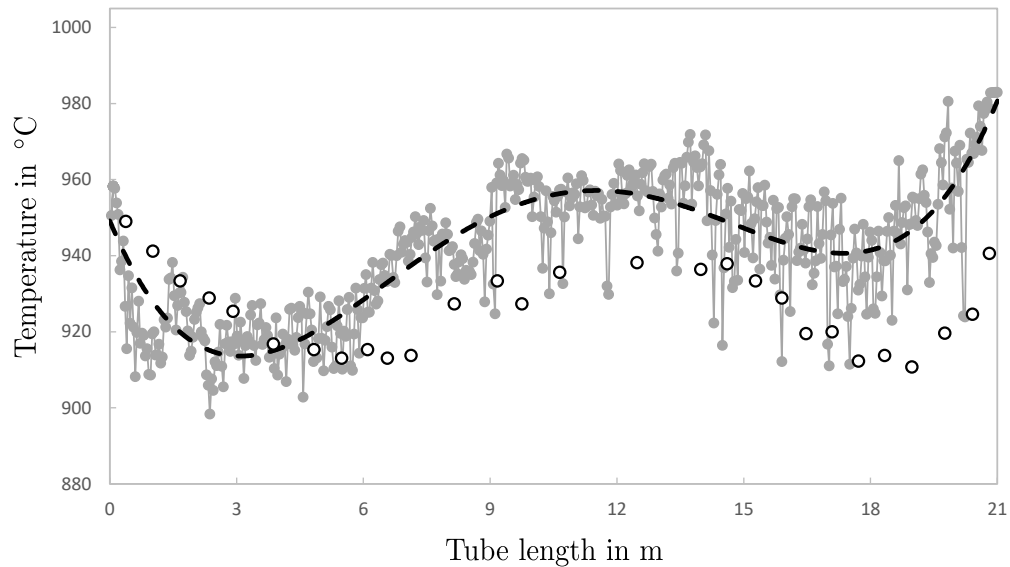
Figure 5.18.: Temperature distribution measured with the IC (grey solid line and dots) and pyrometer (black circles) and the corresponding polynomial fit for the IC measurement (black dashed line) adapted from [2].

be seen. This is due to the measuring principle of a two-colour pyrometer, which ensures independence from the emissivity. On the other hand, no inclination in the temperature profile can be determined. This is based on the temperatures at the global minima at 6.5 and 19 m. At these points, similar temperatures of about 910 °C occur, with a difference of only 3 °C from each other. The maximum temperature at the tube centre, at 12.5 m, is shifted a fraction more to the right side, and reaches a value of 938 °C. Both measurement methods generally show the same temperature distribution trend, and reveal a w-shaped profile. Only the misalignment cannot be detected by the pyrometer. This is probably due to the internal smoothing of the pyrometer. As the measurements demonstrate, the symmetric consideration of the furnace did not allow to capture all of the details. Thus, it can be concluded, that it is necessary to consider the whole furnace.

A comparison of the numerical data, calculated with the symmetric and full geometric case and the infrared camera, is provided in Figure 5.19. As shown above, the pyrometer results readings show some deviations and so are not presented within this illustration. The result of the numerical investigation of the whole furnace is indicated by a dark grey solid line, while the symmetrical investigation is indicated by a lighter grey solid line. In order to ensure good comparability, again the result is mirrored and presented by a light grey dashed line. It is clear that both numerical investigations generally revealed the same behaviour. This has already been stated at the beginning of this section regarding the temperature distributions of both numerical investigations. The misalignment cannot be detected only by the symmetrical investigation. The result of the IC measurement's fitted polynomial, from Figure 5.18, is shown as a black dashed line, which reveals a slightly steeper inclination compared to the simulation results. The difference can be estimated by evaluating the values of the global minima. In the case of the simulation, these are found at a tube length of 3 and 16.5 m, while the minima of the
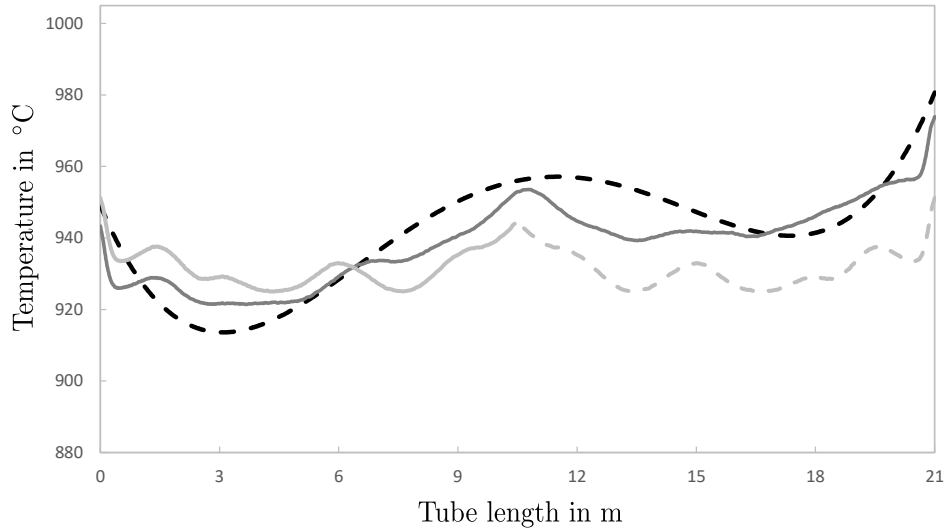
Figure 5.19.: Temperature distribution of the polynomial fitted infrared camera results (black dashed line), the geometrical full (grey solid line) and symmetrical case (light grey solid and dashed line) adapted from [2].

polynomial are located at 3 and 17.5 m. Approximately identical temperatures can be detected at the minima at 16.5 and 17.5 m, whereas the other minima, at 3 m, demonstrate a difference about 8 °C. Nevertheless, very similar values for the maximum at tube centre were obtained. Both the CFD solution and the polynomial from the IC measurement provided a value of about 955 °C at this point, revealing a difference of about 3 °C. The small differences in calculated and measured temperatures, using the IC, allow to conclude that the numerical results are very accurate. Deviations in temperature are in an acceptable range, below 20 °C. Furthermore, the calculated misalignment of the temperature profile along the tube axis can also be captured by the IC. The presence of this was expected since Mayr et al. [192], investigating a pusher type reheating furnace have already shown this effect. This is caused by the identical swirl direction of the flat-flame burner, leading to a temperature imbalance, as described in the previous section regarding the conditions within the combustion chamber. The pyrometer, however, fails to capture this trend, which seems to suppress important effects. Correct measurement of temperatures is of significant importance in the steel industry since strong fluctuations or imbalances can cause a problem in subsequent processing. These inhomogeneities can be affected by several factors, including changes to the heating characteristics of the steel. This is investigated in the next chapter.

In Figure 5.20 the measured temperatures of the single thermocouples in the test tube are represented by solid lines. Additionally, the data of the transient simulation are marked by dashed lines. The location of TC 1 is near the middle of the tube (9.5 m from tubes' end), located on the inner surface. The following TC 2 to TC 4 are 4 m closer to the end face. TC is also mounted on the inner surface on the same side as TC 1. TC 2 is also inside, but on the other side of the tube. TC 4 is the only thermocouple mounted on the outer surface of the tube. TC 5 and 6 are mounted on the inner surface close to the end face to capture the high temperature gradient
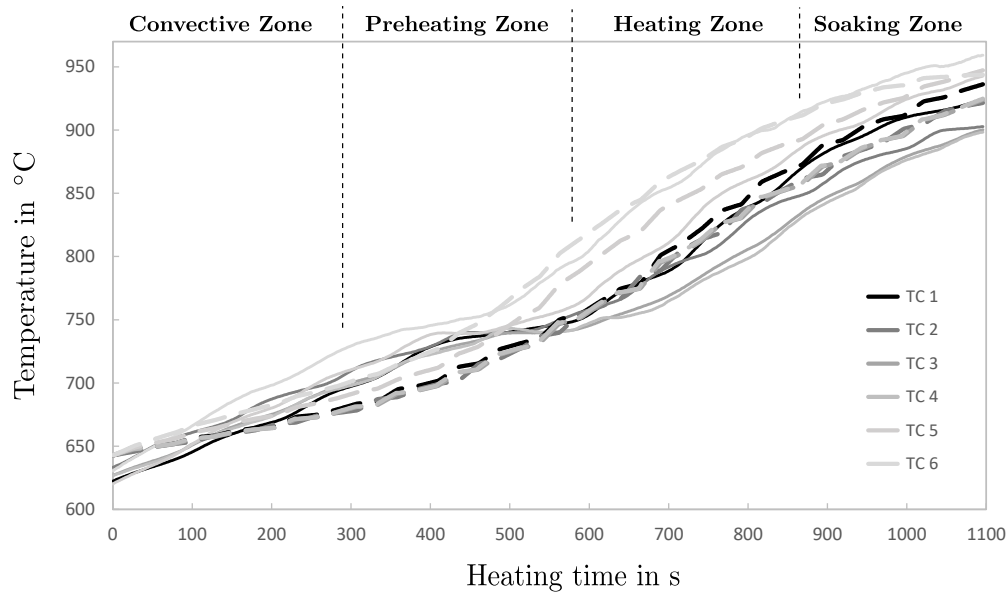
Figure 5.20.: Measured (solid lines) and calculated (dashed lines) temperatures of the individual positions in the test tube adapted from [1].

in this area. Their exact position was shown and discussed in a previous chapter(see Figure 3.1 and Table 3.1). The single thermocouples clearly show the temperature range where the α-γ conversion takes place. This is about 750 °C (after about 500-600 s of heating time), here the specific heat capacity reaches its maximum value with a subsequent strong decrease. This rapid change leads to a momentarily flattening of the temperature profiles, following in a subsequent increase. The simulation reveals a smaller influence of the $\alpha - \gamma$ conversion. The results show no flattening of the temperature profiles. A possible reason may be an inaccurate determination of the specific heat or by fitting the curve in FLUENT by polynomials. This impact is negligible, since the influence was evaluated. Different polynomials were used and the calculated results were compared, revealing insignificant influences. Another possible cause may be the inertia of the thermocouples. Due to the different heating at the measuring points the conversion takes place at different times, leading to an increase in temperature difference. This is illustrated in Figure 5.21, showing the temperature difference between the thermocouples 4 and 6 which show the greatest temperature difference of all thermocouples. In the measurement, the exiting tube shows a maximum temperature difference of 60 °C between TC 6 and TC 4, whereas the simulation reveals a smaller difference of 25 °C. The maximum of almost 100 °C for the measurement and 70 °C for the simulation can be detected in the heating zone. The greatest deviation between measurement and simulation can be detected in the heating zone, with a value of about 75 °C. At this point it should be noted, that the deviations are within an expected range. Improvements to the measurement strategy are not straightforward since there is extensive preparation and costs related to each measurement. The measurement was carried out, reducing errors as best as possible. However, influences due to the requisite preheating in the other furnace and the transport of the tube to the actual furnace before investigation cannot be prevented. Further, errors due to the thermocouples cannot be excluded.
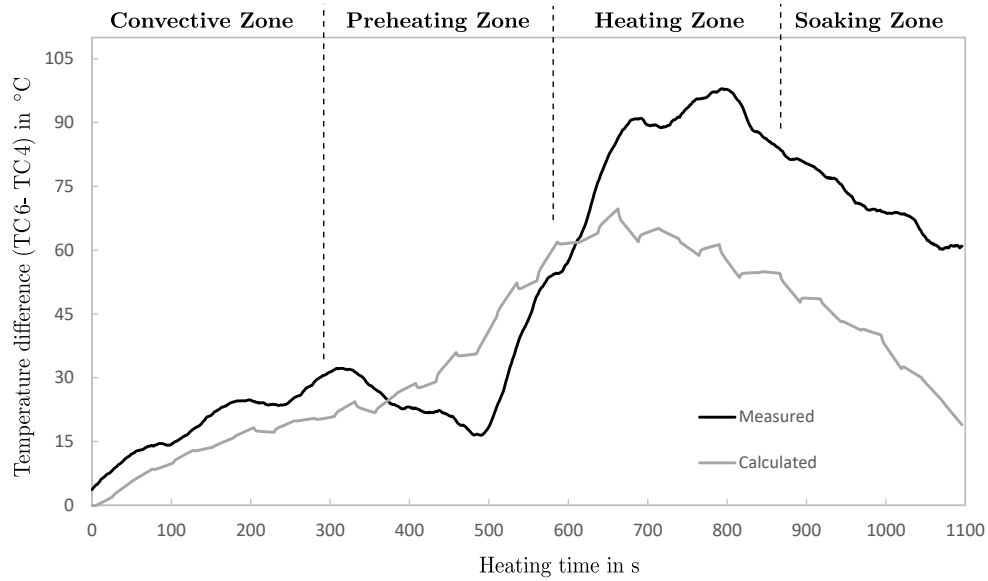
Figure 5.21.: Temperature differences between TC 6 and TC 4 for measured and calculated results adapted from [1].

A small impact of the rotational movement can be detected, leading to wiggles in the heating characteristics. These are much more pronounced in the numerical simulations that were performed. During the measurement sliding of the tube may have occurred resulting in a lower rotational angle than 139°. Thus the tube is heated more strongly on one side explaining the greater deviation of TC 2 to TC 3 and 4 compared to the numerical results. The data also demonstrates the stronger heating at the end and also at the symmetry area of the tube. These are represented by the thermocouples 5, 6 and 1 in Figure 5.20, wherein TC 6, which is located at the very edge, shows the highest temperatures. However, it can be said that radial heating of the tube is not a critical criterion compared to full solid geometries. The two thermocouples TC 3 and 4, each of which is located at the same position on the outside and inside of the tube, show a maximum difference of Δ=2.7 °C occurring in the heating zone. This clearly indicates the swifter heating in radial direction, compared to full solid geometries. Despite the fact that the rotation increases the numerical error the simulations show comparable results with measurements. For better visibility, the results of the test tube and the corresponding tubes are shown for six specific time steps in Figure 5.22. Each tube is labelled with their respective heating time and tube number (position) within the furnace. Here again, tube number 1 and 43 indicate the first and last tube inside the furnace, respectively. The results between 0 s and 204 s indicate the temperature profile in the first area of the furnace, the convective zone. As stated above, the temperature profile is mostly uniform in this zone: only the tube edges heat up quickly.

Subsequent results from the preheating zone (433 s), the heating zone (637 s, 841 s) and the end of the soaking zone (1096 s) affirm the behaviour described above, revealing a small misalignment in the preheating zone (433 s). This intensifies to the rear end of the furnace, where the w-shaped profile also becomes more and more pronounced. The overheating of the tube edges is well detected by the measurements. Similar to the simulations, the overheating
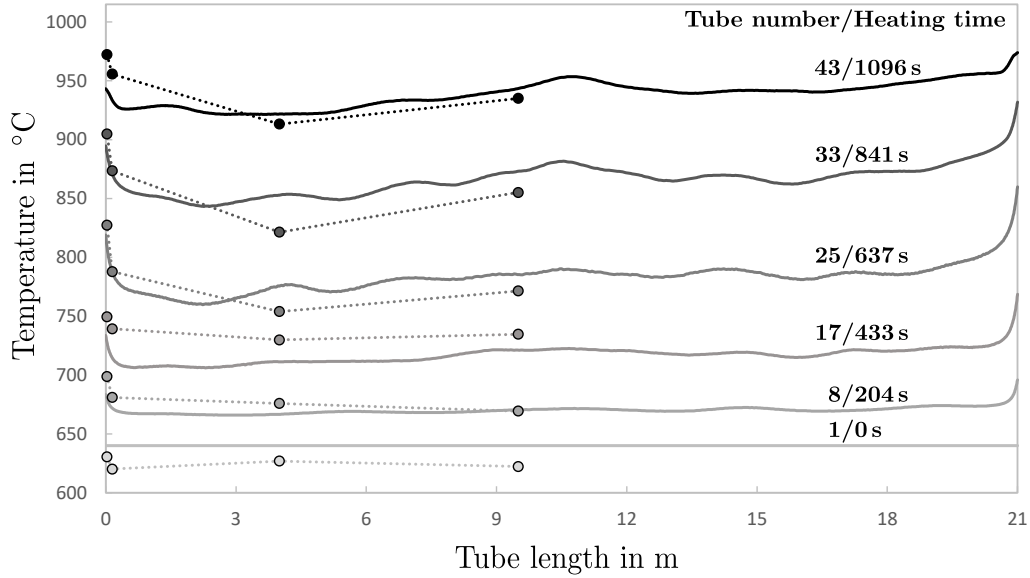
Figure 5.22.: Measured (dots with dashed lines) and calculated (solid lines) axial temperature distribution for six specific time steps adapted from [2].

increases until the heating zone (637 s), and then decreases significantly afterwards. The last tube shown, at 1096 s, corresponds to the exiting tube and reveals a marked homogenization of the temperature profile. Here, both the intensity of the w-shaped profile and the overheating of the edges have decreased. This illustration again reveals the high accordance between the measured and calculated results. Although some deviations can be seen, these are in within an acceptable range at this high temperatures.

Therefore, it can be concluded that the model's accuracy is high and sufficient to describe the heating process of steel tubes, including their complex moving scheme as they pass through the furnace. This has been proven by comparisons with various measurements, using different techniques. Thus, it can be stated that the heat fluxes are calculated correctly in the steady state simulation. This in turn also verifies the steady state simulation since the impact on the transient heating simulation would be drastic. Additionally, it can be said that the numerical approach, considering only this small domain in a transient manner, is highly efficient. A single transient simulation needed about 30 minutes, using an Intel i7 with 6 core CPU and 64 GB RAM, although this small time step size was used. The whole iterative process, including the steady-state combustion simulation and transient heating simulation, needed a total of 7 loops to reach the termination criterion. Therefore, the total computing time needed to reach the presented results was about 2 weeks. This is significantly shorter than a fully transient consideration of the whole domain including combustion in a transient manner. Such an enormously elaborate consideration of the whole furnace would prolong calculation time from weeks to months. The added value of such simulations for the calculated results is questionable. Thus, this model presents an excellent alternative, keeping computational effort within a practicable dimension.

5.4. Investigating Effect of Gas Redistribution on the Heating Characteristics[5]

This section investigates the impact of a gas redistribution within the walking beam type reheating furnace. The aim of this redistribution is to improve temperature homogenization of the exiting steel at the furnace discharge (tube number 43), without any changes regarding the heating time of the tubes. One possibility would be to reduce the thermal input in the rear end of the furnace (soaking zone), which creates a virtual extension of dwelling time. The difference to the initial thermal input has to be supplied in a front zone in order to reach the desired steel temperature of approximately 940 °C. This has been investigated at the real size furnace additionally using numerical simulations. This case does not correspond to a common operation of the real furnace and the volume flow rates of natural gas have been manually adapted by the operator. Approximately one hour was necessary to gain a steady-state operation and allow to take measurements. Due to the great effort needed, no test tube was traced through the furnace. Instead, the temperature profiles of the exiting tubes were measured by the infrared camera and compared to the results of the fixed mounted pyrometer.
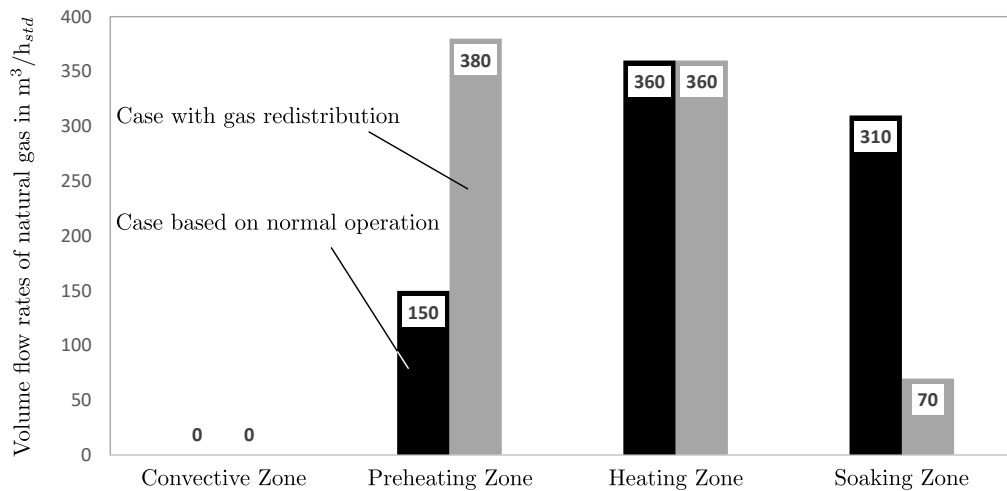
Figure 5.23.: Distribution of natural gas in the individual heating zones of the furnace adapted from [2].

The volume flow rates of natural gas are visualized in Figure 5.23, for both cases. The black bars indicate the case as investigated in the previous chapter, while the grey show the adapted case. In the previous case, large quantities of fuel are fed to the rear of the furnace (soaking zone), to keep furnace efficiency high. In contrast, the preheating zone receives less than half the amount of fuel than the other zones. This represents drastic changes to this type of reheating furnace. The question which now arises is whether the numerical model is also able to cover this unrepresentative operation in detail. If so, the model can clearly be seen as validated for a broad range of operations. Otherwise an adaptation to the model has to be found, to represent furnaces in a more general way.

---

[5]Segments of this section have already been published in [2]
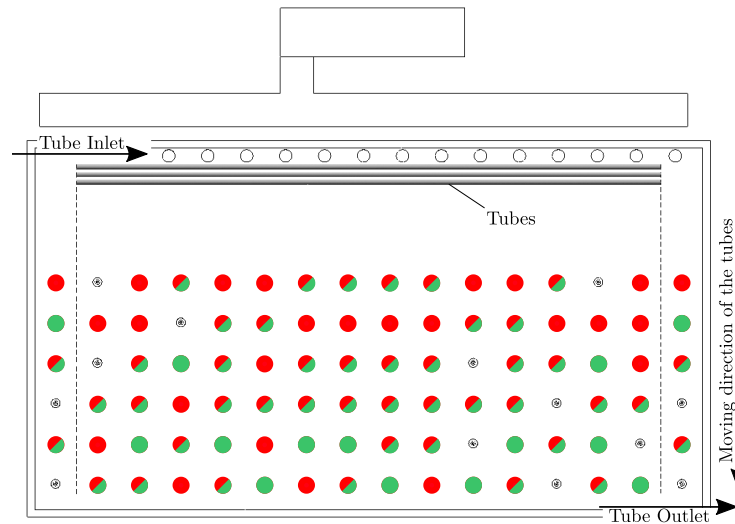
Figure 5.24.: Illustration of the active burners for the previous case (green dots) and the adapted case (red dots) adapted from [2].

In order to incorporate this special operation within the numerical simulation, the boundary conditions have to be adapted. These include the mass flow rates for natural gas and air, as well as the scheme for active burners. These changes do not reflect changes which are necessary for the numerical model, rather they represent actual changes due to the different operation. The changes made are summarized below, while furnace and steel-dependent values such as the emissivity, thermal conductivity etc. are unchanged. The adapted heat distribution, as shown in Figure 5.23, is based on the investigation by Han et al. [17], which identified a positive effect from lower fuel input in the soaking zone. Thus, the aim was to feed additional gas to the front zones, while the same amount of gas is introduced into the heating zone. The furnace is again set to 4 vol% excess oxygen (dry based) at the outlet, which agrees well with the operators measurements. This results in an air flow of approx. $9900\,m^3/h_{std}$ for the previous case and $9700\,m^3/h_{std}$ for the adapted case. The amount of air distributed to the individual zones was equal to the amount of fuel. The total amount of natural gas introduced, differs slightly by about $10\,m^3/h_{std}$ from the previous case. This is similar to a variation in fuel power of $100\,\text{kW}$. The impact is low and influences can be neglected.

The different gas distribution requires an adaptation to the active burner scheme. Otherwise, the burner in the preheating zone would exceed their maximum thermal load of $200\,kW$ per burner. On the basis of gas redistribution, more burners are active in the front region. The scheme was not manipulated by the operator and arises from the implemented system. The differences in active burners are shown in Figure 5.24. Green dots mark the same active burners as in the previous section, while the adapted case is indicated by red dots. The burners marked by green and red dots are active in both cases, while some burners are inactive for both cases; these are not represented. At this point the relevance of the generated geometry and mesh becomes decisive. Already in the former investigation, all burners are taken into account. This allows to easily implement any kind of burner scheme, without the necessity to generate a new geometry or mesh. Thus, such investigations can be done within a reasonable timeframe.
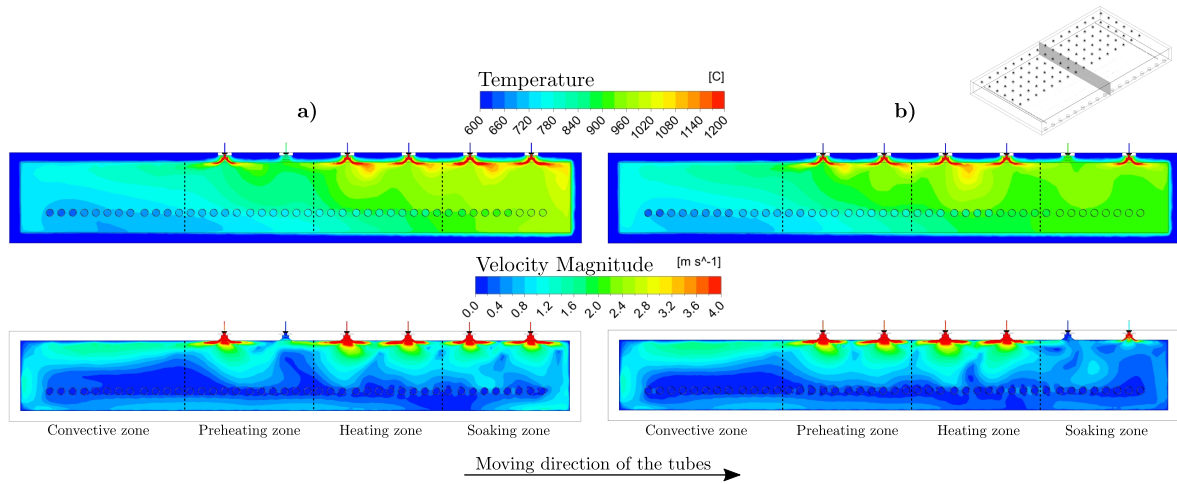
Figure 5.25.: Temperature and velocity distribution within a plane in the combustion chamber for the previous case (a) and the adaption (b) adapted from [2].

In Figure 5.25, the temperature and velocity distributions for the previous case and the adaptations are visualized in a single plane. Both cases differ in terms of gas distributions inside the furnace chamber. Additionally, the direction of movement of the tubes (from left to right), as well as the individual heating zones (dashed vertical lines) are indicated. Figure 5.25 a) shows the results of the previous case. In the soaking- and heating zones, high temperatures and velocities are apparent due to the respective high gas input. In contrast, the convective and preheating zones show lower temperatures, due to the lower fuel input in the front region as well as the colder tubes. The adaptation clearly affects the temperature and velocity distribution within the combustion chamber, shown in Figure 5.25 b). While the heating zone reveals the same behaviour as the initial case, the soaking zone is at a lower temperature level. This can be attributed to the reduced heat input in this zone. This also affects the velocity magnitude, which is lowered. In the front area of the furnace, characterized by the convective zone, no significant difference between either of the cases can be observed, regarding the velocity distribution. Whereas the increase in thermal input, as present in the preheating zone, has repercussions on the temperature in the convective zone. This is elucidated in Table 5.3, indicating the measured and calculated mean zone temperatures for the previously shown and adapted case. Both

Table 5.3.: Measured and calculated mean zone temperatures in °C [2].

Measured/ Calculated	Previous case	Adapted case	Difference (Adapted/Previous)
Convective Zone	741.3/733.8	773.7/762.3	28.5
Preheating Zone	826.5/812.4	884.0/862.4	50.0
Heating Zone	891.0/907.4	915.3/921.3	13.9
Soaking Zone	941.5/950.5	920.0/915.4	-35.1

simulations reflect the measured temperatures very well, with the largest deviation, of about 20 °C, found in the preheating zone of the adapted case. The good consistency proves that the simulations are very well suited to reproduce the real furnace. This suggests that the model developed for the steady-state combustion simulation is also able to capture the modified
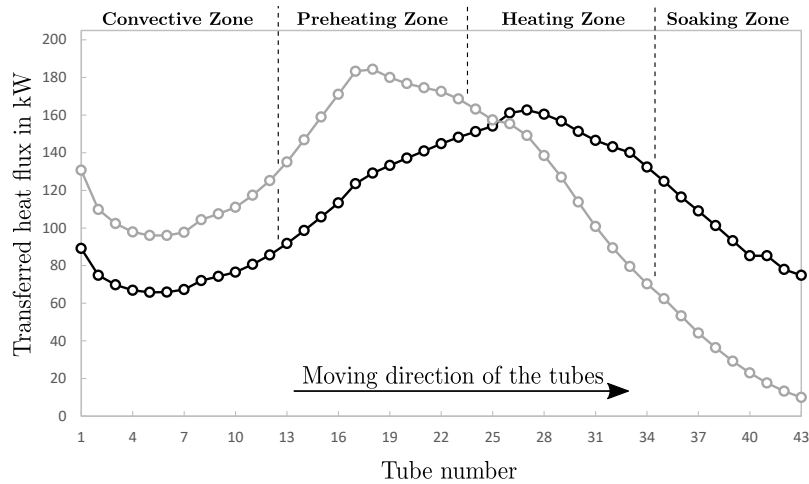
Figure 5.26.: Transferred heat flux to the individual tubes for the previous case (Black) and the adapted case (grey) adapted from [2].

heating characteristic with a high degree of accuracy. The calculated temperatures clearly depict higher temperatures in the first three zones after the tube inlet in the adapted case, including the maximum temperature difference in the preheating zone, of 50 °C. The previous case demonstrate higher temperatures in the soaking zone alone, due to the lower gas input. As a result of the different amounts of gas distributed to the zones, it is possible to detect a difference in the heating characteristics of the tubes. This is visualized in Figure 5.26, where the heat fluxes to the individual tubes are indicated. In the adapted case, comparatively higher heat fluxes are obtained in the convective and preheating zones. This can be directly attributed to the shift in gas distribution. In the heating and soaking zones, the transferred heat fluxes decrease rapidly. Here, lower heat fluxes occur than in the unmodified case. However, the total heat flux to the tubes does not differ greatly in either case. This leads to a furnace-efficiency of almost 60 % for both cases, which constitutes very good efficiency for furnaces of this type and under loads of this kind.

To validate the transient heating simulation, again measurements with the IC has been performed at the real furnace, operating with the adapted gas distribution. The results are shown in Figure 5.27. Similar to the previous measurements, the total set of measurement data (grey dots) are shown in Figure 5.27(a). The results show fluctuations which are significantly increased, compared to the previous case, indicating that the tube's surface is in a different condition. Due to the shifted gas input towards the tube inlet, the tubes reach the critical temperature (when scale starts to form at approx. 750 °C), earlier. This means, it is likely that a thicker and more adhesive scale layer has been formed which has not fallen off by itself during transport. As in the previous investigation, a trend line was fitted to the IC results providing better overview and ensure good comparability. A linear course is well suited to capturing the trend of the data; this is visualized by a black dashed line. The results of the pyrometer measurements for the corresponding exiting tube are visualized as black circles in Figure 5.27(a). Compared to the results of the IC, the pyrometer results do not show a misalignment. Moreover, it reveals a slight difference in temperature profile, with a maximum temperature spread of about 22 °C
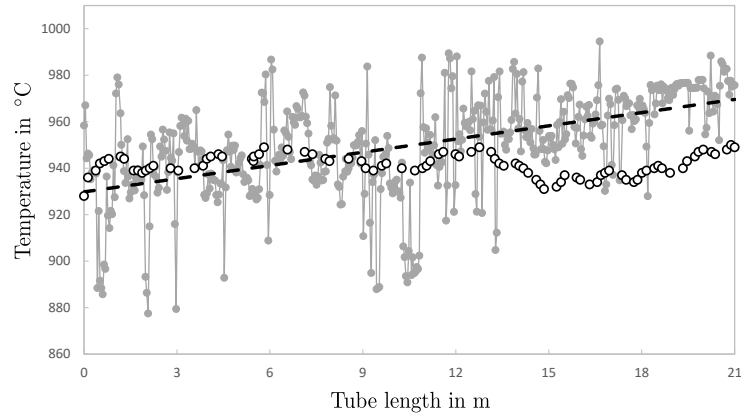
(a) Pyrometer and IC results with the fitted polynomial
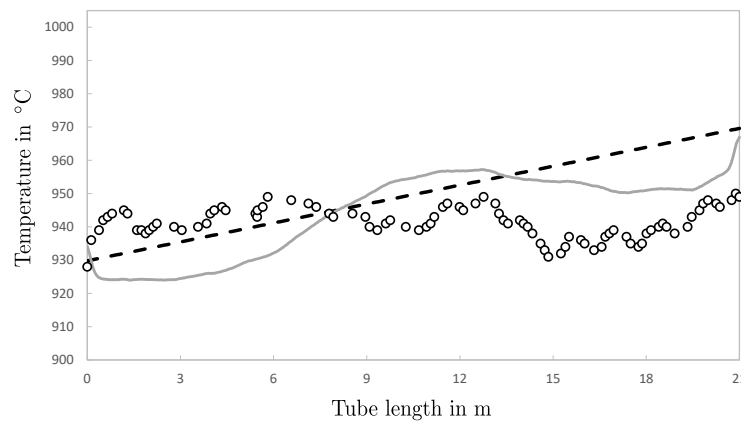
(b) Comparison of the pyrometer, fitted polynomial and numerical results

Figure 5.27.: Results of the temperature profile measured with the pyrometer (black circles) and infrared camera (grey dots/lines), including the polynomial fit (back dashed line), and the numerical results (grey line) adapted from [2].

over the tube length, which is similar to those measured in the previous case.

The actual comparison of the numerical CFD results with measurement data is shown in Figure 5.27(b). The calculated temperature profile again shows a clear imbalance and w-shaped trend. The occurring imbalance of the temperature profile is highly probable since no amendment to the swirl direction has been made. This means that similar to the previous investigation of this furnace, an imbalance in gas temperature within the combustion chamber is to be expected. The w-shaped profile, however, seems plausible since the active burners are again condensed in the centre of the furnace, as shown in Figure 5.24. Analysing the results, it becomes obvious that the IC is once again able to record the misalignment of the temperature profile. Here, the same gradient as calculated with CFD can be detected. However, the w-shaped profile cannot be recorded by the IC. The deviations between the IC and the numerical results can be attributed to a possible scale layer which has been formed. This effect has not been taken into account within this numerical simulation. However, it affects the IC measurement, which goes some way to explain the excessive fluctuations, as seen in Figure 5.27(a). The

pyrometer reveals a clear improvement in the calculated temperature distribution, using the gas redistribution, compared to the previous investigation. The temperature spread over the tube length is reduced from $38\,°\mathrm{C}$ in the previous investigation to $22\,°\mathrm{C}$, demonstrating a clear homogenisation. However, this improvement cannot be captured with CFD nor IC. While the CFD results show a similar temperature trend spread over the tube length as calculated in the previous investigation, the IC seems to be strongly affected by the different operating condition. As a result, the measurement results seem questionable in the present case. Although no clear agreement of the calculated and measured results can be seen, some effects can be captured by the IC and the CFD. Both show the same gradient over the tube length. However, the expected w-shaped profile cannot be measured and can only be calculated using CFD. As the measurements at the real furnace show us, the CFD results are plausible, suggesting that the limit of the IC has been reached. The pyrometer, on the other hand, provides the worst results, revealing an almost horizontal trend with some fluctuations over the tube length. The repeated mistake of the pyrometer calls into question the suitability of the installed pyrometer. Moreover, none of the measurement methods are able to identify the overheating of the edges; only the calculated temperature profile is able to represent this. The CFD model however, seems to represent a wide range of operating conditions with reasonable accuracy.

5.5. Characterization of Scale Formation in Reheating Furnaces[6]

Precise knowledge of the scale mass formed is essential for the production of high quality steel. Therefore, different measurement techniques have been developed to capture even the smallest differences in mass [197]. These led to different mathematical descriptions, which are mostly based on a parabolic approach. These are strongly dependent on the steel alloys and the surrounding atmosphere, as shown in [198]. Craig and Anderson [199] present a detailed collection of scale formation rates for different steels and atmospheres. However, mostly simplified approaches are used which are sufficient to estimate the scale formation in industrial applications. Their focus is on the calculation of total mass which has been formed, neglecting any local influences such as the surrounding atmosphere. This has a significant impact on the scale formation rate during the heating process and is extensively described in literature [200]. The atmosphere significantly effects the formation rates of the individual layers of a typical steel scale layer consisting of hematite (Fe_2O_3), magnetite (Fe_3O_4) and wustite (FeO). The scale layer can also cause a printing effect when descaling is not sufficient, pressing the scale into the steel's surface [201]. Therefore, descaling is important in many processes to ensure a good surface quality of the final product. The degree of descaling is decisively influenced by the atmospheric condition. For example, a higher oxygen content in the atmosphere increases scale formation, while it also becomes more porous and is thus easier to remove [202]. For more detailed discussions of scale layer formation, measuring techniques and other aspects of this topic, the reader is kindly referred to the literature [203–205].

In this context, several different numerical models have been developed to represent the formation of the scale layer. The aim of this research was to develop and improve already existing models to describe scale formation including as many factors as possible. However, most are based on a purely parabolic approach, similar to the theoretical concepts. Schluckner et al. [206] developed a model able to calculate local scale mass depending on the surface temperature of the steel and the local gas atmosphere condition using a user-defined function (UDF). Thus, a very detailed spatial and temporal scale formation can be characterized, depending on the surface mesh and time step used. The results show a very good agreement with experimental data, revealing a strong dependency on excess oxygen in the furnace atmosphere. The impact of varying scales thermal conductivity has been investigated by Chabičovský et al. [207]. Therefore the value has been varied between 0.2 and 0.9 W/mK to reflect different porosities of the scale layer. The data used correspond to data known from the literature [208, 209]. The results reveal a strong impact on the actual heat flux impinging the steel, disclosing the importance of correct material data. Thus, the impact of the insulating effect should not be underestimated in reheating furnaces. To incorporate this in the present furnace, the scale formation model from Schluckner has been extended to characterize the insulating effect of forming scale. Although the heating time is short, a clear influence on the temperature should be apparent due to the high inlet temperature of the tubes.

---

[6]Segments of this section have already been published in [3]

The Numerical Model

The numerical model is again based on the iterative scheme. A steady state simulation is used to describe the combustion process within the furnace. The corresponding heating of the tubes is calculated in a separate transient simulation. The iterative scheme and the models used are unmodified from previous investigations and can be looked up in section 5.2. At this point, the relevance of the reaction kinetic mechanism on calculated furnace atmosphere should be mentioned. Using the SFM with the skeletal25 scheme previously led to reasonable results and produced measurements with high accordance. Therefore, the same highly efficient model developed for normal operation of this kind of furnace was used again. The transient heating simulation had to be modified in order to incorporate the scale formation as proposed by Schluckner. Further adaptations to incorporate the thermal characteristics in the numerical model has to be made. These includes the numerical domain as well as the models used. These are described in the following paragraphs in detail.

As mentioned before, the developed model is based on the scale formation model proposed by Schluckner et al. [206]. Unlike most models to be found in literature, it includes linear and parabolic behaviour for scale formation, as described in Eq. (5.1) and (5.2). The linear law is important in the beginning of the scale formation process and changes into the parabolic law. Both laws can be described by the oxidation rates (k_l and k_p), which can be further described by an Arrhenius approach. Additionally, a dependency of the species concentration in the surrounding has been taken into account, as shown for the parabolic law in Eq. (5.3). Concentrations of CO_2 are not considered separately due to its connection to H_2O for complete oxidation in natural gas combustions. The reaction rate exponents (a, b) are fitted to match the results of Sobotka et al. [210], performing experiments on scale formation for a mild steel and a tempering steel. Within this section, the tempered steel with a carbon content of 0.32 % is used.

$$\frac{\Delta m}{A} = k_l\, t \tag{5.1}$$

$$\left(\frac{\Delta m}{A}\right)^2 = k_p\, t \tag{5.2}$$

$$\left(\frac{\Delta m}{A}\right)^2 = k_p\, t\, [O_2]^a\, [H_2O]^b \tag{5.3}$$

In order to use the scale formation model from Schluckner, the computational domain has to be extended by the surrounding fluid region. This is necessary because the model requires the associated species distribution in the surrounding combustion atmosphere, for O_2 and H_2O, according to Eq. (5.3), in each cell. In order to take heat losses due to the scale layer into account, an additional solid region is necessary. This has been realized in the numerical domain by a 0.1 mm thick region at the surface of the tube. The thickness of this layer was kept constant during the transient simulations and its growth was modelled by adapting its
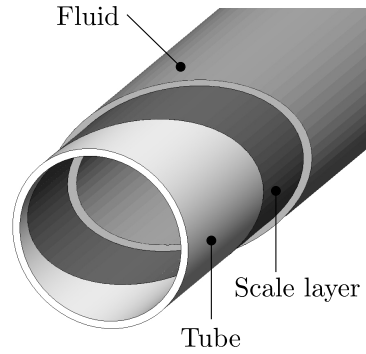
Figure 5.28.: The considered tube of the transient simulation, indicating the scale layer and fluid region adapted from [3].

thermal properties, as explained in detail in this section. The three sub-domains are visualized in Figure 5.28, indicating the fluid, scale and steel (tube) regions. The heat flux profiles are applied on the outer surfaces of this solid region (scale layer). At the corresponding shadow wall, characterizing the fluid region, a stationary wall is set. Here, the No-Slip condition is used with the corresponding calculated specific mass fractions. Between the solid layers (scale/steel) a coupled boundary condition is used. In order to avoid cells with very large aspect ratios, the mesh has been modified compared to previous numerical investigations. The modified mesh consists of 840,840 hexahedral cells. Whereby 60 divisions are placed over the circumference, 3 over tube thickness and 2000 along tube axis. The maximum skewness and aspect ratio occuring in the created mesh is $3.3e^{-2}$ and 101 respectively. In the scale layer and fluid region only a single cell is arranged over the thickness. This is necessary to apply the species to the lattice point nearest the wall. Torres et al. [211] have already pointed out that a single cell is sufficient to depict heat conduction through the thin scale layer. However, plausible values to characterize the physical properties of the scale are indispensable. This method makes it possible to keep the calculation time at a low level with simultaneous use of a small time step.
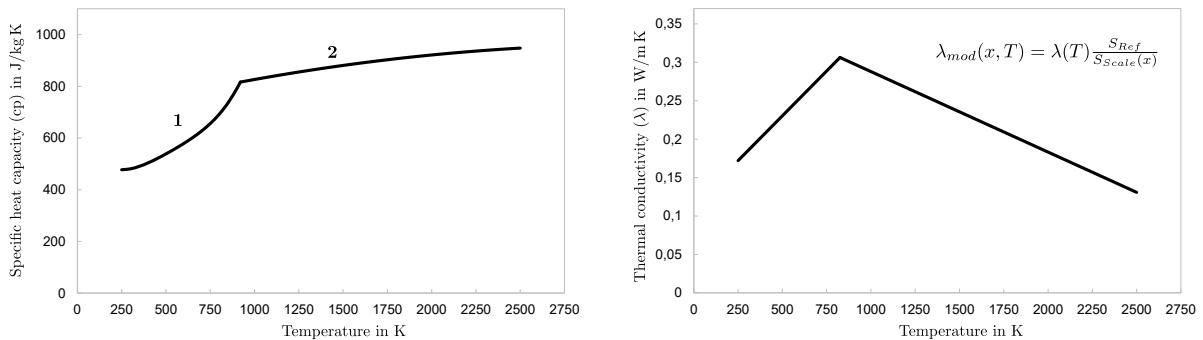
Figure 5.29.: Specific heat capacity (cp) and thermal conductivity (λ) of the scale layer adapted from [3].

The local growth of the scale layer, using a geometric constant thickness, is included by a local modification of scales properties. The modification is explained in detail below. Since the developed model is based on the assumption of pure wustite, its material data are used [208, 209]. The density is set to a constant value of $5900\,kg/m^3$. The value for specific heat

Table 5.4.: Measurement results and the calculated amount of scale at the real-size furnace [3].

	Initial weight in kg	Final weight in kg	Difference (scale mass) in kg	Scale mass relative to initial weight in %
1	3115.1	3111.1	5.13	0.1646
2	3125.01	3120.61	5.61	0.1795
3	3108.0	3104.2	4.91	0.1579
4	3119.5	3115.4	5.28	0.1692
5	3116.9	3112.8	5.23	0.1678

has been implemented via two polynomial profiles. These are presented visually on the left side of Figure 5.29 and marked by 1 and 2. The polynomial at lower temperatures ($<750\,°C$) corresponds to the data for the tempered, unalloyed steel used. At higher temperatures the polynomial follows a more horizontal trend, representing the material data of wustite. The thermal conductivity of wustite, as visible on the rhs of Figure 5.29, is very different from that of steel. This must be modified in the simulations due to the spatially constant scale layer thickness. Another UDF has thus been developed to vary local thermal conductivity of the (scale-) material. The underlying equation is visualized in the Figure for thermal conductivity (λ_{mod}) revealing the dependency of position (x) and temperature (T). S_{Ref} indicates the constant wall thickness of the scale layer, as used in the simulation domain. Whereby S_{Scale} is the locally calculated scale thickness. The maximum value for thermal conductivity has been limited to $1000\,W/m\,K$ to avoid program errors by attempting to divide by zero (scale layer thickness is zero). At this point it should be mentioned that a scale layer thickness of $1\,mm$ has been additionally examined, whereby the results show no difference due to the developed model. However, the order of magnitude for thermal conductivity agrees very well with those used by Sun et al. [212], using a constant value of $0.592\,W/mK$. Similarly to the previous investigations of the furnace, identical material properties of the steel are used. These are described and implemented via user-defined functions. A big difference is the location of the heat flux boundary condition set in the transient simulation. In previous investigations that were neglecting the scale layer, the heat fluxes were imposed directly onto the surface of the steel. Using the presented approach, the heat fluxes are applied to the outer surface of the scale. Thus, the thermal resistance of the thin scale layer reduces the heat flux actually penetrating the tube, representing a real behaviour inside industrial furnaces. Besides this, the residence time of the tubes within the furnace and the time step size used in the simulations is, equal to the previous investigation, set to $1096.5\,s$ and $0.5\,s$, respectively. The calculation time increases for a single transient simulation, from $30\,min$ needed in previous simulations neglecting any scale formation, to a total of $80\,min$, including scale formation. The more expensive computational simulation is the steady-state combustion simulation. Therefore, the total calculation time, to gain the final solution representing the real furnace, is only influenced marginally.

In order to validate the results, the results are compared with measurements at the real furnace. Measurements inside a real-size furnace always represent a major challenge. Moreover, the measurement of scale is even more difficult. Within this thesis a simple approach has been used. Measuring the weight of five tubes before entering the furnace and after descaling, at the
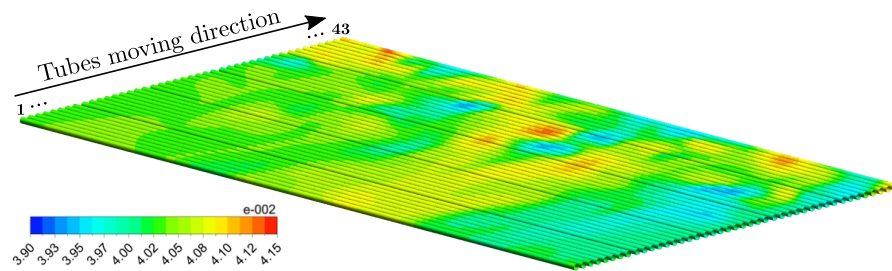
Figure 5.30.: Excess oxygen on tubes surfaces in mol/mol adapted from [3].

furnace exit, allows determining of the loss in tube weight. This corresponds to the loss of steel and has to be converted to represent scale mass which has formed during the reheating process. The molecular weights of steel and oxygen have thus been used, since an assumption of pure wustite has been made. The local available weighing equipment used is a portable device which is able to measure 5–35 tubes at once. The total weight can thus vary between 1 and 5 tons, depending on the number of tubes and their dimensions. The maximum inaccuracies caused by the measuring equipment are specified by the manufacturer as ± 1. Four measurements with 5 tubes each have been performed. The results are displayed in Table 5.4. Additionally, the results of the calculated scale mass are shown, indicating a mean scale mass of 5.23 kg to be formed during steel heating process. This corresponds to 0.1678 % of the initial mean tube weight. The standard deviation between the individual measurements is 0.26 kg, indicating a narrow distribution. The amount of scale formed appears to be very low compared to the results to be found in literature [43, 213], stating values about 10 times higher. This can be mostly attributed to the longer heating times (about 10 times longer). In this section the results of the numerical simulation are shown. The focus is on the transient simulation of scale layer formation while pointing out the most important impacts of the stationary combustion simulation. As already stated out by Schluckner et al. [206], the oxidation rates are significantly influenced by the concentration of the surrounding atmosphere and do not just depend on the steel surface temperature. The resulting species concentration on the tubes surface has thus been evaluated in the stationary simulation. A contour plot of excess oxygen on the tubes surface is shown in Figure 5.30. The concentration profile shows some local variations in the molar fraction of oxygen, ranging from a maximum of 0.0415 to a minimum of 0.039. This small range indicates an almost homogeneous distribution, which could not be analysed with measurements. The cause for these slight variations is the spin of the burners which accelerating the hot flue gases radially. This leads to a clash of the gases of adjacent burners, directing it downwards to the tubes. The same behaviour has already been described in a previous chapter (see 5.12 in chapter 5.2). Nevertheless, the mean species concentrations do not vary significantly in the tube- and the direction of movement.

In a first step, the model of Schluckner et al. [206] is applied. The results are shown in Figure 5.31 indicating the tubes surface temperature on the left and the specific scale mass formed at the exiting tube (tube number 43) on the right. Both plots clearly show a variation along tube length. The trend is same for both cases revealing the global maximum in the front end and
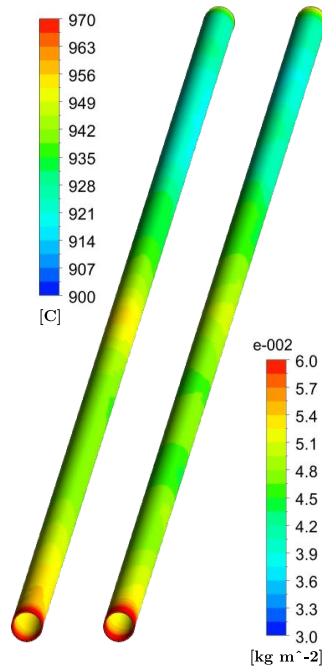
Figure 5.31.: The temperature (left) and specific scale mass (right) of the exiting tube using the model by Schluckner et al. [206] adapted from [3].

another near the tubes middle. This indicates the low impact of the varying atmosphere and a greater one due to tube surface temperature and also residence time. The model is also able to express a statement about the temporal behavior of scale formation, as visualized in Figure 5.32 by a black solid line. For a fast validation the results of a simple parabolic model are visualized by dashed lines. This is based on Eq. (5.2) and includes the Arrhenius approach, which leads to Eq. (5.4). This is the general form as used in many publications and is also proposed in [214]. It depends solely on the steel surface temperature T and time t. R is the universal gas constant, and k_{p0} the pre-exponential factor and E the activation energy. The values for the last two quantities are constants and have to be adapted for the given steel and atmospheric condition. Each author proposes different values and the user has to choose the most appropriate for the

(a) Outer surface of the tubes   **(b)** Inner surface of the tubes   **(c)** End surfaces of the tubes
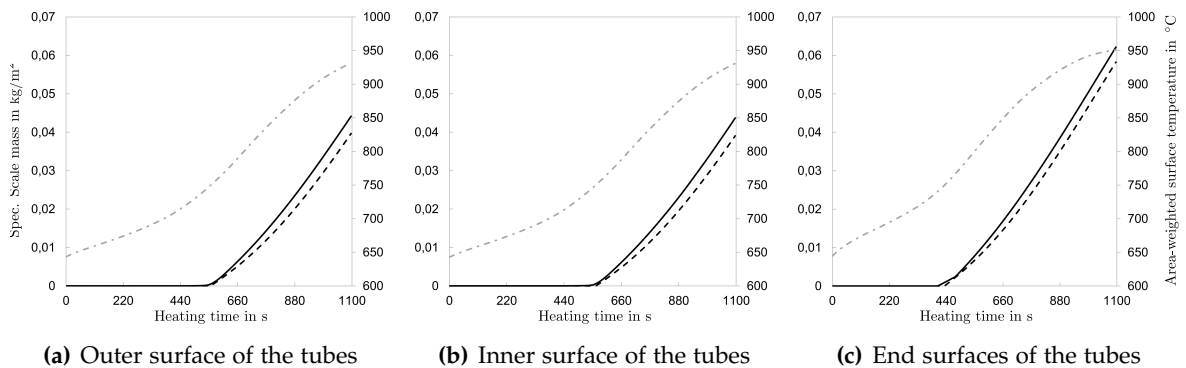
Figure 5.32.: The area-weighted surface temperature (grey dot-dashed line) and specific scale mass formed on the individual surfaces for the simple parabolic approach (Eq. 5.4) (black dashed line) and the CFD results (black solid line) in $\mathrm{kg\,m^{-2}}$ adapted from [3].

given problem.

$$\Delta m = \sqrt{k_{p0}\, exp\, \frac{E}{R\,T} t A} \tag{5.4}$$

Within this thesis the constants for k_{p0} and E are set to $11\,kg^2/m^4\,s$ and $125{,}000\,J/mol$ respectively [215]. Their range of validity is not restricted and can be used for a broad range of steel types. As scale formation starts at $750\,°C$ it was assumed that no scale forms until the area-weighted surface temperature reaches this critical value. Neither of the models shown, however is able to characterize the insulating impact of the growing scale layer on tube surface temperature. The model developed, including the scale layer and its insulating effect, needs 6 additional iterations to gain a converged solution. This results in a total of one week of computing time when the same stationary combustion simulation results, as shown in chapter 5.2 are used as starting condition for the iterative process. Thus, unlike previous investigations starting with a linear temperature profile on the tube surfaces, an already converged solution from the same operating condition is used. To evaluate the impact of scales insulating behaviour, the results are compared in detail to the identical case neglecting the insulating behaviour below. However, to verify the applicability of the present model, local temperatures of the scale layer has been evaluated at different times, whereby the thermal conductivity is calculated according to the Equation visualized in Figure 5.29. The results has been compared to the numerical results indicating identical values. To give an insight into this, the thermal conductivity of the scale layer of the exiting tube is visualized in Figure 5.33. This shows the
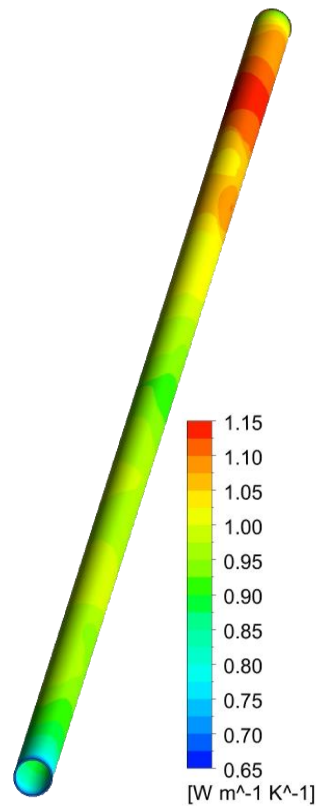
Figure 5.33.: Thermal conductivity of the scale layer at the exiting tube (number 43) adapted from [3].

decreasing conductivity with increasing layer thickness. Thus, the maximum is visible in the

upper right corner. While the minimum appears at both end surfaces. The main impact of the insulating effect is expected on tube temperature, therefore influencing both, the scale amount and scale layer thickness, respectively. The calculated specific scale mass formed on the surface is compared in Figure 5.34.
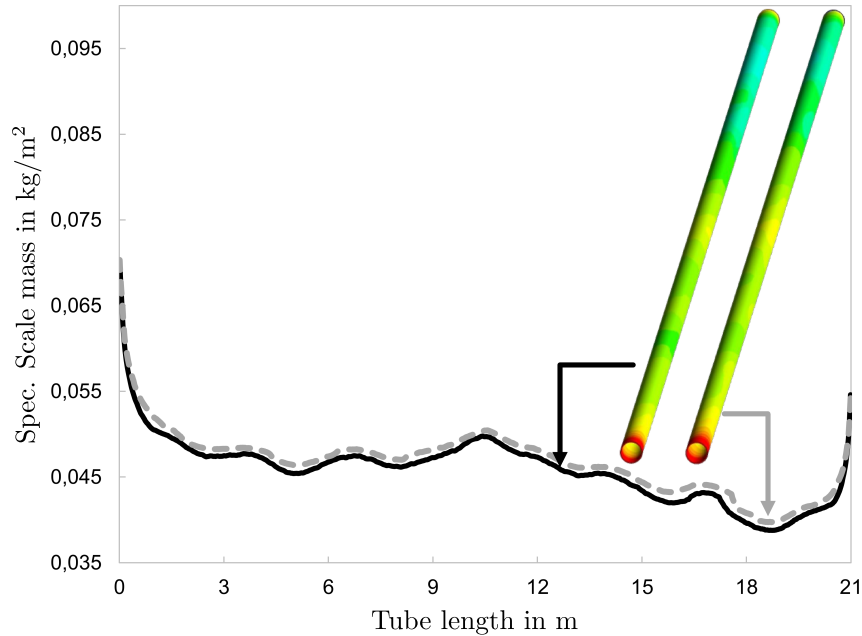
Figure 5.34.: Comparison of the specific scale mass for the model by Schluckner et al. [206] (black solid line) and the present model (grey dashed line) formed on the exiting tube (number 43) adapted from [3].

The black solid line corresponds to the model neglecting thermal conductivity of the scale layer. The grey dashed line indicates the results of the present model, revealing slightly more scale to be formed. Additionally, the associated contour plots are visualized, and also show no big difference. The impact of the scale layer on the surface temperature of the tubes is presented in Figure 5.35. Here again, the results of both models are compared, indicating almost identical
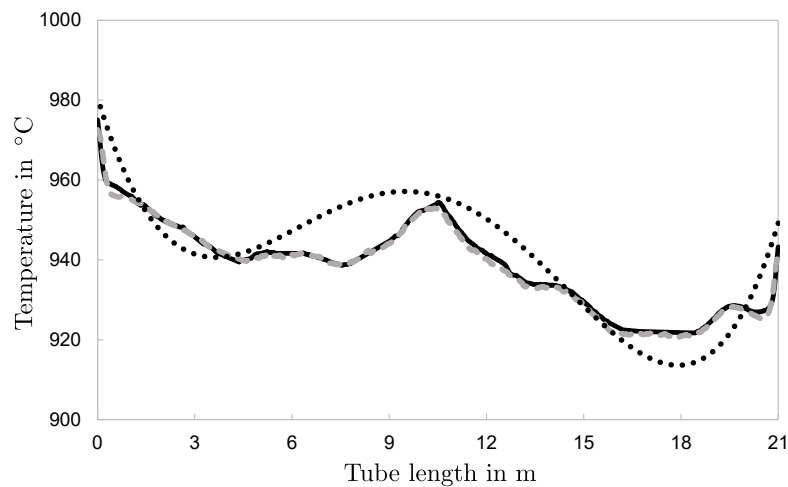
Figure 5.35.: Comparison of the temperature profile of the model of Schluckner (w/o insulating effects)(black solid line), including scales insulating effect (grey dashed line) and the infrared camera measurement (black dotted line), for the exiting tube (number 43) adapted from [3].

temperature profiles. As already stated, the scale formation at the outer and inner surface is almost identical. The clear w-shaped temperature profile becomes obvious as already validated in the previous sections. Thus, in the investigated furnace, the insulating effect of the scale layer can be classified as very low. This can be attributed to the lower heating time and target temperature compared to similar furnaces, heating full geometries. On the other hand, the considered tubes have a significantly larger surface area to volume ratio, which promotes scale formation. This has been evaluated in Figure 5.36, indicating the thickness of the scale layer formed at these surfaces.
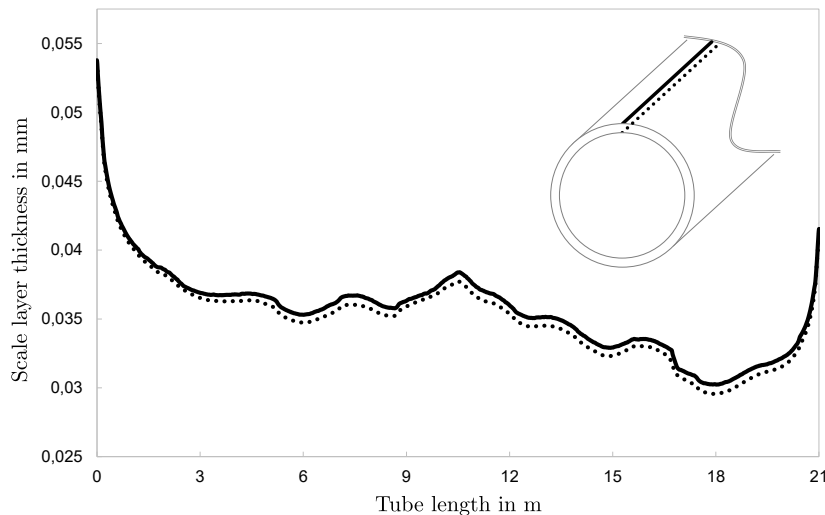
Figure 5.36.: Comparison of the calculated scale layer thickness on the outer (solid line) and inner (dotted line) surface of the exiting tube (number 43)adapted from [3].

Both profiles show a very similar trend, whereby the inner surface shows slightly lower values. The mean difference, between the inner and outer surface, is about $5.4\,\mu$m, corresponding to $1.5\,\%$ of the mean scale layer thickness formed at the inner surface. This small difference can be explained by the marginal temperature difference between the outer and inner surface. A significant impact from local varying species concentration can be ruled out. As already stated, a slight local variation of oxygen concentration on the outer surface of the tubes becomes apparent. These arise from the flow patterns inside the combustion chamber. Whereas an almost constant species concentration can be detected within the tubes, which is due to the very small gas flow. Since the profiles in Figure 5.36 have an approximately constant offset, the impact can be considered as low. However, both small end faces show no significant variation, but exhibit a constant scale layer thickness corresponding to the values found at 0 and 21 m tube length. Furthermore, the temperature gradient across scale thickness was evaluated. A mean temperature difference of $0.12\,°$C, leading to a mean temperature gradient of $4.32\,°$C/mm, can be detected. In Table 5.5 the results of the numerical models, the parabolic approach and the measurements are visualized. The measurement performed merely permit a statement to be made about the total amount of scale mass formed. In the numerical model this corresponds to the scale mass formed on the last tube (tube number 43). Whereas, the numerical models and the parabolic model are able to distinguish between the individual surfaces (outer, inner, end

Table 5.5.: Comparison of the formed scale in % to initial tube weight for the CFD results (including and neglecting any impact by heat conduction), the simple parabolic approach described by Eq. 5.4 and the performed measurements [3].

| | CFD | | Simple model | Measurement |
	w/	w/o	Eq. (5.4)	
Outer surface	0.0827	0.0805	0.0698	
Inner surface	0.07471	0.0732	0.0630	
End faces	$7.5e^{-5}$	$7.49e^{-5}$	$6.92e^{-5}$	
Total	0.1575	0.1537	0.1328	0.1678

faces). It can be seen in Table 5.5 that both CFD models neglect the insulating impact (w/o), as developed by Schluckner and the presented model including any influences (w/), show nearly the same results. However, the present model shows a slightly stronger scaling of the tubes. The difference is only 0.0025 kg/m^2 of formed scale which corresponds to 0.00377 % of initial tube weight. The simple model, based on the parabolic approach described by Eq. 5.4, exhibits less scale to be formed. Nevertheless, the difference to the present model is in an acceptable order of magnitude of 0.025 % to the initial tube weight. The measurements however, reveal that slightly more scale is being formed. The deviation is even smaller compared to the simple model (parabolic approach), revealing 0.01 % more scale formed. This very good agreement shows the applicability of the numerical model. The biggest influencing factors were evaluated, the most important being:

- Inaccuracies by the weighing equipment (± 2 kg)
- Outer atmosphere influencing the tubes after exiting the furnace.
- Leaks of the real furnace influencing the furnace atmosphere.

The influence of the measurement error can be classified as low and neglected. Also impact due to furnace leakage can be neglected too, because the furnace operates at an increased pressure level. This reduces the influence on the furnace atmosphere and restricts this to a small area. The biggest influence is due to the outer atmosphere and the re-formation of scale during the measurements. There were no suitable data for the parabolic scale formation in environmental atmospheres available in literature at the time of publication to the best knowledge of the authors. A rough estimation, however, using the simple model defined by Eq. (5.4), implies that less than 0.13 kg of scale is formed per tube, which corresponds to about 0.02 % of the initial tube weight. The developed model is superior to many others in terms of computing time due to the separation in a stationary and transient simulation. Furthermore, the usage of a simple combustion model (SFM) with a detailed reaction kinetic mechanism make it numerically highly efficient. It allows to implement various additional models without a drastic increase in computing time. This has been shown with the present scale formation model, which is able to calculate scale layers with high accuracy. It combines the ability to calculate the temporal and also local varying scale mass. This is the biggest difference and main advantage over any model developed thus far. Its easy implementation is another advantage, making elaborate measurements redundant.

5.6. Discussion

This chapter presented the numerical investigations of the real-size walking beam type reheating furnace. The global numerical scheme is based on a novel iterative approach using two separate simulations: A steady-state simulation describing the combustion in all its detail and a transient simulation to depict the heating of the tubes. Using this scheme, it is possible to simulate any furnace. The only modifications which need to be done, involve the preceding adaptation of the heat flux profiles to include the steel movement. This means that any type of movement can be modelled with this model. Within the present furnace, a translational and rotational movement of the steel tubes has been taken into account. Beside this, the main advantage of two separate simulations is the lower computation time required, compared to fully transient models. Regarding such big real-size applications, this is very low, when compared to fully transient models. These would prolong calculation time to months, even using a coarser time step size, which allows to perform several case studies within a shorter timeframe. Computing time for all simulations presented was about 2 weeks including about 7 iterative loops to reach the final solution, using an Intel i7 with 6 core CPU and 64 GB RAM. Moreover, the choice of the numerical models enhance the numerically efficiency. The chosen models include the efficient SFM combustion model, using the detailed skeletal25 reaction scheme, incorporating 17 species and 25 reactions. To calculate radiation inside the combustion chamber, again the DO model has been used, which is excellently suited to describe the important solid body and gas radiation. Compared to the previous investigation of a single burner, inlet conditions have been changed to mimic a real behaviour. Therefore, long-term data obtained from common operations of the real furnace has been evaluated and mean values have been calculated. Extreme deviations, caused by longer stops, have been neglected since these do not represent the normal furnace behaviour. However, any fluctuations occurring during steady operation are taken into account in the boundary conditions of the steady state combustion simulation. This affects the calculated results and thus the transient heating simulation of the steel tubes. The simulation was geometrically reduced to a single tube to be considered, applying all heat flux profiles in a successive manner, reflecting the periodic transient moving of the tubes. The small domain, allows a detailed mesh and small time step size to be used without an excessive increase in computing time.

The results of the steady-state combustion simulation provide detailed information about the local temperature and species distribution within the whole combustion chamber. Temperature has been evaluated using the fixed mounted thermocouples installed in each of the heating zones. These have been checked by the usage of additional thermocouples. Due to regular inspections, differences are minor, as was expected. The results reflect the measured temperature distribution with a high degree of accuracy. This verifies the whole numerical model, using the averaged process data. Influences due to a symmetric consideration of the furnace have been evaluated. The burner swirl-vane assembly causes a temperature imbalance inside the combustion chamber. This effect cannot be captured with the symmetric consideration since

the spin direction is also mirrored. Thus, the spin direction differs for both halves. This case is nevertheless able to present major influences: the global flow inside the combustion chamber and heat flux distribution are nearly identical. Both cases indicate the main flow from the burners mounted at the ceiling to the front of the surface. Here, the combustion gases split into a flow towards the outlet, while the rest is led back below the tubes into the combustion chamber. The gases are already cooled, reducing impact on tube heating. In this area below the tubes, the skid system has been neglected since the impact is classified as low. The results calculated inside the furnace effect the transient heating simulation directly. Thus, it can be stated, that the validation process of the transient steel tube heating simulation also validates the steady state combustion simulation.

The transient simulation depicts the impact of the symmetric consideration. The geometric full case calculates a clear w-shaped temperature profile. The symmetric case is able to represent one half of this w-shaped profile which is identical to the mirrored part, due to the mathematical restriction. Therefore, it is able to capture a w-shaped profile, while imbalances over the whole furnace width cannot be captured. To verify the results, the temperature profiles of exiting tubes have been measured using an infrared camera IC, a pyrometer and a test tube equipped with several thermocouples. Depending on the insights to be gained, optical measurement systems are preferable. Within this thesis, an IC and pyrometer are used. Both are able to measure temperatures at specific points. During measurementsusing the IC and the pyrometer, attention must be paid to achieve the correct measuring position, which should be almost orthogonal to the measured surface. The influence of deviations should not be underestimated. Also other influences have to be evaluated, such as any effects regarding the hot flue gases exiting via the tube outlet and scale formation on the steel tubes. Within this thesis, several measuring-positions have been investigated with the IC, although the area between furnace exit and after treatment (descaling) is comparatively short. Nevertheless, local impact can be classified as low and a high accordance between the single locations is achieved. The IC captures the w-shaped temperature profile and misalignment with a high degree of correspondence to the numerical result, although a strong impact on the scale formed could be determined by local fluctuations. This effect is invalid with the two-color pyrometer as mounted at the furnace exit. The pyrometer also captures the w-shaped profile, while it was not able to detect the inclination of the temperature profile. One possible explanation for this is an internal smoothing of the measured temperature profile. Another measuring method often used in steel industry is the usage of a test steel block equipped with several thermocouples. Special attention should be paid to the location of the thermocouples since their number is limited and it is an elaborate method of measurement. One measuring point should be positioned in the core of the steel good, another one on the upper surface and one on the lower surface. Beside this, ideally a wide distribution should be striven for in order to capture any influences over the furnace width. This measurement also showed high accordance with the numerical results. The general agreement of the different measurement methods proves once again the suitability of the individual numerical models. Moreover, this approves the suitability of the iterative scheme, coupling a stationary and transient simulation.

The IC, pyrometer and numerical approach have also been used to investigate the impact of a steeper heating characteristic by inducing more heat in the front area, reducing thermal input in the rear end of the furnace. This has been implemented at the real furnace by manual adoptions since this does not represent a common operation. The furnace indicated a completely different heating characteristic. While the numerical model still calculates a w-shaped profile, the pyrometer showed an improved temperature distribution. This is characterized by a significantly smoother temperature distribution over the tube length. However, the IC measurement revealed even stronger temperature fluctuations and a different, almost linear behaviour. This can be attributed to the increased scale formation on the surface. The cause for this is the tube reaching the temperature of scale formation earlier.

To evaluate the impact, a scale formation model has been applied to the presented results. Although this model makes it possible to show the insulating influence of the scale layer, a negligible impact can be observed in the present furnace. Also much less scale is formed than in other furnaces, which is due to the comparatively fast heating process of hollow geometries. Thus, the residence time can be kept at about one-tenth compared to blocks or slabs, preventing too much scale being formed. The big advantage of the presented model is the integration of temporal and local scale formation effects. These include the local steel surface temperature and corresponding local species for O_2 and H_2O in the surrounding combustion gases, influencing the scale formation rates. In this furnace, major influences can be ruled out, since the main flow of the flat flame burner is near the ceiling. Thus, no strong variation in the gas composition at the tubes surfaces can be seen. The accuracy of the calculated numerical results have been verified by measurements. Therefore, tubes' masses have been determined before and after descaling the surfaces, which allow to see the direct implication for the scale mass formed.

6

Industrial Furnaces Fired with Different Oxidizer/Fuels[1]

The demand of industry with regard to increasing production and efficiency, with the least possible effort, has led to an increasing number of investigations in recent years. Furthermore, a reduction of the ecological footprint has been, and will remain, a big target. To achieve this, Wang et al. [216] investigated the impact of burner arrangement in a real size industrial furnace. Reducing the number of active burners had a positive effect on the temperature distribution inside the combustion chamber, and thus, on the heating characteristic of the steel. This can be attributed to the fact that the flames have more room to spread, leading to longer flames and a more homogeneous temperature distribution. Another approach to increase efficiency is the change from conventional burner type to recuperative burners. This has been investigated by García et al. [217] revealing an increase in efficiency and production by changing to self-recuperative burners. Other publications, such as this by Hou et al. [218], examine the influence of different fuels on the boiler load, emissions and flame length in an industrial boiler. Therefore different compositions of BFG and COG have been analytically and experimentally evaluated. Also the type of oxidizer influences the emissions and can cause an increase in productivity as shown by Oliveira et al. [219], investigating the impact of pure oxygen as oxidizer. Also Han et al. [220] investigated the impact of pure oxygen used as oxidizer, highlighting the advantages regarding efficiency and slab outlet temperature. Other authors investigated the impact of oxygen-enriched combustion on the emissions, flue gas temperature, heat flux distribution and fuel consumption in experimental studies [221, 222]. Other worthwhile improvements may need a reconstruction of the combustion chamber, as investigated by Kremer et al. [223]. In this paper the reduction of NO_X in the flue gas has been achieved by simply lifting the ceiling of the combustion chamber by almost half a meter. This comparatively simple reconstruction produces recirculation zones, leading to retarded reactions and thus to lower gas temperatures. Oh et al. [224] have increased efficiency and reduced energy consumption of a hot stamping roller-hearth furnace. This was achieved by adapting the distance of electric heater to the steel as well as install additional insulation on the furnace walls. Another way to improve industrial furnaces without expensive modifications can be achieved by influencing the flow field inside

---

[1]Segments of this chapter have already been published in [5]

the combustion chamber, as investigated by Kuang et al. [225, 226]. They varied the angle of the overfire air jets and the burner location in a down fired furnace. The resulting flow fields differ and reveal an influence on the fuel burnout and thus the flue gas emissions. The works presented so far only deal with the optimization of existing systems preventing problems to occur. Only a few of these are able to increase the performance of existing furnaces, since most are operating at their production limit. Nonetheless an increase can be achieved by maximizing the heat input. In most cases modifications of furnace geometry or adaptations to the type of energy supply (e.g. burner type) cannot be avoided.

Mayr et al. [192] carried out a design study on an industrial pusher type reheating furnace using numerical CFD simulations. Several additional oxy-fuel jet burners were added to the existing flat flame air-burners. This modification led to an increase of productivity and efficiency of the furnace. Due to the lack of suitable models to describe such systems, one is forced to use either the relatively simple eddy dissipation model (EDM) or the accurate, but computationally expensive, Eddy-Dissipation Concept Model (EDC) to describe turbulence-chemistry interaction. Both models are able to depict several different oxidisers and fuels in a single simulation. The Steady Laminar Flamelet Model (SFM), on the other hand, is not able to handle several different oxidizers and fuels, in a numerically efficient manner. This restricts the implementation to investigations using one oxidizer and fuel each. The EDM, as well as the EDC, also have certain disadvantages. The EDM is restricted to the use of global reaction mechanisms with only two reactions. Thus, this model is not able to describe the formation of radicals. which is of significant importance in oxy-fuel combustion. Neglecting these, leads to drastic overestimations of flame temperatures. On the other hand, the EDC is a very accurate model following in high computational effort needed. Although it is able to depict a detailed reaction mechanism, the computational cost limits to using a simple one. To overcome this limitation, global mechanisms have been evolved to characterize some of the most important radicals [133], as used by Mayr et al. [192]. Nevertheless, some using simple global reaction mechanism, such as Oh et al. [227] investigating a pilot-scale furnace with a burner using natural gas, air and a separate oxygen inlet for oxygen enrichment. Further investigations dealt with the adaptation of several factors to characterize the combustion with the EDC model more accurately [228]. By adapting the reacting fraction of the fine structures (χ) the temperature distribution and lift-off height of the flame can be influenced. As several authors performed research on this topic, a lot of suggestions can be found in literature which are often contradictory [229–234]. Thus, it can be concluded, that there is no optimum setting for the EDC model. At this point it should be noted, that neither of the named publications provide information about the required calculation time for the different combustion models. Investigating real size furnaces, the computational demand, using the EDC model, exceeds simpler models, like the SFM and EDM, by a multiple times. Thus, the computational effort needed becomes the limiting step.

6.1. The numerical model

To overcome the restriction to a single combustion model to be used, a well - known approach has been modified. The aim was to keep it as simple as possible, so it represents an ideal tool for operators and the basis for further developments. The method is based on the spatial separation of the computational domain into parts, using only one oxidizer and fuel each. In literature, this procedure is referred to as the "multi-block" method. One of the first documented mentions came from Yu and Rubbert [235], investigating the flow of a wing-mounted propfan. Additionally, the subdivisions allow to implement parallel calculations on a network of workstations [236, 237]. Calculation time can be decreased significantly, thus efficiency increases, which has been mentioned in several publications [238–240]. This method also allows to optimize meshes of each subzone by aligning grid points with the flow direction [241, 242]. However, most models developed are based on overlapping geometries, to allow reasonable information transfer and calculation of the results [243, 244]. The big drawback of this subdivision is the decomposition into the individual domains, which cannot be done automatically [245]. All cited models are designed for parallel calculation on a computer cluster. This is already implemented in the software used, requiring a computer network. To overcome this issue, the multi-block model was modified to be used on a single computer in a consecutively manner. For this, the interaction of the parts has been simplified to a kind of one way coupling, reducing computational effort drastically. Therefore, a basic understanding of the flow inside the furnace is helpful to set correct cutting planes. This model has been investigated at a real size walking beam type reheating furnace heating steel tubes. In the front region of the furnace, close to the tube inlet, several oxy-fuel burners are mounted. Further into the furnace, in the direction of tube movement, air-flat flame burners are located. A more detailed explanation of furnace construction is presented in a subsequent section. Within this chapter, the SFM, EDM and EDC model have been used. Models for radiation and turbulence have been unchanged from previous investigations. Also the global numerical method is unchanged, based on an iterative manner using a coupled stationary and transient simulation, calculating the combustion process and transient tube heating, respectively. In the following sections, the adaptation of the furnace geometry, mesh and boundary conditions used are explained.

6.1.1. The Multiblock Approach

The presented approach is based on the division of the geometry in several domains. This is schematically visualized in Figure 6.1, indicating the cascade by individual domains numbered from 1 to N. Division is made, so each of these is fired by solely one individual fuel and oxidizer. This procedure roughly fixes the position of the cutting plane within real furnaces, whereby the exact position can vary. Some tips for optimal positioning are presented within this chapter. Figure 6.1 additionally indicates the main gas and steel moving direction, including the main gas outlet in the last domain N. Since most reheating furnaces are based on counter-current principle, the main gas flow is from the back of the furnace to its front. In the present model
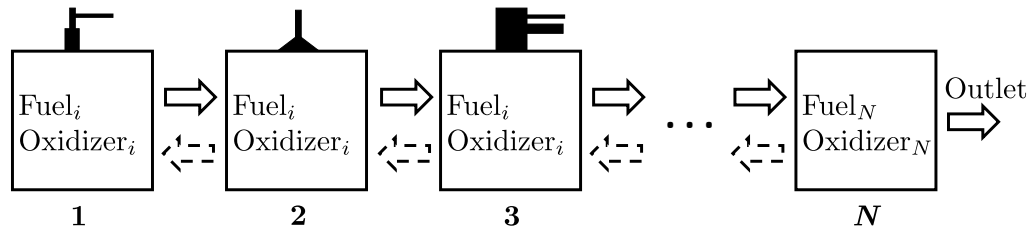
Figure 6.1.: Schematic illustration of the division into the parts indicating the main gas flow with solid arrows and steel moving direction with dashed arrows adapted from [5].

this leads to a flow from one compartment to another, which has to be taken into account. Therefore, in the first sub-domain only inlets, for fuel and oxidizer, are present. The outlet is fixed with the location of the cutting-plane, in which the data is transferred to the next domain. It is recommended to add a subsequent geometrical extension and move the outlet at the respective end to avoid any influences on the cutting plane itself. This ensues that the transferred values, exiting one domain and entering the next, are not affected. Although a mutual interference between two compartments has been neglected, a kind of one-way coupling has been taken into account in the simulations. This means that each compartment *i* affects compartment *i*+1, but not vice versa, which also preset the sequence of the simulations to be performed from domain 1 to *N*. An advantage of this scheme is that each part, of the furnace, can be improved individually. This means that, for example, in each compartment, the most suitable models for turbulence, combustion etc., can be used. The division of the whole domain into smaller domains also allow for further decrease in computational effort for each section. For example, it facilitates finding an optimum burner load for each section. Consequently this model is also useful to investigate furnaces using a single fuel and oxidizer. Although some simplifications have to be made, which are described within the next few sections, the developed model represents an easier alternative to previous investigations of such furnaces to be found in literature.

6.1.2. The Furnace and Mesh

As mentioned in the beginning of chapter 5, describing the construction of the furnace, additional jet-burners are installed in the front region of the furnace, as indicated in Figure 6.2. These are fired with natural gas and pure oxygen and are needed for special operations, defined by different tube dimensions or steel inlet temperatures. In the investigations so far, the burners were inactive, and thus neglected in the numerical domain. The tubes, as considered in this thesis, have a length of 16.9 m and diameters (outer/inner) of 0.181 m/0.163 m respectively. The steel type is unchanged from the previous investigation, using a tempered, unalloyed steel with a carbon content of 0.32 %. The mean inlet temperature of the steel tubes is 417 °C and is heated up to 923 °C. This means that the steel inlet temperature is decreased by 226 °C, compared to the operation investigated in the previous chapter 5. The usage of two different burner types, fired with different oxidizers or fuels, prevent the usage of the SFM, as in the

previous investigations since only a single fuel and oxidizer can be used. The furnace is divided
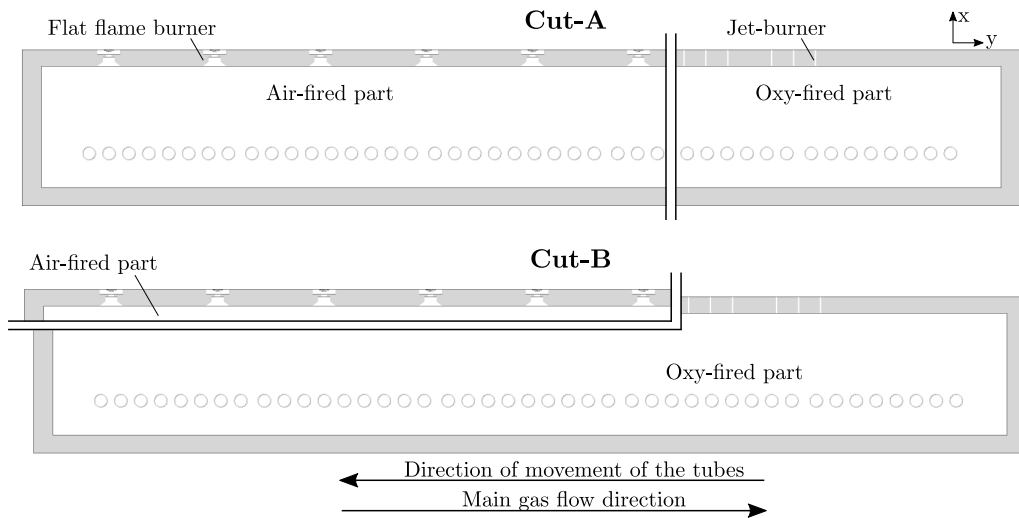
Figure 6.2.: The air and oxy-fired parts used for both cuts: Cut-A (upper) and Cut-B(lower) adapted from [5].

into two sub-domains due to the operation using two different oxidizers (air and pure oxygen), as indicated in Figure 6.2. According to Figure 6.1, domain 1 represents the rear end of the furnace. This corresponds to the area close to the tube outlet, heated by the flat flame burners (air-fuel). Domain 2 represents the front region of the furnace, closer to the tube inlet which contains the jet-burner, heated by fuel and pure oxygen. This also comprises the central flue gas outlet. Subsequently, the domains are referred to as "air-fired", and "oxy-fired" parts. The position of the cutting planes is visualized in Figure 6.3. To provide a better understanding for the resulting sub-domains, these are shown in a cross section of the furnace in Figure 6.2. This illustration includes information about the location of the two burner types, the tubes moving and the main gas flow direction. Within this thesis, two different cuts have been investigated and their results are compared. The two slices are characterized by two planes indicated in Figure 6.3 and named Cut-A and Cut-B, respectively. Compared to the previous investigations, the large number of additional jet-burners would increase the total number of cells required for the whole furnace significantly. Thus, a detailed mesh is not very economical and the presented model represents a logical development. The advantage is to keep down computation time, of the individual sub-domain, using a detailed mesh. Another big advantage is the ease applicability to any furnace geometry. Independent of whether a single or multiple oxidizer and fuel are used, this model is applicable.

The Air-Fired Part

The air-fired part represents the first step of the furnace calculations (domain 1 according to Figure 6.1). This part includes the flat flame burners in the rear zone, neglecting the jet-burners. Therefore, the cutting plane has to be placed between the convective and the subsequent preheating zone. Based on this requirement, two different shapes of the cutting plane have been considered. They lead to completely different shapes for the air-fired part, as shown in

Figure 6.2. As previously mentioned, it is absolutely necessary to extend this part at the cutting plane into the oxy-fired part. With this, the simulation can be kept more stable, reducing the urge for divergence. This region should not be kept too small, enabling to prevent upstream
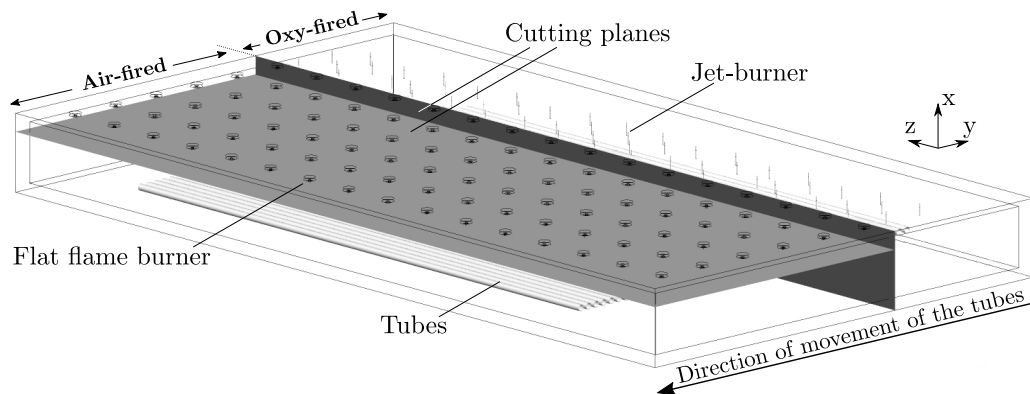
Figure 6.3.: A three-dimensional view of the furnace geometry, including the cutting planes and some furnace details adapted from [5].

effects. Within this furnace, the size of the extension should be almost as large as the oxy-fired part, when considering Cut-A. For this reason, the whole furnace was regarded for the air-fired case. To reduce the number of cells used for the mesh, the jet-burners were neglected within this domain. This is permitted, since their effects will be taken into account in the subsequent consideration of the oxy-fired part. Based on this procedure, the usage of the identical mesh as shown in Figure 5.7 is enabled. It consists of 13,317,500 polyhedral cells, whereby a majority of the cells have been used to resolve the large number of flat flame burners. Different mesh sizes have been investigated in previous works, whereby the used one is a good compromise between accuracy and calculation time. This simulation also serves to provide the boundary conditions for the next domain, the oxy-fired part. The transferred values include a detailed distribution for temperature, species, velocity and turbulence

The Oxy-Fired Part

The second part (subdomain 2 according to Figure 6.1) contains the jet-burners in the front region. The upstream part of the main flow, calculated by the air-fired part, is neglected, leaving the downstream part after the cutting plane. In Figure 6.2, the oxy-fired parts for both cases are shown. The upper illustration, indicating Cut-A, neglects the whole rear area of the furnace. Thus, a reduced number of tubes are present within this domain. As a result, the iterative approach, alternating the steady-state combustion and transient tube heating simulation, requires two steady-state simulations to be calculated. This is due to the fact that, at each iteration step, all tube temperatures are calculated anew in the transient heating simulation, including the retroactive impact on the combustion chamber. Thus, the oxy-fired part has to be used for the first tubes and the air-fired part for the subsequent tubes, in the rear zone of the combustion chamber. On the other hand, solely the oxy-fired part has to be calculated at each iteration step, using Cut-B, since all tubes are present in this case. In order

to describe the additional jet-burners in detail, the mesh has to be refined near the burner tips. The fine mesh has been extended into the combustion chamber to present the flame correctly. A section of the mesh used, is shown in Figure 6.4, indicating the insulation (green), combustion chamber (grey), as well as the jet-burners and the tubes. The very fine mesh near the jet-burners, as well as the fine mesh near the tubes are obvious. Different meshes were investigated previously in a test case considering a single burner. The optimum cell number, in terms of accuracy and computational effort needed, has been transferred to the mesh used in this thesis. Each jet-burner has been resolved by 58,000 hexahedral cells, including the extension into the combustion chamber. Due to the small cell growth used, this leads to a total number of 14,059,400 cells for Cut-A and 15,737,600 cells for Cut-B, respectively. This large number of cells, needed for this comparatively small domain, clarifies the positive effect of the division into two parts. The number of cells needed for the whole furnace, based on the same strategy for mesh generation, would lead to a tremendous computational effort. Thus, design studies to increase e.g furnace performance, are associated with longer calculation times. This requires major adjustments to the mesh, keeping computational effort in a certain range. With the presented method, each compartment can be improved on its own.
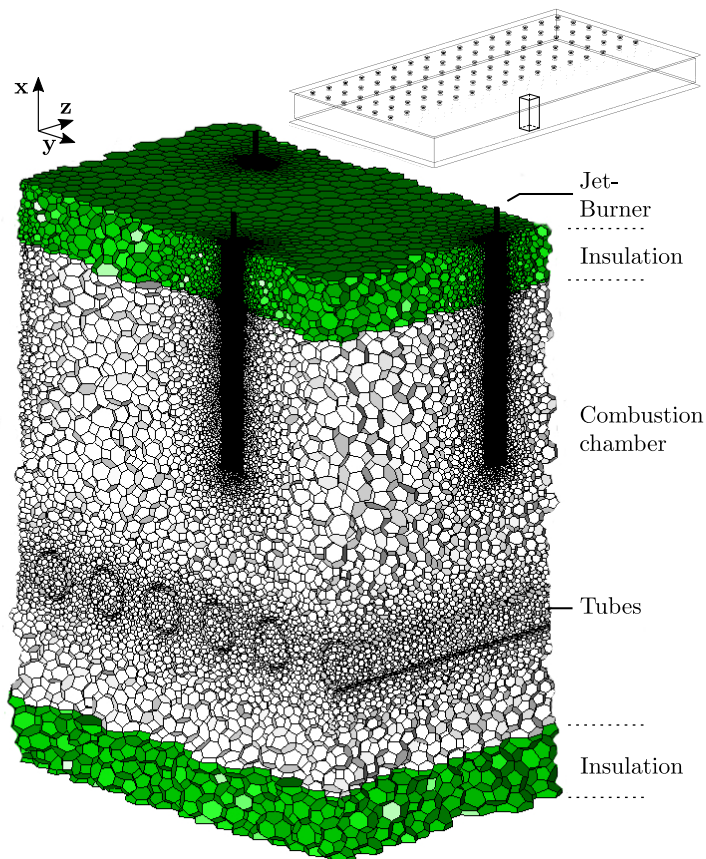
Figure 6.4.: The mesh used in the oxy-fired part, pointing out the high resolution near the jet-burner adapted from [5].

The Entire Furnace

To prove the suitability of the developed approach, the whole furnace has also been considered. To keep the computational effort and the time needed reasonable, fundamental changes to the mesh were made. The global cell growth has been set to 1.2 within the whole domain, while in some areas the cell size was specified manually. Attention has been paid to not affect global flow and to preserve the main flame shape. Therefore, different meshes were simulated and compared. Other than common mesh independence studies, comparing a coarse, middle and fine mesh, the meshes, as used in this thesis, are based on a coarse mesh and were successively refined. This procedure required great awareness of mesh building and its impact on the final solution and is, thus, not an easy operation. The simplified mesh used has still a total number of about 22 million cells. Some implied mesh-dependent influences cannot be prevented, but nevertheless, the main impacts, including the mutual influence of both burner types, are taken into account. Within the present chapter 6, all investigations of the entire furnace, including both burner types, are calculated using exclusively the EDM model. Beside this, an investigation using the SFM model, based on equilibrium calculations, was also conducted, allowing to incorporate three different streams. However, during the calculation process excessive calculation times (despite the usage of different techniques to speed up) were noticed. These are in the range of the EDC model. Therefore, this form of the SFM, as well as the EDC model were excluded due to the restrictions of their computing demand.

6.1.3. Boundary Conditions

In the simulations the data represents several hours of averaged process data from the real furnace, similar to previous investigations. As only minor fluctuations occurred during operation, this assumption is valid, allowing to treat the combustion simulation in a steady-state manner. The measured mass flow rates of the fuel and oxidizer are presented in Table 6.1. During the operation the air is preheated to 349 °C, while the oxygen and fuel enters the furnace with ambient temperature of 25 °C. Thermal conductivity of the insulation was set to 0.7 W/mK, which already led to reasonable results in the previous investigations. Also the emissivity of the furnace walls and steel tubes remained unchanged at a value of 0.7. The outer walls of the insulation have been depicted as convective with a free stream temperature of 25 °C and a heat transfer coefficient of 10 W/m²K.

Table 6.1.: Measured fuel and air mass flow rates in kg/s for each heating zone as used in the simulations [5].

kg/s	Jet-burner	Flat flame burner		
		Preheating	Heating	Soaking
Fuel	0.1414	0.06	0.018	0.0111
Air		1.1098	0.4013	0.2713
Oxygen	0.5673			

In the present investigation, as a first step, the whole furnace (excluding the jet burner) has been regarded in the air fired case. This case represents only a part of the real operation, thus, a comparison with measurement data is not possible. However, the simulation provides data in the cutting planes, needed as boundary conditions for the oxy-fuel cases. At these planes (see Figure 6.3), the results of the air-fired case are stored in profiles. These contain detailed information about the local variation of all three velocity components (u,v,w), turbulence (k and ε), temperature as well as species distributions. In the oxy-fuel cases, the cutting planes, are treated as velocity inlets using the previous calculated detailed information. However, attention has to be paid to the species distribution, using either a detailed and a simplified reaction mechanism. Since some species are not present in the simplified case, these should contribute to the inert nitrogen avoiding extraordinary effects. Using Fluent this is easily implemented by sorting the species, so that nitrogen is listed at the last position.

6.2. Numerical Results

This section is divided into three main parts, presenting the results of the performed numerical steady state simulations. Each part is designated to demonstrate a specific impact, allowing the selection of the best model to characterize the whole furnace. The ulterior motive is to find a model which is very efficient in terms of calculation time. Therefore, different combinations have been investigated and the main pros and cons are highlighted. This model is subsequently compared to several measurements, proving the immense similarity of the model and the real furnace behaviour in detail. After finding the most suitable model, the impact on the transient heating is investigated by the iterative coupling of the steady state and transient simulation.

Part 1
  Comparison of the SFM and EDM model for the air-fired case.

Part 2
  The two oxy-fuel parts (Cut-A and Cut-B) are compared using the EDM model, allowing a fast evaluation and selection of the most suitable one.

Part 3
  The findings of Part 1 and 2 are used to compare the EDM, EDC and SFM model in the oxy-fired part and to select the most suitable one.

6.2.1. Part 1 - Comparison of the EDM and SFM in the Air-Fired Case

This chapter serves to illustrate the impact of different turbulence-chemistry interaction models on the combustion process of flat flame burner. Therefore, the SFM and EDM model are applied to the air-fired part, as shown in Figure 6.3. The EDC model has been omitted due to the restriction to the computational effort needed. Mayr et al. [118] already showed the high accordance of the SFM model and measurements, using the detailed skeletal25 reaction
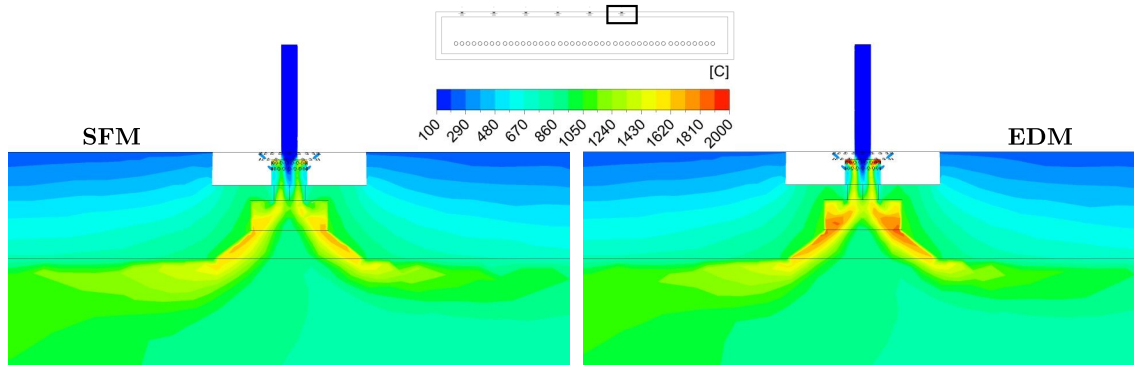
Figure 6.5.: Comparison of the calculated temperature distribution using the SFM and EDM model adapted from [5].

mechanism, investigating a flat flame burner in a semi industrial furnace. Additionally, this model already allowed to capture the real behaviour of industrial furnaces, fired by flat flame burners, revealed in the previous chapter. Buchmayr et al. [143] also showed the benefit of the SFM over the EDC, calculating similar results with a fraction of the required computing time. Thus, it can be stated, that the SFM provides very accurate results and can be seen as benchmark. The resulting temperature distributions, in a cross sectional plane of a flat flame burner, are shown in Figure 6.5. Due to the simple, mixed is burnt approach of the EDM model, high temperatures occur already near the air inlets, in the upper part of the burner. Also below, in the dome of the burner, higher temperatures, than calculated with the SFM, are present. This can be attributed to the neglecting dissociation effects, leading to a difference in maximum temperature of 365.14 K. Nevertheless, the flame shape and length is almost identical. The different flame temperatures, in the vicinity of the burner, have a relatively low impact on the heat flux transferred to the tubes. This is shown in Figure 6.6, where the heat flux per tube is compared for the SFM and EDM model. Both models show a similar heat flux distribution, with positive values in the front region. Wherein, negative heat fluxes, indicating a cooling of the tubes, can be seen at the last tubes from tube number 35 to 43. Using the SFM model,
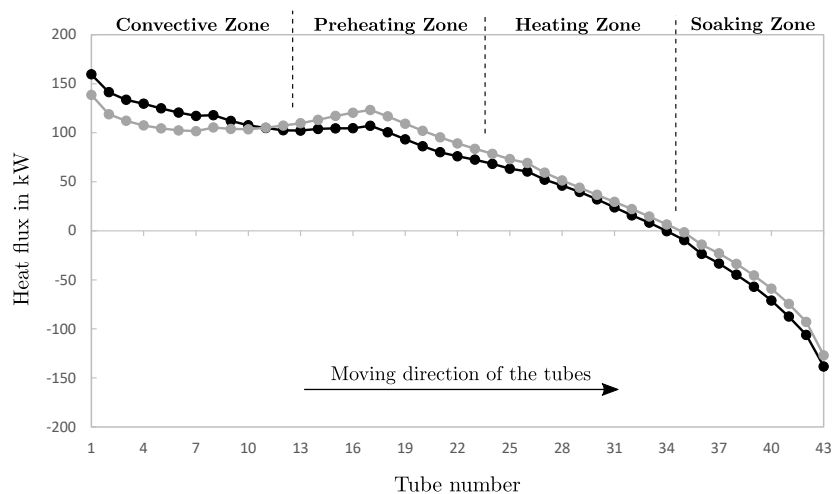
Figure 6.6.: Heat flux to the tubes for the SFM and the EDM model adapted from [5].

an increased heat flux on the first tubes in the furnace, and slightly decreased heat fluxes at the back end of the furnace has been detected, compared to the EDM. The differences can be preliminary attributed to the high flame temperatures in the vicinity of the burners, using the EDM model, increasing the radiative heat transfer to the tubes. This can be seen from tube number 11 further on, characterizing the end section of the convective- , preheating-, heating- and soaking zone. The difference between the models decreases towards the tube outlet. The cause for this is the declining burner load from zone to zone. The lower the load, the shorter the flame, which causes the high temperatures to occur inside the burner, reducing the radiative effect on the tubes. In the convective zone, however, the transferred heat flux is increased using the SFM. All in all, the total heat transferred to the tubes using the SFM model is 2340.8 kW. The
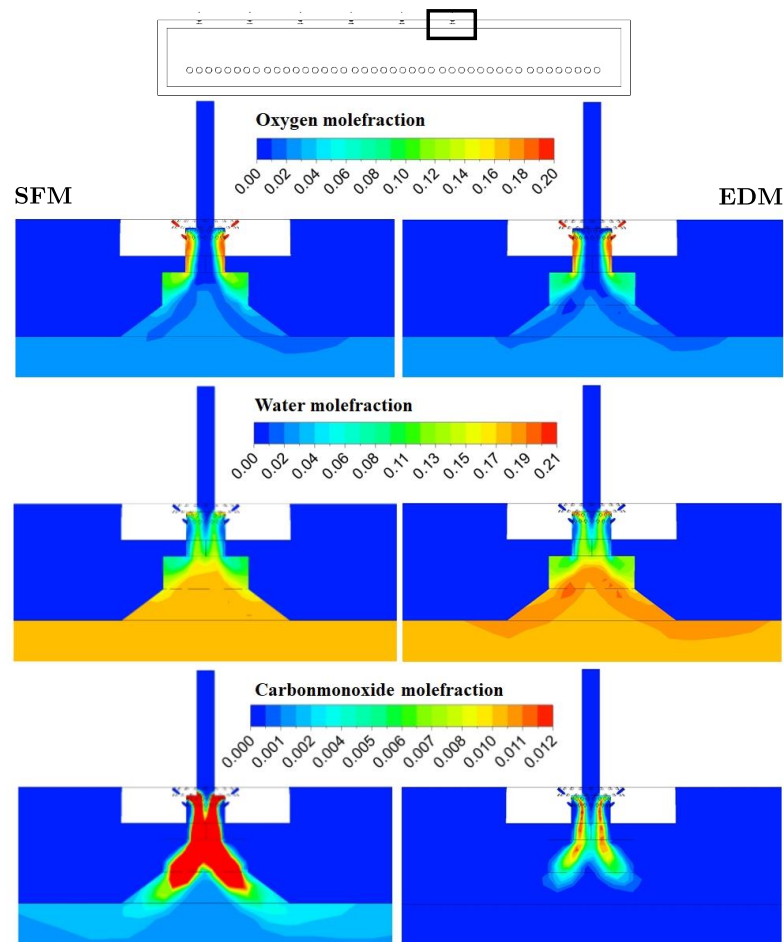
Figure 6.7.: Species distribution for oxygen, water vapour and carbon monoxide for the SFM (left) and the EDM model (right) adapted from [5].

radiative part is 2063.5 kW, corresponding to 88.2 %. The EDM model shows, with a value of 2503.9 kW, more heat to be transferred, wherein also the proportion of radiation, with a value of almost 94.5 %, is increased as explained before. Bigger differences occur regarding the species distribution, as shown in Figure 6.7, indicating the oxygen, water vapour and carbon monoxide mole fractions near a burner. Almost identical values, for the oxygen distribution in the burner region, can be found for both cases. The water vapour distribution shows local higher values in

the regions of high temperatures, using the EDM. Wherein the carbon monoxide concentration is at a significant lower level, compared to the SFM. This indicates that the EDM totally fails to predict correct CO concentrations, as already stated by [32, 143], using the default values for the model constants A and B. Adjustments to these can improve CO predictions. Nevertheless, the composition of the flue gas is almost identical for both cases, using the default model settings, as visualized in Table 6.2. The biggest difference is the higher concentration of carbon monoxide, calculated with the SFM model. Additionally, the flue gas temperature is getting compared, revealing almost identical temperatures, with a deviation of almost $5\,°C$.

Table 6.2.: The mean temperature and species distribution at the outlet using the SFM and EDM in the air-fired case [5].

		SFM	EDM
Temperature	$°C$	633.72	638.55
Mole fraction in mol/mol E-02			
CH_4		0	0
O_2		2.797	2.789
CO_2		8.095	8.242
CO		0.129	0
H_2O		16.238	16.483
N_2		72.357	72.489

It can be concluded, that both models are able to depict the whole furnace in detail. However, the restrictions of the simple EDM model lead to a small deviation in the maximum flame temperature calculated. This results in slight differences in the heat transfer to the tubes, especially the radiative component. Differences in calculation time needed, to gain the final solution, are negligible. Since the SFM, with the detailed mechanism for reaction kinetic, has previously led to plausible results and a high degree of compliance with measurements at the present furnace, its results are used for further investigations.

6.2.2. Part 2 - Evaluation of the two Oxy-Fired Parts

The presented model is based on the separation of the whole furnace into sub-domains, so each uses a single fuel and oxidizer. Thus, the location of the sectional plane is fixed by the arrangement of the burner in the furnace. In the presented furnace, the location had to be chosen to separate the oxy-fuel jet burner, located in the front region, from the air-fuel flat flame burner, in the rear zone. The simplest method is a vertical cut, separating the furnace into a front and rear section, as realized by Cut-A. Nevertheless, some room for the shape of the cut is given, influencing the way of coupling between the geometrically divided parts. The impact of the plane's shape, has been investigated in a second case (Cut-B), using a vertical and horizontal plane. The location of the planes have been chosen to avoid a separation in the highly reactive zones. In both cases the results of the preliminary air-fired case, using the SFM model, were used as a boundary condition, at these cutting planes. In these planes, the values for the hot gas velocity, turbulence, temperature and composition are transferred to the oxy-fired case. Some of

the data used are visualized in Figure 6.8, indicating the local temperature-, velocity- and mole fraction distributions for oxygen and water vapour. This illustration clarifies the importance of using the correct profiles as boundary condition, since strong local fluctuations become obvious. Using mean values, as visualized in Table 6.3, would lead to a drastically different behaviour. For example, with regard to the temperature distribution, very high temperatures can be seen in the upper central area of the furnace. In this area, the flames of the air-fired flat flame burner have a significant impact. In the lower regions of the furnace the combustion gases are at a significantly lower temperature level of about 650 °C.

Table 6.3.: The mean temperature and species distribution in the planes used as boundary condition [5].

		Cut-A	Cut-B
Temperature	°C	660.58	723.09
Mole fractions in mol/mol E-02			
H_2		4.36E-02	4.39E-02
O_2		2.21	2.76
O		1.66E-02	1.77E-02
H		4.86E-03	4.78E-03
OH		2.16E-01	2.37E-01
H_2O		1.23E01	1.42E01
HO_2		8.4E-05	9.32E-05
CO		9.2E-02	9.24E-02
CO_2		6.13	7.10
CH_4		3.57E-07	1.80E-07
CH_3		9.48E-08	4.83E-08
CH_2O		1.26E-09	6.50E-10
HCO		7.89E-13	4.11E-13
CH_3O		1.65E-13	8.70E-14
H_2O_2		1.76E-06	1.94E-06
N_2		5.51E01	6.45E01
N		0	0

Using the air-fired values as boundary conditions in the oxy-fuel part can lead to difficulty with numerical stability. To overcome any problems in convergence during simulation, the under-relaxation factors should be adjusted carefully. For this, especially momentum, turbulence, energy and species should be kept at a lower level (~ 0.6) for the first iterations. After several hundred iterations, these can be raised. Similarly to the previous investigations, the converged simulation used the under-relaxation factors as found in the Appendix B.2.

Investigating the impact of the plane's shape, the computational inexpensive EDM model has been used to calculate the jet-burners. This ensues a fast analysis and comparison of the two cases, emphasising the impact on the flow inside the combustion chamber and heat flux distribution to the tubes. To evaluate the impact of the division process itself and the shape of the cutting plane, the results are compared to the simplified full-size furnace. While focusing on the differences between the cases, the accuracy of the combustion process is evaluated in the next section. In Figure 6.9, the temperature distributions in a longitudinal plane for Cut-A (upper right), Cut-B (upper left) and the full case (lower) are visualized. The plane is located in the middle of the furnace, and the tubes moving direction is from the right hand side to the left. In case of Cut-B and the total furnace solely the front part of the furnace is visualized,
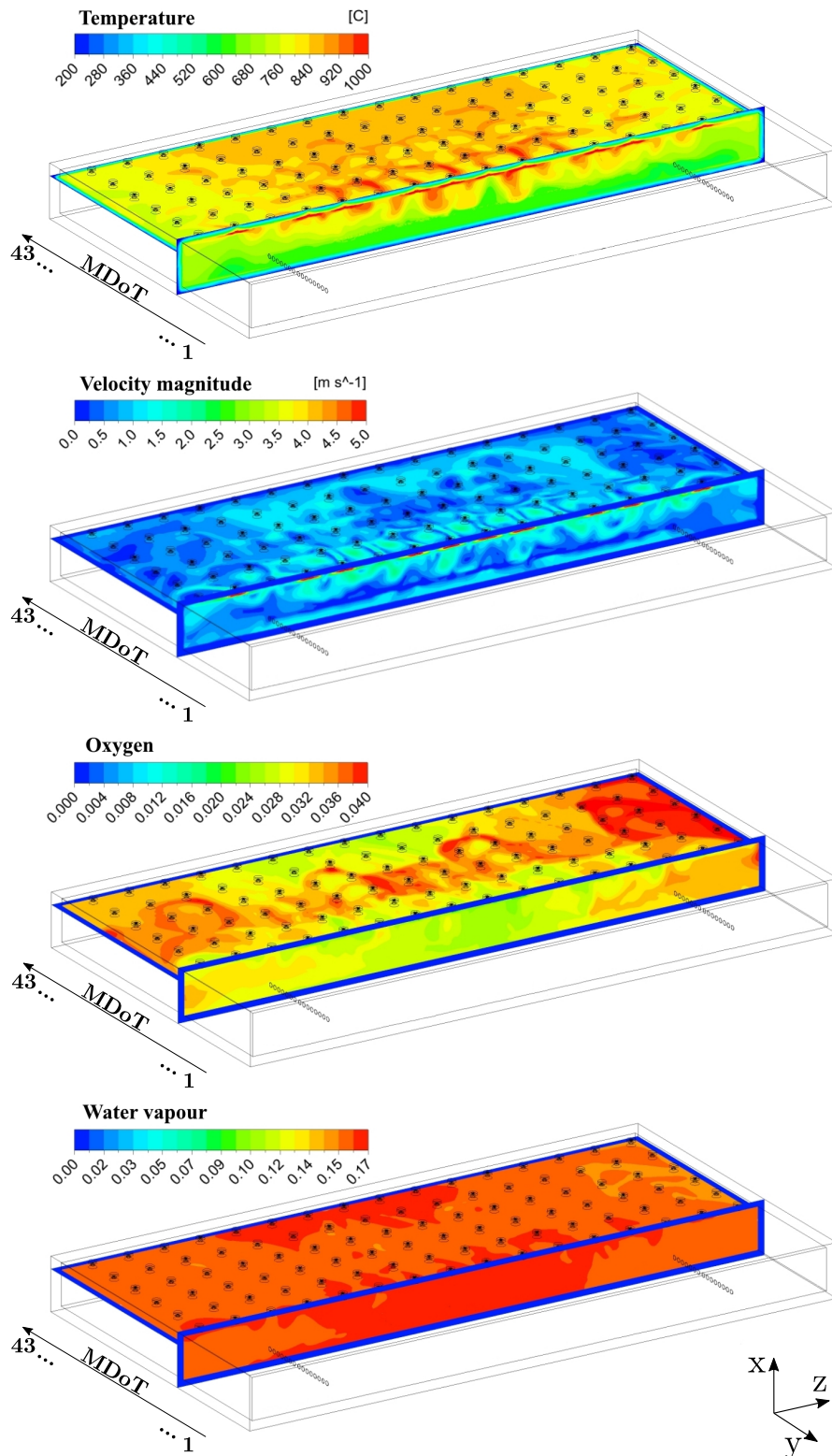
Figure 6.8.: Calculated temperature-, velocity-, oxygen- and water vapour distribution in the sectional planes from the air fired case using the SFM indicating the moving direction of the tubes (MDoT) and tube numbers adapted from [5].

while the rear section is hidden after the S-shape double line. As it is getting obvious, the overall-temperature distribution is very similar. Deviations occur in the deflection of the jets on the furnace floor and due to the boundary condition set at the cutting plane. In Cut-A,
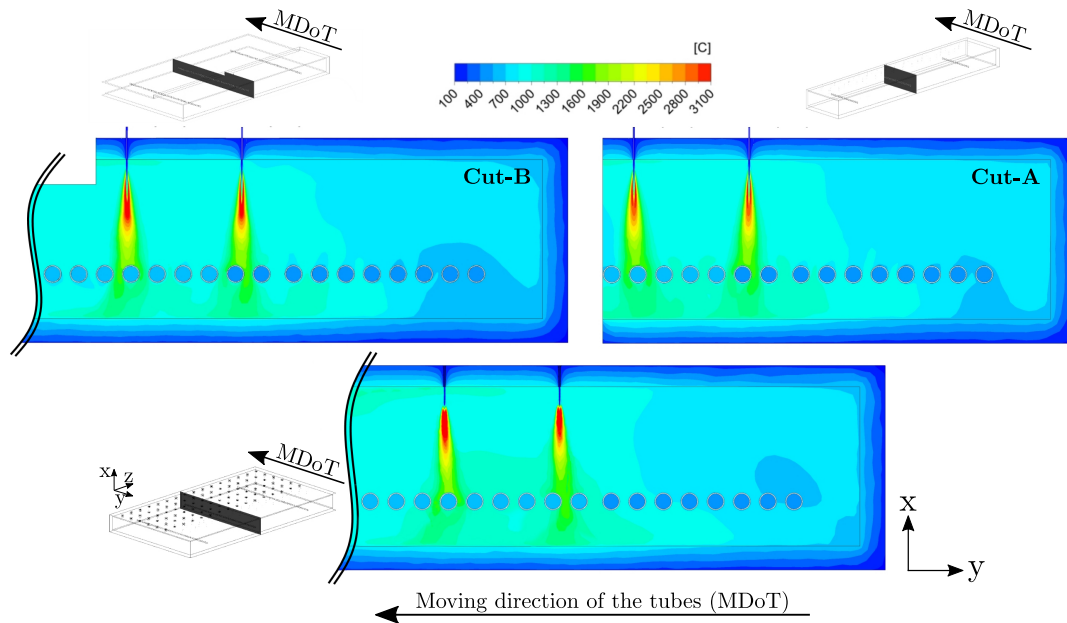
Figure 6.9.: Temperature plot in a plane for Cut-A (upper right) and Cut-B (upper left) and the total furnace (lower) using the EDM adapted from [5].

the flow, to the rear zones of the furnace, is fixed by the boundary condition set. Thus, the main part of the hot combustion gases, of the jet burners, is deflected upwards and towards the flue gas outlet. On the other hand, Cut-B allows stronger backflows to occur, due to the extended volume in this region. The results of the full size furnace, indicate slight deviations to the other cases. For instance, the flame shape differs minimally, due to the coarser mesh used. Nevertheless, this simulation reveals similar gas temperatures to impinge the tubes' surfaces. The deflection of the hot combustion gases on the furnace floor is similar to Cut-B, indicating an enhanced backflow into the rear zones. In order to make this behaviour more vivid, the streamlines of six burners, located in the middle of the furnace, are presented in Figure 6.10 for both cuts. The entire furnace is not visualized, due to the close coherence to Cut-B. The streamlines represent one second of flow and are coloured by the gas temperature. Additionally, the velocity distribution, in tube moving direction is shown by a grey distribution. This distribution correspond to one of the three velocity directions which are extracted and used as boundary condition. Positive values indicate a velocity towards the jet burners, while negative values indicate a flow in tube moving direction MDoTs. The streamlines underline the described behaviour, highlighting the backflow to be more pronounced using Cut-B. The same behaviour appears in the simulation of the entire furnace, which has a direct impact on the heat flux distribution to the tubes as shown in Figure 6.11 The dark grey dots indicate the heat fluxes calculated by the entire furnace, while the light grey dots indicate Cut-B. In both simulation domains, all tubes are present. This is not the case for the simulation domain using Cut-A, shown by black filled dots. It does not embed all 43 tubes, instead only the first 15 tubes after the tube inlet are present. The total heat flux to the tubes using Cut-A and Cut-B are 6367.19 kW and 8635.45 kW respectively. In order to make a statement about the total heat flux transferred to all tubes using Cut-A, the results of the air-fired case, using the SFM,
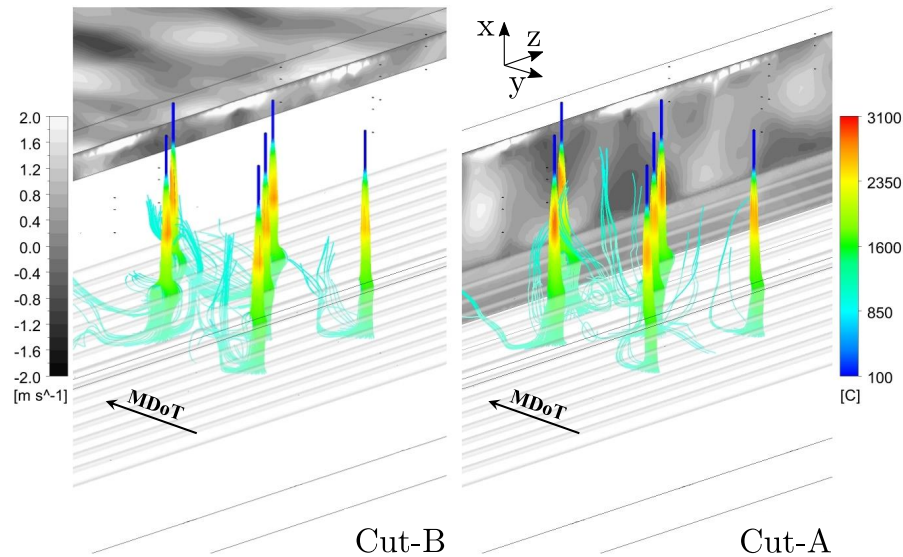
Figure 6.10.: The streamlines of several burners, coloured by temperature, additionally indicating the gas velocity in the tubes' moving direction MDoTs adapted from [5].

are used for the tubes positioned in the rear zone (tube number 16 to 43). These values are visualized as non-filled points. The total heat flux is thus increased by approximately 560 kW to a total of 6926.06 kW. In the case of the entire furnace, the total heat flux transferred to the
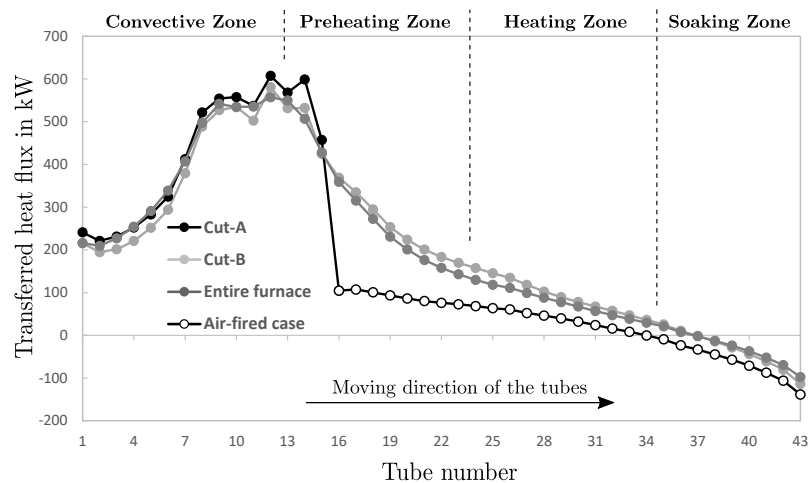
Figure 6.11.: Comparison of the total heat flux transferred to the tubes using Cut-A and Cut-B adapted from [5].

tubes is 8543.19 kW. This indicates only a marginal deviation, between the full geometry and Cut-B. This makes it clear, that the jet burners not only affect the tubes directly underneath, but they also have a clear effect on those further down, in the preheating- and heating zone. This is caused by local flows against the main gas flow direction. Thus, it can be stated that Cut-A is not sufficient to describe the whole furnace in detail. Here, the impeded backflow should be considered by a two-way coupled simulation of the air- and oxy-fired part. This would increase the computational effort drastically by several orders of magnitude. Whereas the difference in required computing time, between Cut-A and Cut-B, not even exceeding a day, is comparatively low. As a conclusion, Cut-B is used for further investigations of the present furnace, comparing different combustion mechanisms. The big advantage is the limitation to a

single additional simulation, needed to calculate the operation with the oxy-fuel burners, since all tubes are present.

6.2.3. Part 3 - Comparison of Cut-B Using SFM, EDM and EDC

In this section, three different combustion models, the SFM, EDM and EDC are used to characterize the furnace in all its detail. Here, the advantage of the divisions becomes obvious, since only a small domain has to be investigated. This allows to perform parametric studies and other investigations within shorter time frames. The performed simulations are based on the previous findings: (1) Using Cut-B to incorporate the retroactive effect on the tubes in the rear zones and (2) applying the results of the air-fired case, using the SFM model as boundary condition. The main focus is on the flame shape and temperature, as well as the species distribution and the correct calculation of the heat flux to the tubes. The results are compared to measurements, to validate the results. Afterwards the most suitable model is used to assess the tube heating, also comparing the results to measurements. In Figure 6.12, the calculated temperature distributions, in a plane, and local heat flux distribution, to some tubes, using the three models, are visualized. Here, clear deviations become obvious, regarding the flame shape. The SFM model shows a very pronounced ignition delay, leading to a very different flame shape, compared to the other models. However, the maximum flame temperature calculated seems plausible with 3141.9 °C. The calculation of the incorrect flame shape can be attributed to the low velocity difference, between the fuel and oxidizer. This results in low strain rates, affecting the scalar dissipation rate, which is, beside the mixture fraction, used to characterize chemistry during flamelet generation. The strain rate distribution, for a representative jet-burner, is visualized in Figure 6.13 and has already been described by Mayr et al. [246]. This means that for burner configurations, in which the inlet velocity, of fuel and oxidizer, is near to unity, this effect becomes decisive. Another big drawback, using the SFM model in either part, are the incorrect species set as boundary condition, at the cutting planes. This is due to the model itself, limiting the species calculation to the mixture fraction and its variance. Using different oxidants or fuels, the definition of the mixture fraction differs, as stated in the model description, shown in Eq. 2.33. Thus, using the same value for mixture fraction leads to a completely different species distribution, when used in the air-fired, as well as in the oxy-fired case. To clarify this, Table 6.4 visualizes the mean species concentration for some selected components, of the air-fired and oxy-fired cases, when using the same mixture fraction profile. The biggest difference is due to the neglection of the nitrogen in the oxidizer, by the oxy-fuel simulation. Consequently, the concentrations of carbon dioxide and water vapour increase slightly, while the oxygen concentration differs strongly. An ease of modification to obviate the high amount of oxygen at the boundary, could be the assumption of flue gas, based on total burn-out, at the boundary. Therefore, a constant mixture fraction ($f \sim 0.06$) has to be set at the cutting planes. Another concept, to avoid incorrect species distributions, would be the transformation of the calculated mixture fraction profile to the new mixture fraction definition. Either of these approaches neglect the nitrogen in the flue gas and thus, it would
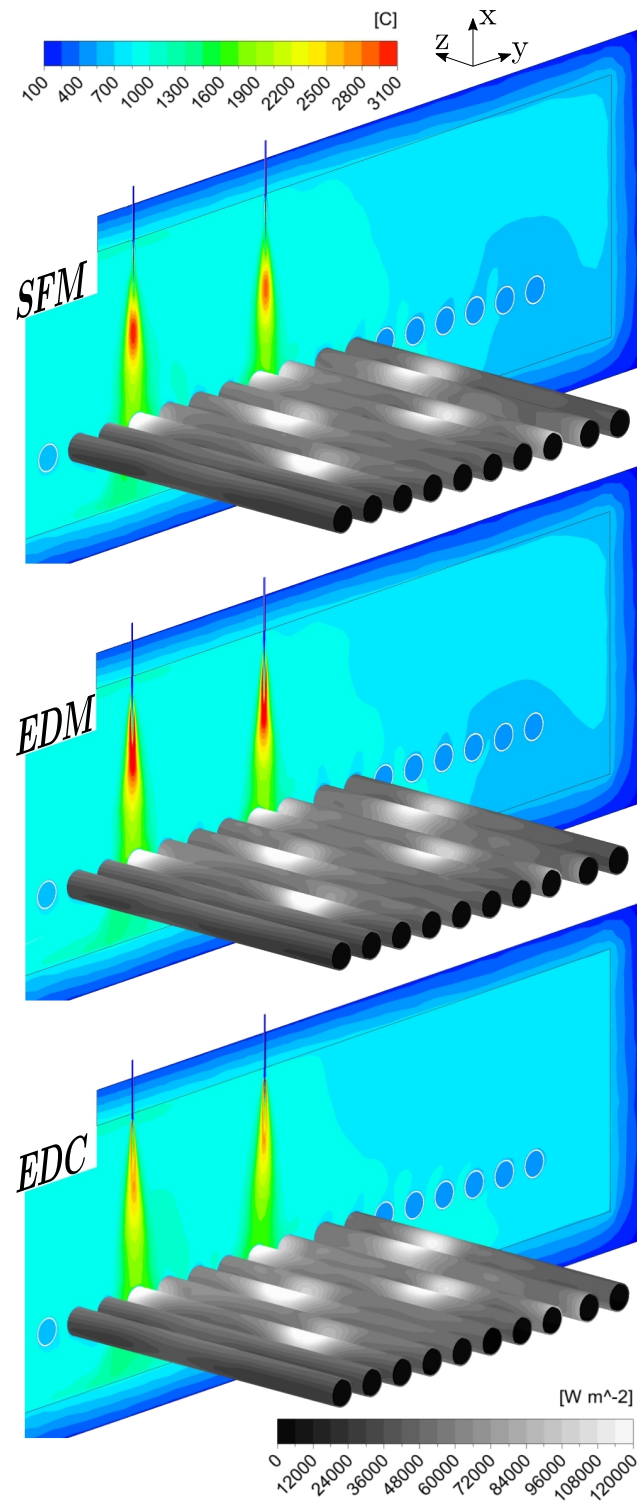
Figure 6.12.: Temperature distribution and resulting heat flux distribution on the tubes surfaces near the oxy-jet burner adapted from [5].

present an over-simplification of the given problem. To overcome this issue using the PDF approach in both parts, other models are available. These are the non-premixed combustion or partially premixed combustion models, calculated for equilibrium state. These can handle up to three streams, whereby the presented partitioning-approach is able to handle far more streams. However, the different concepts do not have any influence on the flame shape. Thus, the SFM
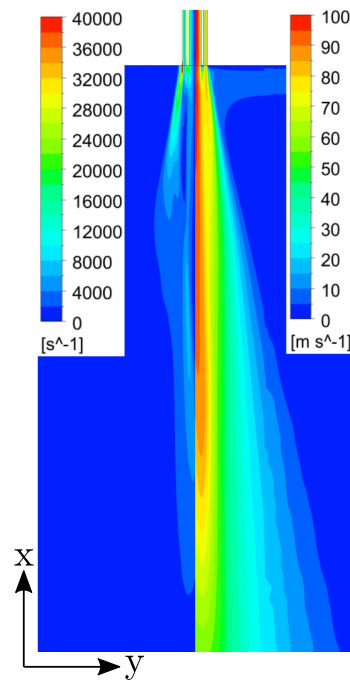
Figure 6.13.: Visualization of the velocity magnitude (right) and the strain rate (left) for a jet-burner using the SFM model adapted from [5].
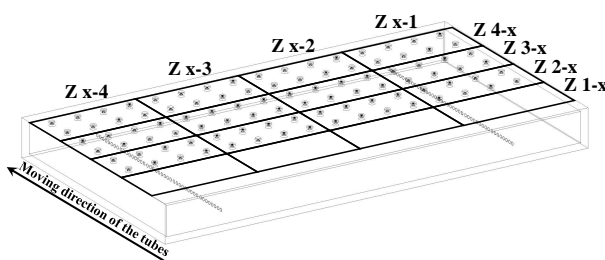
Table 6.4.: Comparison of some species at the boundary for the air-fired and oxy-fired case using the SFM model [5].

Species in mol/mol		
	Air-fired	Oxy-fired
O_2	2.778	67.233
CO_2	7.919	8.537
H_2O	15.694	17.061
N_2	66.452	0

is not advisable for the present burner condition. On the other hand, the EDM and EDC model show similar flame shapes, but differ in the maximum flame temperature calculated. The maximum flame temperature is significantly overestimated, using the EDM, with 3742.4 °C, while the EDC calculates a maximum of 3166.8 °C. Nevertheless, all three models show a similar temperature distribution within the combustion chamber, apart from the flames themselves. A high degree of accordance with measured data can be observed. This is visualized in Table 6.5, indicating the measured and calculated local temperatures, within each main-zone (Z i-x) and sub-zone (Z x-i). In each of these, a thermocouple is mounted at a height of 300 mm above the tubes, measuring the gas temperature. These are shielded to protect the measured results from any influences that are caused by radiation. The results reveal a maximum deviation of 28.4 °C using the SFM model, underestimating the measured temperature in Zone 2-2. Wherein, the EDM model calculates the highest deviation of 22.4 °C (Zone 3-4), which overestimates the temperature measured. These comparatively small deviations indicate the excellent suitability, of all presented models, to capture the condition of the furnace outside the reactive areas. Also the flame temperatures, in contact with the tubes' surfaces, of almost 1811 °C (EDM), is

Table 6.5.: The measured and calculated temperatures in °C at the position of the thermocouples [5].

	Measurement	SFM	EDM	EDC
Zone 1-1	901.4	903.1	920.2	907.7
Zone 1-2	821.1	804.3	817.6	831.5
Zone 1-3	841.8	832.8	836.8	843.9
Zone 1-4	971.7	954.5	971.8	967.7
Zone 2-1	957.2	938.2	953.6	948.2
Zone 2-2	953.5	925.1	953.4	939.0
Zone 2-3	941.9	931.3	938.3	938.8
Zone 2-4	971.2	970.2	959.2	961.0
Zone 3-1	954.2	952.2	957.7	951.0
Zone 3-2	942.5	946.5	949.4	941.6
Zone 3-3	940.2	926.2	931.5	939.2
Zone 3-4	955.2	947.8	977.6	931.4
Zone 4-1	945.9	922.2	938.7	929.6
Zone 4-2	939.0	911.7	923.3	919.0
Zone 4-3	935.6	909.5	936.8	927.7
Zone 4-4	942.5	921.1	939.6	924.1

very similar, with a maximum deviation of $\Delta = 50\,°\text{C}$ between the models. As a result, the local heat flux is of comparable magnitude, as shown by a grey distribution on the tubes surfaces. The maximum in specific heat flux, transferred to the tubes, is $183.37\,\text{kW/m}^2$, also calculated with the EDM model. The maximum deviation, found between the models, is small with $\Delta = 17.4\,\text{kW/m}^2$. This is underlined by Figure 6.14, indicating the total heat fluxes to each individual tube. An almost identical distribution is getting obvious, with a total heat flux of $8638.4\,\text{kW}$ using the SFM, $8635.5\,\text{kW}$ (EDM) and $8752.1\,\text{kW}$ (EDC).
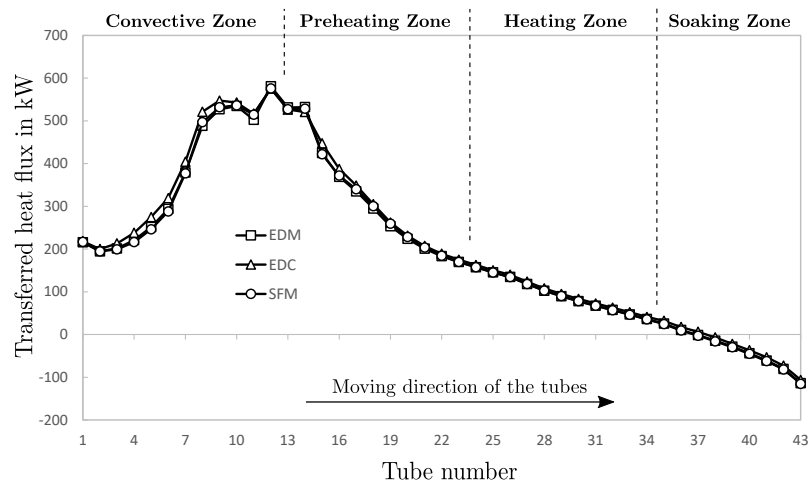
Figure 6.14.: The heat flux distribution to the individual tubes calculated with the SFM, EDM and EDC model adapted from [5].
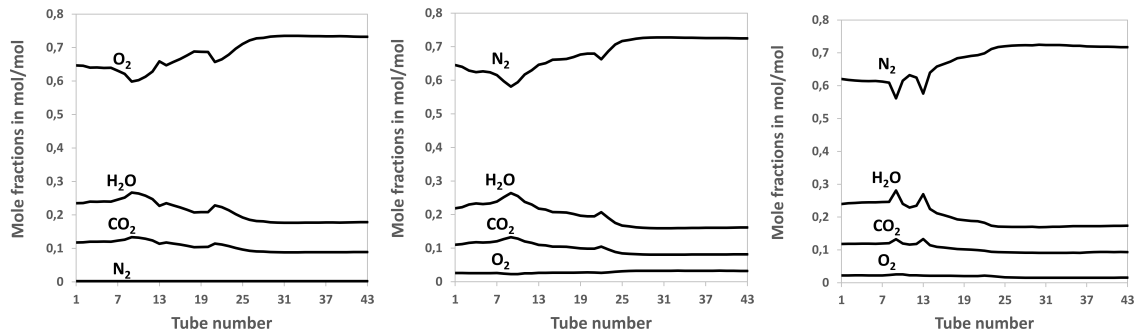
Figure 6.15.: Mean species distribution on the tubes surfaces calculated by the SFM (left), EDM (middle) and EDC (right) model adapted from [5].

This section unveiled a close agreement of the numerical results with measurements. Although the shape and maximum temperature of the flames show some deviations, the flame temperature impinging the tubes' surfaces is very similar in the CFD results. This leads to similar heat fluxes to the tubes, implying a similar heating characteristic of the tubes. Beside the evaluation of different combustion models, the overall approach of geometrical division, can be seen as validated. Thus, the presented model is an excellent alternative to the models used in literature, mostly based on full-size furnaces and often described in a transient manner. This model also allows to keep computational effort low and to optimize burner operation for each domain, which influences the heating characteristics of the steel. This means that various investigations can be performed within a reasonable time frame, even using more complex models. This is of great importance for operators, allowing a fast analysis of any kind of furnace and burner influences. The results of the steady state simulations shown within this section reveal a great consistency of the models regarding temperature and heat flux distribution. The heat flux to the tubes in particular is quite similar for all models. Thus, using all three model configurations for the iterative approach including the transient heating simulations, would not be worth the computational effort needed. However, as described before, the species distributions are clearly different in the combustion chamber using the SFM model, due to the boundary conditions set at the cutting planes. This has been evaluated for each of the three models and is shown in Figure 6.15, displaying the mean species for oxygen, carbon dioxide, water vapour and nitrogen, on the tubes surfaces. While the differences, between the EDM and EDC are minor, the SFM reveals a completely different behaviour.

Beside the correct calculation of the combustion process, including the heat distribution and species distribution, the computational effort needed is of significant relevance, to allow investigations within a reasonable time frame. To evaluate this, the computational demand has been evaluated for all three models, using the oxy-fired part for Cut-B. This is visualized in Table 6.6, which shows the averaged CPU requirements over 1000 iterations. All simulations were performed on an Intel i7 with a 6 core CPU and 64 GB RAM. It is getting apparent that the SFM and EDM model require almost the same wall clock time per iteration. Also the percentage breakdown to the individual sub-models, for flow, turbulence, species and radiation is very similar. As already shown in section 4.4, the number of iterations is also of importance,

when comparing the total computing time needed. Here again, the EDM needed about 1.5 times the iterations of the SFM, to reach the finally converged solution. Using the EDC model, two methods to perform chemistry integration are available: the direct integration (DI) and the in-situ adaptive tabulation (ISAT) method. These differ in the computational effort needed. Both are already discussed in detail in section 2.2.4 and should be summarized here briefly. The DI method is a very CPU intensive method, due to the iterative calculation of the stiff species differential equations. Whereby the ISAT method is very intensive in computer memory needed, which arises from continuous storing and reading of the generated look-up tables. These tables have to be cleared in certain times, to purge entries from the initial condition, demanding a periodical manual operation. Laubscher [156] investigated the impact of the mesh size on the computing time and RAM needed, using the EDC with DI, ISAT and an approach based on artificial neural networks. It is getting obvious, that the difference in calculation time, between the DI and ISAT method, increases linearly, leading to a longer calculation time using DI. On the other hand, the difference in RAM needed revealed an exponentially behaviour, for the benefit of the DI method. Thus, with increasing mesh sizes, the RAM requirements become decisive and the limiting step. This effect has been investigated by using the EDC model with

Table 6.6.: The computational effort needed for the SFM, EDM and EDC model [5].

		SFM	EDM	EDC (DI)	EDC (ISAT)
Time/IT	[s]	152.8	216.4	1049.3	1038.5
Distribution to the individual sub-models in %					
Flow model		23.78	21.26	3.08	2.89
Turbulence		8.94	6.92	0.90	0.90
Radiation		35.89	35.25	5.77	6.91
Enthalpy		11.30	-	-	-
PDF		20.09	-	-	-
Species		-	28.71	89.18	88.23
Temperature		-	7.48	1.07	1.08
Other		0.005	0.026	0.004	0.01

both DI and ISAT method. The results are also shown in Table 6.6. The significant benefit of the ISAT method [188] is not decisive in the present simulations. Both methods require almost the same wall clock time per iteration, revealing a very similar distribution to the individual sub-models. This can be attributed to the comparatively small reaction mechanism used, including solely 7 species. Bigger differences are to be expected using a detailed mechanism, such as the skeletal25. Thereby, additional decreases in computational effort can be achieved by dynamic mechanism reduction and chemistry agglomeration. For such small mechanisms, as used within this investigation, these options are not relevant. More important is the usage of the DI method, since the manual purging of the ISAT table, is omitted. Also the adaptation of the ISAT error tolerance influencing the final result, requiring to re-converge the result, can be prevented. Thus, the DI method is the more user-friendly one and easier to automate. Nevertheless, the EDC model, independent of the chemistry integration method used, needed significantly more time per iteration and further about ten times the iterations, needed by the SFM. This is also in accordance with the findings of the previous section 4.4. Thus, the EDC

stands out by several orders of magnitude, regarding the total computing time needed.

Taking into account all previous information, regarding the numerical results and accuracy, as well as the computational effort needed, the EDM model represents the right choice for the presented furnace. Although the temperature in the highly reactive area is too high, the influence on the heat flux to the tubes is negligible small. In order to validate this statement, the tube's temperature has been compared to measurements. Therefore, a tube equipped with four thermocouples has been traced through the furnace during constant operation. These are mounted at two positions (A and B), on the inner and outer surface of the tube, respectively. The position is marked by 1 (outer) and 2 (inner) in Figure 6.16. The numerical results indicate a high accordance with the measured data. As already shown in the previous chapter, radial heating is rapid. This leads to an insignificant temperature gradient over the tube wall thickness, solely operating with air-fired burners. The same behaviour can be seen during an operation with active oxy-burners.
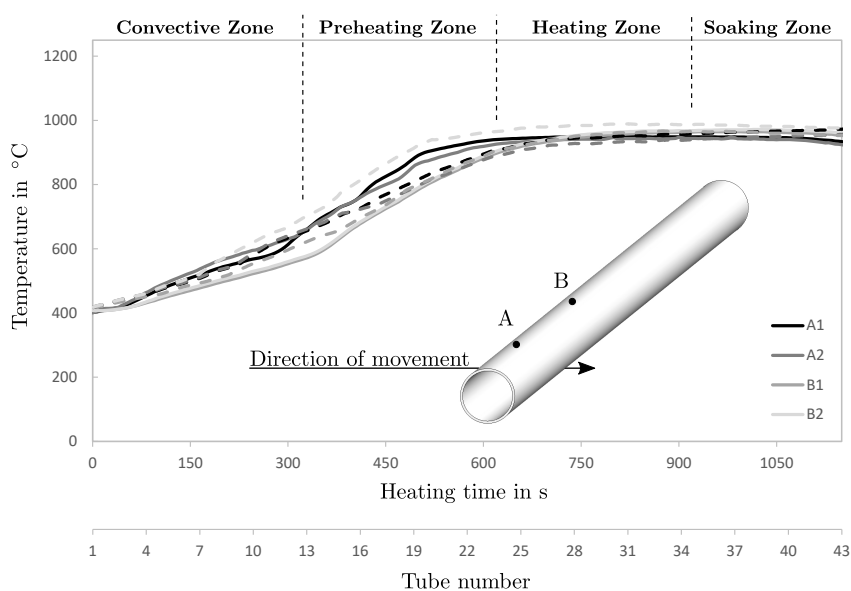
Figure 6.16.: Calculated (dashed line) and measured (solid line) temperature distribution in four distinctive points in the steel using the EDM model adapted from [5].

6.3. Discussion

The presented approach is based on the multi-block method, separating the whole domain (furnace) into several subdomains. Separation is done, so each subdomain is fired by a single oxidizer and fuel only. The main advantage of this method, is the avoidance of the limitations of a single turbulence-chemistry interaction model to be used. Thus, in each domain, the most suitable model can be applied. Moreover, improvements for each individual part, can be examined, keeping computational effort lower, compared to a geometrical full case. The main findings of this chapter are summarized below:

The methane-air fired part has been investigated using the SFM and EDM model. In the highly reactive areas the SFM revealed more plausible results, characterized by the flame temperature in the vicinity of the burner. The local peak temperatures, calculated by the EDM, are too high, wherein the SFM calculated more plausible values. This has a direct influence on the areas far apart from these highly reactive areas. This has been evaluated comparing the heat fluxes to the tubes, which is slightly increased for the EDM. It can be attributed to the increased radiative heat transfer. Nevertheless, both models are able to describe the whole furnace in detail, with a few restrictions, revealing minor differences.

In the second part, the influences of two different cutting-shapes, on the combustion process and heat flux distribution, have been evaluated. The simulations revealed a strong impact due to back-flows, which have been excluded in one investigation (Cut-A). Thus, it can be stated, that knowledge about the global flow inside the combustion chamber is helpful and necessary, in some extent, to set the cutting plane correctly.

The SFM, EDM and EDC model were used to calculate the methane-oxy fired part. The results showed the drawbacks of using the SFM for the oxy- fired part, in combination with the SFM used in the air-fired part. The restriction to one variable, used for species calculation, leads to significant differences in the transferred species distribution in the transmission planes. Moreover, the SFM model is not suitable for burners, with low strain rates, leading to an overstated delay of ignition. The EDM and EDC, using a global mechanism, describe the flame shape correctly. The EDM, however, over-predicts the peak flame temperature, while the EDC correspond with the results of the SFM. Although, the combustion models differ in the calculated results of the flames, the influences on tube heating can been classified as low. Equivalent local heat flux distributions lead to almost identical heating characteristics of the tubes. This shows a high consistency with the real behaviour of the real furnace, approved by measurements.

Concluding remarks, regarding the developed model, are the good accordance in measurements, as long as the main flow is from one subdomain to the next. With increasing amounts of backflows, the model will tend to compute incorrect results. This means, knowledge about the global flow inside the combustion chamber is helpful and necessary, to some extent, to set the cutting plane correctly. Setting the cutting planes in areas with reduced backflows is essential. For instance, inclinations of the furnace ceiling represent ideal areas. Further it can be stated, that there is no concrete answer to the initial question, whether a single numerical model exists to describe industrial furnaces. The simultaneous usage of different oxidizers and/or fuels forces to adjust the models, to represent the whole furnace in detail. The turbulence-chemistry interaction models particularly are limited in their usage and have a significant impact on the calculated solution. The presented model allows to overcome the limitations, allowing to use the same model for each zone, with some obstacles which have to be rectified in future investigations. Besides them, the chosen models, as used for turbulence (realizable k-ε) and radiation (DO), are perfectly suitable for almost any operating condition.

7

Industrial Rotary Hearth Furnace[1]

The present study investigates an iron bloom reheating furnace (RHF), that is used to continuously heat round cast blocks for further processing in the cross-roll piercing mill. Although investigations of RHFs are rare, some investigations can be found in literature. Similar to investigations into other reheating furnaces, models with varying complexity have been developed. Simpler models are based on the zonal method, apply constant wall temperatures and consider only the radiative heat transfer, allowing examinations to be carried out quickly [247, 248]. More complex models include both, fluid flow and radiative heat transfer [18, 21], while the most detailed models also include combustion [135]. Although these models are applicable for use on a steel reheating RHF, very few studies have actually been performed on such furnaces, so far. One of the first was that of Blanco et al. [249], who developed a mathematical model based on the zonal method. Their model is able to predict both, gas and billet temperature distribution, over the furnace length. Later, Mureşan et al. [250, 251] developed a numerical model to characterize billet heating in a real size RHF model, using MATLAB. Their data was then compared to an analytical solution, revealing very high consistency. One of the few publications on the numerical investigation of rotary hearth furnaces is that of DellaRocca et al. [252]. The authors pay particular attention to the flame length of the regenerative burner used. They found, that pairwise operation, in which one burner is active, while the other is inactive, sucking hot flue gas, can lead to serious trouble. Flames that are too long can result in the direct aspiration of the flame, leading the regenerative bed to overheat. Greater damage can also be expected with closer walls. In their study, flameless roof burners are mounted at the rear end of the furnace chamber, although their impact is not explicitly discussed. Another work investigated the results of switching from air-fuel to oxy-fuel burners in an industrial RHF [253]. It identifies a clear decrease in fuel consumption, with a simultaneous increase in reheating capacity.

The same model, based on the iterative scheme (section 2.3), as used for the investigations of the walking beam type reheating furnace, has been used to model the presented RHF. As mentioned before, any kind of furnace can be simulated based on this scheme. Only the way the heat flux profiles are modified has to be adapted to the present moving mechanism. Within

---

[1]Segments of this chapter have already been published in [4]
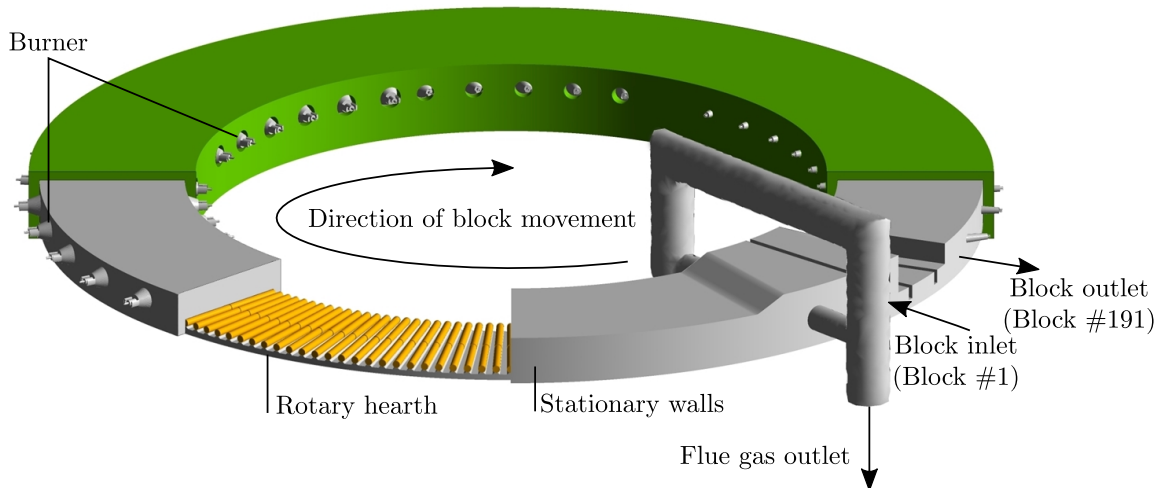
Figure 7.1.: The rotary hearth furnace adapted from [4].

the RHF, this is simpler than for the walking beam type furnace, which was investigated in the previous chapter. This is due to the restriction to a merely translative motion of the steel blocks. Special attention has to be paid to the different burner types installed. In particular the regenerative burner, installed in the front area of the furnace, may have to be treated carefully. This has again been evaluated in a simplified testcase, regarding only a single burner-pair (section 4.4). The results are presented in the next section. In the subsequent sections, the furnace construction and used boundary conditions are shown, pointing out some weaknesses. The results shown represent the final ones, which correspond to the numerical results gained in the last iterative loop. First, the steady state combustion simulation is explained in detail, subsequently the associated transient block heating simulation is shown.

7.1. Furnace Construction

The rotary hearth furnace is located at the beginning of the whole process. It is built to heat up round blocks, with a diameter of 0.23 m and varying lengths (up to 4 m), depending on the final tube length and wall thickness required. The billets enter the furnace with a temperature equal to the ambient conditions. At the furnace exit, a mean block temperature of 1200 °C shall be reached. For further processing, it is necessary that the blocks' core temperature is higher than its surface temperature. The furnace is limited to an usable hearth width of 4 m. It is capable of heating two shorter steel blocks (< 2 m) on each position. Apart from this geometric limitation, the furnace is confined to a maximum capacity of 110 t/h. However, the main limiting factor is not the furnace itself; it is the subsequent production line. The construction is completely different to that of the walking beam furnace. Instead of an elongated form, the base resembles a circular ring. Sometimes this represents a logistical challenge since the charging and discharging of these furnaces is at almost the same position on the circumference. Figure 7.1, showing the three-dimensional geometry of the furnace. A cut through the insulation (green)

and the combustion chamber of the furnace is shown, revealing the steel blocks, colored in orange.
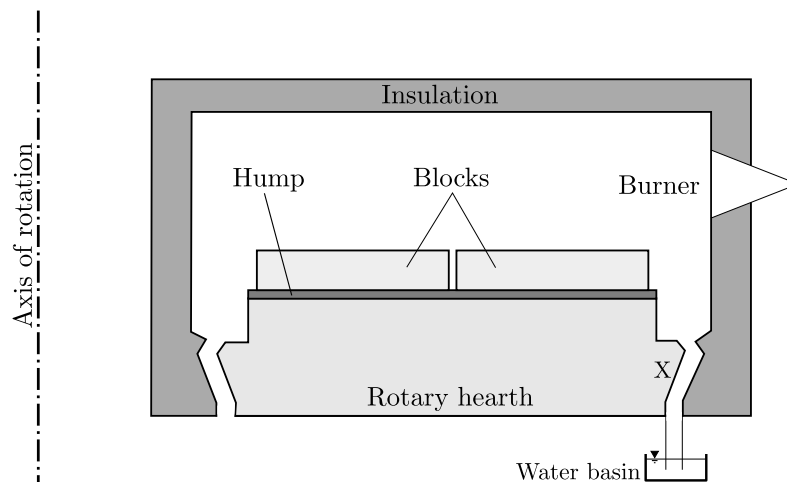
Figure 7.2.: Schematic illustration of the cross section of the rotary hearth furnace not in scale.

The combustion chamber has a mean diameter of 25 m and a hearth width of almost 4.5 m. It has a height of 1.2 m, which increases to a total height of 1.7 m near the exhaust gas channel. The blocks are charged via a gripper, lifting the blocks and placing them on a hump on the rotary hearth. The charging port is indicated on the right side of Figure 7.1. In the present configuration two steel blocks, with a length of 1.9 m each and a distance of 0.05 m from each other, are located on a single hump. After heating, the blocks are discharged just before the charging port. This means that each block performs almost a full rotation on the hearth. Between the entrance and exit doors the furnace ceiling is lowered to a height of 0.5 m. Two baffles ensure that an excessive draught of exhaust gases is embedded between the entry and exit area. An additional baffle in front of the exhaust gas channel forces the hot flue gas to exit via the flue gas outlet. This can also be seen at the rhs of Figure 7.1. This minimizes improper leakage of hot combustion gases through the steel inlet , increasing safety, and allowing for easier control. Special attention should be paid to the seal between the rotary hearth and the stationary furnace walls. This is indicated by an "X" in Figure 7.2, displaying a schematic representation of the furnace cross-section. On the outer and inner walls a gap between the rotary hearth and the wall is present. In the real furnace these are 100 mm wide, decreasing when the furnace expands in hot condition. At the lower part of this gap, rotating and static baffle plates are installed, dipping into a water basin. In the present furnace, the water temperature is controlled to a mean temperature of 30 °C. At high temperatures, special attention should be paid to this region, as damage to the seal results in leakage, which has a drastic affect on the furnace atmosphere. The presented furnace was built in the late 1970s and has often been the target of improvements. This also led to the introduction of a new heating zone. Nowadays, the furnace consists of 7 independent heating zones and an upstream convective zone, as visualized in Figure 7.3. A division into a preheating-, heating-, and soaking zone is hardly possible. The furnace rather consists of a convective zone, followed by three heating zones and four soaking zones, which can also be seen as heating zones.
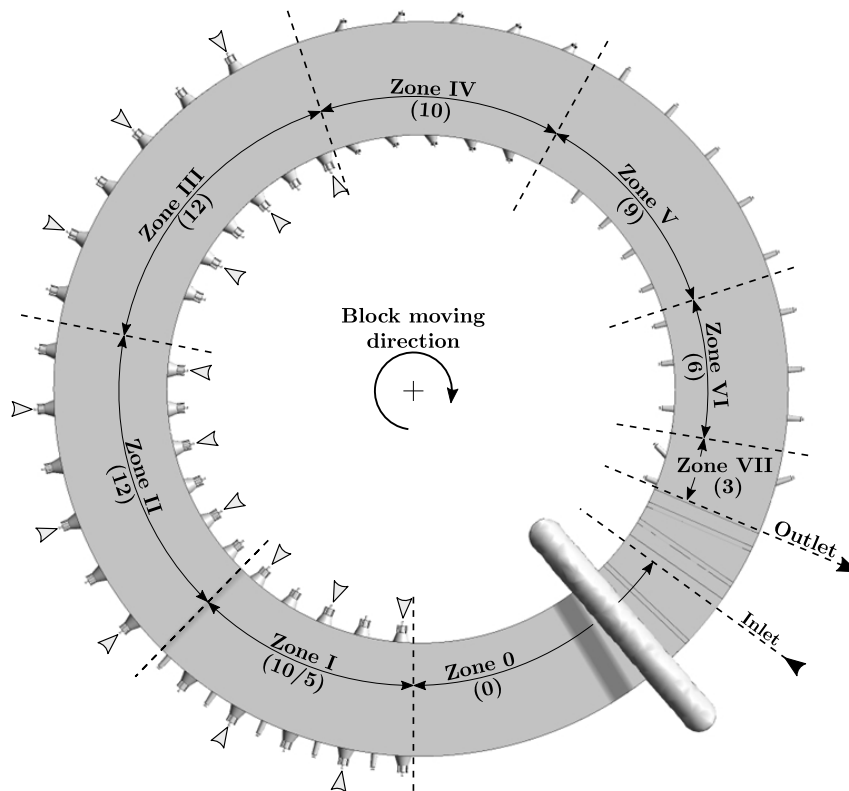
Figure 7.3.: Division of the furnace into the individual heating zones, block inlet and outlet, and active regenerative burner (adapted from [4]).

Each of these zones can be regulated separately to adjust the heating characteristics of the blocks. Additionally, different burner types are installed in the individual zones. In the first three heating zones, regenerative burners, with a maximum output of 1750 kW each, are installed. These are mounted in pairs, on the inner and outer side walls and are alternately active. Active burners are indicated in Figure 7.3 by small grey arrows. While one burner is active, the associated burner on the opposite wall, aspirates a part of the hot combustion gases, thereby heating up the ceramic packing material. Due to the furnace construction, a vacant burner place is present at the inner surface at the beginning of zone III. This in turn, leads to two adjacent inactive burners, located at the outer surface between zone II and zone III. This depicts a real condition and the consequences are shown later. The construction of the burner and accessories is also explained later, when discussing the occurring problems. The accessories, including the regenerative casing and packing material, are not taken into account in the simulations, due to the enormous numerical effort needed. In the simulations a constant temperature of 900 °C for preheated air, is assumed, which corresponds to the mean temperature during one active period. Five regenerative burner pairs are installed in zone I, while six pairs are mounted in zone II and III. Moreover, 5 conventional burners (max. 720 kW) are located on the outer side wall in zone I. These are mainly used to heat up the furnace. In the fourth zone, there are ten Low-NOx burners, which have a maximum output of 730 kW each. In zones V to VII, there are 9, 6 and 3 conventional burners, with maximum outputs of 650, 800 and 350 kW, respectively. These burners differ slightly from those found in zone I since different burner quarls, with a different number of air inlets, are used. In zone I, the burners

(a) Regenerative burner

(b) Low-NOx burner

(c) Conventional burner of zone I

(d) Conventional burner of zone V-VII
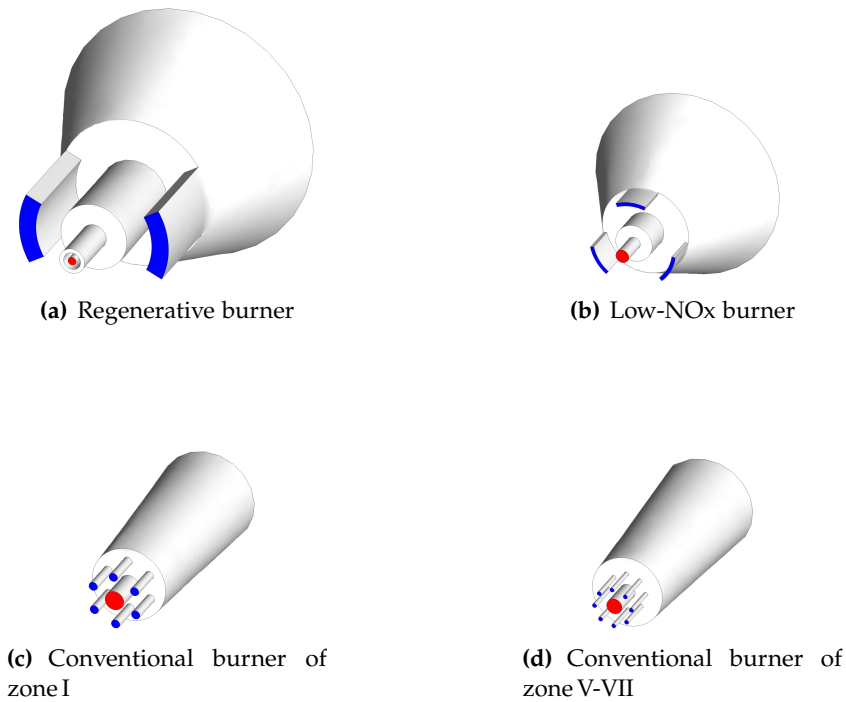
Figure 7.4.: Installed burner in the rotary hearth reheating furnace indicating the fuel (red) and air inlets (blue) adapted from [4].

have 6 air inlets, while the remaining zones have 8 air inlets per burner. All of the burner types are illustrated in Figure 7.4, in which the inlets for natural gas and air are indicated in red and blue, respectively. For the inactive regenerative burners, the air inlets shown are the corresponding flue gas outlets.

7.2. Full-Size Industrial Furnace

This section is divided into three parts, which will present the numerical results for the entire furnace. The first part will present the most important results of the stationary combustion simulation, representing one part of the iterative scheme. It focuses on the temperature and velocity distribution inside the combustion chamber. The temperature has been compared to measurements at the fuel gas outlet and results from fixed thermocouples inside the combustion chamber. Their accuracy is controlled in regular intervals. Within this simulation, the heat fluxes to the blocks are also of interest. The actual transient heating of the steel blocks is calculated in the second part of the iterative scheme. Here, all influences caused by the furnace's construction and burner arrangement on block temperature have been evaluated. Therefore, the calculated results are, similar to the walking beam type furnace, compared to a steel good, equipped with thermocouples, dragged through the furnace. Finally, the last part discusses two of the main problems in RHF furnaces as well as their main causes.

7.2.1. Stationary Combustion Simulation

In this section, the most important results of the stationary combustion simulation are presented, corresponding to those gained in the last iterative loop. The main focus, of this section, is on the impact of the burners on the temperature distribution inside the combustion chamber, as well as on the heat flux to the blocks. The computational grid is based on the same strategy, as the preliminary study of a single burner pair as shown in section 4.4, and consists of 11,707,036 cells. The boundary conditions are also similar, while all different burner types are incorporated in the numerical domain. The gas and air mass flow rates, used in the simulations, are displayed in Table 7.1. Zone I refers to the mass flow rates induced by the regenerative burner and conventional burner, located in this zone. The total methane induced is equivalent to 30.3 MW of fuel heat input. Additional 10.88 MW are supplied via the preheated air mass. It has to be distinguished between combustion air, used for the regenerative burner and other burner types. The air used by the regenerative burner is again 900 °C, while the air used by the Low-NOx and conventional burner is heated up to a temperature of 400 °C, with the downstream central heat exchanger. The three water-cooled baffles, were treated as walls, with a constant heat flux density, as their thermal boundary condition.

Table 7.1.: Mass flow boundary condition for each zone in kg/s [4].

	Fuel mass flow	Air mass flow
Zone I	0.2294	4.1346
Zone II	0.1897	4.0377
Zone III	0.1111	2.3260
Zone IV	0.0395	0.7858
Zone V	0.0098	0.2129
Zone VI	0.0132	0.2288
Zone VII	0.0133	0.2507
Total	0.6059	11.9764

Figure 7.5 shows the temperature distribution in a horizontal plane at burner height. This illustration also indicates the division into the individual heating zones, marked by black dashed lines, as well as the position of the block inlet and outlet. The lowest temperatures, of around 700 °C, occur in the first area after the steel entry, including the convective zone. Here, the preferred flow of the hot flue gas towards the outer opening of the flue gas channel becomes apparent. In zones I to III, the long flames of the active regenerative burner, marked by grey arrows, are clearly visible The alternating active burner arrangement and the slight deflection due to the flow, means that the flames clash in the centre, creating barriers for the global flue gas flow. Also the effect of the two adjacent inactive burners, located between zone II and III, can be seen. In zone IV, lower temperatures can be seen, since this plane does not intersect with the air inlets; thus only the flame borders are visible. In the downstream zones V to VII, the conventional burner create flames with different lengths, depending on their capacity. The burners in zone V have a total heat output of almost 500 kW, corresponding to nearly 8.5 % of the maximum possible output. In both, zone VI and VII, the total heat outputs
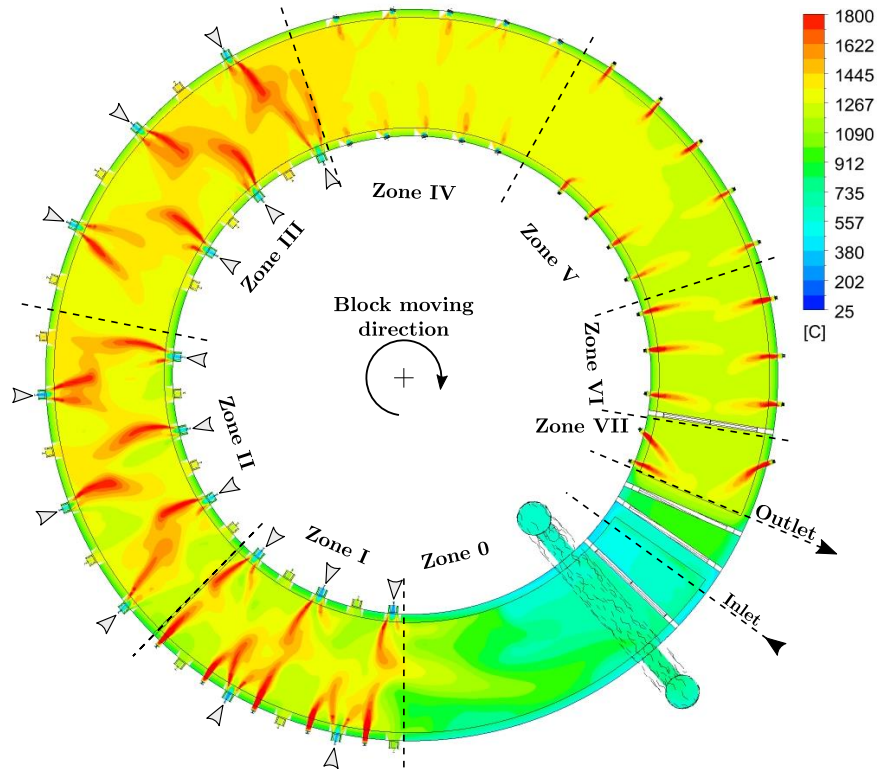
Figure 7.5.: Temperature distribution in a plane at the height of the burner adapted from [4].

are around 600 kW, corresponding to 14% and 63% of their maximum output. The low heat input in the rear zones (zones V-VII) results in a slight decrease in the gas temperature. This behaviour is clarified in Figure 7.6, where the flue gas temperature distribution along the mean circumference of the furnace is shown at the same height as depicted in Figure 7.5. The baffles are displayed in Figure 7.6 as vertical lines, separating the profile into four areas, indicated by circled numbers. The first section ① indicates the short path between the steel outlet and inlet. Here, it is possible to see that the temperature remains relatively constant at 1000 °C. This high temperature is primarily caused by the burners of zone VII, pressing the flue gas under the baffle. In the second section ②, another short path indicates the area between the steel inlet and the baffle before the flue gas channel. Here again, no large gradients can be identified: there is a mean temperature of 640 °C. In the subsequent section ③, which refers to the longest path, from the convective zone up to the end of zone VI, the temperature profile shows a clear increase in the convective zone. The strong fluctuations are caused by the regenerative burners, whose long flames extend to the evaluation line. The subsequent, much more uniform temperature distribution, represents the heating zones IV to VI. Here, a slight decrease in temperature becomes apparent. In the fourth section ④, which indicates zone VII, a slight increase in temperature due to the burners can be detected. The subsequent drop indicates the temperature distribution inside the insulation. To verify the simulations, the calculated results were compared with the mean zone temperatures, that were measured by several fixed mounted thermocouples, as can be seen in Figure 7.7. In each zone several thermocouples are mounted. These are spread over the entire width and zone length of the furnace and are positioned to, ideally, avoid influences due to the flames. In the simulations, the temperature
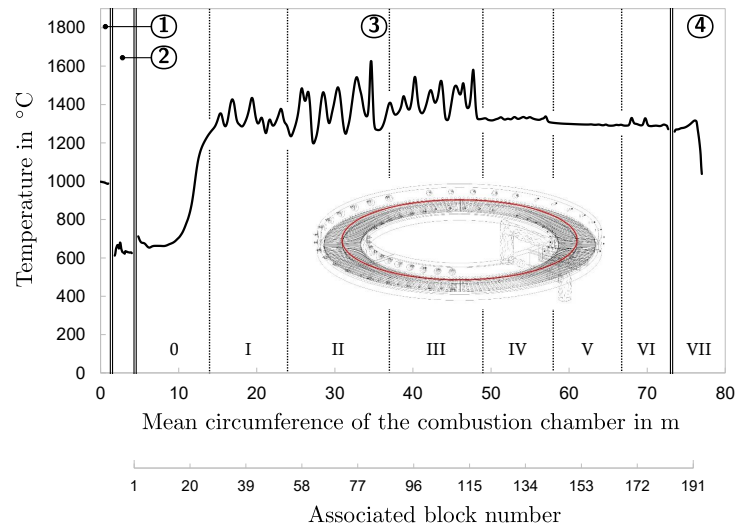
Figure 7.6.: Flue gas temperature distribution in a line about the mean circumference of the furnace, additionally indicating the heating zones 0-VII and baffles (black double line) dividing into the areas: ① Between steel inlet and outlet, ② Between steel inlet and flue gas channel, ③ Combustion chamber and ④ zone VII, adapted from [4].

in the same position has been used and averaged. The results reflect values averaged over all thermocouples in each individual zone. Thus, the results of the mean zone temperatures and the temperature profile, presented in Figure 7.6, can differ. No thermocouples are installed in the convective zone, excluding direct comparison. The remaining zones reflect very good agreement between the results of the numerical simulation and the measurement data. The maximum deviation was less than 20 °C. Table 7.2 presents and compares the calculated and measured flue gas temperature and its composition, at the flue gas outlet. In this context, particular attention was given to the correct execution of the measurements to avoid influences by leakage, radiation and convection. The deviation in calculated and measured temperatures, at the flue gas channel, is 25.4 °C, while the species are below 0.1 %. This very good agreement, between the results, proves the suitability of the numerical model used, including turbulence, combustion and radiation. In addition to the temperature inside the combustion chamber, the velocity distribution is of particular importance.
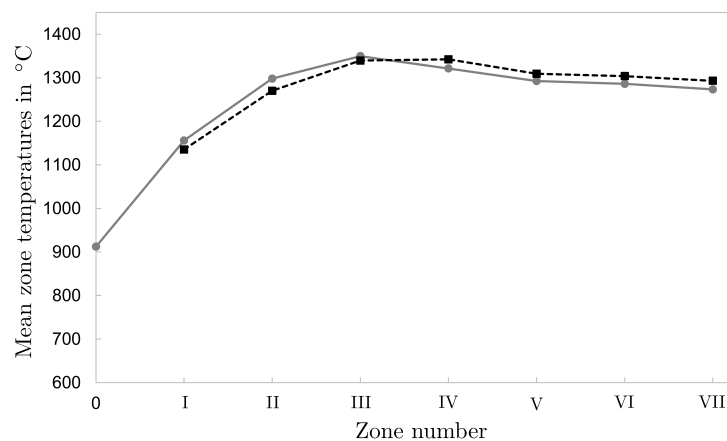
Figure 7.7.: Comparison of the calculated (grey dots) and measured (black dots) mean zone temperatures adapted from [4].
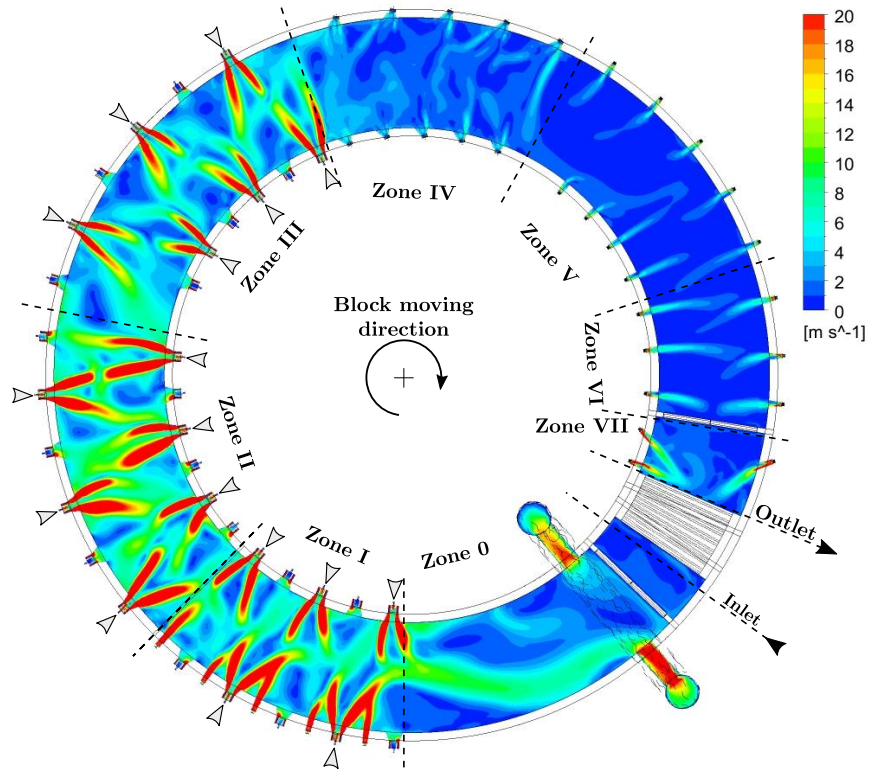
Figure 7.8.: Velocity magnitude in a plane at the height of the burner adapted from [4].

In Figure 7.8 the velocity distribution shows the high flame speeds in the vicinity of the burners. In particular, the regenerative burners exhibits high flame speeds. This suggests that the convective heat transfer is increased in this region. This effect is shown in Figure 7.9, which presents the total heat flux, including the radiative and convective parts, for each block. Looking at Figure 7.9, it is apparent that the radiative heat transport accounts for a large proportion of block heating. The convective heat transfer is high from the steel entry to the beginning of the first heating zone, but decreases slowly in zones II and III. In the last 4 zones the total transmitted heat flux is almost zero, which reflects the furnace's soaking zone. In this area, possible temperature imbalances, are homogenized. This is also necessary to gain the desired temperature variation over the block thickness and allows to gain a hotter core and colder surfaces.

Table 7.2.: Comparison of the calculated (CFD) and measured dry flue gas temperature and composition in mol/mol [4].

		CFD	Measurement
Temperature	$^{\circ}C$	746.9	721.5
O_2	10^{-2}	0.91	1.53
CO_2	10^{-2}	7.55	8.19
CO	10^{-2}	3.18	2.05
N_2	10^{-2}	88.36	88.23
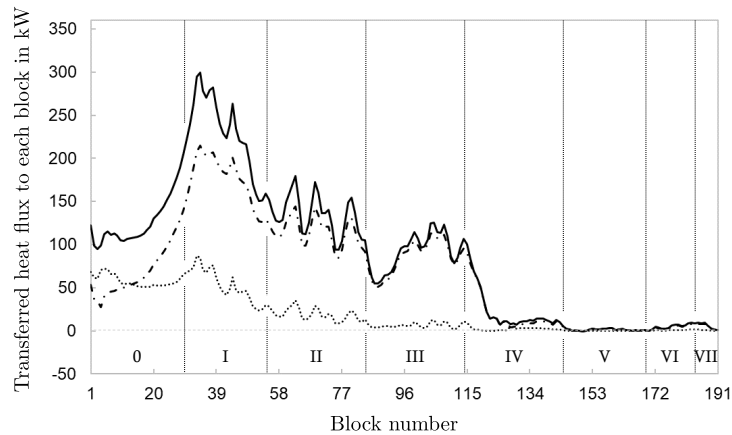
Figure 7.9.: Total incident heat flux (black solid line) indicating the radiative (black dot-dashed line) and convective part (black dotted line) for each block indicating the individual heating zones adapted from [4].

7.2.2. Transient Heating Simulation

This section shows the results of the second simulation of the iterative process: the transient simulation. These also correspond to the last iterative loop, representing the totally converged simulation. The results, presented in Figure 7.9, have a direct impact on the block temperature. This is shown in Figure 7.10, indicating the volume-averaged block temperature. Looking at this figure, it is clear that most of the block heating takes place in the zones I to III, as a result of the regenerative burners.
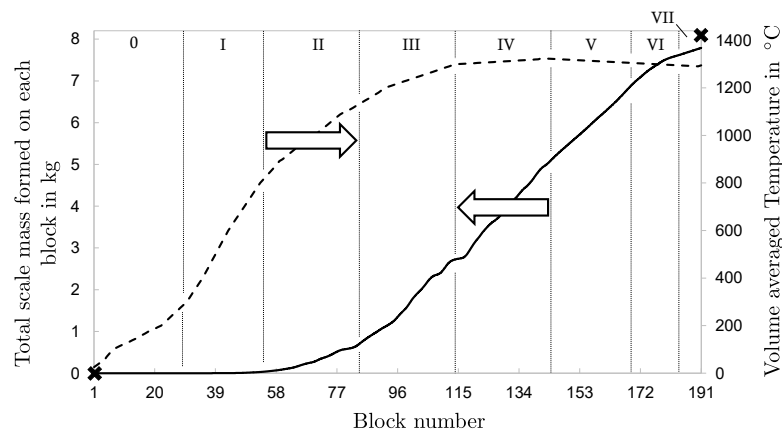
Figure 7.10.: Volume averaged block temperature (black dashed line), calculated scale formation (black solid line) and measured scale mass (black indicators) at the block inlet and outlet adapted from [4].

Figure 7.10 further indicates the scale mass formed during the heating of the blocks. For this, the model of Schluckner et al. [206] is applied to the transient simulation of the block heating. This scale formation model is identical to the model used in section 5.5. It calculates the local scale formation based on the blocks' surface temperature and surrounding atmosphere. Due to the operation of the furnace at elevated excess oxygen levels, the scale is expected to be very brittle and spall during the heating process. Thus, the insulating effect of the scale layer can be safely neglected. The calculated results indicate the scale formation to begin at block number 50, when the block surface temperature is about 750 °C. The formation generally follows a linear trend,

with some fluctuations caused by changes of the local atmospheric composition. At the end of the process, the simulation calculated 7.8 kg of scale to be formed per block. This matches the results of measurements on the real furnace, which found 8.1 kg of scale had formed, as visualized by a marker in Figure 7.10. This corresponds with the findings from section 5.5, indicating that slightly more scale is likely to form under measurements conditions, due to external influences. These include possible leakages which may suck in external atmosphere with higher oxygen content. This is not taken into account in the simulations since these strongly local effects are neither graspable nor quantifiable. The outer atmosphere also has a significant impact after the blocks exit the furnace. This causes further differences in the scale mass to be measured and the mass formed during the heating process. The numerical model is limited to combustion atmospheres, so conditions similar to the ambient atmosphere cannot be covered.
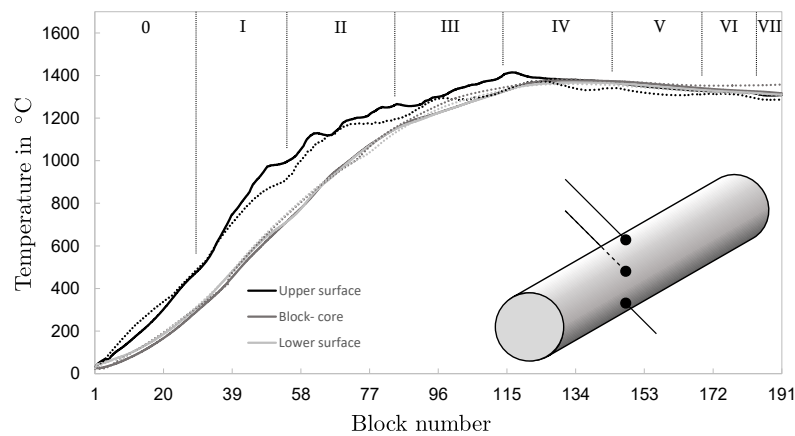
Figure 7.11.: Comparison of the numerical (solid line) and measured temperatures (dotted line) at three different points adapted from [4].

For further verification of the transient simulation, some thermocouples in the steel were traced through the furnace. These are centrally arranged above each other in block length which is positioned on the outer track of the rotary hearth. One is mounted slightly under the upper surface, preventing any radiative influences. Another is located in the core of the block and the last is mounted on the lower surface between block and hump. Their positions are sketched in Figure 7.11. Using an iterative scheme makes it possible to compare the local temperatures directly, with a very high temporal resolution. In Figure 7.11, it is possible to see that the results of this comparison prove the suitability of the present iterative model, due to the excellent agreement between the simulated and measured values. There are only very slight deviations between the temperatures in the core and on the lower surface of the block. However, the position on the upper surface measures slightly higher temperatures. The temperature difference is almost balanced at the center of the furnace. At the rear end, near the block outlet, the blocks temperature is homogenized, as indicated by the almost constant temperature of the thermocouple mounted in the block's core. This behaviour is further reflected in Figure 7.12, which presents the exiting block surface temperature (Block #191), as calculated by the transient simulation. The temperature distribution in a horizontal sectional plane is also shown, highlighting a slight cooling of the outer surface, at the rear end

of the furnace. The inner core of the block remains at a higher temperature, which is necessary for its subsequent processing. It also becomes clear that the blocks at the hearth's inner and outer sides present a nearly symmetrical image.
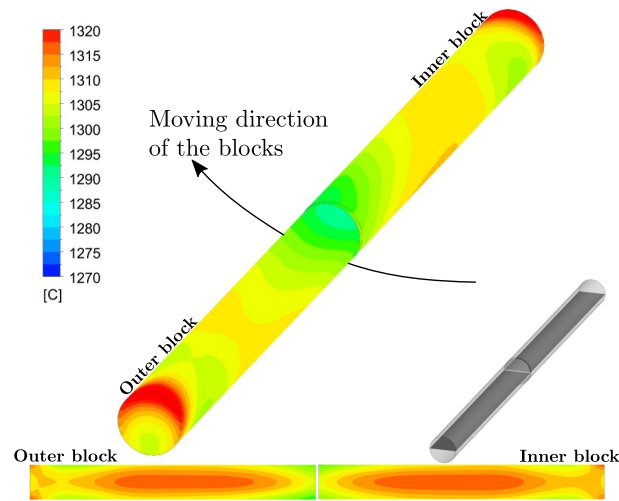
Figure 7.12.: Temperature distribution on the exiting block (#191) surfaces and in a sectional plane adapted from [4].

7.2.3. Problem Identification

This third section serves to point out the main problems with the current furnace design. Its main focus will be on identifying areas of high thermal stress, which may reduce the service life of the furnace, or require it to be repaired more often. In the worst case, an unplanned shutdown of the furnace may even become necessary. Given the costs of such scenarios, numerical simulations are very valuable to help preventing furnace inactivity. In this section,
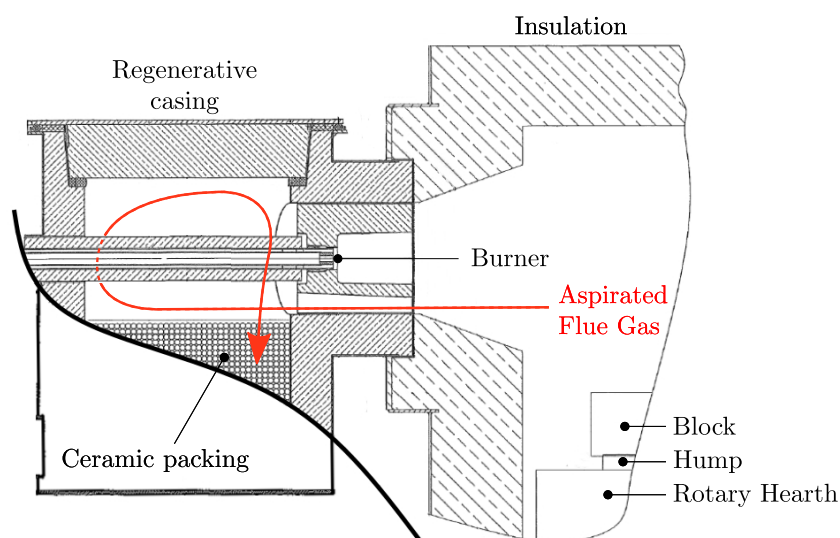
Figure 7.13.: Cut through a regenerative burner including its regenerative casing, which contains the ceramic packing material, some additional furnace details and a possible aspirated flue gas streamline (red arrow).

two of the main problems, typical for such types of reheating furnaces, were investigated. In the course of this, the advantage of the iterative scheme becomes clear once again. The separation into a stationary combustion simulation allowed us to embed a large degree of detail and high spatial resolution. This facilitated the detection and investigation into the causes for existing and emerging problem,s within the combustion chamber, within a reasonable timeframe.

The first problem to be investigated, is the excessive thermal load on the inner area of the regenerative casing of the regenerative burner. In this, the ceramic parts are located which are heated during the inactive period of the burner, aspirating hot flue gases, as visualized in Figure 7.13. It shows a cut through of a regenerative burner and its regenerative part, highlighting the main parts of the furnace construction. Also, the ceramic packaging materials, which are spherical in shape, are shown, increasing the total surface area. A possible streamline for the aspirated flue gas is indicated by a red arrow. The casing walls, as well as the ceramic parts, are designed to withstand high temperatures. Nevertheless, local damage occurs, indicating that higher temperatures than the zone's mean temperatures, must be aspirated. This can be seen in Figure 7.14, showing the inner body of an empty regenerative casing during annual maintenance. The big cracks indicate high thermal stresses which occur during operation. This effect has already been described by Malfa et al. [252], who questioned the use of regenerative burners in furnaces with such narrow combustion chambers. In the furnace considered within the present study the active burners, arranged opposite one another, prevent this behaviour. One burner is the exception to this, located between the second and third heating zones. In this

Figure 7.14.: Damage at the inner walls of a regenerative casing seen during annual shutdown.

area, a single regenerative burner on the inside is shifted by one position, resulting in a vacant place. This can be seen in Figure 7.3, on the inner wall of the furnace, between zones II and III. Thus, two inactive regenerative burners are adjacent to each other on the furnace's outer side. As can be seen in Figures 7.5 & 7.8, the adjacent active burners spread out more, causing the last

burner in zone II to aspirate flue gas at a very high temperature. This is visualized in Figure 7.15, which shows the inner wall temperature near the two inactive burners. The burners shown,
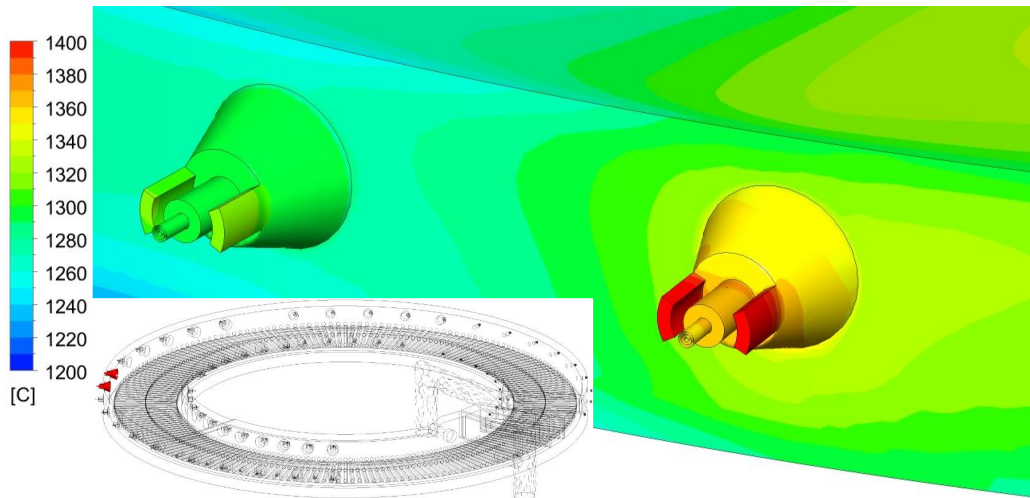
Figure 7.15.: Temperature distribution at the inner furnace wall at the 21st and 23rd regenerative burner adapted from [4].

aspirate flue gas at temperatures of approximately 1250 °C and 1330 °C, respectively. Both of these values are above the average flue gas temperature of 1200 °C, which leads to damage inside the recuperative part, as was determined by the furnace operator. This phenomenon could be prevented by adding a burner into the empty slot and adjusting the active/inactive burner. Otherwise, it would be wise to reduce the burner's load, thus shortening the flame length. The reduced heat input, caused by this change, could be compensated in the rear zones of the furnace, or by installing additional swirl burners, at the ceiling, as in the furnace investigated by [252].

The second major problem, that was identified, concerns the sealing area of the moving and stationary part of the furnace. In this lower region, the refractory material of the rotary hearth and outer furnace walls are exposed to high thermal stresses, this also affects the metal baffles mounted below, dipping into the water basin used for furnace sealing. Some severe damages to the refractory material and its steel fixings, which have been seen during the annual shutdown, are shown in Figure 7.16. These high-temperature resistant steel brackets are mounted on the rotary hearth and have been exposed to temperatures above 1200 °C for a long period of time. On the rotary hearth, all brackets reveal nearly the same damage pattern. On the other hand, the mountings on the stationary outer wall, revealed some more damages in the heating zone III. In this zone, even damages on the steel baffles dipping into the water basin were identified. It can be assumed, that the local flow pattern inside the combustion chamber forces hot flue gases down to the water basin. In this area, the steel baffles are deformed due to the thermal stress, forming another leak, allowing more gases to escape here. This increases thermal stresses in the whole area, accelerating wear and other thermal damages. This effect was subsequently investigated using numerical simulations. The temperature distribution and vertical velocity component were evaluated in the upper part of the sealing gap, which is marked by a dashed line on the rhs of Figure 7.16. As it was mentioned before, the thermal stresses are assumed to
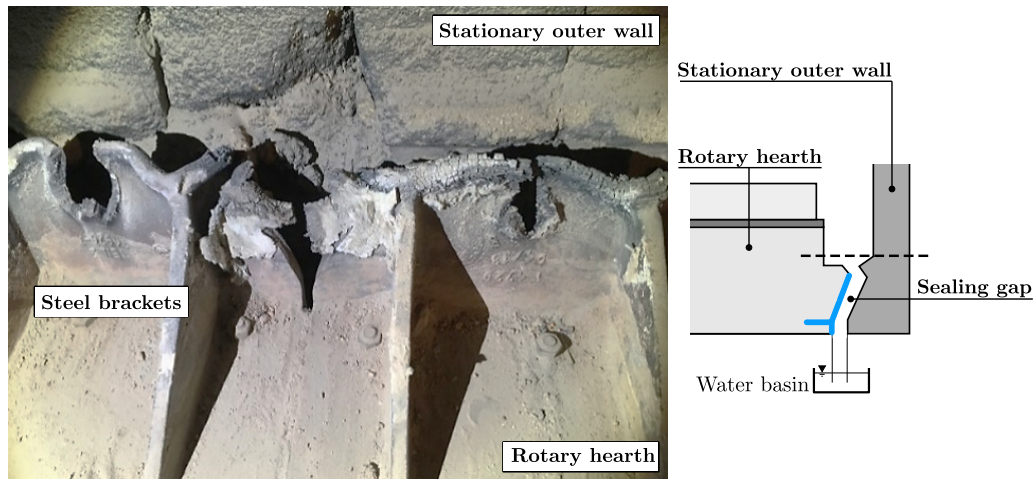
Figure 7.16.: Damage of the steel brackets near the furnace sealing highlighted by a blue line and the numerical evaluation line (dashed line).

be a combination of the flow pattern and high temperatures. Thus, the numerical results for temperature and the vertical velocity component, which presses the hot gasses downwards, are shown in Figure 7.17. This illustration reveals that the highest temperatures, of about 1350 °C, occur in the zones III to IV, exceeding the mean zone temperature. The maximum velocities , of nearly 0.3 m/s, occur in zone I to III, caused by the regenerative burners, located in these zones. Their long flames cause them to be deflected on the opposite wall, which again suggests, that regenerative burners are not ideal for the use in furnaces with such a narrow furnace width. For this burner type, to be used effectively in comparatively small combustion chambers, the furnace would require a more complex seal and the use of materials more resistant to high temperatures. Other burner types, such as those installed in zones IV to VII, do not produce such strong downward flow velocities.

(a)

(b)
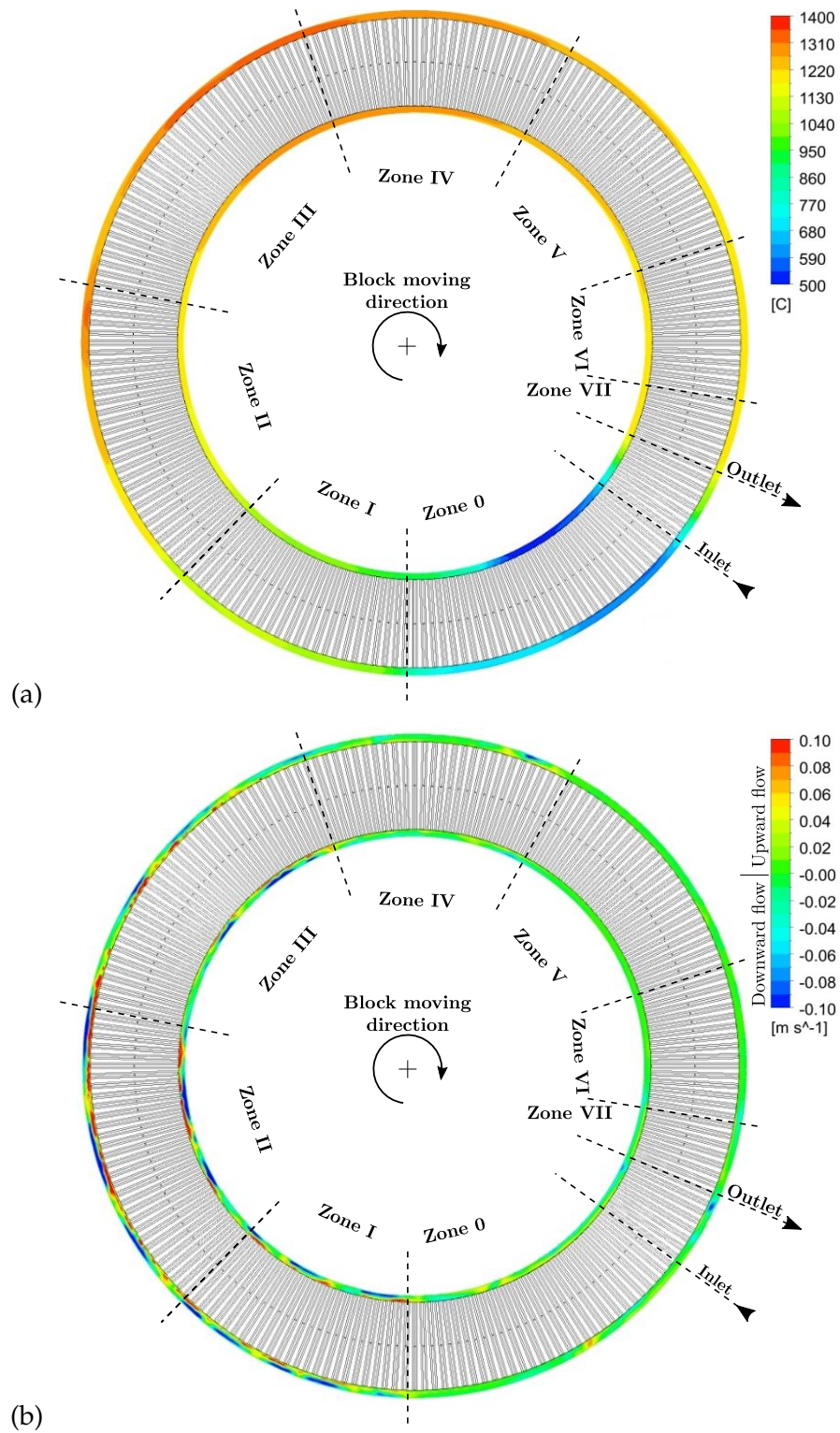
Figure 7.17.: Temperature distribution (a) and vertical velocity component distribution (b) in the sealing gap between the stationary outer walls and the rotary hearth adapted from [4].

7.3. Discussion

This chapter presented a computationally inexpensive numerical model, that is able to depict combustion in a rotary hearth reheating furnace for steel heating. Again, the iterative model has been applied, based on simulations for combustion in a steady state manner and a coupled transient consideration of the steel heating process. The successful implementation proves the suitability of this scheme for different kinds of furnaces. This type of furnaces has not yet been the subject of much scientific research. Thus, the present investigation provided a good overview of the behaviour of such furnaces, including the temperature- velocity- and species distribution. Additionally, the impact of different burner types, on their heating and flow characteristics, were examined. This could improve the understanding for their usage in different kind of furnaces. The main findings of the present study are summarized below.

On the one hand, the stationary combustion simulation calculated mean zone temperatures, with high accordance with measurements. Also the calculated and measured temperatures, at the flue gas exit, revealed minor differences about 25.4 °C. The species distribution showed only a deviation of 0.1 %. This model is, thus, an excellent choice to represent a real-size rotary hearth furnace in full detail and within a reasonable timeframe. Furthermore, the coupled transient heating simulation has been used to characterize the temporal heating of the blocks. The results were verified by tracking a block, equipped with thermocouples, through the furnace. The resulting data show only minor differences to the calculated results, which suggest that the heat flux distribution, inside the combustion, chamber was determined correctly. This allows to incorporate a scale formation model, similar to the investigations into the walking beam type reheating furnace. It describes the local and temporal formation with a high degree of accuracy, which has been compared to measurements on the real size furnace. Therefore, the weight of several steel blocks has been determined, revealing a difference to the calculated results of 0.3 kg ($<$4 %). The high accuracy, combined with the low computational effort needed, makes this model appropriate for researchers of similar topics and furnace operators, at the same time.

The origin of two main problems, in this furnace, were investigated. The first of these was the excessive thermal load on the inside walls of the regenerative casings. The second problem was the thermal stress on the sealing gap between the rotating hearth and static walls. In both cases, the regenerative burners, which produce long flames, are to blame. By reducing the load of these burners, the flame length can be reduced, thus, preventing the problems mentioned. It would then become necessary to compensated for the reduced thermal input in the middle and rear end of the furnace. It is important to ensure that the desired steel block surface cooling is still achieved in the rear end of the furnace. Another option would be to install several flat flame burners, providing the missing thermal input. Their influence on the sealing gap has yet to be examined, but would be interesting grounds for a future study. Moreover, the impact of different burner types, including flameless combustion, can improve efficiency of such furnaces and minimize thermal issues.

8 |

Conclusions

This thesis aimed to replicate two real-size industrial reheating furnaces using numerical CFD simulations. In the course of this various models have been developed and compared in terms of their complexity and accuracy. Measurements have been performed to obtain data for the model validation process. This led to the initial questions:

- What is the optimum degree of simplification ensuing a maximum degree of detail? Is reducing complexity even permissible? If yes - What is the most suitable model?
- What is the optimal measuring technique and is there an optimum number of measurement locations to allow reasonable validation?

First, a numerical model was developed and tested on simplified cases, considering a single burner. During creation of the burner geometry and mesh, it became obvious that a high degree of detail is absolutely necessary to capture the flame shape correctly. Considerable simplifications can disrupt flow with substantial implications on the flame and therefore on the heating characteristics of the whole furnace. In this connection, the right choice of numerical models is essential. Different turbulence-chemistry interaction and radiation models have been compared with regard to their applicability on the real-size application. Our focus was on their suitability to describe flame shape, temperature and species distribution. These have also been compared regarding their computational demand. It is found that the right choice of radiation model is essential to the consideration of reheating furnaces. Here, especially the optical regime of the flue gas is decisive, forcing to use the complex DO model. Having investigating several turbulence-chemistry interaction models, it became clear that the computational effort needed is generally the limiting factor in model selection. Differences by a factor of up to 100 in computing time can be detected between the individual models. In this context, the SFM stands out, requiring the least amount of time, while providing very detailed results. Thus, it represents the right choice for investigations of the present furnaces.

In the second step the numerical model has been adapted to capture the real behaviours of two real-size industrial reheating furnaces. To minimize computational effort, while guaranteeing a high degree of detail, a novel iterative scheme has been developed. In this, the complex combustion simulation is performed by a steady-state simulation, while a transient calculates the steel

heating process. Linkage is given by transferring the required values between the simulations. Special attention was paid to choosing the correct representation of the steel moving type for passing through the furnace since it affects heating characteristics significantly. The walking beam type reheating furnace had to be treated with caution to replicate the translatory and rotatory path of the steel tubes. In the numerical model this type of movement was integrated in an additional intermediate step between the simulations of the iterative scheme. MATLAB was used to modify the transferred results, empowered to include any moving scheme without affecting the actual simulations requiring only a marginal amount of time. Therefore, this iterative scheme features a very efficient way to reduce computational effort. Although using a very detailed mesh for both simulations, total calculation time to gain the final solution was about 2 weeks. An equivalent fully transient simulation would prolong computing time to months. Care was taken to prevent any loss of information and to represent both furnaces with a high degree of accuracy. This has been proven by comparing the calculated results to measurements performed at the real furnaces. For this, the conditions within the combustion chamber and of the steel have been evaluated. In both cases, thermocouples represent a good option to depict temperatures at specific points. Inside the furnace, prudent location may allow to capture any inhomogeneous temperature distributions and allow for a quick response to overcome them. Their usage to capture steel temperatures is more sophisticated. A test tube was equipped with several thermocouples and traced through the furnace to permit a statement about temporal heating at distinctive points. A detailed predication about the exact temperature distribution is not possible. For this, the surface temperature of the exiting steel has been measured, using a pyrometer and an infrared camera, IC. The IC in particular revealed reasonable and reliable results, while the pyrometer exposed some device-dependent discrepancies. The deviations between all three measuring techniques are nevertheless in a close harmony. This means that all measuring devices are able to capture some of the effects of steel temperature. In reheating furnaces, both, the temporal change and spatial temperature of the steel are of significance. Thus, the usage of thermocouples and an IC is highly recommended.

Another great advantage of the computational efficiency of the iterative scheme and the numerical models chosen, is the possible integration of expansions to the model. Within this thesis, a scale formation model has been developed. Compared to any other model to be found in literature, this model is able to calculate a spatially highly resolved scale layer. The formation kinetics is thereby described in terms of dependency on local steel surface temperatures and atmospheric conditions of the surrounding gases. The results are compared to analytical methods and measurements, both proving high concordance. A clear relationship between the steel temperature and residence time within the furnaces on the scale mass can be demonstrated. Thus, influences due to local varying species concentrations on scale formation and thermal resistance of the thin layer can be considered as marginal.

In future works, investigations for further reduction of computational effort should be striven for, allowing faster investigations of furnace behaviours and examinations in respect to problem identification and prevention, as well as, performance improvements. Therefore, computation-

ally inexpensive models to incorporate different oxidizers and fuels within a single simulation should be developed since these provide the basis for future increases in efficiency of the thermal processes. The aim should be to develop a model with high accuracy, including a detailed reaction mechanism with minimum computing time needed.

A

Reaction kinetics

A.1. Skeletal Reaction mechanism

Table A.1.: The skeletal25 reaction mechanism [117]

No.	Reaction	k in $mole/cm^3s$	b	E_A in $cal/mole$
1.	$H + O_2 \rightleftharpoons O + OH$	2.00×10^{14}	0	16800
2.	$O + OH \rightharpoonup O_2 + H$	1.58×10^{13}	0	690
3.	$O + H_2 \rightharpoonup OH + H$	1.80×10^{10}	1	8826
4.	$OH + H \rightleftharpoons O + H_2$	8.00×10^{09}	1	6760
5.	$H_2 + OH \rightleftharpoons H_2O + H$	1.17×10^{09}	1.3	3626
6.	$H_2O + H \rightleftharpoons H_2 + OH$	5.09×10^{09}	1.3	18588
7.	$OH + OH \rightleftharpoons H_2O + O$	6.00×10^{08}	1.3	0
8.	$H_2O + O \rightleftharpoons OH + OH$	5.90×10^{09}	1.3	17029
9.	$H + O_2 + M \rightleftharpoons HO_2 + M$	2.30×10^{18}	-0.8	0
	$CH_4/6.5/H_2O/6.5/CO_2/1.5/CO/0.75/O_2/0.4/N_2/0.4/$			
10.	$H + HO_2 \rightleftharpoons OH + OH$	1.50×10^{14}	0	1004
11.	$H + HO_2 \rightleftharpoons H_2 + O_2$	2.50×10^{13}	0	700
12.	$OH + HO_2 \rightleftharpoons H_2O + O_2$	2.00×10^{13}	0	1000
13.	$CO + OH \rightleftharpoons CO_2 + H$	1.51×10^{07}	1.3	-758
14.	$CO_2 + H \rightleftharpoons CO + OH$	1.57×10^{09}	1.3	22337
15.	$CH_4 \rightleftharpoons CH_3 + H$	2.30×10^{38}	-7	114360
16.	$CH_3 + H \rightleftharpoons CH_4$	1.90×10^{36}	-7	9050
17.	$CH_4 + H \rightleftharpoons CH_3 + H_2$	2.20×10^{04}	3	8750
18.	$CH_3 + H_2 \rightleftharpoons CH_4 + H$	9.57×10^{02}	3	8750
19.	$CH_4 + OH \rightleftharpoons CH_3 + H_2O$	1.60×10^{06}	2.1	2460
20.	$CH_3 + H_2O \rightleftharpoons CH_4 + OH$	3.02×10^{05}	2.1	17422
21.	$CH_3 + O \rightleftharpoons CH_2O + H$	6.80×10^{13}	0	0
22.	$CH_2O + H \rightleftharpoons HCO + H_2$	2.50×10^{13}	0	3991
23.	$CH_2O + OH \rightleftharpoons HCO + H_2O$	3.00×10^{13}	0	1195
24.	$HCO + H \rightleftharpoons CO + H_2$	4.00×10^{13}	0	0
25.	$HCO + M \rightleftharpoons CO + H + M$	6.00×10^{14}	0	14700
	$CH_4/6.5/H_2O/6.5/CO_2/1.5/CO/0.75/O_2/0.4/N_2/0.4/$			
26.	$CH_3 + O_2 \rightleftharpoons CH_3O + O$	7.00×10^{12}	0	25652
27.	$CH_3O + H \rightleftharpoons CH_2O + H_2$	2.00×10^{13}	0	0
28.	$CH_3O + M \rightleftharpoons CH_2O + H + M$	2.40×10^{13}	0	28812
	$CH_4/6.5/H_2O/6.5/CO_2/1.5/CO/0.75/O_2/0.4/N_2/0.4/$			

29.	$HO_2 + HO_2 \rightleftharpoons H_2O_2 + O_2$	2.00×10^{12}	0	0
30.	$H_2O_2 + M \rightleftharpoons OH + OH + M$	1.3×10^{17}	0	45500
	$CH_4/6.5/H_2O/6.5/CO_2/1.5/CO/0.75/O_2/0.4/N_2/0.4/$			
31.	$OH + OH \rightleftharpoons H_2O_2 + M$	9.86×10^{14}	0	-5070
	$CH_4/6.5/H_2O/6.5/CO_2/1.5/CO/0.75/O_2/0.4/N_2/0.4/$			
32.	$H_2O_2 + OH \rightleftharpoons H_2O + HO_2$	1.00×10^{13}	0	1800
33.	$H_2O + HO_2 \rightleftharpoons H_2O_2 + OH$	2.86×10^{13}	0	32790
34.	$OH + H + M \rightleftharpoons H_2O + M$	2.20×10^{22}	-2	0
	$CH_4/6.5/H_2O/6.5/CO_2/1.5/CO/0.75/O_2/0.4/N_2/0.4/$			
35.	$H + H + M \rightleftharpoons H_2 + M$	1.80×10^{18}	$0-1$	0
	$CH_4/6.5/H_2O/6.5/CO_2/1.5/CO/0.75/O_2/0.4/N_2/0.4/$			

B

Numerical Settings

B.1. Flamelet and PDF settings

Table B.1.: The settings used for the flamelet and PDF calculation.

Flamelet Parameter	
Number of Grid Points in Flamelet	40
Maximum number of Flamelets	40
Initial Scalar Dissipation ($1/s$)	0.01
Scalar Dissipation Multiplier	10
Scalar Dissipation Step ($1/s$)	5
Table Parameter	
Number of Mean Mixture Fraction Points	40
Number of Mixture Fraction Variance Points	40
Maximum Number of Species	20
Number of Mean Enthalpy Points	41
Minimum Temperature(K)	298

B.2. Under-Relaxation Factors

Table B.2.: The Under-Relaxation Factors used.

Pressure	0.7
Density	0.7
Body Forces	0.7
Momentum	0.3
Turbulent kinetic Energy	0.7
Turbulent Dissipation Rate	0.7
Turbulent Viscosity	0.7
Energy	0.95
Temperature	0.95
Mean Mixture Fraction	1
Mixture Fraction Variance	1

B.3. Spatial Discretization

Table B.3.: Spatial Discretization settings used.

Gradient	Least Squares Cell Based
Pressure	PRESTO!
Momentum	Second Order Upwind
Turbulent kinetic Energy	Second Order Upwind
Turbulent Dissipation Rate	Second Order Upwind
Energy	Second Order Upwind
Mean Mixture Fraction	Second Order Upwind
Mixture Fraction Variance	Second Order Upwind

C

Settings for the radiation models

C.1. Discrete ordinates (DO)

Table C.1.: Settings used for the DO radiation model.

Energy Iterations per Radiation Iteration	10
Number of bands	0
Solar load	off
Angular Discretization	
Theta Divisions	4
Phi Divisions	4
Theta Pixels	3
Phi Pixels	3

C.2. P1

Table C.2.: Settings used for the P1 radiation model.

Number of bands	0
Solar load	off

C.3. Surface to surface (S2S)

Table C.3.: Settings used for the S2S radiation model.

Energy Iterations per Radiation Iteration	10
Maximum number of Radiation Iterations	5
Residual Convergence Criteria	0.001
Solar load	off

Table C.4.: Settings used for View factor calculation and Clustering.

Clustering	Manual
Faces per Surface Cluster for Flow Boundary Zones	1
View Factor Basis	Face to Face
View Factor Method	Ray Tracing
View Factor Parameter Resolution	10
Zones Participating in View Factor Calculation	all

Bibliography

[1] M. Landfahrer, R. Prieler, B. Mayr, et al. Development of a numerically efficient CFD model to predict transient temperature distribution of mother tubes moving translative and rotative through a gas fired furnace. *Applied Thermal Engineering*, **123** (2017): 290–300.

[2] M. Landfahrer, R. Prieler, B. Mayr, et al. Characterization of the temperature distribution on steel tubes for different operating conditions in a reheating furnace using CFD and three different measuring methods. *Applied Thermal Engineering*, **133** (2018): 39–48.

[3] M. Landfahrer, C. Schluckner, R. Prieler, et al. Numerical and experimental investigation of scale formation on steel tubes in a real-size reheating furnace. *International Journal of Heat and Mass Transfer*, **129** (2019): 460–467.

[4] M. Landfahrer, C. Schluckner, R. Prieler, et al. Development and application of a numerically efficient model describing a rotary hearth furnace using CFD. *Energy*, **180** (2019): 79–89.

[5] M. Landfahrer, C. Schluckner, H. Gerhardter, et al. Numerical model incorporating different oxidizer in a reheating furnace fired with natural gas. *Fuel*, **268** (2020): 117185.

[6] W. Trinks and W. Trinks, eds. Industrial furnaces. 6th ed. Hoboken, N.J: J. Wiley, 2004.

[7] P. Mullinger and B. Jenkins. Industrial and process furnaces: principles, design and operation. 2nd ed. Kidlington, Oxford: Butterworth-Heinemann is an imprint of Elsevier, 2014.

[8] "Continuous Steel reheating Furnaces Specification, Design and Equipment." In: The Energy Technology Support Unit (ETSU), 1994.

[9] Y.-L. Wu, Z.-Y. Jiang, X.-X. Zhang, et al. Process optimization of metallurgical dust recycling by direct reduction in rotary hearth furnace. *Powder Technology*, **326** (2018): 101–113.

[10] Y. Liu, F.-Y. Su, Z. Wen, et al. CFD Modeling of Flow, Temperature, and Concentration Fields in a Pilot-Scale Rotary Hearth Furnace. *Metallurgical and Materials Transactions B*, **45** (2014): 251–261.

[11] I. Sohn and R. J. Fruehan. The reduction of iron oxides by volatiles in a rotary hearth furnace process: Part I. The role and kinetics of volatile reduction. en. *Metallurgical and Materials Transactions B*, **36** (2005): 605–612.

[12] P. Yuan, B. Shen, D. Duan, et al. Study on the formation of direct reduced iron by using biomass as reductants of carbon containing pellets in RHF process. *Energy*, **141** (2017): 472–482.

[13] B. Mayr, R. Prieler, M. Demuth, et al. Modelling of high temperature furnaces under air-fuel and oxygen enriched conditions. *Applied Thermal Engineering*, **136** (2018): 492–503.

[14] D. Chen, B. Lu, F. Dai, et al. Bottleneck of slab thermal efficiency in reheating furnace based on energy apportionment model. *Energy*, **150** (2018): 1058–1069.

[15] Y. Hu, C. Tan, J. Broughton, et al. Model-based multi-objective optimisation of reheating furnace operations using genetic algorithm. *Energy Procedia*, **142** (2017): 2143–2151.

[16] M. Y. Kim. A heat transfer model for the analysis of transient heating of the slab in a direct-fired walking beam type reheating furnace. *International Journal of Heat and Mass Transfer*, **50** (2007): 3740–3748.

[17] S. H. Han, D. Chang, and C. Huh. Efficiency analysis of radiative slab heating in a walking-beam-type reheating furnace. *Energy*, **36** (2011): 1265–1272.

[18] A. Emadi, A. Saboonchi, M. Taheri, et al. Heating characteristics of billet in a walking hearth type reheating furnace. *Applied Thermal Engineering*, **63** (2014): 396–405.

[19] V. I. Lebedev and V. A. Sokolov. Study of the convection component of complex heat exchange in a model of a direct-heating furnace. *Glass and Ceramics*, **33** (1976): 352–354.

[20] V. K. Singh, P. Talukdar, and P. J. Coelho. Performance Evaluation of Two Heat Transfer Models of a Walking Beam Type Reheat Furnace. *Heat Transfer Engineering*, **36** (2015): 91–101.

[21] V. K. Singh and P. Talukdar. Comparisons of different heat transfer models of a walking beam type reheat furnace. *International Communications in Heat and Mass Transfer*, **47** (2013): 20–26.

[22] J. G. Kim and K. Y. Huh. Prediction of Transient Slab Temperature Distribution in the Re-heating Furnace of a Walking-beam Type for Rolling of Steel Slabs. *ISIJ International*, **40** (2000): 1115–1123.

[23] S. H. Han, S. W. Baek, S. H. Kang, et al. Numerical analysis of heating characteristics of a slab in a bench scale reheating furnace. *International Journal of Heat and Mass Transfer*, **50** (2007): 2019–2023.

[24] S. H. Han, D. Chang, and C. Y. Kim. A numerical analysis of slab heating characteristics in a walking beam type reheating furnace. *International Journal of Heat and Mass Transfer*, **53** (2010): 3855–3861.

[25] C.-T. Hsieh, M.-J. Huang, S.-T. Lee, et al. Numerical Modeling of a Walking-Beam-Type Slab Reheating Furnace. *Numerical Heat Transfer, Part A: Applications*, **53** (2008): 966–981.

[26] J. M. Casal, J. Porteiro, J. L. Míguez, et al. New methodology for CFD three-dimensional simulation of a walking beam type reheating furnace in steady state. *Applied Thermal Engineering*, **86** (2015): 69–80.

[27] V. Cuervo-Piñera, D. Cifrián-Riesgo, P.-D. Nguyen, et al. Blast Furnace Gas Based Combustion Systems in Steel Reheating Furnaces. *Energy Procedia*, **120** (2017): 357–364.

[28] R. Jovanović, B. Swiatkowski, S. Kakietek, et al. Mathematical modelling of swirl oxy-fuel burner flame characteristics. *Energy Conversion and Management*, **191** (2019): 193–207.

[29] J. Shen, F. Li, Z. Li, et al. Numerical investigation of air-staged combustion to reduce NOX emissions from biodiesel combustion in industrial furnaces. *Journal of the Energy Institute*, **92** (2019): 704–716.

[30] B. Mayr, R. Prieler, M. Demuth, et al. CFD and experimental analysis of a 115kW natural gas fired lab-scale furnace under oxy-fuel and air–fuel conditions. *Fuel*, **159** (2015): 864–875.

[31] M. Buchmayr, J. Gruber, M. Hargassner, et al. A computationally inexpensive CFD approach for small-scale biomass burners equipped with enhanced air staging. *Energy Conversion and Management*, **115** (2016): 32–42.

[32] R. Prieler, M. Demuth, D. Spoljaric, et al. Evaluation of a steady flamelet approach for use in oxy-fuel combustion. *Fuel*, **118** (2014): 55–68.

[33] R. Prieler, M. Demuth, D. Spoljaric, et al. Numerical investigation of the steady flamelet approach under different combustion environments. *Fuel*, **140** (2015): 731–743.

[34] J. He, Z. Chen, X. Jiang, et al. Combustion characteristics of blast furnace gas in porous media burner. *Applied Thermal Engineering*, **160** (2019): 113970.

[35] X. Shanqing and W. Daohong. Design Features of Air and Gas Double Preheating Regenerative Burner Reheating Furnace. *Energy Procedia*, **66** (2015): 189–192.

[36] G. Rago, G. Rossiello, R. Dadduzio, et al. CFD analysis of a swirl stabilized coal combustion burner. *Energy Procedia*, **148** (2018): 703–711.

[37] A. Đugum and K. Hanjalić. Numerical simulation of coal-air mixture flow in a real double-swirl burner and implications on combustion anomalies in a utility boiler. *Energy*, **170** (2019): 942–953.

[38] M. Ilbas, A. Bektas, and S. Karyeyen. A new burner for oxy-fuel combustion of hydrogen containing low-calorific value syngases: An experimental and numerical study. *Fuel*, **256** (2019): 115990.

[39] T. Morgado, P. J. Coelho, and P. Talukdar. Assessment of uniform temperature assumption in zoning on the numerical simulation of a walking beam reheating furnace. *Applied Thermal Engineering*, **76** (2015): 496–508.

[40] J. Hyun Jang, D. Eun Lee, C. Kim, et al. Prediction of Furnace Heat Transfer and Its Influence on the Steel Slab Heating and Skid Mark Formation in a Reheating Furnace. *Isij International - ISIJ INT*, **48** (2008): 1325–1330.

[41] A. Jaklič, T. Kolenko, and B. Zupančič. The influence of the space between the billets on the productivity of a continuous walking-beam furnace. *Applied Thermal Engineering*, **25** (2005): 783–795.

[42] S. H. Han and D. Chang. Optimum residence time analysis for a walking beam type reheating furnace. *International Journal of Heat and Mass Transfer*, **55** (2012): 4079–4087.

[43] J. H. Jang, D. E. Lee, M. Y. Kim, et al. Investigation of the slab heating characteristics in a reheating furnace with the formation and growth of scale on the slab surface. *International Journal of Heat and Mass Transfer*, **53** (2010): 4326–4332.

[44] A. Jaklič, B. Glogovac, T. Kolenko, et al. A simulation of heat transfer during billet transport. *Applied Thermal Engineering*, **22** (2002): 873–883.

[45] J. Qi, K. Zhou, J. Huang, et al. Numerical simulation of the heat transfer of superheater tubes in power plants considering oxide scale. *International Journal of Heat and Mass Transfer*, **122** (2018): 929–938.

[46] X. Cheng, Z. Jiang, D. Wei, et al. Oxide scale characterization of ferritic stainless steel and its deformation and friction in hot rolling. *Tribology International*, **84** (2015): 61–70.

[47] C. Y. Lee, T. H. Chun, and W. K. In. Effect of change in surface condition induced by oxidation on transient pool boiling heat transfer of vertical stainless steel and copper rodlets. *International Journal of Heat and Mass Transfer*, **79** (2014): 397–407.

[48] S. Liu, D. Tang, H. Wu, et al. Oxide scales characterization of micro-alloyed steel at high temperature. *Journal of Materials Processing Technology*, **213** (2013): 1068–1075.

[49] Y. Tang, J. Laine, T. Fabritius, et al. The Modeling of the Gas Flow and Its Influence on the Scale Accumulation in the Steel Slab Pusher-type Reheating Furnace. *ISIJ International*, **43** (2003): 1333–1341.

[50] T. Husmann and C. S. Magnus. Thermography in incremental forming processes at elevated temperatures. *Measurement*, **77** (2016): 16–28.

[51] M. Švantner, P. Vacíková, and M. Honner. IR thermography heat flux measurement in fire safety applications. *Infrared Physics & Technology*, **55** (2012): 292–298.

[52] S. H. Han, S. W. Baek, and M. Y. Kim. Transient radiative heating characteristics of slabs in a walking beam type reheating furnace. *International Journal of Heat and Mass Transfer*, **52** (2009): 1005–1011.

[53] T. Astarita, G. Cardone, and G. Carlomagno. Infrared thermography: An optical method in heat transfer and fluid flow visualisation. *Optics and Lasers in Engineering*, **44** (2006): 261–281.

[54] M. Švantner, P. Vacíková, and M. Honner. Non-contact charge temperature measurement on industrial continuous furnaces and steel charge emissivity analysis. *Infrared Physics & Technology*, **61** (2013): 20–26.

[55] M. Gu, G. Chen, X. Liu, et al. Numerical simulation of slab heating process in a regenerative walking beam reheating furnace. *International Journal of Heat and Mass Transfer*, **76** (2014): 405–410.

[56] voestalpine Tubulars GmbH & Co KG Technologiekonzern. \\ https://www.voestalpine.com/group/

[57] G. Mosca, D. Lupant, A. Gambale, et al. Effect of the Air Preheating Temperature on Flameless Combustion of Low Calorific, Alternative Fuels. *Proceedings of the European Combustion Meeting* (2013): 7.

[58] J.-K. Lee, I.-B. Lee, and J. Han. Techno-economic analysis of methanol production from joint feedstock of coke oven gas and basic oxygen furnace gas from steel-making. *Journal of Industrial and Engineering Chemistry*, **75** (2019): 77–85.

[59] L. Deng and T. A. Adams. Methanol Production from Coke Oven Gas and Blast Furnace Gas. *Computer Aided Chemical Engineering*, **44** (2018): 163–168.

[60] W.-H. Chen, M.-R. Lin, T.-S. Leu, et al. An evaluation of hydrogen production from the perspective of using blast furnace gas and coke oven gas as feedstocks. *International Journal of Hydrogen Energy*, **36** (2011): 11727–11737.

[61] R. Razzaq, C. Li, and S. Zhang. Coke oven gas: Availability, properties, purification, and utilization in China. *Fuel*, **113** (2013): 287–299.

[62] R. Prieler, B. Mayr, M. Demuth, et al. Prediction of the heating characteristic of billets in a walking hearth type reheating furnace using CFD. *International Journal of Heat and Mass Transfer*, **92** (2016): 675–688.

[63] Z. Ahmed, S. Lecompte, T. d. Raad, et al. Steady State model of a Reheating Furnace for determining slab boundary conditions. *Energy Procedia*, **158** (2019): 5844–5849.

[64] B. Mayr, R. Prieler, M. Demuth, et al. Comparison between solid body and gas radiation in high temperature furnaces under different oxygen enrichments. *Applied Thermal Engineering*, **127** (2017): 679–688.

[65] M. Cavazzuti and M. A. Corticelli. An algorithm for solving steady-state heat conduction in arbitrarily complex composite planar walls with temperature-dependent thermal conductivities. *Applied Thermal Engineering*, **115** (2017): 825–831.

[66] N. Oumarou, D. Kocaefe, and Y. Kocaefe. Investigation of the refractory bricks used for the flue wall of the horizontal anode baking ring furnace. *Ceramics International*, **42** (2016): 18436–18442.

[67] G. E. Totten. Steel Heat Treatment: Metallurgy and Technologies. Portland, Oregon, U.S.A.: Taylor and Francis, 2006.

[68] P. Wang, F. Fan, and Q. Li. Accuracy evaluation of the gray gas radiation model in CFD simulation. *Case Studies in Thermal Engineering*, **3** (2014): 51–58.

[69] H. D. Baehr and K. Stephan. Heat and mass-transfer. Berlin ; New York: Springer, 2006.

[70] F. A. Kulacki. Handbook of thermal science and engineering. New York, NY: Springer Berlin Heidelberg, 2018.

[71] Y. Zhang, Q. Li, and H. Zhou. Theory and calculation of heat transfer in furnaces. Boston, MA: Elsevier, 2016.

[72] H. C. Hottel and A. F. Sarofim. Radiative transfer. Vol. 15. New York: McGraw Hill, 1967.

[73] J. H. Ferziger and M. Perić. Computational methods for fluid dynamics. 3rd, rev. ed. Berlin ; New York: Springer, 2002.

[74] J. F. Wendt and J. D. Anderson, eds. Computational fluid dynamics: An introduction. 3rd ed. Berlin, London: Springer, 2008.

[75] R. Schwarze. CFD Modellierung. Berlin, Heidelberg: Springer Berlin Heidelberg, 2013.

[76] J. Chomiak and J. Jarosiński. Flame quenching by turbulence. *Combustion and Flame*, **48** (1982): 241–249.

[77] D. Bradley. How fast can we burn? *Symposium (International) on Combustion*, **24** (1992): 247–262.

[78] S. B. Pope. Turbulent Flows. Cambridge: Cambridge University Press, 2000.

[79] E. R. Hawkes, R. Sankaran, J. C. Sutherland, et al. Direct numerical simulation of turbulent combustion: fundamental insights towards predictive models. *Journal of Physics: Conference Series*, **16** (2005): 65–79.

[80] T. K. Zhen, M. Zubair, and K. A. Ahmad. Experimental and Numerical Investigation of the Effects of Passive Vortex Generators on Aludra UAV Performance. *Chinese Journal of Aeronautics*, **24** (2011): 577–583.

[81] M. Rudman and H. M. Blackburn. Direct numerical simulation of turbulent non-Newtonian flow using a spectral element method. *Applied Mathematical Modelling*, **30** (2006): 1229–1248.

[82] D. C. Wilcox. Turbulence Modeling for CFD. 3rd. La Canada, California: DCW Industries, 2006.

[83] C. D. Argyropoulos and N. C. Markatos. Recent advances on the numerical modelling of turbulent flows. *Applied Mathematical Modelling*, **39** (2015): 693–732.

[84] M. P. Bulat and P. V. Bulat. Comparison of Turbulence Models in the Calculation of Supersonic Separated Flows. *World Applied Science Journal*, **27** (2013): 1263–1266.

[85] R. C. Morgans, B. B. Dally, G. J. Nathan, et al. Application of the revised Wilcox (1998) k- w turbulence model to a jet in co-flow. *Second International Conference on CFD in the Mineral and Process Industries* (1999): 479–484.

[86] C. G. Speziale, R. Abid, and E. C. Anderson. Critical evaluation of two-equation models for near-wall turbulence. *AIAA Journal*, **30** (1992): 324–331.

[87] S. Hussain, P. H. Oosthuizen, and A. Kalendar. Evaluation of various turbulence models for the prediction of the airflow and temperature distributions in atria. *Energy and Buildings*, **48** (2012): 18–28.

[88] K. Oukassou, S. E. Mouhsine, A. E. Hajjaji, et al. Comparison of the power, lift and drag coefficients of wind turbine blade from aerodynamics characteristics of Naca0012 and Naca2412. *Procedia Manufacturing*, **32** (2019): 983–990.

[89] F. Kuznik, G. Rusaouën, and J. Brau. Experimental and numerical study of a full scale ventilated enclosure: Comparison of four two equations closure turbulence models. *Building and Environment*, **42** (2007): 1043–1053.

[90] H. Yilmaz, O. Cam, S. Tangoz, et al. Effect of different turbulence models on combustion and emission characteristics of hydrogen/air flames. *International Journal of Hydrogen Energy*, **42** (2017): 25744–25755.

[91] S. M. El-Behery and M. H. Hamed. A comparative study of turbulence models performance for separating flow in a planar asymmetric diffuser. *Computers & Fluids*, **44** (2011): 248–257.

[92] A. Escue and J. Cui. Comparison of turbulence models in simulating swirling pipe flows. *Applied Mathematical Modelling*, **34** (2010): 2840–2849.

[93] W. Jones and B. Launder. The prediction of laminarization with a two-equation model of turbulence. *International Journal of Heat and Mass Transfer*, **15** (1972): 301–314.

[94] K. Ghaib. Einführung in die numerische Strömungsmechanik. Wiesbaden: Springer Berlin, 2019.

[95] V. Yakhot and S. A. Orszag. Renormalization group analysis of turbulence. I. Basic theory. *Journal of Scientific Computing*, **1** (1986): 3–51.

[96] H. W. Oh. Computational Fluid Dynamics. Vukovar, Hr: InTech., 2010.

[97] T.-H. Shih, W. W. Liou, A. Shabbir, et al. A new k-e eddy viscosity model for high reynolds number turbulent flows. *Computers & Fluids*, **24** (1995): 227–238.

[98] K. Van Maele, B. Merci, and E. Dick. Comparative Study of k-epsilon Turbulence Models in Inert and Reacting Swirling Flows. *33rd AIAA Fluid Dynamics Conference and Exhibit* (2003): 10.

[99] D. L. Baulch, C. J. Cobos, R. A. Cox, et al. Summary table of evaluated kinetic data for combustion modeling: Supplement 1. *Combustion and Flame*, **98** (1994): 59–79.

[100] D. R. Lide. CRC Handbook of Chemistry and Physics. CRC Press, 1995.

[101] W. Tsang and R. F. Hampson. Chemical Kinetic Data Base for Combustion Chemistry. Part I. Methane and Related Compounds. *Journal of Physical and Chemical Reference Data*, **15** (1986): 1087–1279.

[102] T. Lu and C. K. Law. Toward accommodating realistic fuel chemistry in large-scale computations. *Progress in Energy and Combustion Science*, **35** (2009): 192–215.

[103] G. Smith, D. Golden, M. Frenklach, et al. *GRI-Mech 3.0*. GRI-Mech 3.0. http://combustion.berkeley.edu mech/.

[104] E. Mendoza Orbegoso, F. Luís, L. F. Figueira da Silva, et al. On the predictability of chemical kinetic mechanisms for the description combustion of gaseous fuels. *Proceedings of COBEM*, **20** (2009): 14.

[105] S. Rolland and J. M. Simmie. The comparison of detailed chemical kinetic mechanisms: Application to the combustion of methane. *International Journal of Chemical Kinetics*, **36** (2004): 467–471.

[106] E. S. Oran and J. P. Boris. Numerical Simulation of Reactive Flow. 2nd ed. Cambridge University Press, 2000.

[107] N. Peters. Numerical and asymptotic analysis of systematically reduced reaction schemes for hydrocarbon flames. *Glowinski R., Larrouturou B., Temam R. (eds) Numerical Simulation of Combustion Phenomena. Lecture Notes in Physics*, **241** (1985): 90–109.

[108] J. Warnatz, U. Maas, and R. W. Dibble. Combustion: Physical and Chemical Fundamentals, Modeling and Simulation, Experiments, Pollutant Formation. Vol. 401. Springer Berlin Heidelberg, 1999.

[109] M. D. Smooke, H. Araki, J. Ehlers, et al., eds. Reduced Kinetic Mechanisms and Asymptotic Approximations for Methane-Air Flames: A Topical Volume. Vol. 384. Lecture Notes in Physics. Berlin, Heidelberg: Springer Berlin Heidelberg, 1991.

[110] F. Battin-Leclerc, J. Simmie, and E. Blurock. Cleaner Combustion Developing Detailed Chemical Kinetic Models Preface. New York: Springer, 2013.

[111] T. Turányi and A. S. Tomlin. Analysis of Kinetic Reaction Mechanisms. Berlin, Heidelberg: Springer Berlin Heidelberg, 2014.

[112] H. C. Magel, U. Schnell, and K. R. G. Hein. Simulation of detailed chemistry in a turbulent combustor flow. *Symposium (International) on Combustion*, **26** (1996): 67–74.

[113] A. Kazakov and M. Frenklach. *DRM mechanisms DRM22 and DRM19*. http://combustion.berkeley.edu

[114] D. M. Morett. "A reduced chemical kinetic mechanism for computational fluid dynamics simulations of high brake mean effective pressure, lean-burn natural gas engines." MA thesis. Colorado State University, 2012.

[115] R. Prieler. "Numerical Modelling of Chemistry, Radiation and Transient Heating Characteristics in High Temperature Processes." PhD thesis. Technical University of Graz, 2016.

[116] K. Kundu, P. Penko, and S. Yang. Reduced reaction mechanisms for numerical calculations in combustion of hydrocarbon fuels. *36th AIAA Aerospace Sciences Meeting and Exhibit* (1998): 16.

[117] T. W. J. Peeters. "Numerical modeling of turbulent natural-gas diffusion flames." PhD thesis. Delft University of Technology, 1995.

[118] B. Mayr, R. Prieler, M. Demuth, et al. Computational analysis of a semi-industrial furnace fired by a flat flame burner under different O2/N2 ratios using the steady laminar flamelet approach. *Journal of the Energy Institute*, **90** (2017): 602–612.

[119] R. J. Kee, M. E. Coltrin, P. Glarborg, et al. Chemically Reacting Flow: Theory, Modeling, and Simulation. 2nd ed. Wiley, 2017.

[120] C. K. Westbrook and F. L. Dryer. Simplified Reaction Mechanisms for the Oxidation of Hydrocarbon Fuels in Flames. *Combustion Science and Technology*, **27** (1981): 31–43.

[121] R. Amirante, E. Distaso, P. Tamburrano, et al. Laminar flame speed correlations for methane, ethane, propane and their mixtures, and natural gas and gasoline for spark-ignition engine simulations. *International Journal of Engine Research*, **18** (2017): 951–970.

[122] K. Kuo and R. Acharya. Fundamentals of Turbulent and Multiphase Combustion. Wiley, 2012.

[123] L. P. de Oliveira, D. Hudebine, D. Guillaume, et al. A Review of Kinetic Modeling Methodologies for Complex Processes. *Oil & Gas Science and Technology – Revue d'IFP Energies nouvelles*, **71** (2016): 49.

[124] A. Abou-Taouk and L. Eriksson. Evaluation of Optimized 3-step Global Reaction Mechanism for CFD Simulations on Sandia Flame D. *AIP Conference Proceedings*, **1389** (2011): 66–69.

[125] J. Andersen, C. L. Rasmussen, T. Giselsson, et al. Global Combustion Mechanisms for Use in CFD Modeling under Oxy-Fuel Conditions. *Energy & Fuels*, **23** (2009): 1379–1389.

[126] R. Guderian. Air Pollution by Photochemical Oxidants: Formation, Transport, Control, and Effects on Plants. Berlin, Heidelberg: Springer Berlin Heidelberg, 1985.

[127] N. Peters and F. Williams. The asymptotic structure of stoichiometric methane-air flames. *Combustion and Flame*, **68** (1987): 185–207.

[128] F. Rückert, T. Sabel, U. Schnell, et al. Comparison of different global reaction mechanisms for coal-fired utility boilers. *Progress in Computational Fluid Dynamics, An International Journal*, **3** (2003): 130–139.

[129] N. Peters and B. Rogg, eds. Reduced kinetic mechanisms for applications in combustion systems. Lecture notes in physics. New York: Springer-Verlag, 1993.

[130] R. Bilger. The structure of turbulent nonpremixed flames. *Symposium (International) on Combustion*, **22** (1989): 475–488.

[131] W. Jones and R. Lindstedt. Global reaction schemes for hydrocarbon combustion. *Combustion and Flame*, **73** (1988): 233–249.

[132] J. P. Kim, U. Schnell, and G. Scheffknecht. Comparison of Different Global Reaction Mechanisms for MILD Combustion of Natural Gas. *Combustion Science and Technology*, **180** (2008): 565–592.

[133] C. Yin, L. A. Rosendahl, and S. K. Kær. Chemistry and radiation in oxy-fuel combustion: A computational fluid dynamics modeling study. *Fuel*, **90** (2011): 2519–2529.

[134] F. Hu, P. Li, J. Guo, et al. Global reaction mechanisms for MILD oxy-combustion of methane. *Energy*, **147** (2018): 839–857.

[135] B. Mayr, R. Prieler, M. Demuth, et al. CFD modelling and performance increase of a pusher type reheating furnace using oxy-fuel burners. *Energy Procedia*. INFUB - 11th European Conference on Industrial Furnaces and Boilers **120** (2017): 462–468.

[136] G. H. Yeoh and K. K. Yuen. Computational fluid dynamics in fire engineering: Theory, Modelling and Practice. Elsevier, 2009.

[137] S. De, A. Agarwal, S. Chaudhuri, et al. Modeling and simulations of turbulent combustion. New York, NY: Springer Singapore, 2018.

[138] C. E. Baukal. Heat transfer in industrial combustion. Boca Raton: CRC Press, 2000.

[139] N. Peters. Turbulent Combustion. Cambridge University Press, 2000.

[140] T. Echekki and E. Mastorakos, eds. Turbulent combustion modeling: Advances, new trends and perspectives. Fluid mechanics and its applications 95. Dordrecht: Springer, 2011.

[141] B. F. Magnussen and B. H. Hjertager. On mathematical modeling of turbulent combustion with special emphasis on soot formation and combustion. *Symposium (International) on Combustion*, **16** (1977): 719–729.

[142] D. B. Spalding. Development of the eddy-break-up model of turbulent combustion. *Symposium (International) on Combustion*, **16** (1977): 1657–1663.

[143] M. Buchmayr, J. Gruber, M. Hargassner, et al. Performance analysis of a steady flamelet model for the use in small-scale biomass combustion under extreme air-staged conditions. *Journal of the Energy Institute*, **91** (2018): 534–548.

[144] R. Scharler, T. Fleckl, and I. Obernberger. Modification of a Magnussen Constant of the Eddy Dissipation Model for biomass grate furnaces by means of hot gas in-situ FT-IR absorption spectroscopy. *Progress in Computational Fluid Dynamics*, **3** (2003): 102–111.

[145] A. Shiehnejadhesar, R. Scharler, R. Mehrabian, et al. Development and validation of CFD models for gas phase reactions in biomass grate furnaces considering gas streak formation above the packed bed. *Fuel Processing Technology*, **139** (2015): 142–158.

[146] B. Magnussen, B. Hjertager, J. Olsen, et al. Effects of turbulent structure and local concentrations on soot formation and combustion in C2H2 diffusion flames. *Symposium (International) on Combustion*, **17** (1979): 1383–1393.

[147] P. Wang. The model constant A of the eddy dissipation model. *Progress in Computational Fluid Dynamics, An International Journal*, **16** (2016): 118.

[148] R. Scharler, T. Gruber, A. Ehrenhöfer, et al. Transient CFD simulation of wood log combustion in stoves. *Renewable Energy*, **145** (2020): 651–662.

[149] Q. Li, H. Yang, Y. Wang, et al. Accuracy improvement of the modified EDM model for non-premixed turbulent combustion in gas turbine. *Case Studies in Thermal Engineering*, **6** (2015): 69–76.

[150] B. Magnussen. On the structure of turbulence and a generalized eddy dissipation concept for chemical reaction in turbulent flow. *Aerospace Sciences Meeting*, **19** (1981): 7.

[151] M. Bösenhofer, E.-M. Wartha, C. Jordan, et al. The Eddy Dissipation Concept-Analysis of Different Fine Structure Treatments for Classical Combustion. *Energies*, **11** (2018): 1902.

[152] I. R. Gran and B. F. Magnussen. A Numerical Study of a Bluff-Body Stabilized Diffusion Flame. Part 2. Influence of Combustion Modeling And Finite-Rate Chemistry. *Combustion Science and Technology*, **119** (1996): 191–217.

[153] I. S. Ertesvåg and B. F. Magnussen. The Eddy Dissipation Turbulence Energy Cascade Model. *Combustion Science and Technology*, **159** (2000): 213–235.

[154] B. F. Magnussen. The eddy dissipation concept: A bridge between science and technology. *ECCOMAS Thematic Conference on Computational Combustion* (2005): 25.

[155] S. B. Pope. Computationally efficient implementation of combustion chemistry using in situ adaptive tabulation. *Combustion Theory and Modelling*, **1** (1997): 41–63.

[156] R. Laubscher. "Utilization of artificial neural networks to resolve chemical kinetics in turbulent fine structures of an advanced CFD combustion model." PhD thesis. Stellenbosch University, 2017.

[157] R. W. Bilger. "Turbulent flows with nonpremixed reactants." In: *Turbulent Reacting Flows*. Ed. by P. A. Libby and F. A. Williams. Topics in Applied Physics. Berlin, Heidelberg: Springer Berlin Heidelberg, 1980, 65–113.

[158] B. Merci and T. Beji. Fluid Mechanics Aspects of Fire and Smoke Dynamics in Enclosures. CRC Press, 2016.

[159] R. S. Cant and E. Mastorakos. An Introduction to Turbulent Reacting Flows. London: Imperial College Press, 2007.

[160] T. Poinsot and D. Veynante. Theoretical and Numerical Combustion. 2nd ed. Vol. 28. Philadelphia, PA: R.T. Edwards, 2005.

[161] H. Müller, C. A. Niedermeier, M. Pfitzner, et al. Steady Laminar Flamelet Modeling for turbulent non-premixed Combustion in LES and RANS Simulations. *Sonderforschungsbereich/Transregio 40 (TRR40)-Annual Report* (2015): 139–148.

[162] A. Mukhopadhyay and S. Sen. Fundamentals of Combustion Engineering. CRC Press, 2019.

[163] A. Schwarz and J. Janicka, eds. Combustion noise. Fluid mechanics and its applications. Springer Heidelberg, 2009.

[164] M. F. Modest. Radiative Heat Transfer. Elsevier, 2013.

[165] R. Siegel and J. R. Howell. Thermal radiation heat transfer. 3rd ed. National Aeronautics and Space Administration, 1992.

[166] T. F. Smith, Z. F. Shen, and J. N. Friedman. Evaluation of Coefficients for the Weighted Sum of Gray Gases Model. *J Heat Transfer.* **104** (1982): 602–608.

[167] I. H. Farag and T. A. Allam. Gray-Gas Approximation of Carbon Dioxide Standard Emissivity. *Journal of Heat Transfer*, **103** (1981): 403–405.

[168] P. J. Coelho. Numerical simulation of radiative heat transfer from non-gray gases in three-dimensional enclosures. *Journal of Quantitative Spectroscopy and Radiative Transfer*, **74** (2002): 307–328.

[169] P. S. Cumber and M. Fairweather. Evaluation of flame emission models combined with the discrete transfer method for combustion system simulation. *International Journal of Heat and Mass Transfer*, **48** (2005): 5221–5239.

[170] A. Soufiani and E. Djavdan. A comparison between weighted sum of gray gases and statistical narrow-band radiation models for combustion applications. *Combustion and Flame*, **97** (1994): 240–250.

[171] C. Yin, L. C. R. Johansen, L. A. Rosendahl, et al. New Weighted Sum of Gray Gases Model Applicable to Computational Fluid Dynamics Modeling of Oxy-Fuel Combustion. *Energy & Fuels*, **24** (2010): 6275–6282.

[172] R. Johansson, K. Andersson, B. Leckner, et al. Models for gaseous radiative heat transfer applied to oxy-fuel conditions in boilers. *International Journal of Heat and Mass Transfer*, **53** (2010): 220–230.

[173] J. Zhang, O. Gicquel, D. Veynante, et al. Monte Carlo method of radiative transfer applied to a turbulent flame modeling with LES. *Comptes Rendus Mécanique*, **337** (2009): 539–549.

[174] P. Boulet, A. Collin, and J. L. Consalvi. On the finite volume method and the discrete ordinates method regarding radiative heat transfer in acute forward anisotropic scattering media. *Journal of Quantitative Spectroscopy and Radiative Transfer*, **104** (2007): 460–473.

[175] M. C. W. Dordevich. "Heat transfer analysis of a lab scale solar receiver using the discrete ordinates model." MA thesis. San Diego State University, 2013.

[176] D. Cohen, S. Stamnes, T. Tanikawa, et al. Comparison of discrete ordinate and Monte Carlo simulations of polarized radiative transfer in two coupled slabs with different refractive indices. *Optics Express*, **21** (2013): 9592.

[177] E. Cho and F. Miller. Comparing the Monte Carlo Method to the Discrete Ordinates Methods in Fluent for Calculating Radiation Heat Transfer in a Small Particle Receiver. *Proceedings of the ASME*, **10** (2016).

[178] D. Joseph, P. Perez, and C. Benedicte. Discrete Ordinates and Monte Carlo Methods for Radiative Transfer Simulation applied to CFD combustion modelling. *Journal of Heat transfer*, **131** (2009): 26.

[179] Fluke. *Fluke Industrial Electrical Test Tools, Thermal Imaging, Calibration*. https://www.fluke.com/en.

[180] R. E. Bentley, ed. Handbook of temperature measurement. Singapore ; New York: Springer, 1998.

[181] D. R. Joshi. Engineering Physics: Common for All Engineering Branches. New Delhi: Tata McGraw Hill, 2010.

[182] FLIR. *FLIR Systems*. https://www.flir.com/products/t1030sc/.

[183] M. C. Larciprete, Y. S. Gloy, R. Li Voti, et al. Temperature dependent emissivity of different stainless steel textiles in the infrared range. *International Journal of Thermal Sciences*, **113** (2017): 130–135.

[184] G. G. Gubareff, J. E. Janssen, and R. H. Torborg. Thermal Radiation Properties Survey. Honeywell, 1960.

[185] N. Lallemant, F. Breussin, R. Weber, et al. Flame structure, heat transfer and pollutant emissions characteristics of oxy-natural gas flames in the 0.7-1 MW thermal input range. *Journal of the Energy Institute*, **73** (2000): 169–182.

[186] F. Breussin, N. Lallemant, and R. Weber. Computing of Oxy-Natural Gas Flames using Both a Global Combustion Scheme and a Chemical Equilibrium Procedure. *Combustion Science and Technology*, **160** (2000): 369–397.

[187] E. Ruh and J. S. McDowell. Thermal Conductivity of Refractory Brick. *Journal of the American Ceramic Society*, **45** (1962): 189–195.

[188] T. Ahmad, S. L. Plee, and J. P. Myers. Fluent Theory Guide, ANSYS, Inc., 275 Technology Drive Canonsburg, PA 15317 (2013): 814.

[189] J. Harish and P. Dutta. Heat transfer analysis of pusher type reheat furnace. *Ironmaking & Steelmaking*, **32** (2005): 151–158.

[190] D. Wild, T. Meurer, and A. Kugi. Modelling and experimental model validation for a pusher-type reheating furnace. *Mathematical and Computer Modelling of Dynamical Systems*, **15** (2009): 209–232.

[191] G. W. Lee and M. Y. Kim. On the Thermal Behavior of the Slab in a Reheating Furnace with Radiation. *International Journal of Mechanical and Mechatronics Engineering*, **8** (2014): 922–927.

[192] B. Mayr, R. Prieler, M. Demuth, et al. CFD analysis of a pusher type reheating furnace and the billet heating characteristic. *Applied Thermal Engineering*, **115** (2017): 986–994.

[193] V.-G. V. und Chemieingenieurwesen, ed. VDI-Wärmeatlas. 11th ed. Berlin: Springer Vieweg, 2013.

[194] F.-C. Software. *EES User Manual*. 2018.

[195] J. L. MacNaughton and C. T. Mortimer. Differential scanning calorimetry. Boca Raton: CRC Press, 1975.

[196] C. J. Cremers and H. A. Fine. Thermal Conductivity. Vol. 21. New York: Springer US, 1990.

[197] R. Baboian, ed. Corrosion tests and standards: Application and interpretation. 2nd ed. Conshohocken, PA: ASTM International, 2005.

[198] K. M. Jeong, M. A. Abro, Y. Shi, et al. Corrosion of Fe-(9\$\sim\$37) wt. %Cr Alloys at 700–800\$\grad\$ in (N2, H2O, H2S)-Mixed Gas. *Metals*, **6** (2016): 7.

[199] B. D. Craig and D. B. Anderson, eds. Handbook of corrosion data. 2nd ed. Materials data series. ASM International, 1995.

[200] Z. Ahmad. High Temperature Corrosion. InTechOpen, 2016.

[201] M. Krzyzanowski, J. H. Beynon, and D. C. J. Farrugia. Oxide Scale Behaviour in High Temperature Metal Processing. Weinheim: Wiley-VCH, 2010.

[202] J. B. Adolfi, T. Ekman, J. von Schéele, et al. Scale formation and surface quality of carbon steel at oxyfuel heating. *International Steel Rolling Conference*, **9** (2006): 7.

[203] J. R. Davis. Stainless Steels. ASM International, 1994.

[204] Z. Amjad. Mineral scale formation and inhibition. Brecksville, Ohio: Springer-Verlag New York, 2013.

[205] NIIR Board of Consultants & Engineers. Steel Rolling Technology Handbook. 2nd ed. Delhi: Asia Pacific Business Press Inc., 2018.

[206] C. Schluckner, C. Gaber, M. Demuth, et al. CFD-model to predict the local and time-dependent scale formation of steels in air- and oxygen enriched combustion atmospheres. *Applied Thermal Engineering*, **143** (2018): 822–835.

[207] M. Chabičovský, M. Hnízdil, A. A. Tseng, et al. Effects of oxide layer on Leidenfrost temperature during spray cooling of steel at high temperatures. *International Journal of Heat and Mass Transfer*, **88** (2015): 236–246.

[208] E. Robertson and B. Hemingway. *Estimating heat capacity and heat content of rocks*. Open-File Report 95-622. U.S. Geological Survey, 1995.

[209] T. Akiyama, H. Ohta, R. Takahashi, et al. Measurement and Modeling of Thermal Conductivity for Dense Iron Oxide and Porous Iron Ore Agglomerates in Stepwise Reduction. *ISIJ International*, **32** (1992): 829–837.

[210] C. Sobotka, H. Antrekowitsch, and H. Schnideritsch. The Influence of Oxygen-Enriched Burner Systems on the Scale Formation of Steel Alloys During Heating Processes. *AISTech Proceedings* (2014): 3115–3131.

[211] M. Torres and R. Colás. A model for heat conduction through the oxide layer of steel during hot rolling. *Journal of Materials Processing Technology*, **105** (2000): 258–263.

[212] L. Sun and W. Yan. Prediction of wall temperature and oxide scale thickness of ferritic–martensitic steel superheater tubes. *Applied Thermal Engineering*, **134** (2018): 171–181.

[213] P. Wikström, Y. Weihong, and W. Blasiak. The Influence of Oxide Scale on Heat Transfer during Reheating of Steel. *steel research international*, **79** (2008): 765–775.

[214] R. Bürgel, H. J. Maier, and T. Niendorf. Handbuch Hochtemperatur-Werkstofftechnik: Grundlagen, Werkstoffbeanspruchungen, Hochtemperaturlegierungen und -beschichtungen. 4th ed. Wiesbaden: Vieweg + Teubner, 2011.

[215] B. Buchmayr. Werkstoff und Produktionstechnik mit Mathcad. Berlin, Heidelberg: Springer Berlin Heidelberg, 2002.

[216] J. Wang, Y. Liu, B. Sundén, et al. Analysis of slab heating characteristics in a reheating furnace. *Energy Conversion and Management*, **149** (2017): 928–936.

[217] A. M. García and A. A. Amell. A numerical analysis of the effect of heat recovery burners on the heat transfer and billet heating characteristics in a walking-beam type reheating furnace. *International Journal of Heat and Mass Transfer*, **127** (2018): 1208–1222.

[218] S. S. Hou, C. H. Chen, C. Y. Chang, et al. Firing blast furnace gas without support fuel in steel mill boilers. *Energy Conversion and Management*, **52** (2011): 2758–2767.

[219] F. A. D. Oliveira, J. A. Carvalho, P. M. Sobrinho, et al. Analysis of oxy-fuel combustion as an alternative to combustion with air in metal reheating furnaces. *Energy*, **78** (2014): 290–297.

[220] S. H. Han, Y. S. Lee, J. Cho, et al. Efficiency analysis of air-fuel and oxy-fuel combustion in a reheating furnace. *International Journal of Heat and Mass Transfer*, **121** (2018): 1364–1370.

[221] K.-K. Wu, Y.-C. Chang, C.-H. Chen, et al. High-efficiency combustion of natural gas with 21–30% oxygen-enriched air. *Fuel*, **89** (2010): 2455–2462.

[222] P. Bělohradský, P. Skryja, and I. Hudák. Experimental study on the influence of oxygen content in the combustion air on the combustion characteristics. *Energy*, **75** (2014): 116–126.

[223] H. Kremer, F. May, and S. Wirtz. The influence of furnace design on the NO formation in high temperature processes. *Energy Conversion and Management*, **42** (2001): 1937–1952.

[224] J. Oh, U. Han, J. Park, et al. Numerical investigation on energy performance of hot stamping furnace. *Applied Thermal Engineering*, **147** (2019): 694–706.

[225] M. Kuang, Z. Li, Z. Ling, et al. Effect of overfire air angle on flow characteristics within a small-scale model for a deep-air-staging down-fired furnace. *Energy Conversion and Management*, **79** (2014): 367–376.

[226] M. Kuang, G. Yang, Q. Zhu, et al. Effect of burner location on flow-field deflection and asymmetric combustion in a 600MWe supercritical down-fired boiler. *Applied Energy*, **206** (2017): 1393–1405.

[227] J. Oh, E. Lee, and D. Noh. Development of an oxygen-enhanced combustor for scrap preheating in an electric arc furnace. *Applied Thermal Engineering*, **91** (2015): 749–758.

[228] M. T. Lewandowski and I. S. Ertesvåg. Analysis of the Eddy Dissipation Concept formulation for MILD combustion modelling. *Fuel*, **224** (2018): 687–700.

[229] M. Mansourian and R. Kamali. Modifying the constant coefficients of Eddy-dissipation concept model in moderate or intense low-oxygen dilution combustion using inverse problem methodology. *Acta Astronautica*, **162** (2019): 546–554.

[230] A. Mardani. Optimization of the Eddy Dissipation Concept (EDC) model for turbulence-chemistry interactions under hot diluted combustion of CH4/H2. *Fuel*, **191** (2017): 114–129.

[231] A. Parente, M. R. Malik, F. Contino, et al. Extension of the Eddy Dissipation Concept for turbulence/chemistry interactions to MILD combustion. *Fuel*, **163** (2016): 98–111.

[232] A. De, E. Oldenhof, P. Sathiah, et al. Numerical Simulation of Delft-Jet-in-Hot-Coflow (DJHC) Flames Using the Eddy Dissipation Concept Model for Turbulence–Chemistry Interaction. *Flow, Turbulence and Combustion*, **87** (2011): 537–567.

[233] J. Aminian, C. Galletti, and L. Tognotti. Extended EDC local extinction model accounting finite-rate chemistry for MILD combustion. *Fuel*, **165** (2016): 123–133.

[234] J. Aminian, C. Galletti, S. Shahhosseini, et al. Numerical Investigation of a MILD Combustion Burner: Analysis of Mixing Field, Chemical Kinetics and Turbulence-Chemistry Interaction. *Flow, Turbulence and Combustion*, **88** (2012): 597–623.

[235] N. Yu, S. Samant, and P. Rubbert. Flow prediction for propfan configurations using Euler equations. *Fluid Dynamics, Plasma Dynamics, and Lasers Conference*, **17** (1984): 9.

[236] J. Alonso, A. Jameson, J. Alonso, et al. An efficient multiblock method for aerodynamic analysis and design on distributed memory systems. *Computational Fluid Dynamics Conference*, **13** (1997): 27.

[237] D. Drikakis. A parallel multiblock characteristic-based method for three-dimensional incompressible flows. *Advances in Engineering Software*, **26** (1996): 111–119.

[238] M. Leschziner and F. Lien. Computation of Physically Complex Turbulent Flows on Parallel Computers with a Multiblock Algorithm. *Proceedings of the Parallel CFD Conference* (1998): 3–14.

[239] A. Mambro, E. Galloni, F. Congiu, et al. Modelling of low-pressure steam turbines operating at very low flowrates: A multiblock approach. *Applied Thermal Engineering*, **158** (2019): 113782.

[240] H. R. Kheirandish and J. Nakamichi. Development of a Multi-Block/Overset Grid Solver. *International Congress of the Aeronautical Sciences*, **24** (2004): 10.

[241] Z. Ali, P. Tucker, C. Dhanasekaran, et al. Optimal multi-block mesh generation for CFD. *International Journal of Computational Fluid Dynamics* (2017): 19.

[242] N. J. Yu, H. C. Chen, T. Y. Su, et al. Development of a General Multiblock Flow Solver for Complex Configurations. *Proceedings of the Eighth GAMM-Conference on Numerical Methods in Fluid Mechanics*, **29** (1990): 603–612.

[243] H. Nilsson, S. Dahlström, and L. Davidson. Parallel multiblock CFD computations applied to industrial cases. *Parallel Computational Fluid Dynamics 2000* (2001): 525–532.

[244] Y. Zhang, Y. Jia, and S. S. Y. Wang. A Conservative Multi-block Algorithm for Two-dimensional Numerical Model. *International Journal of Mathematical, Computational, Physical, Electrical and Computer Engineering*, **1** (2007): 43–55.

[245] C. d. Nicola, R. Tognaccini, and P. Visingardi. Multiblock structured algorithms in parallel CFD. *Parallel Computational Fluid Dynamics* (1996): 1–8.

[246] B. Mayr, R. Prieler, M. Demuth, et al. The usability and limits of the steady flamelet approach in oxy-fuel combustions. *Energy*, **90** (2015): 1478–1489.

[247] Y. Hu, C. Tan, J. Broughton, et al. Development of a first-principles hybrid model for large-scale reheating furnaces. *Applied Energy*, **173** (2016): 555–566.

[248] R. Tucker and J. Ward. Identifying and quantifying energy savings on fired plant using low cost modelling techniques. *Applied Energy*, **89** (2012): 127–132.

[249] E. Blanco, J. M. Vargas, F. Medina, et al. Mathematical Model of the Heating of Round Billets in a Rotary Hearth Furnace for the Production of Seamless Steel Tubes. *IFAC Proceedings Volumes*, **22** (1989): 161–166.

[250] V. Mureșan, M. Abrudean, and T. Colosi. Modeling and Simulation of the billet's heating process in a furnace with rotary hearth. *International Conference on System Theory, Control and Computing*, **15** (2011): 1–6.

[251] V. Mureşan and M. Abrudean. The Control of the Billets Heating Process in a Furnace with Rotary Hearth. *IFAC Proceedings Volumes*, **45** (2012): 735–740.

[252] E. Malfa, V. Battaglia, A. DellaRocca, et al. Advanced design methods for rotary hearth furnaces. *Steel Times International* (2012): 5.

[253] M. Lantz, D. Hassenzahl, A. Lugnet, et al. 25% Increased Reheating Throughput and 50% Reduced Fuel Consumption by Flameless Oxyfuel at ArcelorMittal Shelby - Tubular Products, Ohio. *AISTech Proceedings*, **6** (2009): 29–36.